FEDERAL UNIVERSITY OF ESPÍRITO SANTO

TECHNOLOGICAL CENTER

GRADUATE PROGRAM IN ELECTRICAL ENGINEERING

LEANDRO CASSA MACEDO

MASTERS DISSERTATION

Fault diagnosis in electrical motors through vibration monitoring using Fiber Bragg Grating-based accelerometers

---

Vitória, ES, Brazil
2023

UFES

FEDERAL UNIVERSITY OF ESPÍRITO SANTO

MASTERS DISSERTATION

Fault diagnosis in electrical motors through vibration monitoring using Fiber Bragg Grating-based accelerometers

---

Author:
Leandro Cassa Macedo

Supervisors:
Prof. Dr. Arnaldo Leal-Junior
Prof. Dr. Anselmo Frizera

A dissertation submitted in fulfillment of the requirements
for the degree of Master in Electrical Engineering

in the

LabSensores
Electrical Engineering Department

Vitória, ES, Brazil
2023

UFES

Ficha catalográfica disponibilizada pelo Sistema Integrado de
Bibliotecas - SIBI/UFES e elaborada pelo autor

Cassa Macedo, Leandro, 1996-
C343f Fault diagnosis in electrical motors through vibration monitoring using Fiber Bragg Grating-based accelerometers / Leandro Cassa Macedo. - 2023.
152 f. : il.

Orientador: Arnaldo Gomes Leal Junior.
Coorientador: Anselmo Frizera Neto.
Dissertação (Mestrado em Engenharia Elétrica) - Universidade Federal do Espírito Santo, Centro Tecnológico.

1. Optical fiber sensors. 2. Fiber Bragg Grating based accelerometers. 3. Fault diagnosis. 4. Structure health monitoring. I. Gomes Leal Junior, Arnaldo. II. Frizera Neto, Anselmo. III. Universidade Federal do Espírito Santo. Centro Tecnológico. IV. Título.

CDU: 621.3

LEANDRO CASSA MACEDO

Fault diagnosis in electrical motors through vibration monitoring using Fiber Bragg Grating-based accelerometers

Dissertation presented to the Graduate Program in Electrical Engineering of the Federal University of Espírito Santo, as a partial requirement for the degree of Master in Electrical Engineering

Arnaldo Gomes Leal Junior

Prof. Dr. Arnaldo Gomes Leal Junior - Advisor
Graduate Program in Electrical Engineering
Federal University of Espírito Santo

Anselmo Frizera Neto

Prof. Dr. Anselmo Frizera Neto - Co-Advisor
Graduate Program in Electrical Engineering
Federal University of Espírito Santo

Prof. Dr. Camilo Arturo Rodríguez Díaz
Graduate Program in Electrical Engineering
Federal University of Espirito Santo

Rui Min

Prof. Dr. Rui Min
Center for Cognition and Neuroergonomics
State Key Laboratory of Cognitive Neuroscience and Learning
Beijing Normal University, Zhuhai, China

Abstract

Structural Health Monitoring (SHM) techniques have been explored in fault and damage diagnosis in structures and machines. These techniques are explored within the scope of Industry 4.0 and Smart Cities, where the data provided by SHM techniques are used in the development of predictive and preventive maintenance plans, avoiding catastrophic failures, reducing machinery downtime, and providing more security in the cities. Sensor development plays an important role in this scenario since these devices are responsible for turning physical measurements into data that are capable of being processed to provide data-based decisions in industrial processes and city management. Different types of sensors are developed to attend to industrial requirements, such as thermocouples for temperature measurements, accelerometers for acceleration measurements, and strain gauges for strain measurements. In this context, optical fiber sensors can offer some advantages for sensor applications: they can be immunity to electromagnetic interference (ideal for industrial harsh environments), can be easily embedded into structures since they are thin and flexible, can be multiplexed (i.e. produce multiple sensors in the same optical fiber cable), and can combine sensing and data transmission over long distances applications using the same optical fiber cable. In this work, a Fiber Bragg Grating-based accelerometer design is reported for machinery fault diagnosis. Different geometries are analyzed as candidates for developing FBG-based accelerometer projects. Through analytical models, the flexible hinge structure was selected based on the sensitivity and natural frequency features to attend to the project requirements. The geometric dimensions are then selected by a multi-objective optimization procedure, in which a variety of combinations of geometric parameters are evaluated with respect to sensitivity and natural frequency. This procedure served as an efficient tool for varying different geometric parameters to find combinations that maximize sensitivity and natural frequency. Four structures are selected to compose this work and, before fabrication, they are analyzed using a Finite Element Modal Analysis. These results were compared to the analytical model results, implying relative errors of 23%, 33%, 14%, and 6% for accelerometers 1, 2, 3, and 4, respectively. These errors are related to idealizations assumed and neglected effects in the analytical models. The sensors were then fabricated and characterized. The experimental natural frequencies were 607.8 Hz, 366.7 Hz, 294.7 Hz, and 236.5 Hz for accelerometers 1, 2, 3, and 4, respectively. The experimental sensitivities are characterized by the exciting frequencies of 17 Hz, 35 Hz, and 50 Hz. For 17 Hz, the experimental sensitivities were 180 pm/g, 690 pm/g, 380 pm/g, and 400 pm/g, for accelerometers 1, 2, 3, and 4, correspondingly. For 35 Hz, the experimental sensitivities were 150 pm/g, 510 pm/g, 290 pm/g, and 230 pm/g, for accelerometers 1, 2, 3, and 4, respectively. For 50 Hz, the experimental sensitivities were 120 pm/g, 410 pm/g, 150 pm/g, and 160 pm/g, for accelerometers 1, 2, 3, and 4, respectively. These sensors were applied in fault diagnosis experiments for 9 fault conditions, where the results were compared and validated by a commercial piezoelectric accelerometer. The comparison between the identified peaks by the FBG-based accelerometers with the results obtained by the PZT-based accelerometers can be used to estimate an average relative error. For the FBG-based accelerometer 2, the relative errors are 0.48%, 0.62%, 0.50%, 0.32%, 0.76%, 0.26%, 0.39%, 0.40%, and 0.48%, for fault conditions 1, 2, 3, 4, 5, 6, 7, 8, and 9, respectively. For the FBG-based accelerometer 3, the relative errors are 0.27%, 0.72%, 0.39%, 0.22%, 0.95%, 0.29%, 0.29%, 0.40%, and 0.85%, for fault conditions 1, 2, 3, 4, 5, 6, 7, 8, and 9, respectively. For all cases, the FBG-based accelerometer frequency vibration spectra were similar to the piezoelectric accelerometer measurements, and it was concluded that the projected accelerometers in this work identified correctly the vibration pattern in all fault conditions.

Keywords: optical fiber sensors, Fiber Bragg Grating based accelerometers, fault diagnosis, structure health monitoring.

Resumo

Técnicas de Monitoramento de Saúde Estrutural (SHM) têm sido exploradas no diagnóstico de falhas e danos em estruturas e máquinas. Essas técnicas são exploradas no escopo da Indústria 4.0 e Cidades Inteligentes, no qual os dados fornecidos pelas técnicas de SHM são utilizados no desenvolvimento de planos de manutenção preditiva e preventiva, evitando falhas catastróficas, reduzindo o tempo de inatividade das máquinas e proporcionando maior segurança nas cidades. O desenvolvimento de sensores desempenha um papel importante nesse cenário, uma vez que esses dispositivos são responsáveis por transformar medições físicas em dados que podem ser processados para fornecer decisões baseadas em dados em processos industriais e gerenciamento de cidades. Diferentes tipos de sensores são desenvolvidos para atender a requisitos industriais, como termopares para medições de temperatura, acelerômetros para medições de aceleração e extensômetros para medições de deformação. Nesse contexto, os sensores de fibra óptica podem oferecer algumas vantagens para aplicações de sensores: eles podem ser imunes a interferências eletromagnéticas (ideais para ambientes industriais hostis), podem ser facilmente incorporados em estruturas, pois são finos e flexíveis, podem ser multiplexados (ou seja, produzir vários sensores no mesmo cabo de fibra óptica) e podem combinar o sensoriamento e a transmissão de dados em aplicações de longa distância usando o mesmo cabo de fibra óptica. Neste trabalho, um projeto de acelerômetro baseado em Grade de Bragg de Fibra Óptica (FBG) é relatado para diagnóstico de falhas em máquinas. Diferentes geometrias são analisadas como candidatas para o desenvolvimento de projetos de acelerômetros baseados em FBG. Através de modelos analíticos, a estrutura de articulação flexível foi selecionada com base nas características de sensibilidade e frequência natural para atender aos requisitos do projeto. As dimensões geométricas são então selecionadas por um procedimento de otimização multiobjetivo, no qual diversas combinações de parâmetros geométricos são avaliadas em relação à sensibilidade e à frequência natural. Esse procedimento serviu como uma ferramenta eficiente para variar diferentes parâmetros geométricos a fim de encontrar combinações que maximizassem a sensibilidade e a frequência natural. Quatro estruturas foram selecionadas para compor este trabalho e, antes da fabricação, foram analisadas usando uma Análise Modal de Elementos Finitos. Esses resultados foram comparados com os resultados do modelo analítico, implicando erros relativos de 23%, 33%, 14% e 6% para os acelerômetros 1, 2, 3 e 4, respectivamente. Esses erros estão relacionados a idealizações assumidas e efeitos negligenciados nos modelos analíticos. Os sensores foram então fabricados e caracterizados. As frequências naturais experimentais foram de 607,8 Hz, 366,7 Hz, 294,7 Hz e 236,5 Hz para os acelerômetros 1, 2, 3 e 4, respectivamente. As sensibilidades experimentais são caracterizadas pelas frequências excitadoras de 17 Hz, 35 Hz e 50 Hz. Para 17 Hz, as sensibilidades experimentais foram de 180 pm/g, 690 pm/g, 380 pm/g e 400 pm/g, para os acelerômetros 1, 2, 3 e 4, respectivamente. Para 35 Hz, as sensibilidades experimentais foram de 150 pm/g, 510 pm/g, 290 pm/g e 230 pm/g, para os acelerômetros 1, 2, 3 e 4, respectivamente. Para 50 Hz, as sensibilidades experimentais foram de 120 pm/g, 410 pm/g, 150 pm/g e 160 pm/g, para os acelerômetros 1, 2, 3 e 4, respectivamente. Esses sensores foram aplicados em experimentos de diagnóstico de falhas para 9 condições de falha, nos quais os resultados foram comparados e validados por um acelerômetro piezoelétrico comercial. A comparação entre os picos identificados pelos acelerômetros baseados em FBG com os resultados obtidos pelos acelerômetros baseados em PZT pode ser usada para estimar um erro relativo médio. Para o acelerômetro baseado em FBG 2, os erros relativos são de

0,48%, 0,62%, 0,50%, 0,32%, 0,76%, 0,26%, 0,39%, 0,40% e 0,48%, para as condições de falha 1, 2, 3, 4, 5, 6, 7, 8 e 9, respectivamente. Para o acelerômetro baseado em FBG 3, os erros relativos são de 0,27%, 0,72%, 0,39%, 0,22%, 0,95%, 0,29%, 0,29%, 0,40% e 0,85%, para as condições de falha 1, 2, 3, 4, 5, 6, 7, 8 e 9, respectivamente. Para todos os casos, os espectros de vibração de frequência dos acelerômetros baseados em FBG foram semelhantes às medições do acelerômetro piezoelétrico, e concluiu-se que os acelerômetros projetados neste trabalho identificaram corretamente o padrão de vibração em todas as condições de falha.

Palavras-chave: sensores baseados em fibras ópticas, acelerômetros baseados em redes de Bragg, monitoramento estrutural, identificação de falhas.

Acknowledgements

My sincere gratitude goes out to LabSensores, Laboratório de Telecomunicações (LabTel), Laboratório de Dinâmica de Sistemas e Estrutursa Mecânicas (LabDin), Institute of Applied Computational Intelligence - I^2CA, and Centro de Pesquisa, Inovação e Desenvolvimento (CPID). This work would not be possible without these laboratories and institutions. Additionally, I would like to extend my sincere gratitude to my supervisors, Prof. Dr. Arnaldo Leal-Junior and Prof. Dr. Anselmo Frizera. The patience and support you provided were fundamental to the success of this project. My sincere appreciation goes out to all of my colleagues, each of you has made a significant contribution to this project. Last but not least, I would like to thank my university, the Federal University of Espírito Santo, and the Graduate Program in Electrical Engineering for the structure and the wealth of knowledge offered to the university community.

This research is financed by FAPES (973/2022, 256/2021, 1004/2022, 2021-07KJ2, 2022-C5K3H, 459/2021), CNPq (310709/2021-0, 440064/2022-8, 405336/2022-5, 304049/2019-0), MCTI/FNDCT/FINEP 2784/20 and 0036/21.

Contents

Abstract **ii**

Resumo **v**

Acknowledgements **vi**

1 Introduction **1**
- 1.1 Motivation . . . 1
- 1.2 Justification . . . 2
- 1.3 Objectives . . . 3
- 1.4 Contributions . . . 4
- 1.5 Document structure . . . 4

2 Theoretical Background **5**
- 2.1 Electric Motors Faults . . . 5
- 2.2 Optical Fibers . . . 8
- 2.3 Fiber Bragg Gratings . . . 12
- 2.4 Optical Fiber Accelerometer Design . . . 18
- 2.5 Multi-objective optimization . . . 22

3 Materials and Methods **26**
- 3.1 Machinery Fault Simulator . . . 26
- 3.2 Fiber Bragg Grating-based Accelerometer Design . . . 27
  - 3.2.1 Grating inscription . . . 27
  - 3.2.2 Analytical models . . . 27
    - 3.2.2.1 Double-L Cantilever Structure . . . 28
    - 3.2.2.2 Single Cantilever . . . 29
    - 3.2.2.3 Triangular Cantilever . . . 30
    - 3.2.2.4 Clamped-Clamped Cantilever . . . 31
    - 3.2.2.5 Steel Tube-Mass Block Elastic Structure . . . 32
    - 3.2.2.6 Flexible Hinges . . . 33
  - 3.2.3 Multi-objective optimization . . . 34
  - 3.2.4 Finite element method analysis . . . 36
  - 3.2.5 Project Requirements . . . 36
- 3.3 Experimental setup . . . 37
  - 3.3.1 Temperature influence . . . 37
  - 3.3.2 Accelerometers characterization . . . 38
  - 3.3.3 Machinery fault diagnosis experiments . . . 39
- 3.4 Data analysis . . . 41

4 Results and Discussions 42
4.1 Analytical models . . . 42
4.1.1 Double-L Cantilever Structure . . . 42
4.1.2 Single cantilever . . . 42
4.1.3 Triangular cantilever . . . 44
4.1.4 Clamped-Clamped Cantilever . . . 45
4.1.5 Steel Tube-Mass Block Elastic Structure . . . 45
4.1.6 Flexible Hinges . . . 46
4.1.7 Analytical results summary . . . 47
4.2 Multi-objective optimization . . . 47
4.3 Finite element analysis . . . 48
4.4 FBG-Based accelerometers characterization . . . 49
4.5 Machinery fault diagnosis . . . 56
4.5.1 Fault condition 1 . . . 56
4.5.2 Fault condition 2 . . . 62
4.5.3 Fault condition 3 . . . 68
4.5.4 Fault condition 4 . . . 74
4.5.5 Fault condition 5 . . . 79
4.5.6 Fault condition 6 . . . 84
4.5.7 Fault condition 7 . . . 89
4.5.8 Fault condition 8 . . . 92
4.5.9 Fault condition 9 . . . 97
4.5.10 Results summary . . . 100

5 Conclusions and future work 102

A Analytical models mathematical full development 104
A.1 Analytical models . . . 104
A.1.1 Double-L Cantilever Structure . . . 104
A.1.2 Single Cantilever . . . 107
A.1.3 Triangular Cantilever . . . 109
A.1.4 Clamped-Clamped Cantilever . . . 111
A.1.5 Steel Tube-Mass Block Elastic Structure . . . 112
A.1.6 Flexible Hinges . . . 113

Bibliography 117

List of Figures

2.1 Schematic representation of ball bearing faults. 6
2.2 Schematic representation of shaft misalignment. 6
2.3 Schematic representation of imbalance. 7
2.4 Schematic representation of rotor broken bar. 8
2.5 Graded and step-index schematic representation. 9
2.6 Trench-assisted profile schematic representation. 9
2.7 Photonic crystal profile schematic representation. 10
2.8 D-shaped index profile schematic representation. 10
2.9 Schematic representation of Tilted Fiber Bragg Gratings. 12
2.10 Schematic representation of Phase-shifted Fiber Bragg Grating. 13
2.11 Schematic representation of Long-period Fiber Bragg Grating. 14
2.12 Schematic representation of Chirped Fiber Bragg Grating. 14
2.13 Schematic representation of uniform Fiber Bragg Grating. 15
2.14 Schematic representation of phase mask fabrication technique. 16
2.15 Schematic representation of FBG-based accelerometer structures. . . . 21
2.16 Schematics representation of resonant frequency and acceleration sensitivity for accelerometers. 22
2.17 NSGA-II workflow represented in a flowchart diagram. 24

3.1 Machinery Fault Simulator Lite. 26
3.2 MFS Mechanical System. 27
3.3 Schematic representation of Double-L Cantilever based on FBGs. . . . 28
3.4 Mechanical model of the Double-L Cantilever structure. 28
3.5 Single cantilever structure and its mechanical model. 29
3.6 Schematic of triangular cantilever structure. 30
3.7 Side and bottom view of a Clamped-Clamped beam structure. 31
3.8 Steel tube-mass block elastic structure-based accelerometer geometry. . 32
3.9 Flexible hinges accelerometer structure. 33
3.10 Flexible hinges accelerometer mechanical model under an external acceleration. 34
3.11 FEA Modal boundary conditions for the flexible hinges structures. . . 37
3.12 FBG-based accelerometers experimental characterization setup. 40
3.13 FBG-based accelerometers attached to the MFS bearings. 41

4.1 Natural frequency and sensitivity for the double-l cantilever structure. 43
4.2 Natural frequency and sensitivity for the single cantilever structure. . 44
4.3 Natural frequency and sensitivity for the triangular cantilever structure. 45
4.4 Natural frequency and sensitivity for the clamped-clamped cantilever structure. 46
4.5 Natural frequency and sensitivity for the steel tube-mass block elastic structure. 46
4.6 Natural frequency and sensitivity for the steel tube-mass block elastic structure. 47

4.7 Multi-objective optimization Pareto front. 49
4.8 FEA Modal analysis results for (A) Accelerometer 1, (B) Accelerometer 2, (C) Accelerometer 3, and (D) Accelerometer 4. 50
4.9 Acceleration-output voltage relationship for the vibration test system power amplifier for 17, 35, and 50 Hz. 51
4.10 Sensitivity characterization results for (A) Accelerometer 1, (B) Accelerometer 2, (C) Accelerometer 3, and (D) Accelerometer 4. 52
4.11 Natural frequency characterization results for (A) Accelerometer 1, (B) Accelerometer 2, (C) Accelerometer 3, and (D) Accelerometer 4. . . 53
4.12 Fault condition 1 vibration frequency spectra for rotor speed at 17 rps for (A) FBG Acc. 2, (B) PZT Acc. at Bearing 1, (C) FBG Acc. 2 (unb), and (D) PZT Acc. at Bearing 1 (unb). 58
4.13 Fault condition 1 vibration frequency spectra for rotor speed at 35 rps for (A) FBG Acc. 2, (B) PZT Acc. at Bearing 1, (C) FBG Acc. 2 (unb), and (D) PZT Acc. at Bearing 1 (unb) 59
4.14 Fault condition 1 vibration frequency spectra for rotor speed at 17 rps for (A) FBG Acc. 3, (B) PZT Acc. at Bearing 2, (C) FBG Acc. 3 (unb), and (D) PZT Acc. at Bearing 2 (unb) 60
4.15 Fault condition 1 vibration frequency spectra for rotor speed at 35 rps for (A) FBG Acc. 3, (B) PZT Acc. at Bearing 2, (C) FBG Acc. 3 (unb), and (D) PZT Acc. at Bearing 2 (unb) 61
4.16 Fault condition 2 vibration frequency spectra for rotor speed at 17 rps for (A) FBG Acc. 2, (B) PZT Acc. at Bearing 1, (C) FBG Acc. 2 (unb), and (D) PZT Acc. at Bearing 1 (unb). 64
4.17 Fault condition 2 vibration frequency spectra for rotor speed at 35 rps for (A) FBG Acc. 2, (B) PZT Acc. at Bearing 1, (C) FBG Acc. 2 (unb), and (D) PZT Acc. at Bearing 1 (unb) 65
4.18 Fault condition 2 vibration frequency spectra for rotor speed at 17 rps for (A) FBG Acc. 3, (B) PZT Acc. at Bearing 2, (C) FBG Acc. 3 (unb), and (D) PZT Acc. at Bearing 2 (unb) 66
4.19 Fault condition 2 vibration frequency spectra for rotor speed at 35 rps for (A) FBG Acc. 3, (B) PZT Acc. at Bearing 2, (C) FBG Acc. 3 (unb), and (D) PZT Acc. at Bearing 2 (unb) 67
4.20 Fault condition 3 vibration frequency spectra for rotor speed at 17 rps for (A) FBG Acc. 2, (B) PZT Acc. at Bearing 1, (C) FBG Acc. 2 (unb), and (D) PZT Acc. at Bearing 1 (unb). 70
4.21 Fault condition 3 vibration frequency spectra for rotor speed at 35 rps for (A) FBG Acc. 2, (B) PZT Acc. at Bearing 1, (C) FBG Acc. 2 (unb), and (D) PZT Acc. at Bearing 1 (unb) 71
4.22 Fault condition 3 vibration frequency spectra for rotor speed at 17 rps for (A) FBG Acc. 3, (B) PZT Acc. at Bearing 2, (C) FBG Acc. 3 (unb), and (D) PZT Acc. at Bearing 2 (unb) 72
4.23 Fault condition 3 vibration frequency spectra for rotor speed at 35 rps for (A) FBG Acc. 3, (B) PZT Acc. at Bearing 2, (C) FBG Acc. 3 (unb), and (D) PZT Acc. at Bearing 2 (unb) 73
4.24 Fault condition 4 vibration frequency spectra for rotor speed at 17 rps for (A) FBG Acc. 2, (B) PZT Acc. at Bearing 1, (C) FBG Acc. 2 (unb), and (D) PZT Acc. at Bearing 1 (unb). 75
4.25 Fault condition 4 vibration frequency spectra for rotor speed at 35 rps for (A) FBG Acc. 2, (B) PZT Acc. at Bearing 1, (C) FBG Acc. 2 (unb), and (D) PZT Acc. at Bearing 1 (unb). 76

4.26 Fault condition 4 vibration frequency spectra for rotor speed at 17 rps for (A) FBG Acc. 3, (B) PZT Acc. at Bearing 2, (C) FBG Acc. 3 (unb), and (D) PZT Acc. at Bearing 2 (unb). 77
4.27 Fault condition 4 vibration frequency spectra for rotor speed at 35 rps for (A) FBG Acc. 3, (B) PZT Acc. at Bearing 2, (C) FBG Acc. 3 (unb), and (D) PZT Acc. at Bearing 2 (unb). 78
4.28 Fault condition 5 vibration frequency spectra for rotor speed at 17 rps for (A) FBG Acc. 2, (B) PZT Acc. at Bearing 1, (C) FBG Acc. 2 (unb), and (D) PZT Acc. at Bearing 1 (unb). 80
4.29 Fault condition 5 vibration frequency spectra for rotor speed at 35 rps for (A) FBG Acc. 2, (B) PZT Acc. at Bearing 1, (C) FBG Acc. 2 (unb), and (D) PZT Acc. at Bearing 1 (unb). 81
4.30 Fault condition 5 vibration frequency spectra for rotor speed at 17 rps for (A) FBG Acc. 3, (B) PZT Acc. at Bearing 2, (C) FBG Acc. 3 (unb), and (D) PZT Acc. at Bearing 2 (unb). 82
4.31 Fault condition 5 vibration frequency spectra for rotor speed at 35 rps for (A) FBG Acc. 3, (B) PZT Acc. at Bearing 2, (C) FBG Acc. 3 (unb), and (D) PZT Acc. at Bearing 2 (unb). 83
4.32 Fault condition 6 vibration frequency spectra for rotor speed at 17 rps for (A) FBG Acc. 2, (B) PZT Acc. at Bearing 1, (C) FBG Acc. 2 (unb), and (D) PZT Acc. at Bearing 1 (unb). 85
4.33 Fault condition 6 vibration frequency spectra for rotor speed at 35 rps for (A) FBG Acc. 2, (B) PZT Acc. at Bearing 1, (C) FBG Acc. 2 (unb), and (D) PZT Acc. at Bearing 1 (unb). 86
4.34 Fault condition 6 vibration frequency spectra for rotor speed at 17 rps for (A) FBG Acc. 3, (B) PZT Acc. at Bearing 2, (C) FBG Acc. 3 (unb), and (D) PZT Acc. at Bearing 2 (unb). 87
4.35 Fault condition 6 vibration frequency spectra for rotor speed at 35 rps for (A) FBG Acc. 3, (B) PZT Acc. at Bearing 2, (C) FBG Acc. 3 (unb), and (D) PZT Acc. at Bearing 2 (unb). 88
4.36 Fault condition 7 vibration frequency spectra for Accelerometer 2 for rotor speed at (A) 17 rps, (B) 17 rps (unbalanced), (C) 35 rps, and (D) 35 rps (unbalanced). 90
4.37 Fault condition 7 vibration frequency spectra for Accelerometer 3 for rotor speed at (A) 17 rps, (B) 17 rps (unbalanced), (C) 35 rps, and (D) 35 rps (unbalanced). 91
4.38 Fault condition 8 vibration frequency spectra for rotor speed at 17 rps for (A) FBG Acc. 2, (B) PZT Acc. at Bearing 2, (C) FBG Acc. 2 (unb), and (D) PZT Acc. at Bearing 2 (unb). 93
4.39 Fault condition 8 vibration frequency spectra for rotor speed at 35 rps for (A) FBG Acc. 2, (B) PZT Acc. at Bearing 2, (C) FBG Acc. 2 (unb), and (D) PZT Acc. at Bearing 2 (unb). 94
4.40 Fault condition 8 vibration frequency spectra for rotor speed at 17 rps for (A) FBG Acc. 3, (B) PZT Acc. at Bearing 1, (C) FBG Acc. 3 (unb), and (D) PZT Acc. at Bearing 1 (unb). 95
4.41 Fault condition 8 vibration frequency spectra for rotor speed at 35 rps for (A) FBG Acc. 3, (B) PZT Acc. at Bearing 1, (C) FBG Acc. 3 (unb), and (D) PZT Acc. at Bearing 1 (unb). 96
4.42 Fault condition 9 vibration frequency spectra for Accelerometer 2 for rotor speed at (A) 17 rps, (B) 17 rps (unbalanced), (C) 35 rps, and (D) 35 rps (unbalanced). 98

4.43 Fault condition 9 vibration frequency spectra for Accelerometer 3 for rotor speed at (A) 17 rps, (B) 17 rps (unbalanced), (C) 35 rps, and (D) 35 rps (unbalanced). 99

A.1 Schematic representation of Double-L Cantilever based on FBGs. . . . 104
A.2 Mechanical model of the Double-L Cantilever structure. 105
A.3 Geometrical representation for Double-L Cantilever structure submitted to small angular displacement. 107
A.4 Single cantilever structure and its mechanical model. 108
A.5 Schematic of triangular cantilever structure. 110
A.6 Side and bottom view of a Clamped-Clamped beam structure. 111
A.7 Steel tube-mass block elastic structure-based accelerometer geometry. . 113
A.8 Flexible hinges accelerometer structure. 114
A.9 Flexible hinges accelerometer mechanical model under an external acceleration. 114

List of Tables

2.1 Different combinations of sensitivity, resonant frequency, and geometries in FBG-based accelerometers. 20

3.1 Range of acceptable values for the MOO variables. 36
3.2 Acceleration intensity measured by the commercial PZT-based accelerometers. 38
3.3 FBG-based accelerometers' acceleration sensitivity directional requirement for each bearing. 38
3.4 Fault conditions. 39

4.1 Geometric parameters used in Double-L Cantilever Structure analytical model. 43
4.2 Geometric parameters used in single cantilever analytical model. . . . 43
4.3 Geometric parameters used in triangular cantilever analytical model. . 44
4.4 Geometric parameters used in clamped-clamped cantilever analytical model. 45
4.5 Geometric parameters used in the steel tube-mass block elastic Structure analytical model. 46
4.6 Geometric parameters used in the flexible hinges analytical model. . . 47
4.7 Summary of the analytical model's primary assessment. 48
4.8 Geometric parameters and accelerometer features for the flexible hinges structure resulted from a multi-objective optimization procedure. . . . 48
4.9 FEA natural frequencies results by the modal analysis using ANSYS 2019 R3. 49
4.10 Accelerometer features. 54
4.11 Frequency vibration harmonics identification summary. 101

Chapter 1

Introduction

1.1 Motivation

Structural Health Monitoring (SHM) in electrical motors is an advantageous technique to identify different types of failure, mechanical or electrical, in advanced or early stages [1]. It is through this technique that predictive and preventive maintenance plans can be projected in an assertive manner that is capable of avoiding catastrophic failures of equipment and reducing unnecessary maintenance [2]. Some parameters can be used to monitor the structural health of the motors, such as temperature, mechanical vibration, strain, and particulates in lubricants [3]. These parameters can be measured using a variety of sensors and techniques, such as piezoelectric accelerometers [4], Fiber Bragg Gratings-based sensors [5], thermocouples [6], and wear debris analysis in conjunction with spectrometric analysis [7]. Using artificial intelligence techniques, the type of fault and its location can be identified [8].

In addition to providing safety and long life to machines and structures, SHM techniques can also contribute economically to industries by reducing the direct costs of carrying out preventive inspections and the indirect costs associated with interrupted service and downtime for equipment [9]. Additionally, the data provided by the SHM technique supports the development of smart cities by identifying potential damage to civil structures and high energy consumption by machines operating under abnormal conditions [10].

The concept of Industry 4.0 is often viewed through the prism of digital technologies that enable convergence between industrial and business components, and between production models and internal processes [11]. One of the key concepts of Industry 4.0 is the Smart Industry (SI), i.e. an establishment between the world of information technology and the physical world of operational technologies [12]. SHM techniques are related to the Industry 4.0 paradigm by providing data-based strategic decisions, enhancing manufacturing efficiency, and permitting industry adaptation to lead with market demands [13].

As aforementioned, SHM techniques are strategic to avoid catastrophic failure and reduce operational costs [14]. The data provided by the sensors can be used to feed different algorithms capable of identifying the type of failure. This will provide an effective tool for technical groups to search for the root of the problem [15]. Signal processing, such as Fourier transform and filtering, is also fundamental to separating the interesting data from the noise. From these techniques, structural health diagnosis can be applied to monitor failure since its early stages [16]. Mechanical vibration is one of the key parameters used to monitor the structural health of structures and motors and it has been explored in the literature in different scenarios [17]–[20]. From conception to experimental validation, this work addresses a Fiber Bragg Grating-based accelerometer project using multi-objective optimization aiming to validate it in electrical motor fault diagnosis applications. This work presents a method capable of attending to different project requirements for failure monitoring using mechanical vibration as the key parameter. For the performance assessment of the fabricated sensors, a machinery fault simulator was used to simulate fault conditions in electrical motors for the detection of faults based on the vibration patterns measured by the accelerometers.

1.2 Justification

Mechanical vibration analysis has been explored in different fields, from industrial applications to seismic monitoring [21]. Different transducers can be used for this measurement, such as displacement, velocity, and acceleration sensors [22]. Displacement sensors aim to measure the distance between an object and the sensor element. They can use a variety of technologies such as ultrasonic [23], laser [24], or capacitive [25]. Mechanical vibration is inferred through those sensors by measuring the frequency of displacement variation. Velocity sensors typically consist of a permanent magnet, attached to the vibration element, and a coil of wire (a reference to a stationary point). In these sensors, commonly applied to low-frequency vibration monitoring, the movement of the vibration element induces a voltage proportional to its velocity [26], [27]. Accelerometers are usually composed of mass and stiffness elements, attached to a base. When this system is excited, setting up a base-excited system, there will be a relative displacement, proportional to the acceleration caused by the vibration [28]. Different sensors can be used to produce accelerometers, such as optical fibers [29], piezoelectric [30], microelectromechanical [31], capacitive [32], and accelerometer inertial measurement unit (IMU) [33]. The use of traditional accelerometers based on piezoelectric or capacitive principles is risky in highly explosive or flammable environments. In high-voltage or strong electromagnetic environments, their measurements may be perturbed. Alternatively, fiber optic sensing is the most suitable choice due to its inherent advantages of remote sensing and electromagnetic immunity [34]. The main advantage of optical fiber accelerometers is their ability to withstand harsh environments. Further, optical fiber accelerometers feature low noise, electrical isolation, and the capability to multiplex a large number of sensors [35].

Since the 1960s, optical fibers have revolutionized long-haul data transmission due to their low attenuation and the rapid development of long-haul transmission data optical systems has been accomplished by the emergence of low-cost optical devices [36]. Besides telecommunication applications, optical fibers have been used in sensors development due to their intrinsic advantages: immunity to electromagnetic interference, small size and weight, biocompatibility, and multiplexing capability, i.e. the capability to produce multiple sensors in the same optical fiber [37]. These advantages led to the development of a variety of sensors: temperature [38], liquid level [39], pressure [40], curvature [41], refractive index [42], shape reconstruction in structural elements [43], and vibration monitoring [44].

Optical fiber-based accelerometers can be designed in various ways, including Fabry-Perot interferometers [45], Fiber Bragg Gratings [29], Phase-Modulated [46], Frequency-Modulated [47], and Intensity Variation [48]. A Fabry-Perot accelerometer measures acceleration by a configuration composed of optical fibers and mirrors in which the distance between the optical fiber tip and the reflector induces variation in the interference pattern of the light, which can be detected and used to measure acceleration [45]. Using Fiber Bragg Grating (FBG) accelerometers, the driving forces caused by acceleration induce strain into the fibers, which results in a shift in the Bragg wavelength caused by variations in the effective refractive index, in the grating period, and photoelastic effects can be used to measure acceleration [29]. The working principle of a phase-modulated fiber-based accelerometer is based on the measurement of the phase shift of an optical carrier wave that is modulated by the acceleration-induced strain of a sensing element. Acceleration-induced strain causes a phase shift in the optical carrier wave, proportional to acceleration. The phase shift is then demodulated to obtain a voltage output linearly proportional to acceleration [46]. Frequency-modulated accelerometers use interference optical waves for acceleration measurement. The accelerometer's sensing element can be an optical fiber Michelson interferometer. The interference optical waves are modulated by a sinusoidal signal, and the phase shift of the interference fringes is proportional to acceleration. The modulated signal is then demodulated by a lock-in amplifier to obtain the phase shift, which is proportional to acceleration [47]. An intensity-variation accelerometer is based on the variation of the intensity of light propagating through an optical fiber cable due to the acceleration of a proof mass. The proof mass is typically attached to a spring-mass system designed to resonate at a specific frequency. When the proof mass is subjected to acceleration, it moves relative to the spring-mass system, causing a change in the length of the optical fiber cable, implying a variation in the intensity of the transmitted signal. This variation is detected by a photodetector and used to measure acceleration [48].

FBG-based accelerometers offer distinct advantages over other optical fiber accelerometers. Their immunity to electromagnetic interference makes them suitable for applications in electrically noisy environments, such as industries where there are different electric machines generating electromagnetic field [49]. Additionally, Fiber Bragg Grating accelerometers demonstrate high sensitivity, allowing precise detection of subtle accelerations. Moreover, their compact and lightweight design facilitates easy integration into space-constrained applications, setting them apart from other bulky optical accelerometers [50]. The robustness and corrosion resistance of optical fiber materials used in Bragg grating accelerometers make them well-suited for deployment in harsh and corrosive environments, a feature not shared by all-optical accelerometer types. In addition, their long-term stability ensures reliable and accurate measurements over extended periods, making them the preferred choice for applications requiring continuous monitoring [51].

1.3 Objectives

This master's dissertation aims to develop an optical fiber-based accelerometer for measuring mechanical vibration in electrical motors and identifying failures. The specific objectives of this work are:

- Assembly of a prototype capable of simulating different types of machinery failures;
- Development of Fiber Bragg Grating-based accelerometers capable of measuring mechanical vibration;
- Fabrication of Fiber Bragg Grating-based accelerometers;
- Experimental characterization of accelerometers;

- Validation of the accelerometers for different types of failure in machinery fault simulator.

1.4 Contributions

Over the course of this dissertation, two journal papers and one conference paper were published. Additionally, these works involve collaboration with other researchers and international groups. Among the works, there are those used in the dissertation as well as those derived from collaborations and parallel research. The publications resulting from this dissertation are listed below:

1. **Macedo, L.**, Pedruzzi, E., Avellar, L., Castellani, C.E.S., Segatto, M.E., Frizera, A., Marques, C. and Leal-Junior, A., 2022. High-Resolution Sensors for Mass Deposition and Low-Frequency Vibration Based on Phase-Shifted Bragg Gratings. IEEE Sensors Journal, 23(3), pp.2228-2235.
2. **Macedo, L.**, Souza, E.A., Frizera, A., Pontes, M.J., Marques, C. and Leal-Junior, A., 2023. Static and Dynamic Multiparameter Assessment of Structural Elements Using Chirped Fiber Bragg Gratings. Sensors, 23(4), p.1860.
3. Silveira, M., Avellar, L., Cruzeiro, F., **Macedo, L.**, Leal-Junior, A., Garcia, G., Frizera, A. and Díaz, C., 2022, December. A Fiber Bragg Grating based Accelerometer for Monitoring the Vibration of an Industrial Engine Prototype: A Preliminary Study. In Journal of Physics: Conference Series (Vol. 2407, No. 1, p. 012039). IOP Publishing.

1.5 Document structure

This document is divided into five chapters. In Chapter 1, a comparison is made between the relevance of this work and other existing technologies and how it contributes to the Structural Health Monitoring and Industry 4.0 paradigms. Additionally, the main objectives of this master's dissertation and the literature contributions made during its writing are described. In Chapter 2, the theoretical background is presented to support the concepts used in this work related to Electrical Motor Faults, Optical Fibers, Fiber Bragg Gratings, Optical Fiber Accelerometer Design, and Multi-Objective Optimization. In Chapter 3, the steps employed in the Fiber Bragg Grating-based accelerometer are described, involving analytical model analysis, finite element modal analysis, multi-objective optimization, and experimental characterization. Furthermore, the experimental setup used in machinery fault simulation experiments is presented and explained. In Chapter 4, the results of analytical model analysis, finite element modal analysis, multi-objective optimization procedure, and experimental characterization are presented and discussed. Moreover, machinery fault diagnosis experiments are presented and discussed under 9 different fault conditions. Finally, in Chapter 5, conclusions and future works are presented.

Chapter 2

Theoretical Background

2.1 Electric Motors Faults

Condition monitoring and SHM are important issues to anticipate actions through predictive and preventive maintenance aiming to avoid catastrophic failures, enhance operation safety, and reduce production costs. The general study conducted by the Institute of Electrical and Electronics Engineers (IEEE) on the reliability of motors has categorized the percentage failure by component as follows: bearing (41%), rotor (10%), stator-related (37%), and others - cooling, connections, and terminal boxes, for example (12%) [52].

Bearing faults are the most common failure type [52]. Besides the frequency of occurrence, its monitoring is strategic to avoid higher economic damages, since the exchange of a faulted ball bearing, for example, represents approximated 3% of the entire motor price [53]. Mechanical vibration plays an important role in bearing fault detection since each failure condition imposes a vibration signature [54]. This vibration signature is related to harmonic frequencies, i.e. multiple frequencies of nominal in which the rotor is operating. In real-life operations, these harmonics will appear when a frequency domain analysis of the mechanical vibration signal is carried out, although when their signal amplitude is higher than the nominal frequency, it indicates bearing faults [55].

An alternative to fault diagnosis by mechanical vibration is the current signals analysis. In many cases, mechanical signals cannot be acquired, mainly in harsh environments, therefore electrical signals would be preferable [56]. Voltage and/or current signals are, ideally, non-invasive methods to acquire information about the engine's structural health. However, the physical link between electrical signals and bearing faults is not clearly defined, thus it requires dedicated signal processing in information extraction [57].

Inner or outer race faults in ball bearings can be detected by the mechanical vibration analysis in the frequency domain. These fault frequencies are related to geometric aspects of the bearing such as rotational velocity, ball diameter, pitch diameter, and contact angle [58]. These characteristic frequencies are proportional to the frequency at which each ball passes on a failure point and this modulates the amplitude of the vibrational signal according to the damage intensity. Different techniques of data processing can be applied for inner or outer race faults, such as envelope analysis and Hilbert transform to assess parameters like the root-mean-square value of the vibration velocity, the crest factor, and kurtosis [59]. These faults are schematically represented in Figure 2.1.

Misalignment is also a common malfunction in electrical motors, schematically represented in Figure 2.2. Different reasons can cause this malfunction, such as improper machine assembly, thermal distortion, and asymmetry in applied load [60]. Perfect alignment can never be achieved practically, although a correct machinery

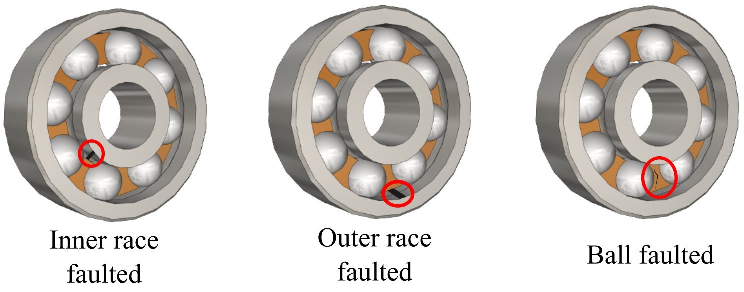

FIGURE 2.1: Schematic representation of ball bearing faults.

operation admits a certain level of misalignment without compromising the motor's health. When the level of the misalignment is higher than an acceptable value, it causes reaction forces in the coupling, which affect the machines and are often a major cause of machinery vibration [61]. Experimental studies have indicated that the second harmonic is related to misalignment [62]. Nevertheless, there are other faults that imply the appearance of the second harmonic, such as crack and stiffness asymmetry. Full spectrum analysis is an alternative to identify correctly the misalignment [63] and nowadays artificial intelligence-based techniques [64].

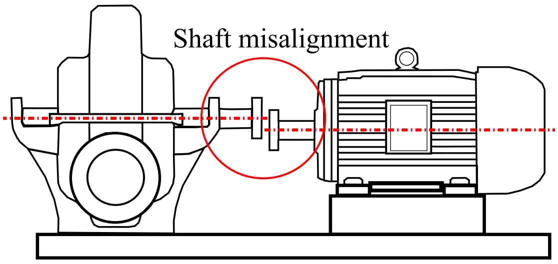

FIGURE 2.2: Schematic representation of shaft misalignment.

An imbalance is defined as a lack of equilibrium in the sum of forces in a system, changing the state of equilibrium, and it may appear in two ways: static and dynamic [65]. This fault condition is schematically represented in Figure 2.3. In case of dynamic imbalance, centrifugal forces are applied on bearings at the nominal rotational frequency, proportional to the square of rotor speed. Besides, these imbalanced forces cause vibration in the manner that there will be 90 degrees of the phase difference between bearings, tangential, and radial nominal frequency components [66]. Vibration peaks showing imbalance in the radial and tangential direction should be compared and the severity of the imbalance will be indicated by the closeness of these peaks in both directions [67]. Recently, methods based on artificial intelligence techniques have been proposed for early imbalance fault detection in induction motors [68].

Mechanical looseness in electrical motors is a common problem caused by loose bolts, structural damage, improper fit, or increased clearance between components, resulting in increased mechanical vibration and wear [69]. The identification of mechanical looseness can be done by vibration analysis and/or voltage/current measurements [70]. In addition, belt looseness can also cause mechanical looseness in induction motors [71]. The monitoring of the one-half and one-third sub-harmonics components in the instantaneous power spectrum can serve as a reliable indicator of mechanical looseness in induction motors [54], [69].

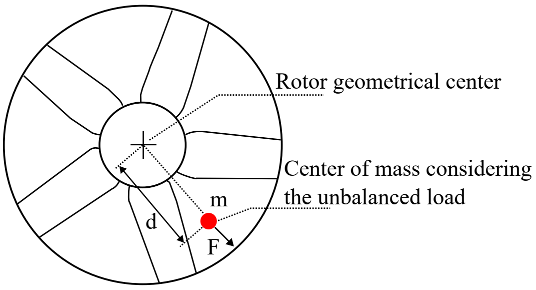

FIGURE 2.3: Schematic representation of imbalance.

The bowed rotor in electrical motors can be caused by different sources such as asymmetrical heat distribution/deformation, manufacturing defects (it may have inherent imbalances), excessive load, and time wear and tear [72]. In this failure condition, a dynamic eccentricity occurs which defines the condition when the minimum air gap revolves with the rotor [73]. This air gap field component, produced by the dynamic eccentricity, rotates at $f_s \pm f_r$ with corresponding $p \pm 1$ pole-pairs where f_s is the supply frequency, f_r is the rotational frequency of the rotor and p is the pole-pair number of the motor [74].

Stator winding faults are mainly related to inter-turn short circuits and are caused by the breakdown of insulation between the windings, which leads to heavy inrush currents that damage the stator windings [75]. These faults can be detected and diagnosed using various techniques, including spectral analysis of symmetrical current components, wavelet-based fault detection and diagnosis, and motor current signature analysis [76]. By mechanical vibration signal, the envelope analysis can be applied to identify stator winding faults and differentiate them from unbalanced supply [77].

Single-phasing in electrical motors is a fault that occurs when one of the three phases of the power supply is lost, resulting in the motor operating with only two phases [78]. This can cause the motor to overheat and fail due to damages in the stator winding insulation system (leading to a reduction in the expected lifespan of the motor by approximately 50%) and to mechanical faults such as locked rotor and brief or prolonged overload, which can increase the current drawn by the motor and cause further overheating [79]. Vibration analysis can be carried out to identify single-phasing faults by monitoring some line frequency harmonics: $F_1 = 1X$, $F_2 = 2f - \frac{f}{3}$, $F_3 = 2f$, $F_4 = 2f + \frac{f}{3}$, and $F_5 = 4f$, where $1X$ is the rotation velocity of the motor in rps and f is the line supply frequency [80].

Broken rotor bars are a fault that can be caused by different sources such as manufacturing faults, repeated starting of the machine, mechanical stress, and thermal stress [81]. If the rotor part is damaged, as schematically represented in Figure 2.4, the rotor symmetry of the machine is lost and a reverse rotating magnetic field related to an inverse sequence component of the rotor currents, at frequency $-sf$ (s denotes the slip and f the supply frequency), appears. This inverse sequence is reflected on the stator side and produces the frequency component $(1 - 2s)f$. Consequently, a torque ripple and a speed ripple are generated at a frequency of $2sf$ which modulates the rotating magnetic flux [82].

Each type of failure will affect the mechanical vibration pattern, which can be used to monitor and identify the cause, location, and intensity of the problem. In addition, mechanical vibration is a natural consequence of dynamic motion. As there is motion, mechanical vibration is expected, making this parameter a strategic

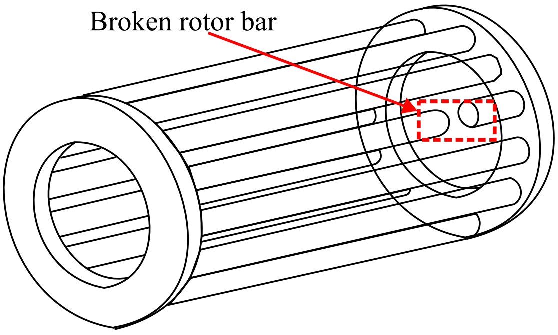

FIGURE 2.4: Schematic representation of rotor broken bar.

parameter for SHM techniques [28]. Using this key parameter, some artificial intelligence algorithms can be developed to identify the vibration pattern measured by accelerometers and compare it with the well-known failure vibration pattern applied to train the algorithms models [83], [84]. Although artificial intelligence techniques can be used in machinery fault diagnosis, in this work there is no implementation of these techniques. This is because the focus is on the development of an FBG-based accelerometer for machinery fault diagnosis, validating the results using a commercial piezoelectric accelerometer. The analysis for these experiments will be done offline, comparing the mechanical vibration spectra for identifying fault vibration signatures for electric motor structural health monitoring.

2.2 Optical Fibers

Optical fibers are thin, flexible, and transparent cables made of glass or plastic that transmit light signals over long distances with little signal quality loss [85]. They consist of a core and a cladding layer, with different refractive indices. Due to this difference in the refractive index, light propagates inside the core by total reflection. The core's refractive index is higher than the cladding's [86]. With their low attenuation (ranging from 0.2 dB/km to 0.5 dB/km at a wavelength of 1550 nm, for silica optical fibers), optical fibers have revolutionized data transmission, enabling long-haul data transmission over thousands of kilometers [87].

There are different refractive index (RI) profiles in optical fibers. The RI profile depends on the manufacturing process and design specification. The most RI common profiles are step-index profile, graded-index profile, trench-index profile, microstructured (photonic crystal) profile, and D-shaped profile [88]. In the step-index profile, the refractive index of the fiber core is uniform across the entire core region and abruptly drops at the boundary with the cladding. This refractive index profile is simple and easy to manufacture, but it can suffer from high modal dispersion and other nonlinear effects such as third-harmonic generation, four-wave mixing, and nonlinear refraction which are all related to the third-order susceptibility $\chi(3)$ [89]. In a graded-index profile, the refractive index of the fiber core decreases gradually from the center of the core to the boundary with the cladding. This profile is designed to minimize modal dispersion and other nonlinear effects and can support higher bandwidths than step-index fibers [90]. Figure 2.5 illustrates the graded-index and step-index profiles schematically. In a step-index profile, the refractive index changes abruptly at the boundary between the core and the cladding. This results in light traveling straight in single-mode fibers or reflecting at various angles in multi-mode fibers [89]. In contrast, in a graded index fiber, the refractive index varies smoothly from the center to the edge of the fiber. Due to this gradient, light bends gradually and follows a sinusoidal path, causing rays traveling nearer to the fiber's center to move more slowly than those traveling nearer to its edge. Consequently, graded index fibers can transmit data efficiently with reduced dispersion as compared to multi-mode step-index fibers [90].

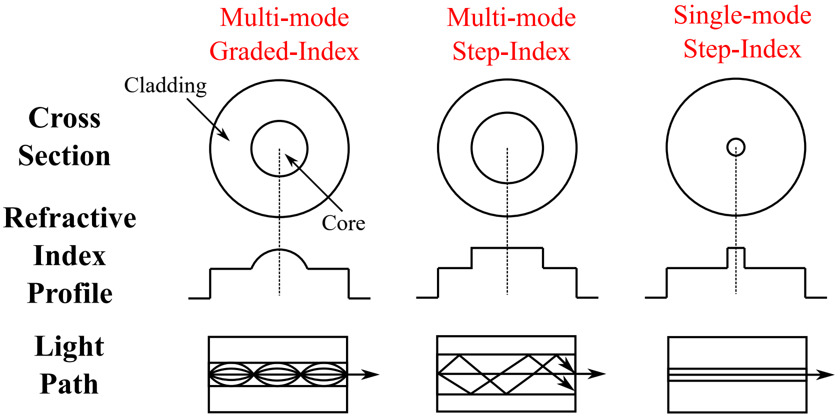

FIGURE 2.5: Graded and step-index schematic representation.

In a trench-assisted profile, a small trench or groove is etched into the cladding region of the fiber, which helps to confine the light within the core and reduce the effects of bending and microbending losses [91]. Figure 2.6 illustrates the trench refractive index profile schematically. This trench causes light that might otherwise escape from the core during tight bends to be reflected back into the core. This is due to the refractive index disparity between the core, the trench, and the cladding [92]. Essentially, light gets confined more effectively within the core, even when the fiber bends. It is particularly advantageous to use a trench refractive index profile in environments where bending is inevitable in order to ensure stable transmission performance and minimize the threat of signal degradation [93].

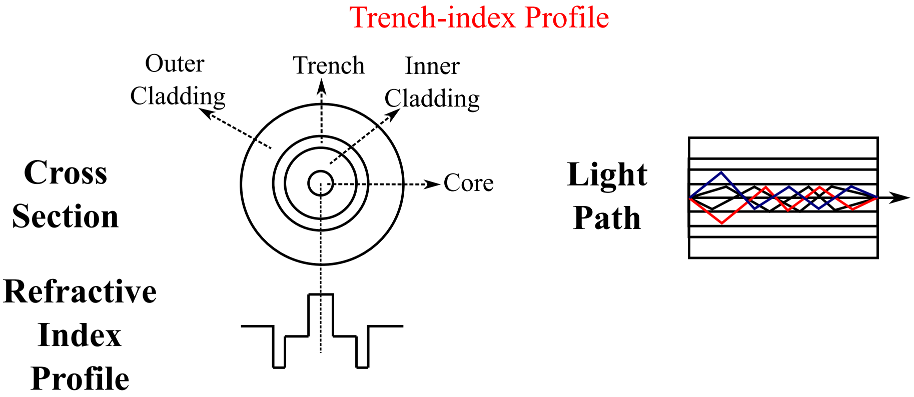

FIGURE 2.6: Trench-assisted profile schematic representation.

In a photonic crystal profile, the refractive index of the fiber core and cladding is periodically modulated to form a photonic crystal structure. This profile is designed to confine the light within the core and enhance its interaction with the surrounding environment, making it useful for sensing and dispersion feature control [94]. Figure 2.7 illustrates the photonic crystal index profile schematically. Instead of relying purely on refractive index differences between the core and cladding, photonic crystal fibers (PCF) feature a periodic array of microscopic air holes running along the entire fiber length. These air holes create a microstructured pattern that produces photonic bandgaps, regions of forbidden optical frequencies, and the light is guided through the core by modifying total internal reflection or by these bandgaps [95]. Depending on the design, PCFs can be made to support single-mode operation over a wide wavelength range or exhibit unique properties like high nonlinearity or endlessly single-mode behavior. As a result of the arrangement and size of the air holes, the fiber's dispersion and confinement properties can be tailored, resulting in greater control [96].

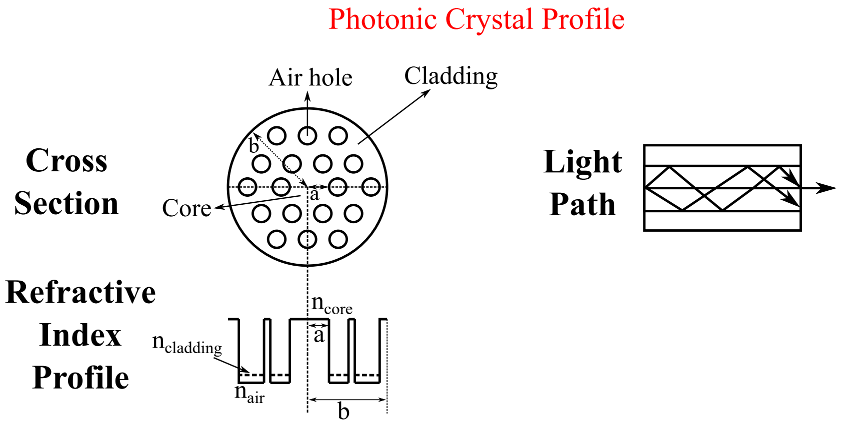

FIGURE 2.7: Photonic crystal profile schematic representation.

In a D-shaped profile, the fiber is shaped into a flat, rectangular cross-section, which makes it easy to attach to flat surfaces and reduces the effects of bending and microbending losses [97]. Figure 2.8 illustrates the D-shaped index profile schematically. As a result of this configuration, part of the evanescent wave is exposed, which is the portion of the optical wave that extends just outside the core boundary. By doing so, the D-shaped fiber allows for interactions between this evanescent wave and external materials placed near the flat side [98]. This design is particularly advantageous for sensors, as the exposed evanescent wave can interact with surrounding chemicals or physical changes, causing measurable variations in the light's properties. As a result, the light in a D-shaped fiber remains primarily within its core but is accessible for external interactions on its flat side, making it a versatile tool for specialized applications such as biochemical sensing [99], [100].

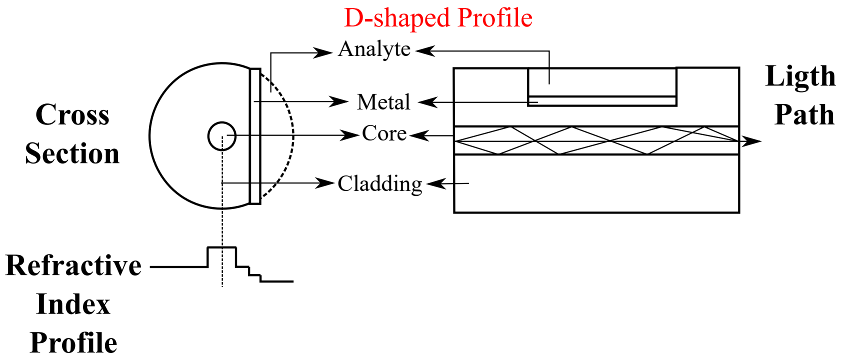

FIGURE 2.8: D-shaped index profile schematic representation.

The phenomenon of total internal reflection occurs when a light ray traveling in a dense medium encounters a boundary with a less dense medium at an angle of incidence exceeding a critical angle [101]. In place of refracting towards this boundary, the light ray is entirely reflected back into the dense medium. A material or medium with a higher density will have a higher refractive index as a result of high-frequency interaction between light waves and atoms or molecules. This leads to a greater reduction in the speed of light in such materials/media [102]. The critical angle is defined by Snell's law, also known as the Law of Refraction. This law states a relationship between the incident and refraction angle and the refractive indices of the media [103], mathematically written in Equation 2.1.

$$n_1 \sin\theta_1 = n_2 \sin\theta_2 \tag{2.1}$$

In Equation 2.1, n_1 is the refractive index of the medium where the incident ray is traveling, n_2 is the refractive index of the medium where the refracted ray is traveling, θ_1 is the angle of incidence, which is the angle between the incident ray and the normal to the surface at the point of incidence, and θ_2 is the angle of refraction, which is the angle between the refracted ray and the normal to the surface at the point of refraction. Following Snell's law, the critical angle is defined as the angle of incidence at which the refracted angle is 90° [103]. Manipulating Equation 2.1, yields in Equation 2.2.

$$\theta_c = \arcsin \frac{n_2}{n_1} \tag{2.2}$$

In Equation 2.2, θ_c is the smallest angle in which the total internal reflection occurs. Numerical aperture (NA) is another important concept when it comes to optical fibers. In optical fibers and other optical systems, NA refers to the maximum angle at which light can enter and be transmitted. By increasing the numerical aperture, more light can be collected and transmitted, resulting in a higher sensitivity as well as a higher signal-to-noise ratio. A larger numerical aperture, however, also entails greater vulnerability to distortion and other forms of signal degradation [104]. Mathematically, NA is written by Equation 2.3, where n_{co} is the core and n_{cl} is the cladding refractive indices, respectively.

$$NA = \sqrt{\left(n_{co}^2 - n_{cl}^2\right)} \tag{2.3}$$

The refractive index of a material is wavelength-dependent because the response of the material to electromagnetic fields changes with frequency. This leads to a dispersion of the refractive index, which causes different wavelengths of light to travel at different speeds through the material. This phenomenon is defined as chromatic dispersion [103]. Telecommunications professionals must be familiar with this effect because light pulses tend to spread over time or distance, which can increase bit error rates, limit bandwidth, reduce transmission distance, and cause interference [105]. An additional type of dispersion is modal dispersion, which occurs because of the difference in propagation speeds between different light propagation modes [103]. Light travels along different paths (or modes) in a multimode fiber. There is a difference in propagation velocity for each mode, and therefore, a difference in transit time. As a result, the different modes may arrive at the receiving end at different times, causing the aforementioned dispersion problems [106].

An optical fiber's attenuation can be defined as the reduction in light intensity as it travels through the fiber. An optical fiber communication system's maximum transmission distance and data rate are determined by this parameter, which is commonly expressed in decibels per kilometer. Attenuation can be caused by a variety of sources, including absorption, scattering, and bending losses. A material absorbs light energy when it is exposed to impurities in the fiber or water molecules. Scattering occurs when light is scattered in different directions as a result of irregularities in the fiber (such as variations in the refractive index or microbends). When a fiber is bent too sharply, some light is lost as a result of bend losses [107], [108]. Single-mode fibers with a bend radius of less than 30 mm may experience significant bend losses, particularly at longer wavelengths (i.e., 1550 nm) [109]. In contrast, newer fibers designed for reduced bend sensitivity, which are sometimes referred to as bend-insensitive fibers, are capable of handling much tighter bends, sometimes as tight as 5-10 mm, without suffering any significant damage [110]. Microbends can also cause signal loss. A fiber bend or deformation usually occurs during the manufacturing, cabling, or installation process. In microbends, light can refract from the core and into the cladding or even outside the fiber [111]. Besides, it is important to mention that attenuation is affected by environmental factors such as temperature and pressure [112]. In addition to telecommunication applications, optical fibers have intrinsic advantages that make them suitable for sensor development [37].

2.3 Fiber Bragg Gratings

There are different types of Bragg gratings in optical fibers: tilted, phase-shifted, long-period, chirped, and uniform FBGs [113]. In Tilted Fiber Bragg Gratings (TFBG), the gratings are tilted relative to the perpendicular plane of the fiber axis. This causes the coupling of the core-guided light in the cladding and subsets a large number of cladding modes [114]. These modes have different sensitivities to external perturbations such as temperature [115], strain [116], refractive index [117], and biochemical applications [118]. By monitoring the changes in the reflected spectrum of the TFBG, one can measure the corresponding changes in the external parameter being sensed [119]. Figure 2.9 shows a schematic representation of TFBG.

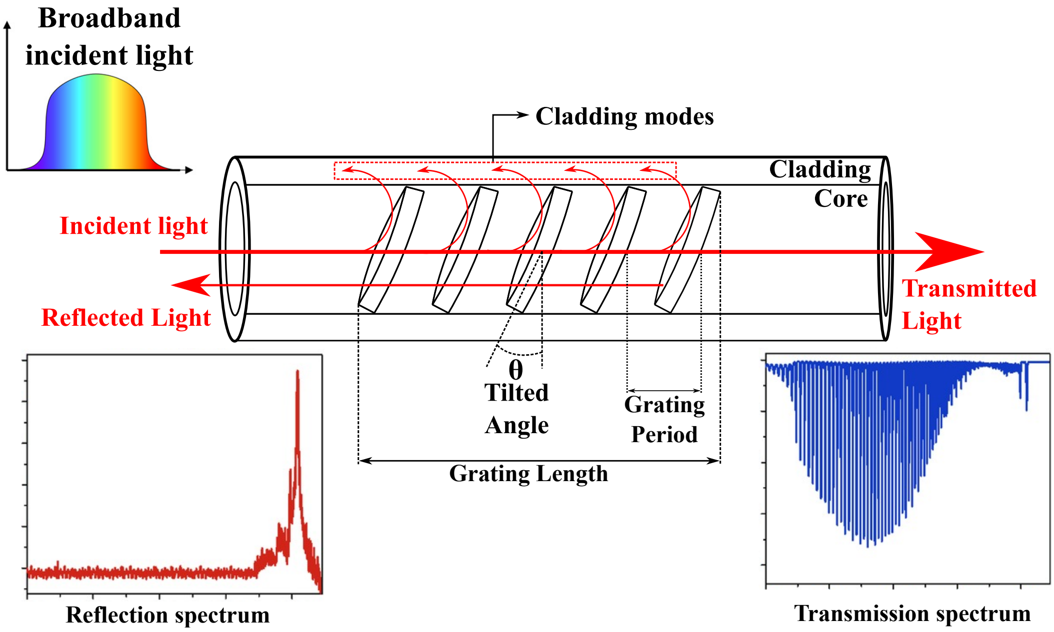

FIGURE 2.9: Schematic representation of Tilted Fiber Bragg Gratings.

PSFBGs (phase-shifted fiber Bragg gratings) introduce a phase shift in the grating structure that alters the reflection spectrum of the FBG [120]. Phase shifts change the phase of reflected light, which changes the interference pattern between reflected light from phase-shifted and unshifted sections of the grating, determining PSFBG's reflection spectrum [121]. It is possible to optimize the phase shift to achieve specific spectral characteristics, such as narrowband filtering [122] or increased sensitivity to external perturbations such as ultrasonic detection [123]. Different methods can be used to introduce phase shifts, including ultraviolet light (UV) irradiation [124], post-fabrication thermal processing [125], and electric heating [126]. As a result of their high sensitivity, reliability, and versatility, PSFBGs are widely used in optical fiber sensing applications such as ultrasonic wave detection [123], humidity sensing [127], pressure sensing [128], and wavelength demultiplexing [120]. Figure 2.10 shows schematically the working principle of PSBFGs.

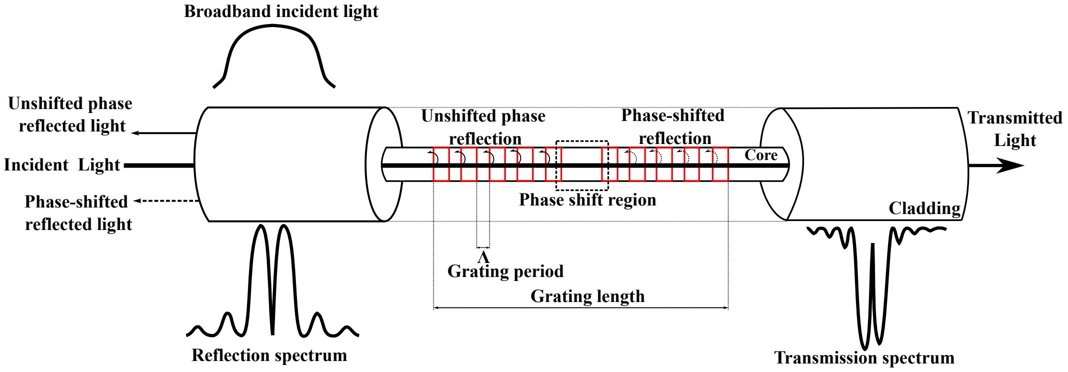

FIGURE 2.10: Schematic representation of Phase-shifted Fiber Bragg Grating.

Long-period fiber Bragg grating (LPFBG) is a type of fiber grating that exhibits periodic variations in refractive index over a relatively long distance (typically several millimeters to several centimeters) [129]. Unlike a uniform FBG, which reflects a narrow band of light centered around a specific wavelength, an LPFBG reflects a broadband of light over a variety of wavelengths [130]. LPFBGs work by coupling the forward-propagating core mode and the backward-propagating cladding mode in an optical fiber. As a result of periodic variations in refractive index along the fiber axis, these modes are coupled, resulting in the transfer of power from the core mode to the cladding mode, and also determining the coupling strength and resonance wavelength of the LPFBG [113]. In order to introduce LPFBGs into optical fibers, a variety of techniques can be used, including CO_2 laser irradiation [131], electric arc discharge [132], and mechanical pressure [133]. Additionally, the LPFBG can be cascaded with other LPFBGs with different periods to achieve a wider bandwidth or a more complex spectral response [134]. There are many applications for LPFGs, including band-rejection filters and gain equalizers in fiber optic communication systems [135], temperature and strain sensors [136], as well as chemical and biosensors sensors [137]. Figure 2.11 shows schematically the working principle of LPFBGs.

A chirped Fiber Bragg Grating (CFBG) is an optical fiber sensor in which the refractive index of the fiber core is periodically changed [138]. As shown schematically in Figure 2.12, the grating is termed chirped because the spacing between the variations in the core refractive index changes along the fiber′s length. As a result, the CFBG is able to reflect a broad spectrum of wavelengths rather than a single wavelength (in contrast to a uniform FBG) [138]. As light passes through the fiber, some of it is reflected back by the grating at specific wavelengths, known as Bragg wavelengths. This results in an interference pattern between the incident light and the reflected light, where constructive interference occurs at Bragg wavelengths, determined by the spacing between variations in the refractive index and the effective

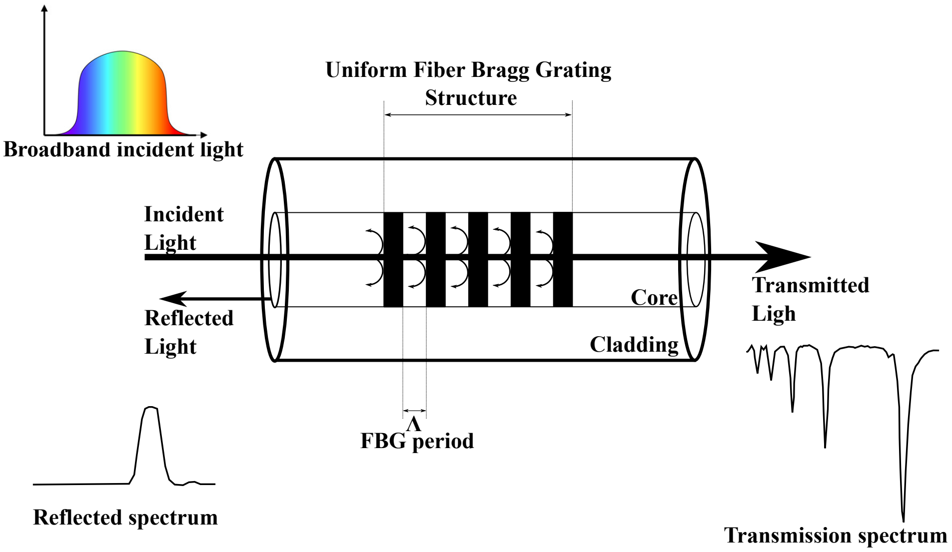

FIGURE 2.11: Schematic representation of Long-period Fiber Bragg Grating.

refractive index of the core [139]. The phase mask technique can be used to introduce CFBGs into optical fibers [140]. In this method, a phase mask is used to create a refractive index modulation pattern in the fiber core by using a diffractive element. Typically, the fiber is exposed to a medium-power UV, KrF, or Ti:sapphire laser, which is guided through a phase mask and onto the core of the fiber [139]. The refractive index modulation of the fiber core is caused by the interference pattern created by the phase mask and the laser. It is possible to use CFBGs for monitoring the structural health of structures and composites [141], localizing and estimating high-pressure events [142], monitoring transmission lines [143], and distributed strain sensing in dentistry [144].

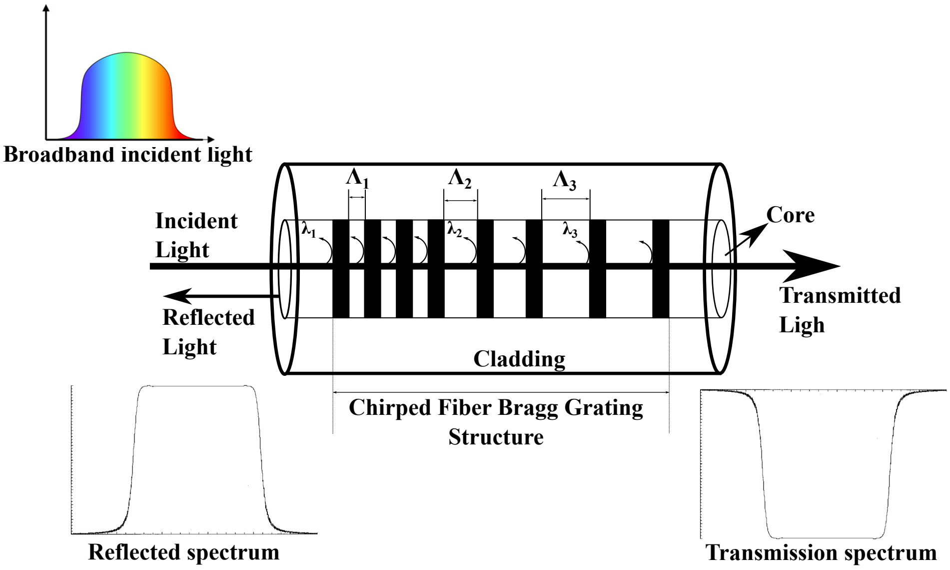

FIGURE 2.12: Schematic representation of Chirped Fiber Bragg Grating.

The uniform fiber Bragg grating (FBG) is a type of Bragg grating in which the refractive index modulation is uniform throughout the grating's length [138], shown schematically in Figure 2.13. At every point along the grating, the refractive index modulation amplitude is the same and the period is constant [138]. The periodic variation in the refractive index of the fiber core causes light of a particular wavelength to be reflected back when incident on the grating [145]. A grating's period is chosen so that the reflected light waves interfere constructively, resulting in strong reflections at a very narrow wavelength, known as the Bragg wavelength, typically below one-nanometer [145]. Through a process called interference lithography, FBGs can be engraved into optical fiber by interfering with two or more laser beams, in which a pattern of interference fringes is created, which is then transferred to the fiber core through exposure to the fringe pattern. It is typically exposed using a phase mask, which is a transparent plate with a periodic pattern of lines or dots that serves as a diffraction grating [146]. Phase masks are placed in contact with fiber cores and illuminated with UV laser beams to produce interference fringe patterns, shown schematically in Figure 2.14. In this schematic representation, before reaching the phase mask, the laser beam is shaped by a cylindrical lens and a slit. In order to prevent undesirable curvatures, the fiber is placed between two clamps and kept in tension (identified by XYZ stages). With the use of a single-mode silica pigtail, a temporary connection is made. Real-time monitoring of the grating growth is achieved through the use of an interrogation system. Photochemical reactions in the fiber core result in periodic changes in refractive index, resulting in the grating, and By adjusting the angle and wavelength of the laser beams, the spacing between the fringes determines the period of the grating [146]. As soon as the grating has been formed, it is typically annealed at high temperatures in order to stabilize the refractive index modulation and improve its spectral characteristics [147]. There are numerous applications for FBGs, including narrowband filters for wavelength division multiplexing (WDM) systems [148], temperature sensing [149], level sensing [150], acceleration measurements [49], and shape reconstruction in structural elements [43].

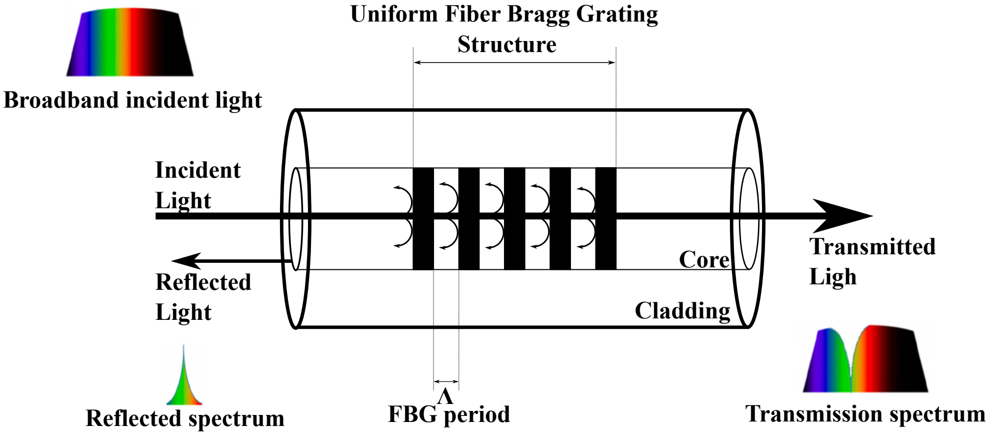

FIGURE 2.13: Schematic representation of uniform Fiber Bragg Grating.

Other techniques for producing gratings in optical fibers include direct UV writing, point-by-point technique, and femtosecond laser inscription, in addition to the phase-mask technique described above. The direct UV writing inscription technique is used to fabricate FBGs in optical fibers without the necessity of a phase mask. Fibers are coated with a photosensitive material that undergoes a refractive index change when exposed to UV light. An objective lens with a high numerical aperture (NA) focuses the UV laser beam onto the fiber core, resulting in a small spot

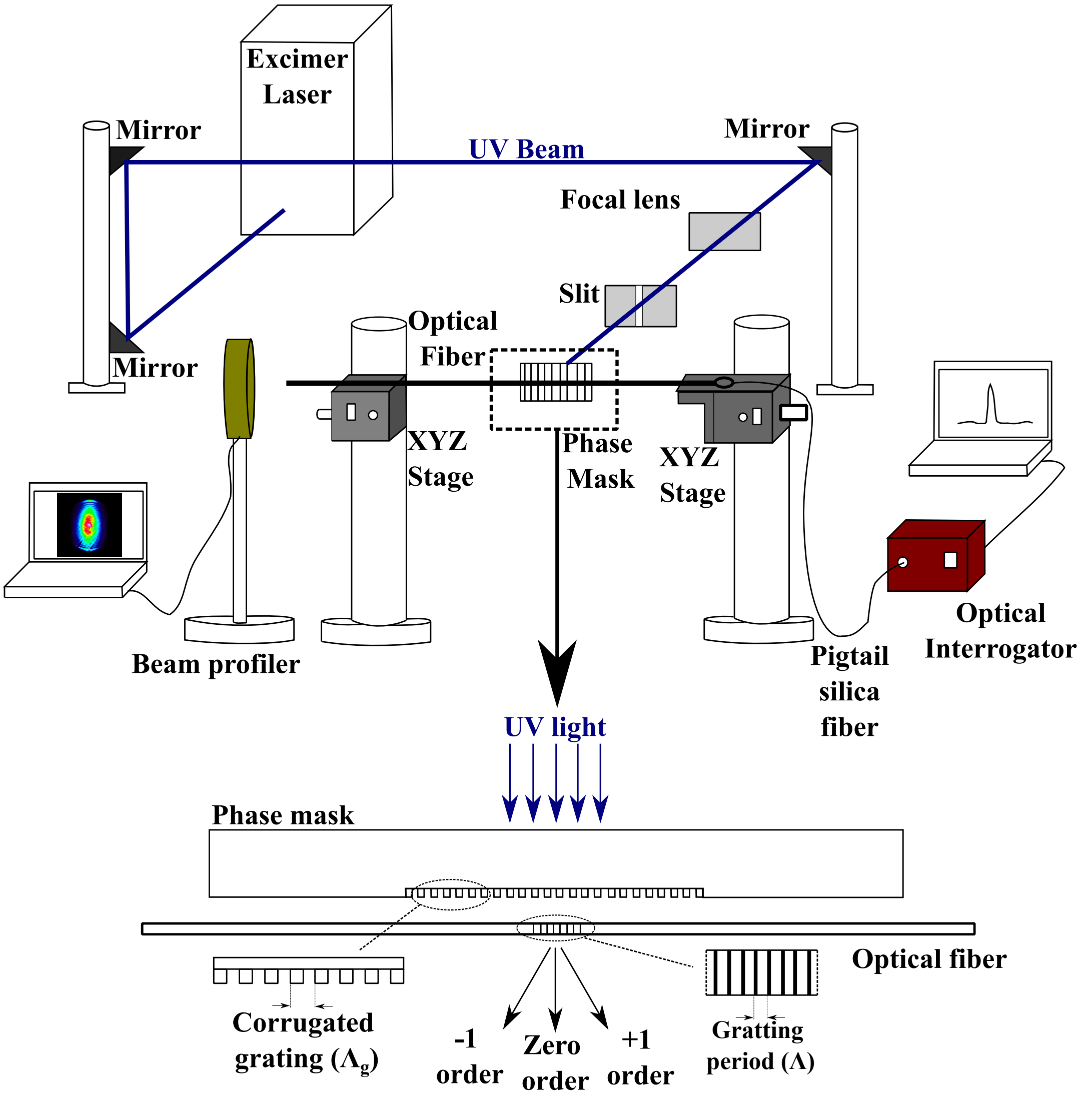

FIGURE 2.14: Schematic representation of phase mask fabrication technique.

size. A periodic modulation of the refractive index of the fiber core is then created by scanning the laser beam across it in a predetermined pattern [151]. By adjusting the scanning speed and pulse frequency of the laser, the spacing between the laser pulses determines the period of the grating. For the fabrication of FBGs with arbitrary grating periods and apodization profiles, direct UV writing inscription is a flexible and precise technique. In addition, the method is fast and cost-effective, making it suitable for the mass production of FBGs. It requires, however, a photosensitive material with a high degree of photosensitivity and stability that is compatible with the UV laser wavelength [152].

Point-by-point (PbP) inscription is a technique for fabricating FBGs in optical fibers by using a focused UV laser beam to create the grating pattern point by point. In this method, the fiber is mounted on a high-precision translation stage that allows it to be moved in three dimensions with submicron accuracy [153]. Using a high numerical aperture (NA) objective lens, the UV laser beam is focused onto the fiber core, resulting in a small spot size. In order to create periodic modulations in the refractive index of the fiber core, the laser beam is scanned across the fiber core in a predetermined pattern. Laser pulse spacing determines the period of the grating, which can be controlled by adjusting the scanning speed and pulse frequency of the laser. PbP inscription is an effective method for fabricating FBGs with arbitrary grating periods and apodization profiles. In spite of this, the process is time-consuming and not suitable for mass production of FBGs [154].

With femtosecond laser inscription, the fiber is exposed to a focused beam of femtosecond laser energy with a high peak power and a short pulse duration. Laser beams are focused onto fiber cores using high numerical aperture (NA) objective lenses, which produce small spots on the fiber. In response to the high peak power of the laser beam, the refractive index of the fiber core changes nonlinearly, creating periodic changes in the refractive index [155]. The period of the grating is determined by the length of the laser pulse and the speed at which the laser beam is scanned. A femtosecond laser inscription process is a flexible and precise method for fabricating FBGs with arbitrary grating periods and apodization profiles. It is also a fast and efficient method that does not require the use of photosensitive materials or phase masks. Nevertheless, it requires a highly precise laser system and a skilled operator to control the laser parameters and ensure that the grating is of high quality [156], [157].

As mentioned above, Bragg wavelengths are determined by the spacing of the refractive index modulation and the grating period [145]. In the presence of a perturbation, such as strain, temperature, or pressure, the effective refractive index of the fiber and the grating period change. This results in a shift in the Bragg wavelength. Mathematically, this phenomenon is described as follows. The Bragg wavelength is given by Equation 2.4 [138].

$$\lambda_B = 2n_{\text{eff}}\Lambda \tag{2.4}$$

In Equation 2.4, λ_B is the Bragg wavelength, n_{eff} is the effective refractive index, and Λ is the grating period. As aforementioned, the Bragg wavelength shift is sensitive to mechanical deformation and thermal effects, described in Equation 2.5 [158].

$$\Delta\lambda_B = \lambda_B\left[(1 - P_\varepsilon)\,\varepsilon + (\alpha + \zeta)\Delta T\right] \tag{2.5}$$

In Equation 2.5, P_ε is the effective photoelastic constant (for a germano-silicate fiber at room temperature $P_\varepsilon \approx 0.22$), ε is the applied strain, α is the coefficient of thermal expansion, ζ is the thermo-optic coefficient, and ΔT is the temperature variation.

2.4 Optical Fiber Accelerometer Design

Optical accelerometer design has different configurations. The most common optical accelerometer designs include FBG-based accelerometers, interferometric accelerometers, intensity-based accelerometers, and Micro-Opto-Electro-Mechanical Systems (MOEMS) accelerometers [159]. Interferometric accelerometers use the principle of light interference to measure acceleration. Generally, incident light is split into two beams that are recombined to produce an interference pattern that is detected by a photodetector. When an acceleration is applied to one of these two beams, driving forces are generated, resulting in strain in the optical fibers. As a result, the generated interference pattern is proportional to acceleration, and this can be used to measure acceleration [160].

The Mach-Zehnder interferometer (MZI) is an optical device that uses interference to measure light intensity changes. It consists of two parallel waveguides that split and recombine the light, creating an interference pattern. When an inertial force due to acceleration is applied perpendicularly to an MZI-based accelerometer, the floating waveguide in the MZI is deflected and expanded [161]. As a result, the MZI's interference condition is changed and its output intensity is modulated. The system contains a proof mass to amplify the impact of acceleration and driving forces on the interference pattern, enhancing the sensor's sensitivity [162].

In the Michelson interferometer (MI), a beam of light is split into two separate beams that travel along different paths before being recombined. In the process of recombining the beams, an interference pattern is created that can be analyzed to determine changes in the length of one of the paths [163]. Accelerometers based on MI measure the phase shift of the interference pattern created by recombined beams of light. A proof mass is attached to the sensing element of the accelerometer. As the proof mass is subjected to acceleration, one of the arms of the interferometer changes in length, resulting in a phase shift in the interference pattern. The phase shift is then detected and analyzed to determine the acceleration. Frequency modulation techniques can be used to increase the sensitivity of the accelerometer by improving the signal-to-noise ratio [47].

A Fabry-Perot interferometer (FPI) works by reflecting light back and forth between two parallel mirrors. As a result of the interference between the reflected beams, a series of constructive and destructive interference patterns are created, resulting in a series of bright and dark fringes. Fringe spacing is determined by the distance between the mirrors and the wavelength of the light [164]. A proof mass is attached to one of the mirror elements in FPI accelerometers. When the accelerometer experiences acceleration, the mass block moves, causing a change in the distance between the reflective surfaces. The change in distance results in a corresponding change in the interference pattern, which can be measured and used to determine the acceleration. The sensor's sensitivity is affected by the distance between reflective surfaces and the light wavelength [165].

The Sagnac Interferometer (SI) operates according to the Sagnac effect, which is a result of the interference of two counter-propagating light beams. As a result of the Sagnac effect, a phase shift occurs between the two beams, which is proportional to the rotation rate of the loop. A phase shift can be measured by recombining the two beams and observing the interference pattern that results [166]. An SI-based accelerometer is based on the principle of spring-mass systems involving a coiled polarization-maintaining fiber (PMF) which undergoes a lateral force applied to its plane by an inertial mass that results in an interferometric phase change based on the acceleration experienced by the mass attached to one side of the PMF coil. The acceleration can be measured by measuring the interference pattern changes [167].

Intensity-based accelerometers can be designed in a variety of ways. One possible configuration is based on the modulation of light intensity caused by the mechanical motion of a sensing element [168]. Mass-spring systems, such as a cantilever beam, can be attached to one end of an optical fiber split into two parts while the other end remains fixed, coupled to a photodetector. It is also possible to use a Fabry-Perot interferometer as the sensing element in combination with a mechanical system attached to the sensor arm [169]. In response to the mechanical motion of the sensing element, the optical path length changes, which modulates the intensity of the light transmitted through the sensing element. A photodetector detects the modulated light and converts it into an electrical signal proportional to the acceleration. Afterward, the electrical signal is processed to determine the acceleration information [34]. An alternative configuration utilizes a spring-mass structure that exploits the fiber's sensitivity to microbending in order to convert the displacement of the structure into a change in the optical power. A sharp cutting tool can be used to groove the fiber in order to increase its sensitivity to bending. As a result of the driving forces generated by acceleration, the output optical power can be measured by photodetectors, and it is proportional to acceleration [168]. In another configuration, light is received through two fixed fibers that are connected to photodetectors. A fiber is attached to a spring-mass system and the fixed fibers are used to estimate acceleration. When the spring-mass structure vibrates as a result of acceleration, the intensity of the light received by the photodetectors changes, and this change in intensity allows the acceleration to be determined. Accelerometer sensitivity and bandwidth are determined by the type of fiber used and the design of the spring-mass structure [170].

The working principle of MOEMs (Micro-Opto-Electro-Mechanical Systems) accelerometers is based on the deflection of a proof mass attached to a compliant suspension in response to an acceleration of the structure [171]. A metric that can be used to measure acceleration is derived from the deflection of the proof mass or the deformation of the suspension. It is possible to measure the deflection of the proof mass using optical techniques such as intensity modulation, interferometry, or resonant frequency shift [172]. Davies, E. et al. have developed an accelerometer based on MOEMs that use the FPI principle. In the device, an FPI cavity is formed by reflections from the end surface of a cleaved optical fiber. This is done by mounting the mirror on a V-beam structure. Before transduction, the proof mass displacement is mechanically amplified by a V-beam structure. This increases the sensor's sensitivity without compromising its bandwidth [173]. Abozyd, S. et al. have developed a triaxial MOEMs-based accelerometer. The proposed sensor works on the power variation technique. The sensor consists of a light source such as a Light Emitting Diode (LED), a Micro-electromechanical Systems (MEMS) part consisting of a mass-spring system, and a Quadrant Photodiode (QPD). This sensor measures acceleration by moving the proof mass in response to acceleration. The proof mass is suspended by four folded springs, allowing 3D movement. When acceleration is applied, the proof mass moves by a certain amount on the corresponding axis. This causes some quadrants of the quadrant detector to receive more light than others. The differential light signal read by the four detectors changes as the proof mass moves. This change in the light signal can be used to determine the acceleration [174].

Accelerometers based on FBGs work by shifting the Bragg wavelength as a result of deformation in the optical fiber caused by acceleration. Whenever mechanical deformation is applied to an FBG sensor, the grating period is changed due to strain, and the effective refractive index is changed due to photoelastic effects, which implies a change in Bragg wavelength (see Equation 2.4) [175]. As a result of the harmonic loads exerted on the sensors, there is a harmonic shift in the Bragg wavelength, which is directly proportional to the acceleration. Once this has been accomplished, frequency domain analysis can be performed to determine the intensity of acceleration and failure at different stages [54]. To satisfy project requirements, parameters such as geometry, dimensions, and material are selected and projected in a manner tailored to the required natural frequency and sensitivity to acceleration. Natural frequency refers to the range of frequencies in which the sensor can operate, while sensitivity refers to the intensity of the measurement (in this case, acceleration) [176]. Contrary to interferometric accelerometers that rely on phase shift detection and require meticulous alignment and coherence maintenance, FBG accelerometers offer simplicity and robustness against environmental perturbations. The FBG provides a stable and inherent wavelength-encoded response in contrast to intensity-based accelerometers, which measure changes in light intensity. In contrast, MOEMS accelerometers combine optical and micromechanical components to detect acceleration. In spite of their potential for miniaturization and system integration, their fabrication can be challenging. In environments where reliability and resilience are paramount, FBG-based accelerometers stand out because of their compact size, immunity to electromagnetic interference, and relative ease of deployment [177]–[181]. Several combinations of natural frequency, geometry, and sensitivity of FBG-based accelerometers have already been reported in the literature. Table 2.1 presents some of the combinations of natural frequency, geometry, and sensitivity of FBG-based accelerometers and Figure 2.15 shows a schematic representation of these structures.

TABLE 2.1: Different combinations of sensitivity, resonant frequency, and geometries in FBG-based accelerometers.

Sensitivity [pm/g]	**Resonant Frequency [Hz]**	**Geometry**	**Reference**
804	102	Flexible hinges	[182]
754.3	103	Double grid-diaphragms	[183]
41	890	Symmetrical double flexure hinges	[184]
7.5	940	Polymer composite single cantilever	[185]
406.7	86	Double-L cantilever	[186]

In the realm of accelerometers, resonance frequency and acceleration sensitivity are pivotal concepts that have a profound impact on their performance and their applicability. A resonant frequency is a natural frequency at which a system tends to oscillate with maximum amplitude when subjected to an external force [28]. In the context of accelerometers, this can be calculated using modal analysis or determined experimentally by subjecting the device to varying frequencies of vibration and determining the frequency at which maximum amplitude is observed [187]. To ensure accuracy and reliability, the accelerometer must be operated below its resonant frequency, which is referred to as the usable frequency region or bandwidth. A consistent and predictable response is provided by the accelerometer within this

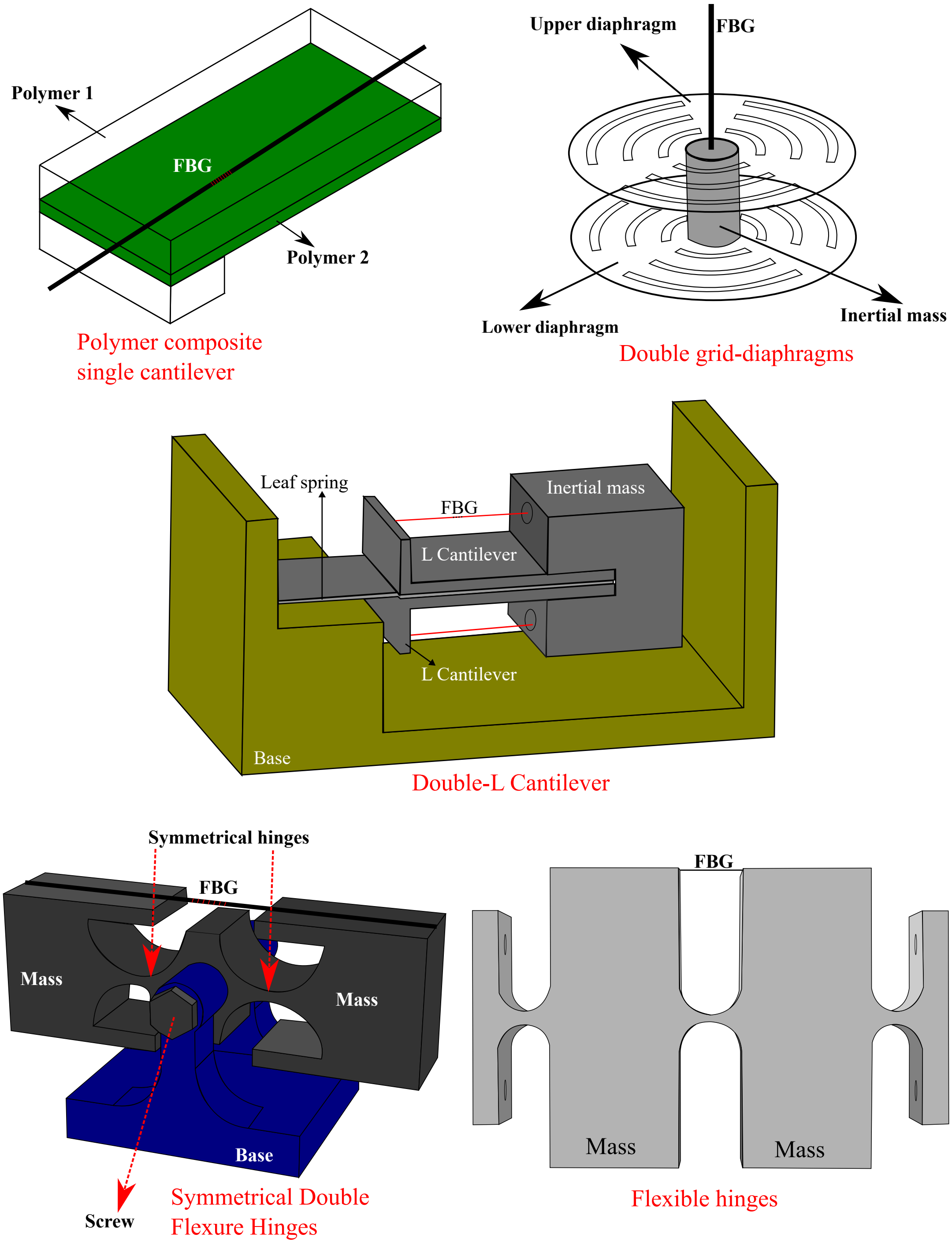

Polymer composite single cantilever

Double grid-diaphragms

Double-L Cantilever

Symmetrical Double Flexure Hinges

Flexible hinges

FIGURE 2.15: Schematic representation of FBG-based accelerometer structures.

region [188]. In contrast, sensitivity to acceleration refers to the output signal generated per unit of acceleration applied to the accelerometer [28]. Under controlled test conditions, this can be calculated by dividing the output signal by the input acceleration [187]. A high-sensitivity accelerometer is capable of detecting minute accelerations, making it suitable for vibration measurements at low levels, whereas a low-sensitivity accelerometer is more suitable for high shocks or high frequencies [189], [190]. To calibrate and ascertain sensitivity, practical tests can be conducted in known acceleration environments or using reference devices [191]. This implies that it is not only essential to be aware of these two attributes when selecting an accelerometer, but that it is equally important to know how to determine them either theoretically or empirically. The resonant frequency and sensitivity acceleration are schematically represented in Figure 2.16.

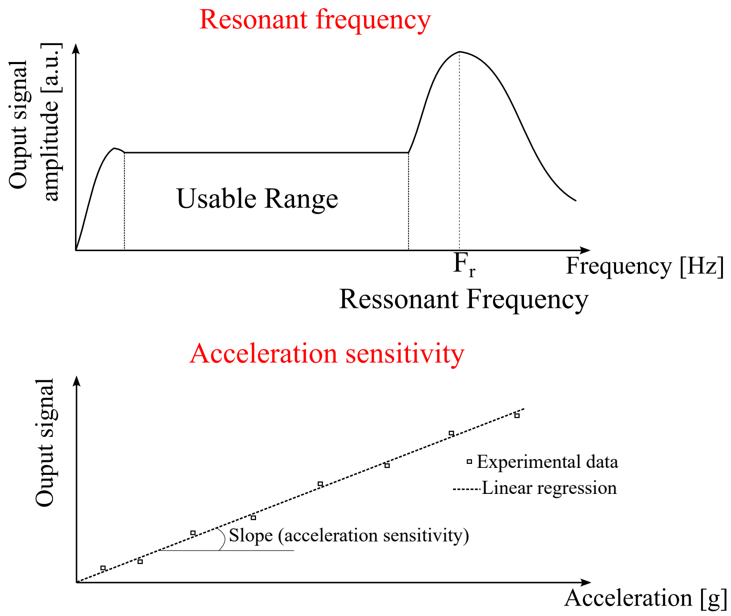

FIGURE 2.16: Schematics representation of resonant frequency and acceleration sensitivity for accelerometers.

2.5 Multi-objective optimization

Multi-objective optimization (MOO) refers to the process of optimizing multiple objectives simultaneously, rather than just one. This is necessary when there are multiple goals to be achieved, and these goals may conflict with each other [192]. In this type of problem, there is no single solution that can optimize all objectives at the same time, so the goal is to find a set of solutions that can achieve a reasonable trade-off between the different objectives [193]. MOO is also known as vector optimization, and it is used in a variety of fields, including engineering, finance, and environmental management [194].

There are three main categories of MOO methods: methods articulating preferences *a priori*, methods articulating preferences *a posteriori*, and methods without articulating preferences. In methods with *a priori* articulation of preferences, the decision-maker indicates the relative importance of the objective functions or desired goals before running the optimization algorithm [194]. An objective function is typically weighted or a range of acceptable values is specified for each objective function [195]. As a result, the optimization algorithm seeks to find a set of solutions that are optimal in terms of these preferences. Examples of methods with *a priori* preference articulation include weighted sum, epsilon-constraint, and goal programming [196].

An *a posteriori* preference method involves selecting a single solution from a set of mathematically equivalent solutions. Prior to running the optimization algorithm, the decision-maker does not specify preferences; instead, they view the set of Pareto optimal solutions and choose the solution that most effectively meets their preferences [194]. In the criterion space, the Pareto optimal set is typically depicted. As part of the decision-making process, the decision-maker may also view potential solutions in the design space. The Pareto-based methods Non-dominated sorting genetic algorithm II (NSGA-II) and Strength Pareto Evolutionary Algorithm 2 (SPEA2) are examples of methods that articulate preferences *a posteriori*. Due to the fact that only one solution is selected and the time spent determining other Pareto optimal points is wasted, these methods are less efficient in terms of CPU time than those with *a priori* articulation of preferences [197], [198].

Methods with no articulation of preferences do not require the decision-maker to concretely define their preferences. Instead, these methods seek to find a set of solutions that are optimal with respect to all objective functions or goals simultaneously. Most of the methods in this category are simplifications of methods with *a priori* or *a posteriori* articulation of preferences, typically excluding method parameters [194]. A global criterion method is an example of a method without articulation of preferences, in which an exponential sum is formed by setting all weights to one. The result is a single function that is optimized to find the set of Pareto optimal solutions [199], [200].

NSGA-II works by maintaining a population of candidate solutions, called individuals, and iteratively improving them through selection, crossover, and mutation operations. The algorithm uses a Pareto-dominance-based selection mechanism to drive the population towards the Pareto front (PF) of the problem, which represents the set of non-dominated solutions. NSGA-II also employs a crowding distance classification mechanism to maintain diversity in the population and prevent premature convergence. First, a random parent population is created and sorted based on non-domination. Each solution is assigned a fitness (or rank) equal to its non-domination level. Binary tournament selection, recombination, and mutation operators are used to create an offspring population. In order to form the next generation, the best solutions from the parent and offspring populations are selected. The offspring population is also sorted based on non-domination and crowded distance estimation is used to maintain diversity [201], [202]. Figure 2.17 shows the NSGA-II algorithm workflow represented by a flowchart.

In the NSGA-II algorithm, the initialization step is the first step. During this process, a random parent population is created. Typically, the size of the population is predetermined and fixed. A vector of decision variables is used to represent each individual in the population. Within their respective bounds, the decision variables are generated randomly. To obtain the values of the objective functions, the population is evaluated by the objective functions. In the next step, non-dominated sorting is performed, where one solution is said to dominate another solution if it is better in at least one objective and not worse in any other. After partitioning the solutions into different non-dominated fronts, the first front contains the solutions that are not affected by solutions in the first front, and the second front contains the solutions that are covered only by solutions in the first front. Next, the fitness assignment step involves assigning a fitness (or rank) to each solution in the population based on its

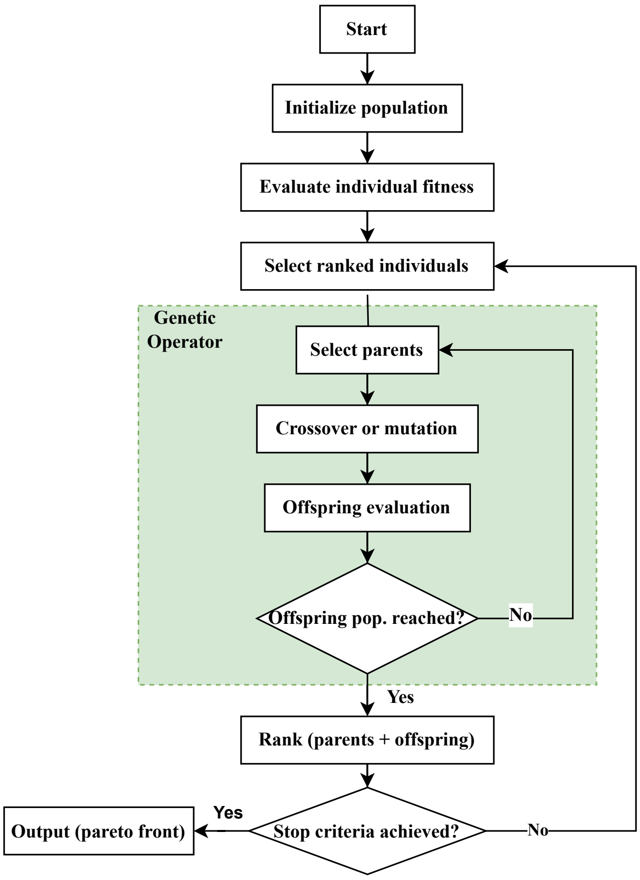

FIGURE 2.17: NSGA-II workflow represented in a flowchart diagram.

non-domination level. The solutions in the first front are assigned a fitness value of 1, the solutions in the second front are provided with a fitness value of 2, and so on. As a result of this assignment of fitness, the search is directed towards non-dominant solutions. In the environmental selection step, fitness values are used to select the best solutions for the next generation. Further, in the selection step, individuals from the current population are chosen to create the next generation. Based on a binary tournament selection operator, two individuals are randomly selected from the population and the individual with the highest fitness value (lower rank) is selected as the parent. This process is repeated until the required number of parents is selected. Binary tournament selection is used to maintain the diversity of the population and to prevent premature convergence [203]–[207].

In NSGA-II, the recombination and mutation steps involve creating new offspring solutions from selected parents. As part of the recombination process, two parents' genetic information is combined to create a new offspring solution. A crossover operator such as simulated binary crossover (SBX) or polynomial crossover (PCX) is typically used for this purpose. To introduce new genetic diversity into the offspring solution, the mutation step involves randomly perturbing the genetic information. In most cases, polynomial mutations or Gaussian mutations are used to accomplish this task. Through the process of recombination and mutation, a diverse set of offspring solutions is created that explore the search space and maintain genetic diversity within the population. After the new population has been created, it is resubmitted to the non-dominated sorting of offspring described above. In the next step, the next-generation population is selected based on the combined parent and offspring populations. The solution is compared based on their non-domination level and crowding distance using a crowded comparison operator. In the objective space, the crowding distance measures the density of solutions around a particular solution. It is preferred to choose solutions that are less crowded over those that are more crowded. As part of the environmental selection process, the best solutions for the next generation are selected to ensure that diversity is maintained in the population. Finally, the algorithm is completed when any of the stop criteria has been met. A stop criterion is usually determined by the number of iterations or the size of the population. In determining these criteria, consideration is given to the computational cost of running NSGA-II. Following the selection of the finalist solutions, each solution is characterized with respect to the objective functions [203]–[207].

Accelerometer design has two main features: acceleration sensitivity and resonant frequency. In general, there is a trade-off between these two features, and a multi-objective optimization technique can be used to define geometry dimensions that establish an equilibrium between sensitivity and resonant frequency to satisfy the project requirements [208]. The NSGA-II algorithm has already been used in this project type where different geometric and material aspects were evaluated within an acceptable range (usually defined by the dimensions of the body which is being monitored for acceleration). In this case, the PF contains a combination of natural frequency and acceleration sensitivity features that are generated by setting the geometric and material features. Through this result, the designer can easily study the effect of each parameter in the sensor's features to adjust the geometry and the material to meet project requirements. This is strategic mainly for attending quasi-distributed mechanical vibration monitoring, where the project requirement is different along the structure/motor body [209]–[211].

Chapter 3

Materials and Methods

3.1 Machinery Fault Simulator

The Machinery Fault Simulator (MFS) Lite (SpectraQuest Inc.), shown in Figure 3.1, is used to diagnose machinery faults. MFS consists of three main components: a frequency inverter, an alternating current (AC) motor, and a mechanical system. The frequency inverter controls the rotation of the electrical motor. An inertial disk, a couple of bearings, and a coupling comprise the mechanical system. Different faulted motors and bearings can be combined in this commercial setup in order to study the vibration patterns caused by each type of failure.

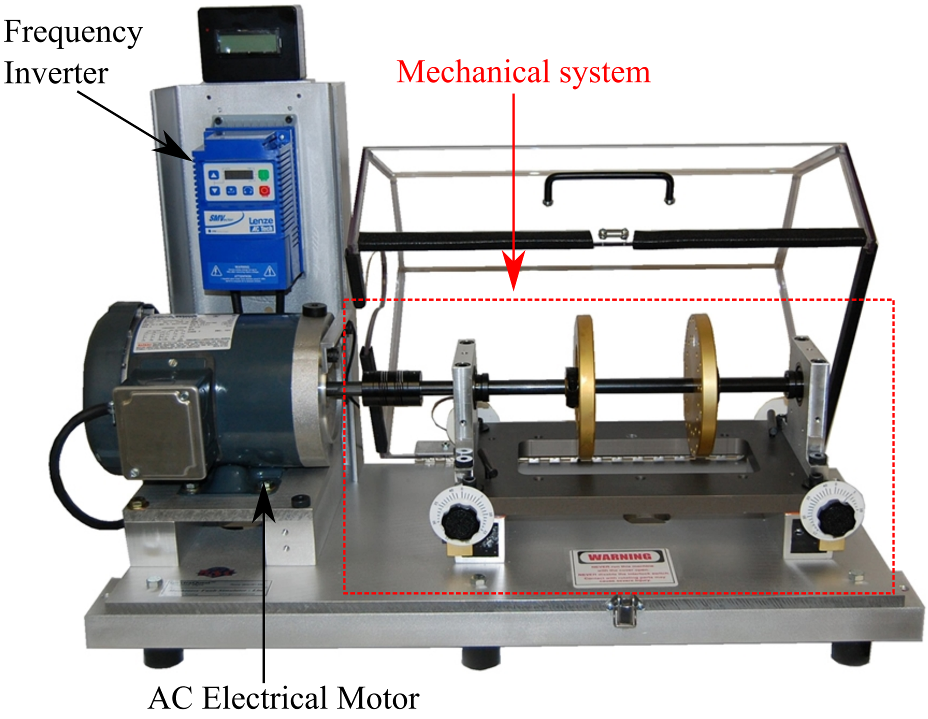

FIGURE 3.1: Machinery Fault Simulator Lite.

A commercial piezoelectric (PZT) accelerometer, model 608A11 (PCB Piezotronics, Inc.), is included in the MFS kit for measuring acceleration. This accelerometer is uniaxial and is mounted at the bearings, as shown in Figure 3.2, and is used as a reference to compare the results of the vibration pattern measured by the projected FBG-based accelerometer in this work. In this commercial setup, there are four PZT accelerometers, two in each bearing, for measuring acceleration in both vertical and horizontal directions.

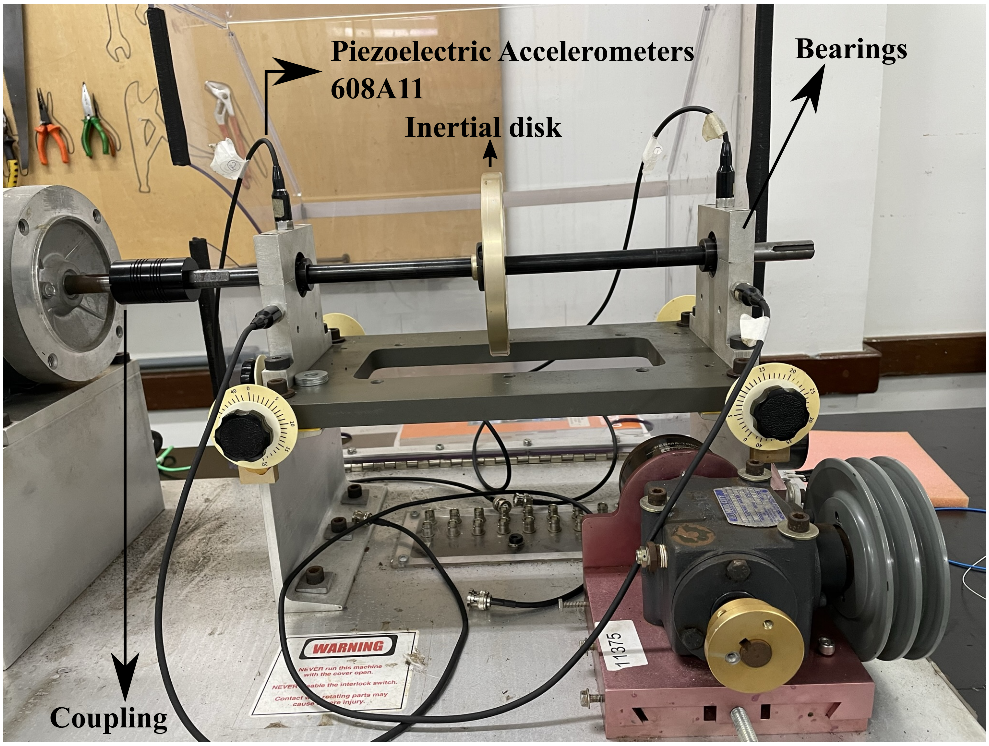

FIGURE 3.2: MFS Mechanical System.

3.2 Fiber Bragg Grating-based Accelerometer Design

3.2.1 Grating inscription

A pulsed Q-switched Nd:YAG laser system (LOTIS TII LS-2137U) emitting the fourth harmonic (266 nm) was employed to produce uniform FBGs, using an emission power lamp energy of 26 J and a measured pulse energy of 12 μJ with a repetition rate of 1 Hz. The laser beam profile was circular with a diameter of around 8 mm and a divergence of less than 1.0 mrad. The laser beam was focused onto the fiber core using a plano-convex cylindrical lens with an effective focal length of 320 mm. The beam's effective spot size on the fiber surface was 8-mm wide and 30-μm high. The phase mask employed was 10-mm long with a pitch of 1064 nm, designed for 266-nm irradiation. This procedure is reported in [212].

3.2.2 Analytical models

Different geometries must be considered and analyzed analytically and numerically when selecting an accelerometer design. The following geometries are considered in this work: a Double-L Cantilever, a Triangular Cantilever, a Clamped-Clamped Beam, a Single Cantilever, a Capillary Steel Tube, and a Flexible Hinge. These structures were selected based on the ease of fabrication of these mechanical structures. In this section, the main equations describing the natural frequency and the acceleration sensitivity features for each geometry are presented. The full mathematical development can be found in Appendix A.

3.2.2.1 Double-L Cantilever Structure

The Double-L Cantilever analytical model considered in this work is based on [186]. This geometry is schematically shown in Figure 3.3.

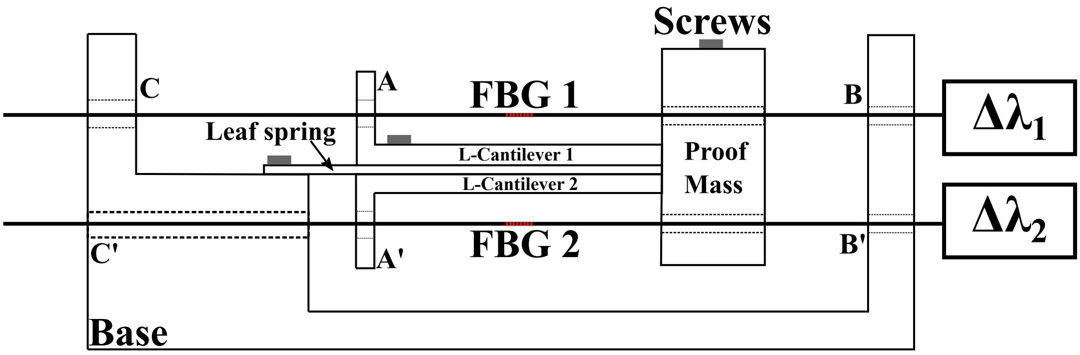

FIGURE 3.3: Schematic representation of Double-L Cantilever based on FBGs.

According to Figure 3.3, the mechanical sensor head consists of a thin rectangular leaf spring, two rigid L-shaped cantilevers, and an inertial mass. Each of these components is screwed together to form a single unit that is attached to the base at the leaf spring end. The proof mass, L-cantilevers, and walls of the base are drilled out to facilitate the insertion of two FBGs (FBG 1 and FBG 2). The FBGs are pre-tensioned and fixed at points A, B, A′, and B′. A mechanical model of the Double-L Cantilever structure is shown in Figure 3.4.

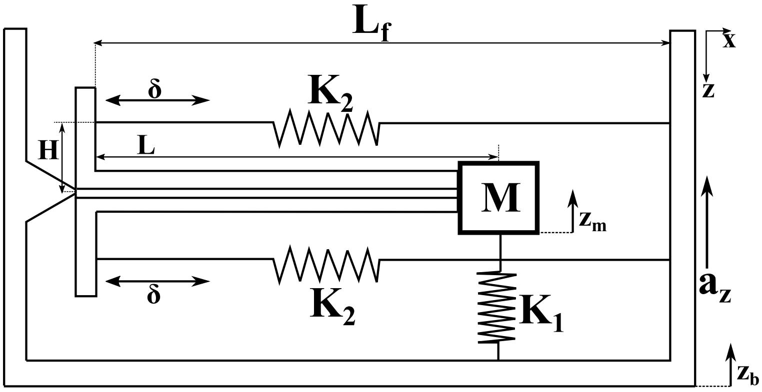

FIGURE 3.4: Mechanical model of the Double-L Cantilever structure.

In the mechanical model shown in Figure 3.4, the optical fibers are represented by the stiffness K_2, and K_1 represents the combination of Double-L Cantilever and the leaf spring stiffness. After fixing the Double-L Cantilever in the leaf spring using screws, its behavior becomes similar to a T-Cantilever [213]. In this model, L is the Double-L Cantilever length, L_f is the length of the sensing fiber between the fixation points A, and B, H is the L-shaped beam height, and M is the mass of the proof mass. The leaf spring is a rectangular sheet of metal of length L_s, width W_s, and thickness T_s. K_1 is mainly related to the geometric and material features and it is mathematically defined by Equation 3.1.

$$K_1 = \frac{E_s W_s {T_s}^3}{4\left({L_s}^3 + 3{L_s}^2 L + 3L_s L^2\right)} \tag{3.1}$$

In Equation 3.1, E_s is Young's modulus of spring steel. The stiffness K_2 is defined by Equation 3.2.

$$K_2 = \frac{E_g A}{L_f} \tag{3.2}$$

In Equation 3.2, E_g is Young's modulus of the optical fibers and A is its cross-sectional area, defined by $A = \frac{\pi d_f^2}{4}$, where d_f is the optical fibers diameter. The natural frequency of the system is defined by Equation 3.3.

$$w_n = \sqrt{\frac{K_{eq}}{M}} = \sqrt{\frac{K_1 + 2K_2\left(\frac{H}{L}\right)^2}{M}} \tag{3.3}$$

The maximum value of the axial strain across the FBGs is given by Equation 3.4, where Z is the maximum displacement suffered by the beam during the motion of the structure when submitted to acceleration.

$$\delta_{max} = z_{max}\left(\frac{H}{L}\right) = Z\left(\frac{H}{L}\right) \tag{3.4}$$

The maximum strain in the optical fiber can be obtained by dividing both sides of Equation 3.4 L_f, yielding in Equation 3.5.

$$\varepsilon_{x,\max} = \frac{\delta_{\max}}{L_f} = \frac{Z}{L_f}\left(\frac{H}{L}\right) = \frac{-A}{L_f w_n^2}\left(\frac{H}{L}\right) \tag{3.5}$$

As aforementioned, in Equation 3.5 can be observed that the acceleration is directly proportional to the strain in the FBGs. Finally, the strain sensitivity of the FBG is given by Equation 3.6.

$$S_\varepsilon = \left|\frac{\varepsilon_{x,\max}}{A}\right| = \frac{1}{L_f w_n^2}\left(\frac{H}{L}\right) \tag{3.6}$$

3.2.2.2 Single Cantilever

The single cantilever analytical model considered in this work is based on [28], [214]. This structure and its mechanical model are schematically shown in Figure 3.5, which is composed of a rectangular beam with width b, thickness h, length L, and mass m_b. This beam configuration is a clamped-free condition. At the free end, an inertial mass M is added to enhance the amplitude of the mechanical vibration. Yet in Figure 3.5, a mechanical model of the structure is shown, configuring a spring-mass-damper system.

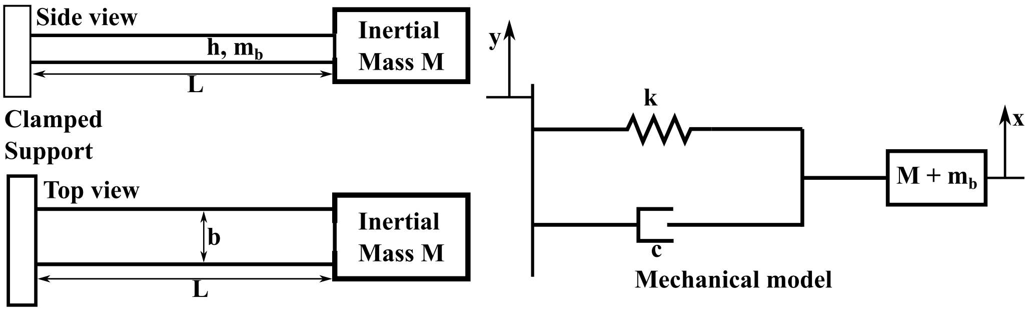

FIGURE 3.5: Single cantilever structure and its mechanical model.

The structure sensitivity to acceleration is given by Equation 3.7.

$$S_0 = \frac{\epsilon}{\ddot{y}} = \frac{3h}{2L^2\omega_n^2} \tag{3.7}$$

Considering a perfect strain transmission from the beam's top surface to the FBG, since it is attached at the top surface, the S_0 sensitivity can be rewritten in terms of wavelength shift in pm/g in Equation 3.8, considering an FBG centered near 1.55 μm.

$$S_\lambda \approx 1.2 \cdot 10^{-3} \cdot S_0 \cdot g \tag{3.8}$$

The natural frequency of the system is given by Equation 3.9, considering the beam's mass, where E is the beam Young's modulus.

$$\omega_n = \sqrt{\frac{E \cdot b \cdot h^3}{4 \cdot L^3 \left(\frac{33}{140} \cdot m_b + M\right)}} \tag{3.9}$$

3.2.2.3 Triangular Cantilever

The triangular cantilever analytical model considered in this work is based on [214], [215]. The triangular cantilever structure is schematically shown in Figure 3.6. In this structure, one of the ends of the triangular beam is fixed at a clamped support, and an inertial mass is attached at the free end. The triangular beam has, at the clamped end, width b and thickness h.

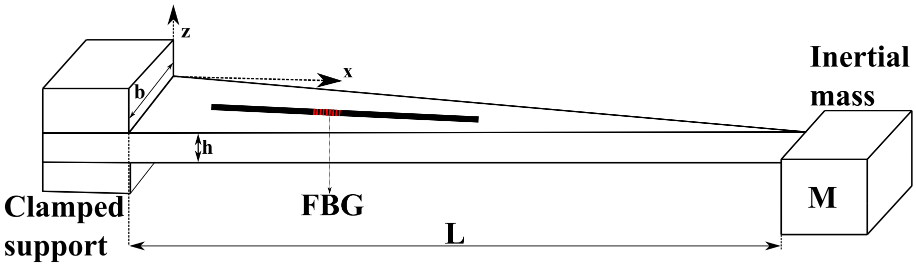

FIGURE 3.6: Schematic of triangular cantilever structure.

The system acceleration sensitivity, S_0, is defined in Equation 3.10, where ω_n is the natural frequency of the triangular cantilever.

$$S_0 = \frac{\epsilon_x}{\ddot{y}} = \frac{3h}{4L\omega_n^2} \tag{3.10}$$

Considering a perfect strain transmission from the beam's top surface to the FBG, since it is attached at the top surface, the S_0 sensitivity can be rewritten in terms of wavelength shift in pm/g in Equation 3.11, considering an FBG centered near 1.55 μm.

$$S_\lambda \approx 1.2 \cdot 10^{-3} \cdot S_0 \cdot g \tag{3.11}$$

In Equation 3.11, g is the acceleration due to gravity. For a triangular beam, the stiffness, at $x = L/2$, is given by Equation 3.12, where E is the beam Young's modulus.

$$K = \frac{Ebh^3}{8L^3} \tag{3.12}$$

Finally, the natural frequency is given by Equation 3.13, where M is the mass attached to the free end of the beam.

$$\omega_n = \sqrt{\frac{K}{M}} \tag{3.13}$$

3.2.2.4 Clamped-Clamped Cantilever

The Clamped-Clamped beam model considered in this work is based on [216]. The clamped-clamped beam structure is schematically shown in Figure 3.7. This structure is composed of two parallel rectangular plates, each supported in such a way as to have clamped-free-clamped-free boundary conditions. A concentrated mass is placed between the plates. Because two of the plate edges are free, the modeling of the plates as beams is warranted for the lower-order vibration modes, and a Poisson correction factor can be added to account for two-dimensional effects.

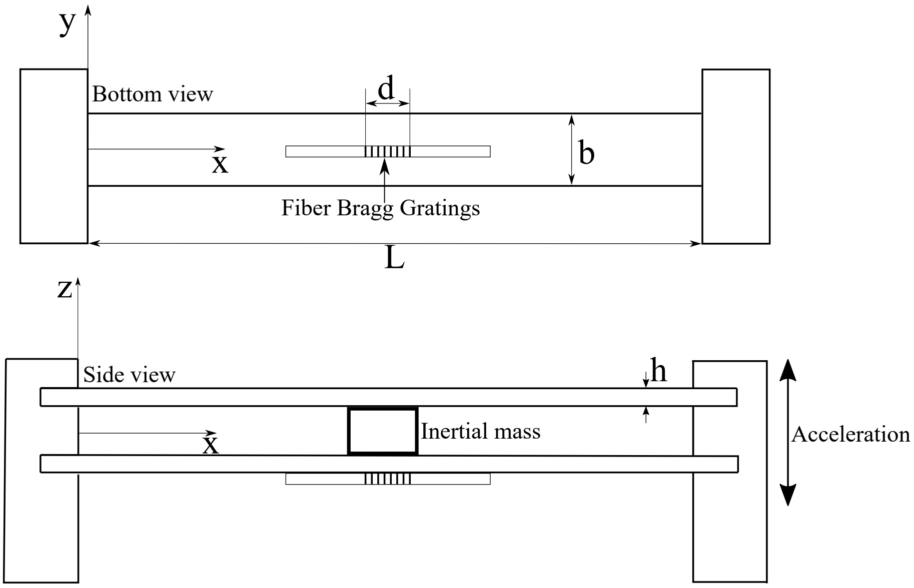

FIGURE 3.7: Side and bottom view of a Clamped-Clamped beam structure.

The lowest natural frequency of the clamped-clamped beam structure is given by Equation 3.14.

$$\omega_n = 0.915\sqrt{\frac{Ebh^3}{L^3\left(M + 0.793m_b\right)\left(1-\nu^2\right)}} \tag{3.14}$$

In Equation 3.14, E is the plate Young's modulus, b, h, L are its width, thickness, and length, respectively, M is the mass of the inertial mass and m_b is the total mass of the plates, and ν is the Poisson's ratio. This natural frequency corresponds to the first symmetric transverse vibration mode of the system, which has a maximum displacement at the center, where the concentrated mass is placed.

From a strain perspective, an average strain over the grating length will be sensed. For a surface strain field given by ϵ_{xx}, this average strain can be expressed by Equation 3.15.

$$\bar{\epsilon}_{xx} = (1/d)\int_{L/2-d/2}^{L/2+d/2} \epsilon_{xx} dx \tag{3.15}$$

In this analytical model approach, an ideal strain transfer between the beam and the grating has been assumed. The division of the average strain by the magnitude of the acceleration, yields in Equation 3.16.

$$S_f = \left(\frac{M + 1.046m_b}{M + 0.793m_b}\right)\left(\frac{gh}{4\pi^2 L^2}\right)\left(\frac{10^6}{\omega^2 - \omega_n^2}\right)\Psi(\kappa) \tag{3.16}$$

In Equation 3.16, $\Psi(\kappa) = (4.175\sin(2.365\kappa) - 0.555\sinh(2.365\kappa))/\kappa$, $\kappa = \frac{d}{L}$, g is the acceleration due to gravity, and ω is the excitation frequency. The limit of S_f as $\omega \rightarrow 0$ is the sensitivity S_0 of the device, given by Equation 3.17.

$$S_0 = \left(\frac{0.030gL\,(M + 1.046m_b)\,(1 - \nu^2)\,10^6}{Ebh^2}\right)\Psi(\kappa) \tag{3.17}$$

Considering an FBG centered near 1.55 μm, the S_0 scale factor can be rewritten in terms of the wavelength shift (in pm/g), given by Equation 3.18.

$$S_\lambda \approx 1.2 \cdot 10^{-3} \cdot S_0 \tag{3.18}$$

3.2.2.5 Steel Tube-Mass Block Elastic Structure

The steel tube-mass block elastic structure-based accelerometer analytical model is based on [217]. The structure of this accelerometer is shown schematically in Figure 3.8. This structure is composed of a capillary steel tube with length L, a cylinder-shaped mass block, a shell, and an optical fiber with two FBGs embedded in the steel tube. The capillary steel tube with FBGs is inserted in the shell and pre-stretched by rotating the nuts and then serves as a spring element. The two FBGs output opposite wavelength shifts caused by the inertial force of the mass along the axial vibration direction. Therefore, using the difference between the two opposite wavelength shifts of the two FBGs as the sensing signal, the influence of temperature cross-sensitivity could be avoided and the sensitivity can be improved.

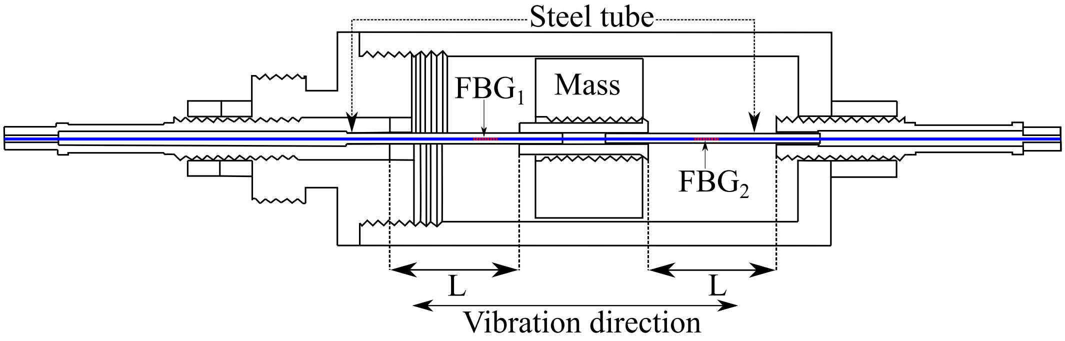

FIGURE 3.8: Steel tube-mass block elastic structure-based accelerometer geometry.

The relationship between strain and acceleration in the structure is given by Equation 3.19.

$$a = \frac{F}{m} = \frac{2ES}{m} \cdot \varepsilon \tag{3.19}$$

In Equation 3.19, F is the vibration inertia force of the mass block, S is the cross-sectional area of the capillary steel tube, m is the quality of mass black, and E is

Young's modulus of the capillary steel tube. The stiffness of the capillary steel tube is defined by Equation 3.20.

$$\begin{aligned} F &= 2ES \cdot \varepsilon = 2ES\frac{\Delta L}{L} = \left(\frac{2ES}{L}\right) \cdot \Delta L = k \cdot \Delta L, \\ k &= \frac{2ES}{L} \end{aligned} \tag{3.20}$$

The first natural frequency is given by Equation 3.21.

$$\omega_n = \sqrt{\frac{k}{m}} = \sqrt{\frac{2ES}{mL}} \tag{3.21}$$

Modeling the steel tube-mass block elastic structure as a spring-mass system, the sensitivity of the sensor is defined by Equation 3.22.

$$S_a = \frac{1}{\omega_n^2 L} = \frac{m}{2ES} \tag{3.22}$$

3.2.2.6 Flexible Hinges

The flexible hinges analytical model is based on [218]. The design of the structure is shown in Figure 3.9. This sensor is composed of two inertial masses, three straight circular flexure hinges, two FBGs, and a base. This structure is symmetrical, the sizes of flexure hinge 2 and flexure hinge 3 are exactly the same. Two FBGs are pre-stretched and attached at the top and bottom surfaces of the structure.

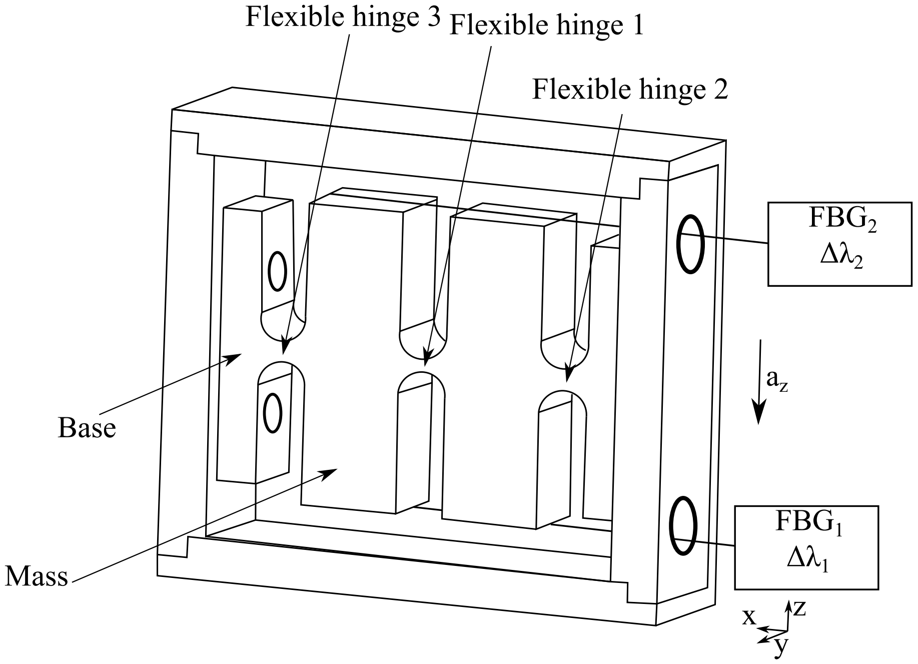

FIGURE 3.9: Flexible hinges accelerometer structure.

As a result of inertial forces acting on the sensors, the two masses will rotate slightly around the center of the flexible hinges 2 and 3, respectively, when an external acceleration is applied to the sensor's sensitive direction. The mechanical model of the sensor is shown in Figure 3.10. The stiffness of each flexible hinge is defined by Equation 3.23, where $s = \frac{r}{t}$, E is the flexible hinges Young's modulus, w is the flexible hinges structure thickness, and r is the flexible hinges curvature radius.

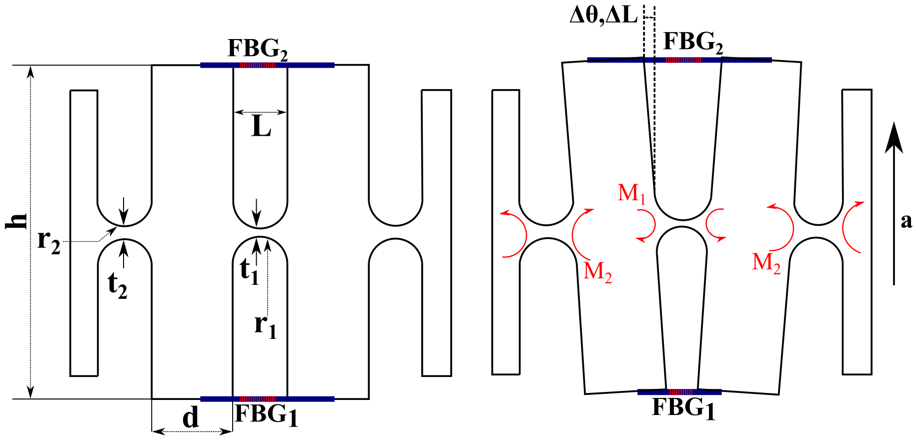

FIGURE 3.10: Flexible hinges accelerometer mechanical model under an external acceleration.

$$K = \frac{Ewr^2}{24} / \left[\frac{s^3\left(6s^2+4s+1\right)}{(2s+1)(4s+1)^2} + \frac{6s^4(2s+1)}{(4s+1)^{5/2}} \arctan\sqrt{4s+1} \right] \tag{3.23}$$

The stiffness of the optical fiber is considered in this analytical model, defined by Equation 3.24.

$$k_f = \frac{A_f E_f}{l}, \tag{3.24}$$

The resonant frequency, in Hertz, of the system is defined by Equation 3.25.

$$\omega_n = \frac{1}{2\pi}\sqrt{\frac{k_f h^2 + K_1 + K_2}{J}} \tag{3.25}$$

According to the moment of inertia formula and the parallel axis theorem, the moment of inertia can be obtained by the following, where m is the weight of the inertial mass, h is the inertial mass height, d is the inertial mass width, and r_2 is the external straight circular flexure hinge curvature radius:

$$J = m\frac{d^2+h^2}{12} + m\left(r_2 + \frac{d}{2}\right)^2 \tag{3.26}$$

The sensitivity of the sensor is defined by Equation 3.27 in pm/g.

$$S = \frac{\Delta\lambda}{a} = \frac{4\lambda\left(1-P_e\right)\Delta l}{al} = \frac{\lambda\left(1-P_e\right)}{l}\frac{2mh\left(r_2+\frac{d}{2}\right)}{k_f h^2 + K_1 + K_2} \tag{3.27}$$

In Equation 3.27, K_1 and K_2 are the stiffness for the flexible hinge 1 and the flexible hinge 2, respectively, λ is the Bragg wavelength of the FBG sensors, P_e is the photoelastic coefficient, and l is the distance between the two inertial masses, defined by $l = 2 \cdot r_1$.

3.2.3 Multi-objective optimization

Multi-objective optimization was carried out using the Python package Pymoo [193]. This package provides a variety of MOO algorithms, where NSGA-II was chosen to run the MOO in the accelerometer design [206]. The NSGA-II algorithm is a well-established multi-objective optimization algorithm and has been successfully applied to the design of accelerometers [208], [210]. NSGA-II's crowding distance mechanism provides a wide range of Pareto-front solutions. In the case of designing accelerometers, where multiple design configurations may meet the criteria, having a variety of options may allow designers to select from a greater range of options, taking into account practical constraints or secondary criteria [208]. A further advantage of NSGA-II is that it is able to handle problems with multiple objectives and constraints efficiently. With this capability, accelerometers can be designed in a range of geometric dimensions that are not associated with bulky sensors [210].

A preliminary analysis was conducted before running the MOO to determine analytical natural frequency and sensitivity for each geometry described in Section A.1 for different geometric parameters. As will be shown in Section 4.1, the flexible hinges structure is the only structure that met simultaneously the natural frequency and the sensitivity project requirements on the basis of the analytical model results. Due to this, this structure is selected to run the MOO analysis between all the analyzed structures. The MOO analysis is carried out to find some combinations of geometric dimensions that have an equilibrium between natural frequency and sensitivity in order to meet the requirements of the FBG-based accelerometer project. Furthermore, to validate the MOO, we have also selected geometry parameters that maximize sensitivity and natural frequency. To find the geometry parameters, Equations 3.28 and 3.29 were both designed to be simultaneously optimized by the Pymoo package using the NSGA-II algorithm.

$$f_1 = -\sqrt{\frac{k_f x_4^2 + K_1 + K_2}{J}} \tag{3.28}$$

$$f_2 = -\frac{\lambda\left(1-P_\mathrm{e}\right)}{l}\frac{2mx_4\left(x_5+\frac{x_3}{2}\right)}{k_f x_4^2 + K_1 + K_2} \tag{3.29}$$

In Equations 3.28 and 3.29, x_4 represents the height of the flexible hinges (h in Figure 3.10), x_5 represents the curvature radius of the external hinges (r_2 in Figure 3.10), and x_3 is the width of the inertial mass (d in Figure 3.10). Furthermore, λ is the central wavelength of the FBG (here considered $\lambda = 1.55\ \mu m$), P_e is the photoelastic constant of the silica optical fiber (here defined as $P_e = 0.22$), m is the weight of the inertial mass block derived as $m = x_3 \cdot x_4 \cdot x_2 \cdot \rho$, where x_2 is the flexible hinges structure thickness and ρ is the material's density that was selected for the fabrication (in this work is considered carbon steel with $\rho = 7800\ kg/m^3$). k_f, K_1, K_2, and J are defined as follows:

$$s_1 = \frac{r_1}{x_0}, \tag{3.30}$$

$$s_2 = \frac{x_5}{x_1}, \tag{3.31}$$

$$K_1 = \frac{Ex_2r_1^2}{24} / \left[\frac{s_1^3\left(6s_1^2+4s_1+1\right)}{(2s_1+1)(4s_1+1)^2} + \frac{6s_1^4(2s_1+1)}{(4s_1+1)^{5/2}}\arctan\sqrt{4s_1+1}\right], \tag{3.32}$$

$$K_2 = \frac{Ex_2x_5^2}{24} / \left[\frac{s_2^3\left(6s_2^2+4s_2+1\right)}{(2s_2+1)(4s_2+1)^2} + \frac{6s_2^4(2s_2+1)}{(4s_2+1)^{5/2}}\arctan\sqrt{4s_2+1}\right], \tag{3.33}$$

$$J = m\frac{x_3^2 + x_4^2}{12} + m\left(x_5 + \frac{x_3}{2}\right)^2, \tag{3.34}$$

$$k_f = \frac{A_f E_f}{l}, \tag{3.35}$$

where x_0 is the thickness of the internal flexible hinge (t_1 in Figure 3.10), x_1 is the thickness of the external flexible hinge (t_2 in Figure 3.10), A_f is the cross-section of the optical fiber (here considered as $A_f = 1.227 \cdot 10^{-8}$ m^2), E_f is the silica Young's modulus ($E_f = 70 \cdot 10^9$ Pa), l is the bonding span of the optical fiber ($l = 2r_1 = 15$ mm), E is the flexible hinges material Young's modulus ($E = 200 \cdot 10^9$ Pa), and $r_1 = 7.5$ mm. A stop criterion of 30000 iterations was used for the NSGA-II algorithm. A range of acceptable values was established for the variables x_0, x_1, x_2, x_3, x_4, and x_5 in the NSGA-II algorithm. These values were combined and applied in Equations 3.28 and 3.29. The results were analyzed and the local maxima were identified as potential optimized solutions. Table 3.1 shows the adopted range of values for each variable. Based on the dimensions of the bearings that were attached to the accelerometers, the range of values was selected (the accelerometers must not be bulky otherwise, they can alter the vibration pattern of the body), and a range of dimension x_2 was chosen to be close to 25.4 mm in order to reduce fabrication time (the raw steel used for fabrication of the sensors had a thickness of 25.4 mm).

TABLE 3.1: Range of acceptable values for the MOO variables.

	x_0 [mm]	x_1 [mm]	x_2 [mm]	x_3 [mm]	x_4 [mm]	x_5 [mm]
Minimum value	1.5	2	20	30	50	5
Maximum value	2.5	3	25.4	50	70	9

3.2.4 Finite element method analysis

The natural frequencies of the designed structures were numerically evaluated using ANSYS 2023 R2. As in the case of the multi-objective optimization, this analysis was carried out for the flexible hinges structure because this structure has fulfilled simultaneously the sensitivity and the natural frequency, as will be shown in Section 4.1. Based on the multi-objective optimization procedure, four combinations of geometric parameters were obtained. These geometries were selected to perform finite element modal analysis. For all geometries, a triangular mesh was used with an element size of 1 mm, 1 mm, 1 mm, and 1.5 mm for accelerometers 1, 2, 3, and 4, respectively. The modal analysis was carried out by the modal package in the Ansys workbench. For all cases, carbon steel alloy was selected for the material properties in the simulation procedure. To represent the optical fiber stiffness, a spring connection was added for all geometries with a stiffness of 57260 N/m. The fixed support boundary conditions for all flexible hinge structures are shown in Figure 3.11.

3.2.5 Project Requirements

For FBG-based accelerometers, sensitivity and natural frequency must be defined as project requirements. Due to the fact that the proposed project and method are

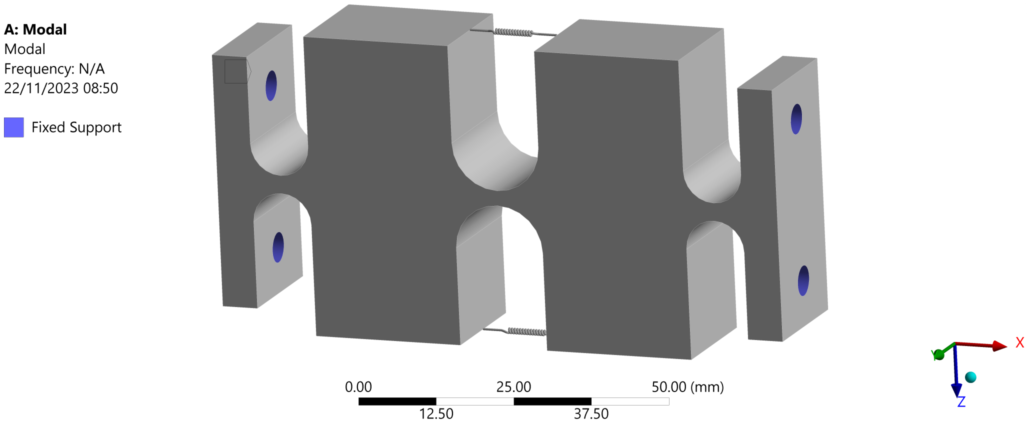

FIGURE 3.11: FEA Modal boundary conditions for the flexible hinges structures.

validated in a bench machinery fault simulator in this work, the experimental environment is controlled. There are no special requirements for material resistance, such as corrosion and thermal resistance, as in harsh environments. In this work, FBG-based accelerometers are designed for failure diagnosis for electrical motor rotation operating at 17, 35, and 50 rps. These values were adopted to easily separate the electric influence from the mechanical vibration spectrum. Since none of the adopted test rotation speeds is multiple of 60 Hz (power grid frequency used to feed all the experimental setup), some harmonics of this frequency can be attributed to the electric influence and separated from the mechanical vibration signals in the frequency domain.

Since the desired application is to diagnose faults in electrical motors, the harmonics generated by a failure must be considered at the project stage. In this work, we consider the project to cover fault diagnosis until the fifth harmonic. This is for covering faults such as misalignment, bent shaft, eccentric pulleys or gears, looseness, unbalance, internal misalignment, and excessive axial clearance [54]. In accelerometer design, it is recommended that the sensor's natural frequency must be at least twice the exciting frequency [219]. The fifth harmonic of the highest exciting frequency, in this work, results in $\omega_0 = 250$ Hz. So, the natural frequency requirement for the FBG-based accelerometer design is $\omega_{n_{req}} = 500$ Hz. The PZT accelerometers were used to assess the acceleration at the bearings in both vertical and horizontal directions to establish the sensitivity requirements for FBG-based accelerometers, shown in Table 3.2. An optical interrogator with a resolution of 2 pm (model Hyperion si255, LUNA Inc.) is used to measure the Bragg wavelength shift. By dividing the intensity of the measured accelerations by the resolution of the optical interrogator, the sensitivity requirements were determined. The sensitivity requirements are summarized in Table 3.3. For the FBG-based accelerometers, the required sensitivity is 100 pm/g in order to meet the sensitivity requirements.

3.3 Experimental setup

3.3.1 Temperature influence

As mentioned in the theoretical background section, temperature influences the Bragg wavelength shift due to thermal expansion and thermo-optic effects. In this work, all experiments are conducted in a temperature-controlled room ($T_{room} \approx 24°C$).

TABLE 3.2: Acceleration intensity measured by the commercial PZT-based accelerometers.

Rotor speed [rps]	Acceleration intensity [g] Bearing 1 Horizontal Direction	Bearing 1 Vertical Direction	Bearing 2 Horizontal Direction	Bearing 2 Vertical Direction
17	0.022	0.0208	0.031	0.021
35	0.062	0.047	0.1	0.061
50	0.091	0.063	0.133	0.091

TABLE 3.3: FBG-based accelerometers' acceleration sensitivity directional requirement for each bearing.

Rotor speed [rps]	Sensitivity requirement [pm/g] Bearing 1 Horizontal Direction	Bearing 1 Vertical Direction	Bearing 2 Horizontal Direction	Bearing 2 Vertical Direction
17	92	96	64	93
35	32	43	20	33
50	22	32	15	22

Moreover, when FBG-based accelerometers measure acceleration, the frequency of the strain caused due to driving forces generated by the applied acceleration is considerably higher than the variation in the room temperature. Then, the effect of the temperature in the Bragg wavelength, compared to the strain, can be neglected. Furthermore, since the frequency of the strain effect is higher than the temperature, a high-pass filter can be used to enhance strain sensitivity in the data analysis process.

3.3.2 Accelerometers characterization

For the accelerometer characterization, an experimental setup composed of an electrodynamic shaker system (model TV51110, TIRA), a commercial interrogator (model Hyperion si255 with an acquisition rate of 5000 Hz, LUNA Inc.), a signal generator (model AFG3021C, Tektronix), and a computer was used, shown in Figure 3.12. In the setup (identified by "I) Accelerometer characterization"), in Fig. 3.12, the accelerometers were mounted in a pendulum configuration. This configuration was used to avoid an overload on the shaker system, preserving its integrity.

The sensor's sensitivity was evaluated by using three sinusoidal signals with amplitudes of 5 Vpp and frequencies of 17, 35, and 50 Hz. Natural frequencies were characterized using a sinusoidal sweep signal with an amplitude of 5 Vpp, a start frequency of 5 Hz, a stop frequency of 1000 Hz, and a sweep time of 10 s. These signals were amplified and converted to analog signals by the electrodynamic shaker's power amplifier. The output voltage of the power amplifier that fed the shaker controlled the output acceleration. During sensitivity characterization, the output voltage of the power amplifier ranged from 1.0 to 2.5 V in steps of 0.3 V. During natural frequency characterization, the output voltage remained stable at 1.5 V. Based on the fact that the FBG-based accelerometers are attached to the shaker, the driving forces generated by the acceleration applied by the shaker cause a Bragg wavelength shift. For the sensitivity characterization, the data was collected for 30 seconds at each voltage stage using the optical interrogator at a rate of 5 kHz. In the natural frequency characterization, data was collected for 1 minute for each accelerometer. All the data was recorded three times at each step using a computer, for both sensitivity and natural frequency characterizations.

To measure the shaker's output acceleration (or the accelerometer's input base acceleration), a commercial FBG-based accelerometer (Accelerometer OS 7230, Luna Inc.) was used in the same pendulum configuration, as shown in Figure 3.12, identified by "II) Acceleration characterization". The wavelength shift was measured using the same optical interrogator used for accelerometer characterization. A computer recorded the data three times for 30 seconds at each of the following power amplifier output voltages: 1.0, 1.3, 1.5, 1.6, 1.9, 2.2, and 2.5 V. A relationship was established between output voltage and output acceleration by using this procedure.

3.3.3 Machinery fault diagnosis experiments

For machinery fault diagnosis experiments, the piezoelectric accelerometers that compose the MFS kit are substituted for the projected FBG-based accelerometers, as shown in Figure 3.13. To evaluate the performance of the projected sensors in fault diagnosis, different combinations of faults were considered in this study, summarized in Table 3.4. For each fault condition, the AC electrical motor's rotation was set at 17 and 35 rps. The Bragg wavelength shift was measured by a commercial optical interrogator (Hyperion si255, Luna Inc.) with a data acquisition rate of 1 kHz. The data was recorded for each condition for 30 s using a computer. In order to simulate each condition shown in Table 3.4, at 17 Hz and 35 Hz, two variations were performed: with and without an unbalanced load attached to the inertial disk.

TABLE 3.4: Fault conditions.

Condition	**Bearing condition**	**AC Motor**	**Acc. 2 position**	**Acc. 3 position**
1	Ball faulted	Healthy	Bearing 1	Bearing 2
2	Combination faulted	Healthy	Bearing 1	Bearing 2
3	Inner race faulted	Healthy	Bearing 1	Bearing 2
4	Outer race faulted	Heatlhy	Bearing 1	Bearing 2
5	Healthy	Healthy	Bearing 1	Bearing 2
6	Healthy	Broken rotor bars	Bearing 1	Bearing 2
7	Healthy	Broken rotor bars	Bearing 2	Bearing 1
8	Healthy	Faulted bearings	Bearing 2	Bearing 1
9	Healthy	Faulted bearings	Bearing 1	Bearing 2

The fault conditions shown in Table 3.4 were designed based on the faulted motors' availability and focused on covering different bearing faults since they are the most common failure type as discussed in the theoretical background section. The operating rotation speeds for the motor were chosen to avoid electric network harmonics (60 Hz and 120 Hz) and separate the electric interference from the mechanical vibration frequencies in the frequency vibration spectra.

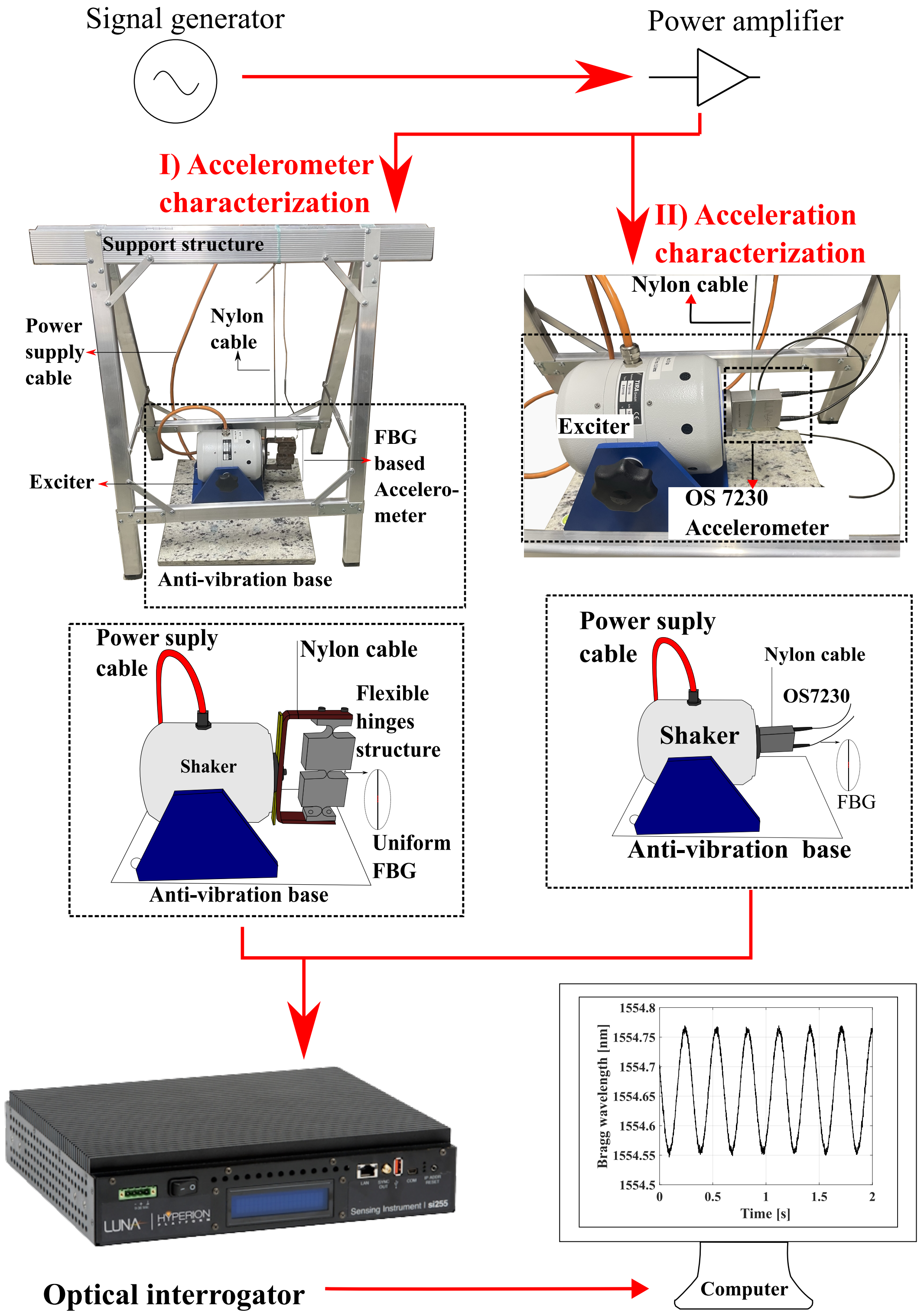

FIGURE 3.12: FBG-based accelerometers experimental characterization setup.

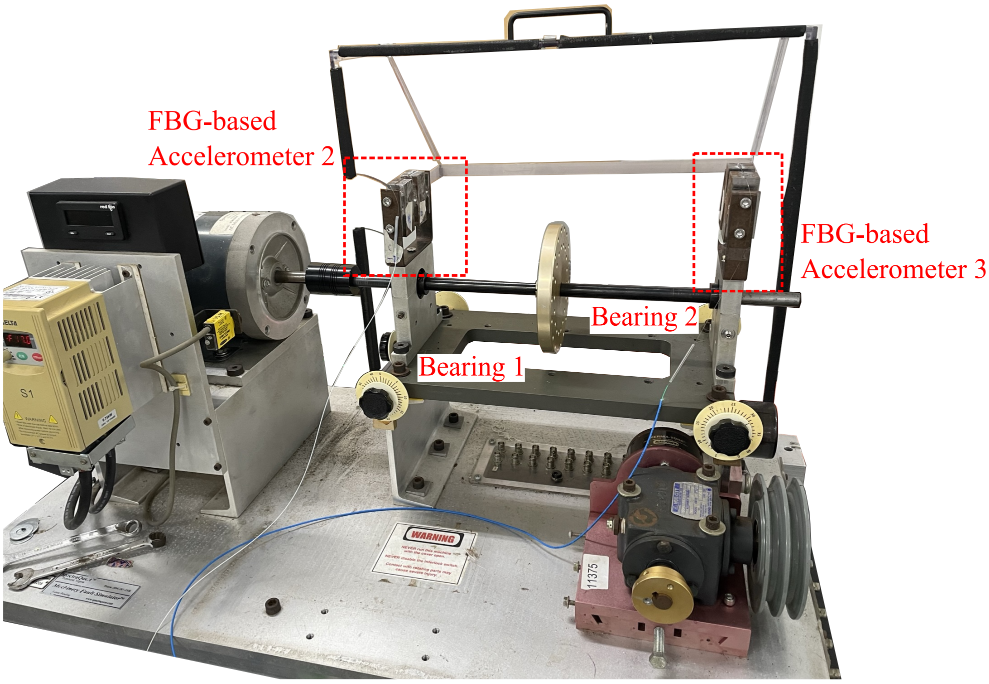

FIGURE 3.13: FBG-based accelerometers attached to the MFS bearings.

3.4 Data analysis

Different stages of the data analysis were performed. A Python algorithm was developed to generate response curves for natural frequency and sensitivity for each geometry described in the analytical models' section (Section A.1) by varying the geometric parameters that influence these characteristics. MATLAB algorithms were used to analyze the FBG-based accelerometer characterization and machinery fault diagnosis experiments data to process these data in the frequency domain (for fault diagnosis and natural frequency characterization) and to establish fit functions to experimentally evaluate the sensitivity of each sensor.

Chapter 4

Results and Discussions

4.1 Analytical models

In this section, the analytical models' results are presented. For all results in this section, the blue lines represent the natural frequency while the orange lines indicate the acceleration sensitivity. In both cases, the solid line represents the lower limit of the analyzed parameter. The dashed line illustrates the upper limit of this parameter in the evaluated range. The natural frequency project requirement is shown by a blue dotted line while the acceleration sensitivity requirement is indicated by an orange dotted line. To facilitate the reader's comprehension, when the calculated natural frequency or acceleration sensitivity lines intercept the natural frequency or acceleration sensitivity requirement lines, it means that the respective project requirement was achieved.

4.1.1 Double-L Cantilever Structure

To evaluate the natural frequency and the sensitivity for different values of geometric parameters for the Double-L Cantilever Structure, a range of inertial mass and Double-L Cantilever length were considered. The used parameters are shown in Table 4.1. This range of values was chosen based on the dimensions of the bearings where the sensors would be attached, avoiding bulky dimensions for accelerometers. In this table, E_s is the leaf spring Young's modulus, W_s is the leaf spring width, T_s is the leaf spring thickness, L is the Double-L Cantilever length, M is the inertial mass attached to the beam's free end, L_f is the optical fiber length between the attachment points, d_f is the optical fiber diameter, L_s is the leaf spring length, E_g is the optical fiber's Young's modulus, and H is the height of the Double-L Cantilever structure. The length of the double-L cantilever ranges from 20 to 100 mm and the inertial mass ranges from 10 to 75 g. The results for the double-L cantilever natural frequency and sensitivity are shown in Figure 4.1. In this graph, both acceleration sensitivity and natural frequency project requirements are plotted. For the evaluated range, the natural frequency requirement was only achieved for a beam length of $L = 20$ mm and for an inertial mass less than $m = 15$ g, nonetheless, the sensitivity requirement is not met in this configuration. To achieve the natural frequency requirement, the beam length would be less than $L = 10$ mm, which would imply difficulties for FBG sensor attachment to the double-L structure. As a result, this structure is discarded for multi-objective optimization.

4.1.2 Single cantilever

For the single cantilever structure, the natural frequency and the sensitivity are mainly affected by the length of the beam and the inertial mass attached to the

TABLE 4.1: Geometric parameters used in Double-L Cantilever Structure analytical model.

E_s [Pa]	W_s [mm]	T_s [mm]	L [mm]	M [g]	L_s [mm]	D_f [mm]	L_f [mm]	E_g [Pa]	L_2 [mm]
$50 \cdot 10^9$	11	0.3	20 - 100	10 - 75	$1.25 \cdot L$	0.125	$1.3 \cdot L$	$71.63 \cdot 10^9$	25

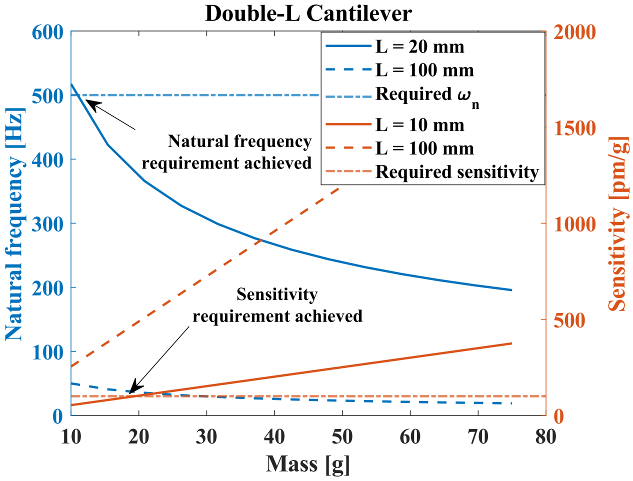

FIGURE 4.1: Natural frequency and sensitivity for the double-l cantilever structure.

free in a clamped-free beam configuration. Other geometric parameters influence the characteristics of these sensors, such as the material's Young's modulus, its density, and the dimensions of its cross-section. Table 4.2 shows the parameters used in this preliminary study. Here, E is the material's Young's modulus, b is the cross-section width, h is the cross-section height, ρ is the material's density, L is the beam's length, and m is the inertial mass. During this preliminary study, an aluminum alloy was considered to evaluate the sensor's characteristics (sensitivity and natural frequency) in relation to its geometric dimensions. The results of this analysis are shown in Figure 4.2, where the beam's length ranges from 30 to 100 mm while the inertial mass ranges from 5 to 100 g. In this graph, both acceleration sensitivity and natural frequency project requirements are plotted. In the evaluated range, the sensitivity requirement was only achieved for a beam length of $L = 100$ mm and an inertial mass higher than $m = 70$ g. As such, in this configuration, the natural frequency requirement is not met. For beam lengths higher than $L = 30$ mm and less than $L = 55$ mm, the natural frequency requirement can be satisfied, but to the detriment of sensitivity. Finally, in the evaluated range, the single cantilever structure could not fulfill both sensitivity and natural frequency requirements. For multi-objective optimization, this structure is discarded.

TABLE 4.2: Geometric parameters used in single cantilever analytical model.

E [GPa]	**b [mm]**	**h [mm]**	**ρ [kg/m³]**	**L [mm]**	**m [g]**
70	5	10	2710	30-100	5-100

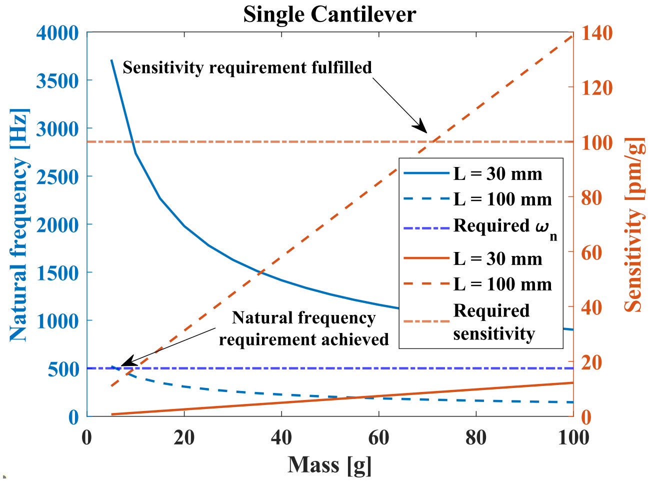

FIGURE 4.2: Natural frequency and sensitivity for the single cantilever structure.

4.1.3 Triangular cantilever

The natural frequency and sensitivity of a triangular cantilever are mainly determined by the inertial mass attached to the free end and the length of the beam in a clamped-free beam condition. To evaluate the impact of geometric parameters on sensor characteristics (natural frequency and sensitivity), an aluminum alloy was used for the preliminary study. Table 4.3 summarizes the geometric parameters used for this preliminary study, whose Young's modulus E is the material's Young's modulus, b is the cross-section width at the clamped end of the triangular beam, t is the cross-section height, ρ is the material's density, L is the beam's length and m is the inertial mass attached to the free end of the beam. Figure 4.3 shows the results for these geometric parameters, where the beam length varies from 25 to 100 mm, and the inertial mass varies from 5 to 100 g. In the evaluated range of geometric parameters, the sensitivity requirement was achieved. However, the natural frequencies were less than 100 Hz and did not meet the natural frequency requirement. Due to the preliminary evaluation of this structure, it has been discarded for the multi-objective optimization process in this work.

TABLE 4.3: Geometric parameters used in triangular cantilever analytical model.

E [GPa]	**b [mm]**	**t [mm]**	**ρ [kg/m^3]**	**L [mm]**	**m [g]**
70	30	5	2710	25-100	5-100

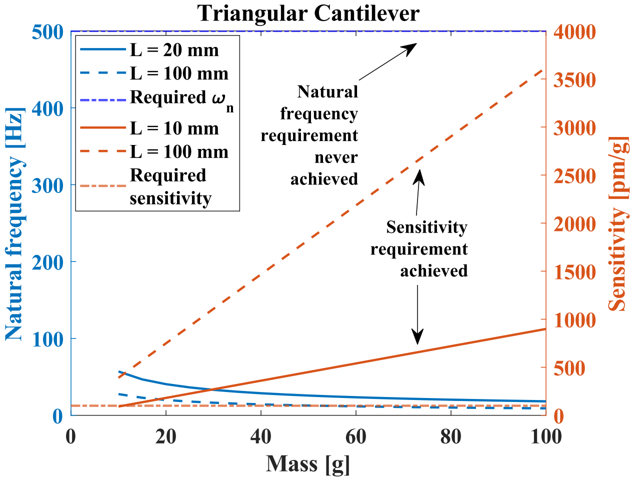

FIGURE 4.3: Natural frequency and sensitivity for the triangular cantilever structure.

4.1.4 Clamped-Clamped Cantilever

To evaluate the impact of geometric parameters on the sensitivity and natural frequency of the clamped-clamped cantilever structure, an aluminum alloy was also adopted. Table 4.4 summarizes the used parameters in this preliminary study, where E is the material's Young's modulus, b is the beam's cross-section width, h is the beam's cross-section height, L is the beam's length, ν is the material's Poisson's ratio, m is the inertial mass, ρ is the material's density, and d is the grating length in the optical fiber sensor. Figure 4.4 illustrates the variation of natural frequency and sensitivity with respect to those parameters, where the beam length ranges from 25 to 100 mm and the inertial mass ranges from 5 to 100 mm. In view of the analyzed parameters, the natural frequency requirement was achieved for a beam length of $L = 30$ mm for an inertial mass less than 20 g. The sensitivity requirement was met for $L = 100$ mm for an inertial mass higher than 60 g. But in these configurations, both natural frequency and sensitivity were not simultaneously achieved. Finally, for this work, this structure is discarded for the MOO procedure.

TABLE 4.4: Geometric parameters used in clamped-clamped cantilever analytical model.

E [GPa]	b [mm]	h [mm]	ρ [kg/m³]	L [mm]	m [g]	ν	d [mm]
70	9	0.5	2710	25-100	5-100	0.334	10

4.1.5 Steel Tube-Mass Block Elastic Structure

For the steel tube-mass block elastic structure, a steel alloy was adopted in this preliminary study to assess the impact of geometric parameters on the natural frequency and sensitivity of the sensor. Table 4.5 summarizes the used parameters, where E is the material's Young's modulus, d_i is the tube's inner diameter, d_o is the tube's outer diameter, L is the tube's length and m is the inertial mass. Figure 4.5 shows the results for those geometric parameters. According to the figure, this structure achieved the natural frequency requirement, but at the expense of the sensor's sensitivity. It could not meet all of the project requirements at once. This structure is discarded for multi-objective optimization.

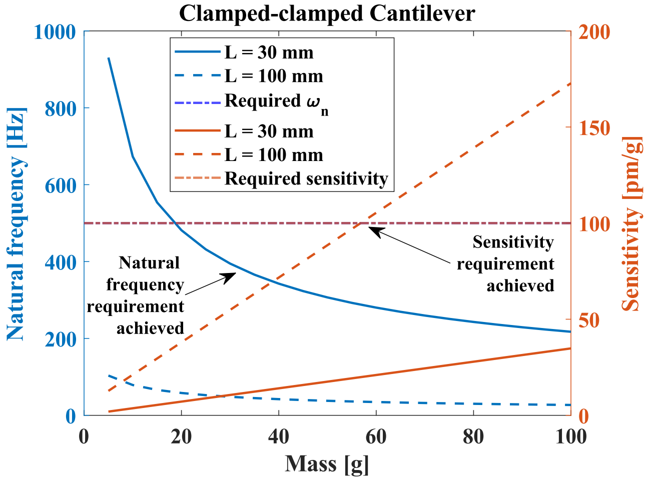

FIGURE 4.4: Natural frequency and sensitivity for the clamped-clamped cantilever structure.

TABLE 4.5: Geometric parameters used in the steel tube-mass block elastic Structure analytical model.

E [Gpa]	d_i [mm]	d_o [mm]	L [mm]	m [g]
210	0.6	1	10-100	10-75

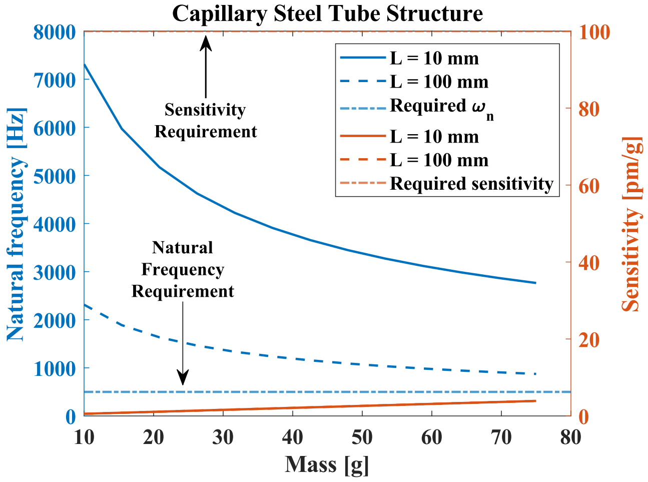

FIGURE 4.5: Natural frequency and sensitivity for the steel tube-mass block elastic structure.

4.1.6 Flexible Hinges

For the flexible hinges structure, a steel alloy ($E = 210$ GPa and $\rho = 7850$ kg/m^3) is analyzed to evaluate the impact of the geometric parameters on the sensor's natural frequency and sensitivity. The Bragg wavelength for this preliminary study is $\lambda = 1.55$ μm with a photoelastic coefficient $P_e = 0.22$. The optical fiber diameter was considered as $d_f = 125$ μm, resulting in a cross-section area $A_f = 1.227 \cdot 10^{-8}$ m^2 and the silica's Young's modulus was considered as $E_g = 70$ GPa. Table 4.6 summarizes the geometric parameters used for the flexible structure. The sensitivity and natural frequency variation according to these parameters is shown in Figure 4.6. For the evaluated range, the flexible hinge structure met simultaneously natural frequency and sensitivity project requirements. In Figure 4.6, for $h = 45$ mm and $h = 50$ mm the requirements are attended to. Finally, the flexible hinge structure is selected for multi-objective optimization.

TABLE 4.6: Geometric parameters used in the flexible hinges analytical model.

r_1 **[mm]**	t_1 **[mm]**	r_2 **[mm]**	r_2 **[mm]**	w **[mm]**	d **[mm]**	h **[mm]**	L **[mm]**
7.5	2.5	5	3	25.4	20-50	20-80	15

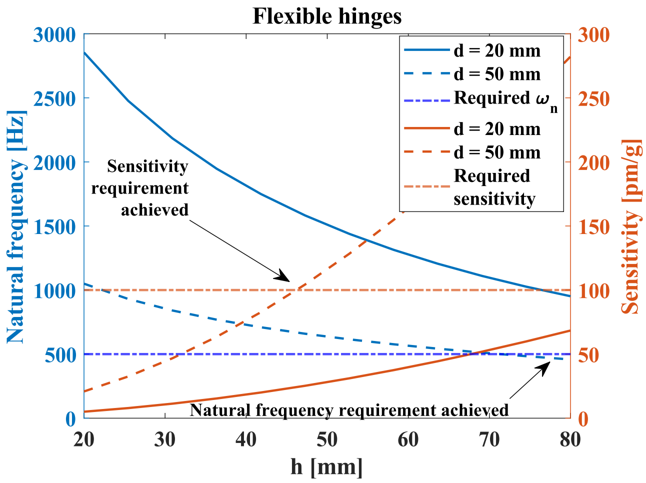

FIGURE 4.6: Natural frequency and sensitivity for the steel tube-mass block elastic structure.

4.1.7 Analytical results summary

In summary, each geometry has its own advantages and drawbacks. Depending on the project requirements, the geometry of accelerometers must be selected to fulfill both natural frequency and sensitivity requirements. The first feature is related to the frequency operational range. This defines the frequency flat operational range for the sensor. It must be adequate based on the rotor speed so that the running speed is in this range. The second feature is related to the amplitude of input acceleration that causes a measurable output signal in the sensor. It must be carefully assessed because otherwise, the sensor cannot measure acceleration. Table 4.7 summarizes the results of the primary assessment using analytical models. It can be seen that the flexible hinge structure met the project requirements for this work.

4.2 Multi-objective optimization

Using the multi-objective optimization algorithm, several combinations of geometric parameters were achieved. The geometric parameters for the selected combinations are summarized in Table 4.8. In this, a variety of geometries were obtained, resulting in distinct accelerometer characteristics, as shown in Figure 4.7. Multi-objective optimization provides a versatile tool for addressing diverse project requirements. In experimental applications, acceleration varies along the machinery or structure body. This is particularly relevant to mechanical vibration monitoring at different points along the machine. As a result, geometric parameters can be selected in an

TABLE 4.7: Summary of the analytical model's primary assessment.

Geometry	Natural frequency requirement	Sensitivity requirement	Requirement fulfilled simultaneously
Double-L cantilever	x	x	
Single cantilever	x	x	
Triangular cantilever		x	
Clamped-clamped cantilever	x	x	
Steel Tube-Mass Block Elastic Structure	x		
Flexible hinges	x	x	x

optimal manner to meet the needs of different points of the machine that are aimed to be covered by the accelerometer project. The Accelerometer 1 was designed to achieve the highest natural frequency of the evaluated geometric parameters. The Accelerometer 2 was projected to meet the project requirements established in this work for machinery fault diagnosis, as well as for the Accelerometer 3. The Accelerometer 3 has higher sensitivity than Accelerometer 2, and it is more suitable to be attached to bearing 2 (see Figure 3.13) where the amplitude of acceleration is smaller than in bearing 1 (due to its proximity to the rotor). Finally, the Accelerometer 4 was designed to achieve the highest sensitivity to the evaluated geometric parameters. These accelerometers have been selected to validate the multi-objective optimization technique as a versatile tool for FBG-accelerometer design. It is pertinent to note that the geometric parameters for all accelerometers were adequate for fabrication by rounding some of these parameters to values that are in the resolution of the computer numerical control machine used to fabricate the sensors.

TABLE 4.8: Geometric parameters and accelerometer features for the flexible hinges structure resulted from a multi-objective optimization procedure.

r_1 [mm]	t_1 [mm]	r_2 [mm]	t_2 [mm]	w [mm]	d [mm]	h [mm]	Analytical ω_n [Hz]	Analytical Sensitivity [pm/g]	Acc. Number
7.5	2.5	5	3	20	25	50	898.42	85.12	1
7.5	1.5	5	3	21	30	60	566.45	193.30	2
7.5	2.5	5	3	25.4	30	65	599.36	175.27	3
7.5	2.5	9	3	25.4	50	70	271.92	549.96	4

4.3 Finite element analysis

The results of the finite element analysis (FEA) carried out in the ANSYS 2023 R2 software are summarized in Table 4.9. There are relative errors between the FEA modal analysis and the analytical model related to non-linear phenomena neglected in the analytical model. Furthermore, the FEA modal analysis uses numerical approximations to solve the problem. There are intrinsic differences between the analytical model and the FEA analysis, so divergence in the results is expected. The results of the modal FEA analysis are shown in Figure 4.8. These results show the first natural frequency and vibration mode. When flexible hinge structures are subjected to acceleration, the inertial displacement pulls the optical fiber attached to the top surface of the flexible hinge structure. Thus, a strain is applied to the optical

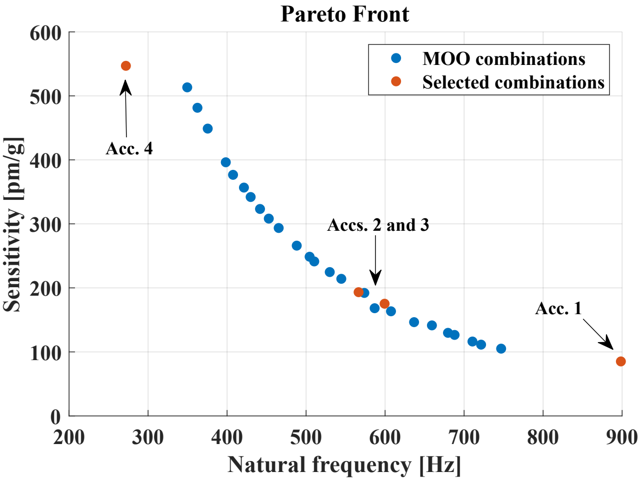

FIGURE 4.7: Multi-objective optimization Pareto front.

fiber, resulting in a Bragg wavelength shift due mainly to photoelastic effects and a change in the grating period caused by axial traction applied by the inertial mass block. This phenomenon can be used to measure acceleration since the Bragg wavelength shift is proportional to acceleration. It is also pertinent to note that besides the relative errors between analytical natural frequency and FEA natural frequency, accelerometers 2 and 3 continue to fulfill the project requirement for this feature.

TABLE 4.9: FEA natural frequencies results by the modal analysis using ANSYS 2019 R3.

Accelerometer	FEA ω_n [Hz]	Analytical ω_n [Hz]	Relative Error [%]
1	933.14	898.42	4
2	548.3	566.45	3
3	636.72	599.36	6
4	259.77	271.92	4.5

4.4 FBG-Based accelerometers characterization

An acceleration-output voltage relationship for the electrodynamic shaker power amplifier is defined for sensitivity characterization for this work. Notably, the force exerted by the electrodynamic shaker exhibits variability in response to the mass being excited. Consequently, this characterization is essential to elucidate the nuanced interplay between input parameters and the resultant force and acceleration applied by the electrodynamic shaker. This result is shown in Figure 4.9. As shown in this figure, greater output voltage in the power amplifier implies higher acceleration amplitudes, as expected. Furthermore, acceleration amplitudes have increased with exciting frequency. This is due to the fact that the electrodynamic shaker was operated in voltage mode. During this mode, the output voltage of the power amplifier that feeds the shaker remains stable while the current varies in order to maintain the voltage constant. However, the force applied by the shaker to the accelerometer structure is proportional to the current. Due to the variation in force, different acceleration sensitivities may be observed based on the frequency of excitation [28], [187], [220].

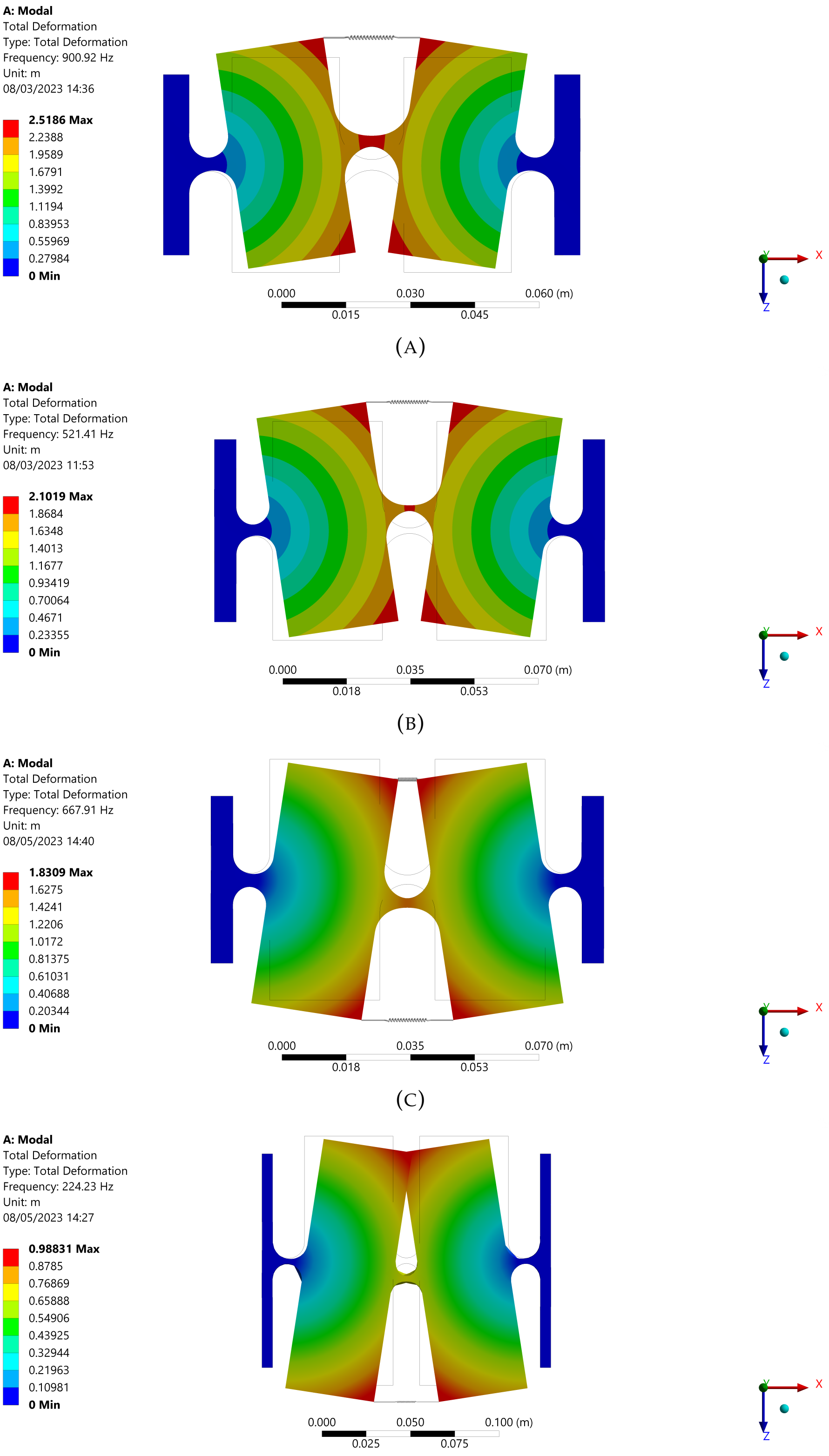

(A)

(B)

(C)

(D)

FIGURE 4.8: FEA Modal analysis results for (A) Accelerometer 1, (B) Accelerometer 2, (C) Accelerometer 3, and (D) Accelerometer 4.

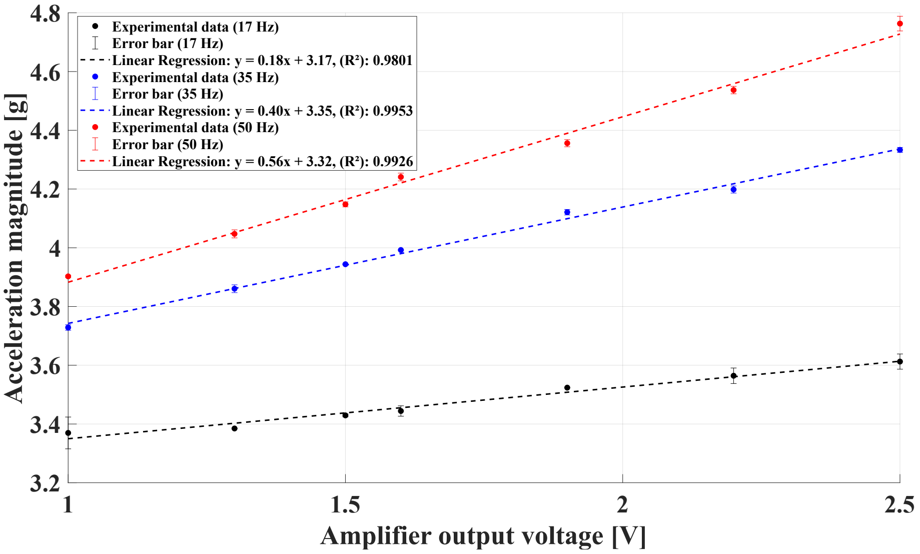

FIGURE 4.9: Acceleration-output voltage relationship for the vibration test system power amplifier for 17, 35, and 50 Hz.

The accelerometers' acceleration sensitivity characterization results are shown in Figure 4.10. As shown in this figure, the increase in acceleration amplitude implies increased driving forces caused by the displacement of the inertial mass. As the optical fibers are attached to the top surface of the inertial block mass, they are subjected to greater strains. Due to the applied strain at the optical fiber, a higher Bragg wavelength shift is expected. For all accelerometers, there was a linear relationship between the Bragg wavelength shift and acceleration. The sensitivity of the accelerometer sensors decreases with increasing frequency, which can be attributed to the difference in the applied force caused by the electrical shaker in the accelerometer structures at different excitation frequencies. Furthermore, as the excitation frequency increases, the accelerometer mass becomes more susceptible to inertial effects. Consequently, the mass may not move as much in response to the force applied, resulting in a smaller strain on the attached FBG, as well as a reduction in strain transfer from the accelerometer mechanical system to the optical fiber sensor, thus reducing the strain applied to the FBG sensor[221]–[223]. Figure 4.11 depicts the results for the natural frequency characterization for the accelerometers. According to the figure, the naturally occurring frequencies of accelerometers 1, 2, 3, and 4 are 607.8, 366.7, 294.7, and 236.5 Hz respectively. These results are summarized in the Table 4.10.

The higher sensitivity was expected for the accelerometer 4 since it has the greater inertial mass in the spring-mass system. Nevertheless, the experimental sensitivity is highly influenced by the pre-tension applied to the optical fiber in the paste span [224]. The higher the pre-tension, the greater the experimental sensitivity, since the optical fiber will be stretched more. Therefore, a lower amplitude acceleration will result in a higher strain when compared to a weaker pre-tension. In the analytical model, all the strain suffered by the flexible hinges was transmitted to the optical fiber. In real-world applications, there is energy loss for inertial effects, neglected by analytical models. Then, it was expected that there would be a divergence between analytical and experimental results. Furthermore, the optical fibers were manually attached to the top surface of the flexible hinge structures, so the pre-tension application was uneven. For an assertive experimental sensitivity comparison, it would

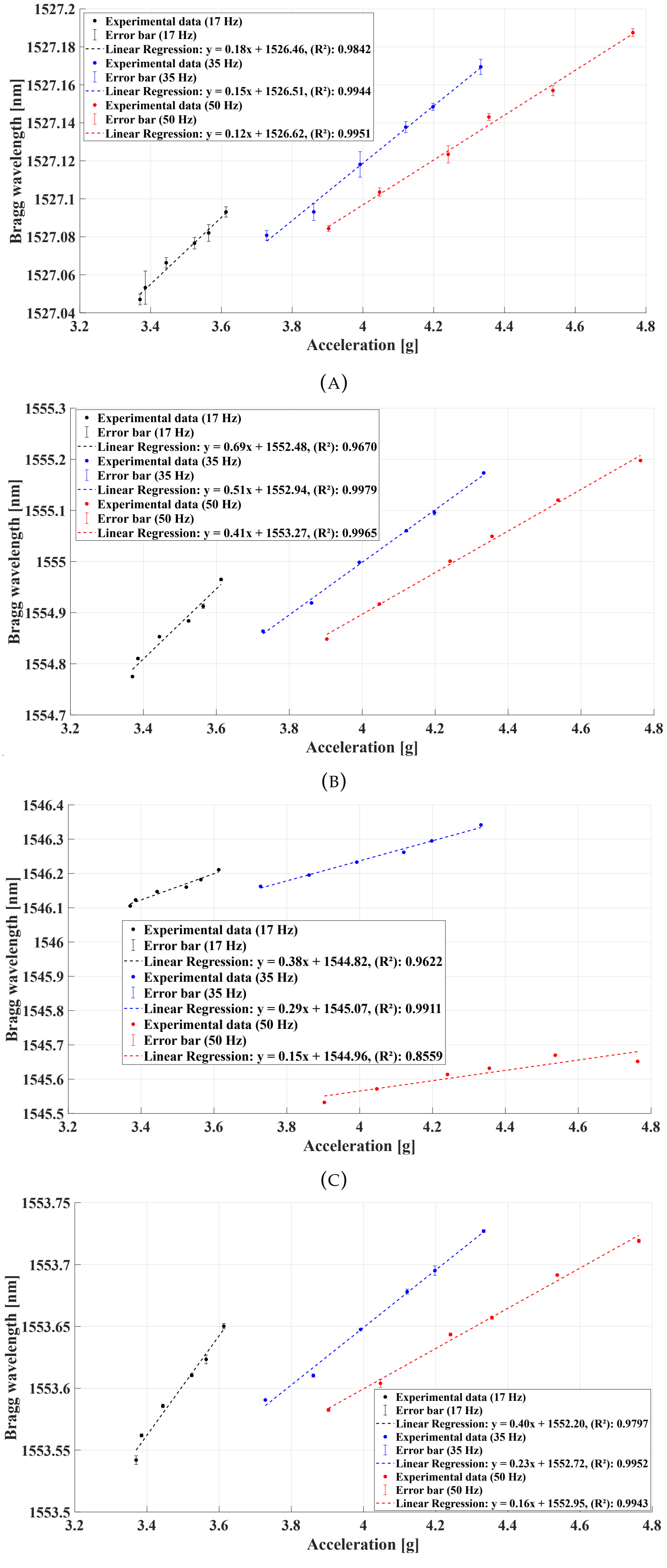

(A)

(B)

(C)

(D)

FIGURE 4.10: Sensitivity characterization results for (A) Accelerometer 1, (B) Accelerometer 2, (C) Accelerometer 3, and (D) Accelerometer 4.

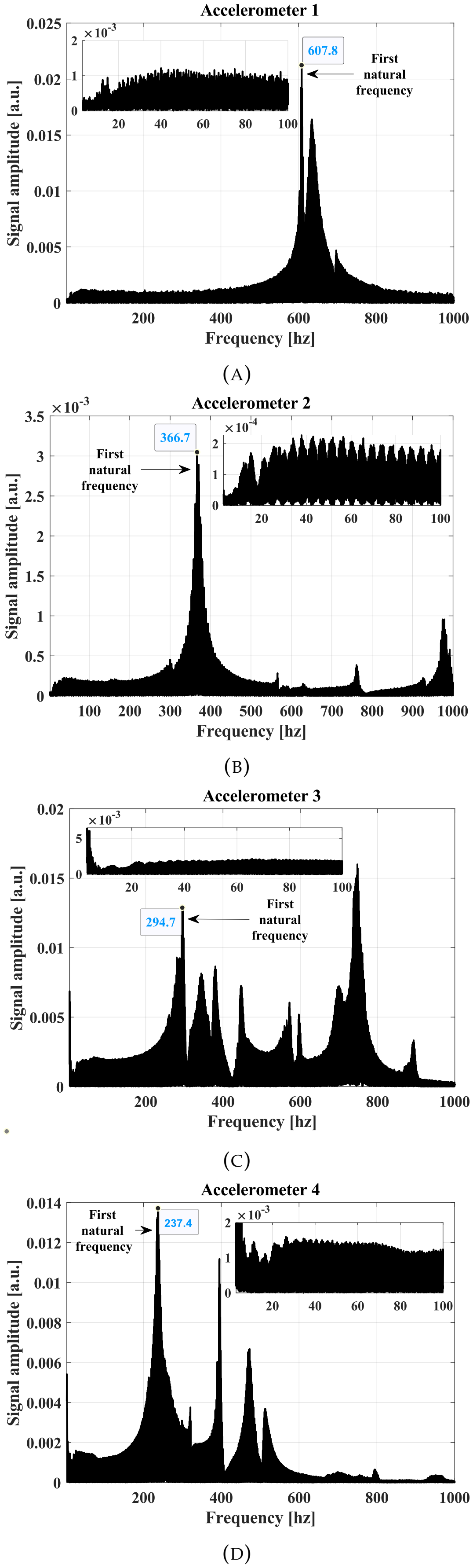

(A)

(B)

(C)

(D)

FIGURE 4.11: Natural frequency characterization results for (A) Accelerometer 1, (B) Accelerometer 2, (C) Accelerometer 3, and (D) Accelerometer 4.

TABLE 4.10: Accelerometer features.

Acc.	**Analytical** ω_n **[Hz]**	**FEA** ω_n **[Hz]**	**Experimental** ω_n **[Hz]**	**Analytical Sensitivity [pm/g]**	**Experimental Sensitivity [pm/g]**
1	898.42	933.14	607.8	85.12	180 (17 Hz)
					150 (35 Hz)
					120 (50 Hz)
2	566.45	548.3	366.7	193.30	690 (17 Hz)
					510 (35 Hz)
					410 (50 Hz)
3	599.36	636.72	294.7	175.27	380 (17 Hz)
					290 (35 Hz)
					150 (50 Hz)
4	271.92	259.77	235.5	546.96	400 (17 Hz)
					230 (35 Hz)
					160 (50 Hz)

be necessary to have a mechanism that guarantees the same pre-tension application in the pasted span.

In the case of accelerometer 1, the relative errors between analytical sensitivity and experimental sensitivity are 111%, 76%, and 41% at 17 Hz, 35 Hz, and 50 Hz, respectively. For accelerometer 2, the relative errors between analytical sensitivity and experimental sensitivity are 257%, 164%, and 65% at 17 Hz, 35 Hz, and 50 Hz, respectively. In accelerometer 3, the relative errors between analytical sensitivity and experimental sensitivity are 117%, 65%, and 14%, respectively, at 17 Hz, 35 Hz, and 50 Hz. The relative error between analytical sensitivity and experimental sensitivity for accelerometer 4 is 27%, 58%, and 71%, respectively, at 17 Hz, 35 Hz, and 50 Hz. Obtaining an initial estimate and insight into the performance of FBG-based accelerometers through analytical models is typically a valuable first step. The use of an analytical model provides a systematic method for exploring design parameters and predicting sensitivity based on theoretical assumptions. When compared with experimental results, analytical models may not fully capture the complexities and practical limitations of real-world situations. It is possible that they may overlook error sources such as heterogeneity of materials within the FBG itself or variations in the bonding process during sensor fabrication, which can have a significant impact on the sensitivity of the sensor. The experimental results provide a more accurate assessment of sensitivity by taking into account factors such as sensor imperfections, environmental influences, and inertial effects. Consequently, the accelerometer's performance can be evaluated in a more realistic and comprehensive manner. Due to these limitations, although analytical models serve as a useful starting point for design optimization, the ultimate validation and refinement of sensitivity measurements in FBG-based accelerometers typically rely on experimental data.

The acceleration intensity used in this characterization has other errors that should be noted. The sensitivities of the manufactured FBG-based accelerometers used in this study differ according to their excitation frequency, as the acceleration has varied with the excitation frequency (see Figure 4.9. A commercial FBG-based accelerometer was characterized to determine the effect of mass on acceleration intensity. Due to the differences in mass between commercial and manufactured FBG-based accelerometers, the acceleration amplitude (and the applied force exerted by the electrodynamic shaker) in each case will be intrinsically different, resulting in some experimental errors (a limitation of the setup used). By attaching an external accelerometer to the base of the structure, the acceleration intensity of the structure can be measured directly during the characterization process, thus reducing experimental error. A variation is also observed between the inputted acceleration in the FBG-based accelerometer base and the outputted strain transmitted from the flexible hinge structure to the FBG sensor. Figure 4.11 illustrates this phenomenon, mainly when the excitation frequency was 17 Hz. Additionally, this variation can result in a variation in acceleration sensitivity as a function of the excitation frequency.

For accelerometers 1, 2, 3, and 4, the relative errors between analytical natural frequency and experimental natural frequency are 32%, 35%, 51%, and 13%, respectively. Based on the numerical results compared to the experimental characterization, the relative errors are 54%, 50%, 116%, and 10%, respectively. Analytical models provide a theoretical foundation for predicting natural frequencies based on design parameters and assumptions. However, these models may not always fully account for real-world complexities. For instance, they might overlook errors arising from variations in the FBG material properties or the bonding process of the FBG sensor to the mechanical structure during sensor fabrication. This can influence the accuracy of predicting natural frequencies. Experimental characterizations, on the other hand, directly measure the accelerometer's actual response. They are sensitive to non-homogeneities in the accelerometer's material and environmental effects such as temperature and corrosion. Corrosion may cause material loss and change the sensor's natural frequency [225]. Discrepancies between analytical predictions and experimental results can arise due to these real-world effects, highlighting the need to validate and fine-tune analytical models in order to better reflect the practical performance of FBG-based accelerometers. In order to ensure accurate natural frequency determination in accelerometer designs, it is crucial to understand both analytical and experimental approaches thoroughly.

There are often differences between simulation and experimental results due to the inherent distinctions between the two types of measurement. By using mathematical models and computational simulations, finite element modal analysis is able to predict the natural frequencies of a structure based on the design specifications and material properties. Despite the fact that this approach can provide valuable insight into the accelerometer's theoretical behavior, it may not fully capture the nuances of real-world conditions and potential sources of error, such as manufacturing variations or environmental factors (as in the case of analytical models). In addition, numerical methods can handle more complex geometries and boundary conditions than analytical methods. Models based on analytical methods are often limited to simple geometries and boundary conditions, which do not accurately represent real-world structures. Numerical methods also provide more accurate results than analytical models by taking into account more realistic conditions, such as material properties, loading conditions, and boundary conditions [226]–[228]. This can lead to more accurate results.

4.5 Machinery fault diagnosis

For the diagnosis of machinery faults, the vibration frequency spectrum is analyzed by applying the Fourier transform to the data collected by the FBG-based accelerometer in each condition depicted in Table 3.4. The results of the FBG-based accelerometer will be compared with those from a piezoelectric (PZT)-based accelerometer attached to the same bearing and measuring acceleration in the same direction in order to verify their accuracy. By applying the Fourier transform to the time-domain data recorded by the PZT accelerometers at a data acquisition rate of 2 kHz, the vibration frequency spectrum of the PZT accelerometers is also obtained.

4.5.1 Fault condition 1

In fault condition 1, a ball-faulted bearing was attached to the bearing that accelerometer 2 was attached to. A vibration frequency spectrum exhibiting high-order frequencies is expected in this type of failure. Different factors are responsible for these high-order frequencies. The impact generated by each pass of a rolling element over a defect in a bearing occurs when the bearing begins to fail, such as through pitting, flaking, or cracking of the raceways or rolling elements. A pulse or shock is generated by this impact, not only at the fundamental fault frequency but also at a wide range of frequencies. The impulses can cause resonances in the bearing structure, casing, or other components of the machine, which will often appear in frequency analysis as high-order harmonics. It is common for bearing faults to result in non-linear and asymmetric behavior in the system. By means of various processes such as doubling and tripling, this non-linearity converts fundamental frequencies and their harmonics into higher-order harmonics. This non-linear behavior becomes more significant as the severity of the fault increases. Bearing defects cause periodic impulses as defects in the inner race, outer race, or rolling elements repeatedly contact one another. It is important to note that these impulses are not sinusoidal in nature and contain a wide spectrum of frequencies, including a considerable amount of energy at high frequencies [53]–[55].

Figure 4.12 illustrates the result comparison between the FBG-based accelerometer 2 and the PZT-based accelerometer attached to bearing 1 when the rotor was operated at 17 rps, while Figure 4.13 shows the results when the rotor was operated at 35 rps. Figures 4.14 and 4.15 shows the results following the same structure mentioned above for FBG-based accelerometer 3 and PZT-based accelerometer attached to the bearing 2.

At 17 rps, the accelerometer has identified the nominal frequency close to 17 Hz (1X), the third harmonic close to 34 Hz (3X), the fourth harmonic close to 68 Hz (4X), and the fifth harmonic close to 85 Hz (5X). The high-order frequencies characteristic of ball-faulted bearings were identified as being close to 257 Hz. The same vibration pattern was identified for the unbalanced condition, with a difference in the amplitude of the vibration at the nominal frequency. This was due to an unbalanced load attached to the inertial disk. Since the added load rotates at the same frequency as the rotor, there is rotational motion amplification at this frequency. This implies higher acceleration amplitudes. In ball-fault bearings, the third harmonic appearance can be related to the eccentricity between the inner and outer races [229]. Furthermore, the frequency at which a damaged ball or roller spins on its own axis, the Ball Spin Frequency (BSF), can manifest near 4X or 5X harmonics [230]. For the rotor operating at 17 rps, in balanced and unbalanced conditions, BSF was manifested near 4X. For the rotor operating at 35 rps, the nominal frequency was near 35 Hz

(1X), the second harmonic near 70 Hz (2X), the third harmonic was close to 105 Hz (3X), and high-order frequencies were identified for both with and without unbalanced load conditions. The increase in the amplitude at the nominal frequency was identified by comparing balanced and unbalanced conditions. The appearance of the second harmonic can be related to misalignment between the inner and outer races of the bearing [230]. These results are compared and validated by vibration pattern recognition by the PZT-based accelerometer attached to bearing 1. The rotor operating at 17 rps had a nominal frequency close to 17 Hz and a sixth harmonic close to 102 Hz, along with high-order frequencies characteristic of a bearing with faulted balls. For the rotor at 35 rps, the nominal frequency close to 35 Hz (1X), the second harmonic close to 70 Hz (2X), the third harmonic close to 105 Hz (3X), the fourth harmonic near 140 Hz, and high-order frequencies were identified for both balanced and unbalanced conditions. Since the frequency vibration spectra obtained for the FBG and PZT-based accelerometers were similar, for balanced and unbalanced conditions, it is assumed that the FBG-based accelerometer 2 has correctly identified fault condition 1.

In FBG-based accelerometer 3, for the rotor at 17 rps, the obtained frequency vibration spectra were similar to the accelerometer 2, for balanced and unbalanced conditions, in which the nominal frequency about 17 Hz (1X), the third harmonic close to 34 Hz (3X), the fourth harmonic approximately 68 Hz (4X), and the fifth harmonic around 85 Hz (5X) were detected beside the high-order frequencies characteristics of the ball-faulted bearing. For the rotor at 35 rps, the nominal frequency and the second harmonic, and high-order frequencies were identified. These results are compared with the measurements of the PZT-based accelerometer attached to bearing 2. For the rotor at 17 rps, the nominal, the third harmonic, the sixth harmonic, and high-order frequencies were found. In the unbalanced condition, the increase in the amplitude of the nominal frequency suppressed other harmonics, but high-order frequencies could still be detected. For the rotor at 35 rps, the nominal, the second, the third, the fourth, the sixth, the seventh, and high-order frequencies were identified. In the unbalanced condition, the increase in the amplitude of the nominal frequency suppressed other harmonics, but high-order frequencies could still be recognized. Since the frequency vibration spectra obtained for the FBG and PZT-based accelerometers were similar, for balanced and unbalanced conditions, it is assumed that the FBG-based accelerometer 3 has correctly identified fault condition 1.

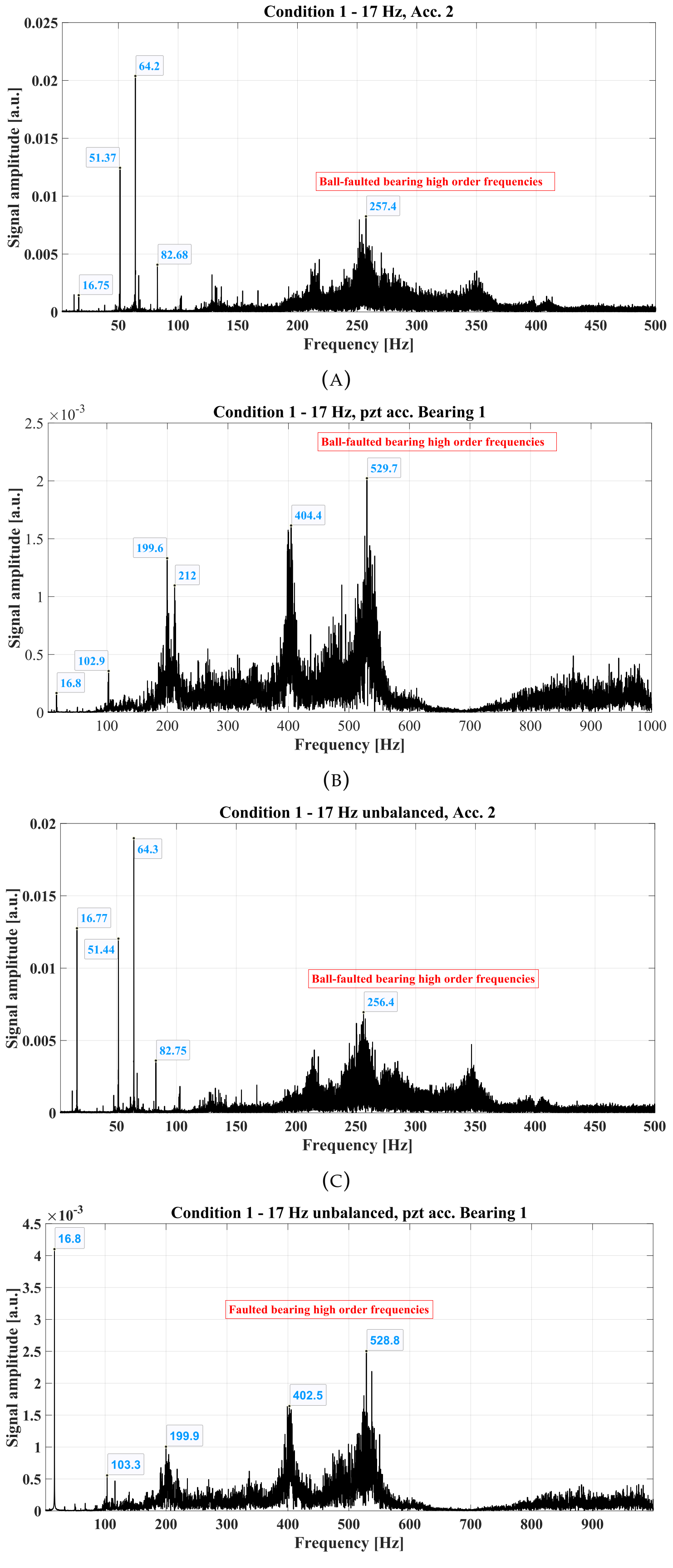

(A)

(B)

(C)

(D)

FIGURE 4.12: Fault condition 1 vibration frequency spectra for rotor speed at 17 rps for (A) FBG Acc. 2, (B) PZT Acc. at Bearing 1, (C) FBG Acc. 2 (unb), and (D) PZT Acc. at Bearing 1 (unb).

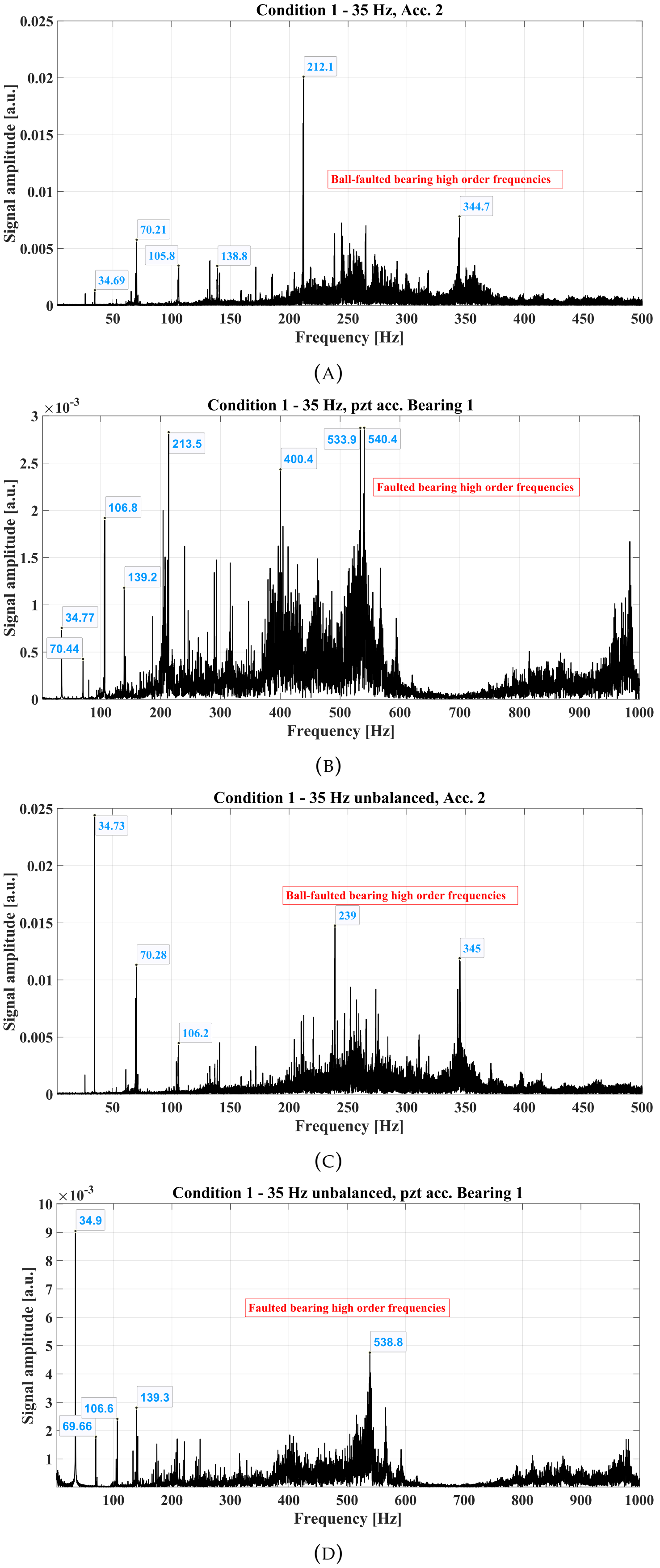

Condition 1 - 35 Hz, Acc. 2

(A)

Condition 1 - 35 Hz, pzt acc. Bearing 1

(B)

Condition 1 - 35 Hz unbalanced, Acc. 2

(C)

Condition 1 - 35 Hz unbalanced, pzt acc. Bearing 1

(D)

FIGURE 4.13: Fault condition 1 vibration frequency spectra for rotor speed at 35 rps for (A) FBG Acc. 2, (B) PZT Acc. at Bearing 1, (C) FBG Acc. 2 (unb), and (D) PZT Acc. at Bearing 1 (unb)

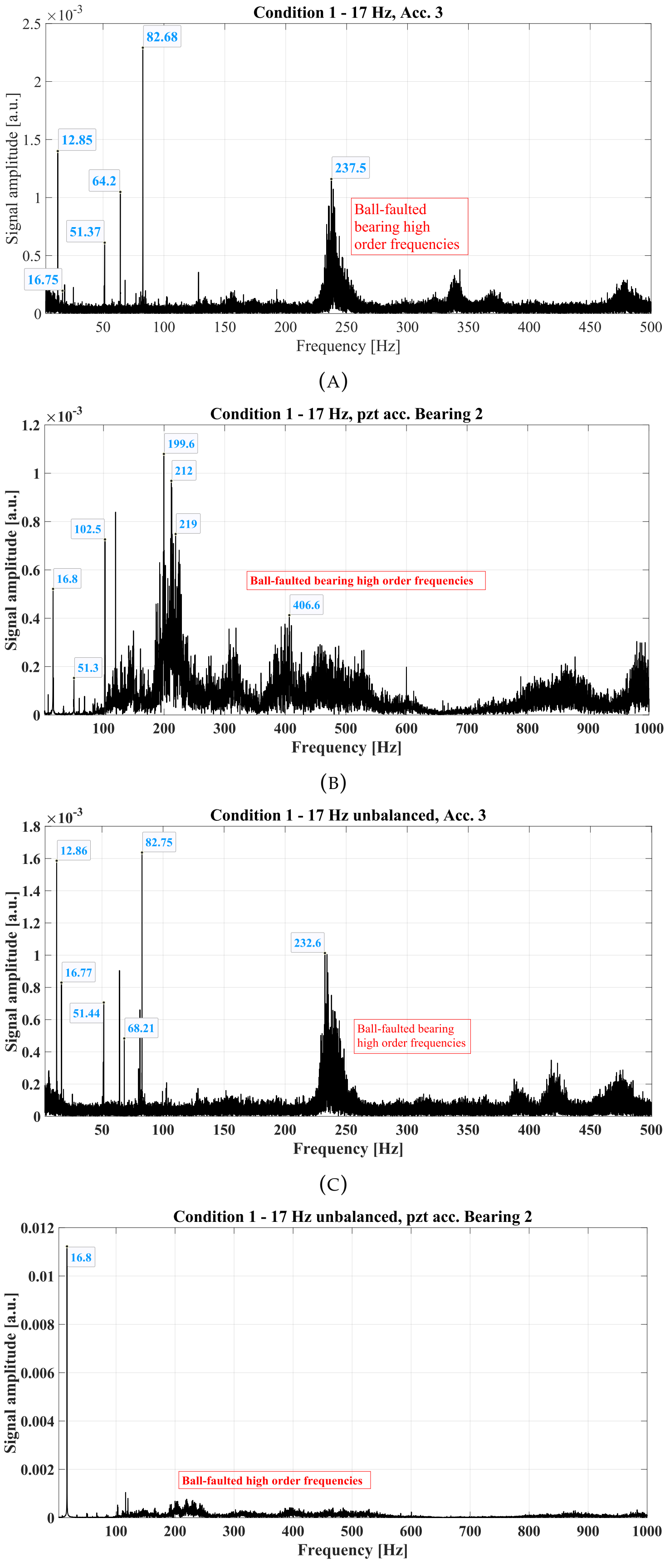

(A)

(B)

(C)

(D)

FIGURE 4.14: Fault condition 1 vibration frequency spectra for rotor speed at 17 rps for (A) FBG Acc. 3, (B) PZT Acc. at Bearing 2, (C) FBG Acc. 3 (unb), and (D) PZT Acc. at Bearing 2 (unb)

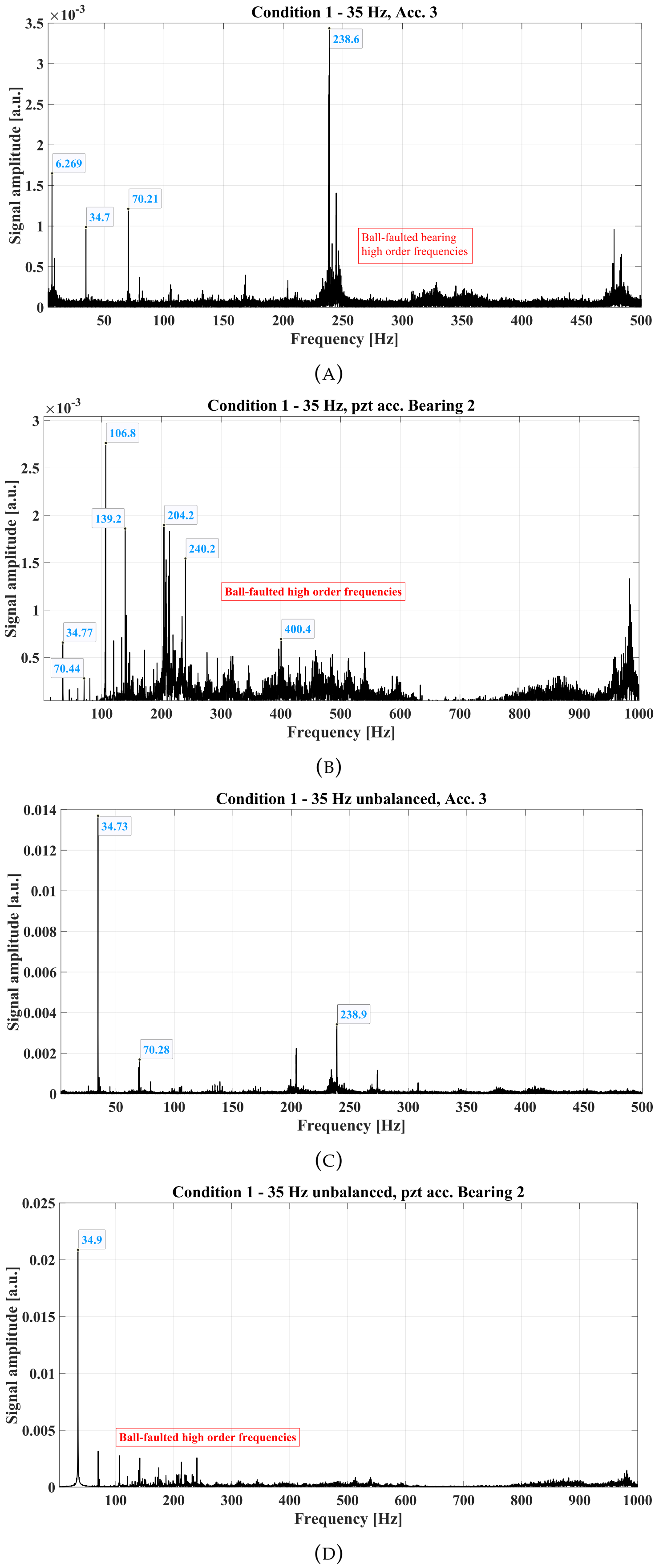

(A)

(B)

(C)

(D)

FIGURE 4.15: Fault condition 1 vibration frequency spectra for rotor speed at 35 rps for (A) FBG Acc. 3, (B) PZT Acc. at Bearing 2, (C) FBG Acc. 3 (unb), and (D) PZT Acc. at Bearing 2 (unb)

4.5.2 Fault condition 2

In fault condition 2, a bearing with a combination fault in the inner and outer races was attached to bearing 1, to which the FBG-based accelerometer 2 was attached. There are multiple harmonics of the fundamental frequency and high-order frequencies present in the frequency vibration spectrum characteristic of this fault condition. Additionally, there are two important frequencies, the Ball Pass Frequency Inner Race (BPFI) and the Ball Pass Frequency Outer Race (BPFO). Each of these frequencies corresponds to the frequency at which each roller element passes through the faulted point of the inner and outer races, respectively. When both faults are present, the vibration signal consists of a superposition of both frequencies. As a result, multiple harmonics are observed in the spectrum of both BPFI and BPFO frequencies. There can be modulation effects and sidebands around the fundamental frequency due to the interaction between the BPFI and BPFO frequencies. In addition to the fundamental frequency and its harmonics, sidebands may appear in different harmonic orders, such as 2X, 3X, 4X, and so forth. As a result of non-linear effects within the bearing system, such as varying stiffness and clearance, harmonics may be generated. Furthermore, transient conditions or complex fault interactions may result in the modulation of fundamental fault frequencies. These high-frequency components are prone to irregularities due to the unique geometry and design of the bearings, as well as manufacturing defects, causing the effects aforementioned in fault condition 1 [58], [59], [231]–[233].

Figures 4.16 and 4.17 illustrate the frequency vibration spectra for the FBG-based Accelerometer 2 when the rotor operates at 17 and 35 rps, with additional variation for an unbalanced condition, comparing these results with the obtained by the PZT-based accelerometer attached to bearing 1. In these frequency vibration spectra the nominal, second, third, fourth, eighth harmonics, and high-order frequencies were identified. This frequency vibration spectrum is characteristic of ball-bearing combination faults. Moreover, the BFPI and BFPO were identified at 17 rps (approximately 263 Hz and 266 Hz, respectively) and at 35 rps (around 273 Hz and 276 Hz, respectively). These results are compared and validated by the results of the PZT-based accelerometer attached to bearing 1. These results show the presence of the nominal frequency and some harmonics, with the proneness of the third, and high-order frequencies caused by the combination fault of the ball bearing. It is pertinent to note the presence of the 120 Hz harmonic caused by electromagnetic interference of the motor in the line used to feed the experimental setup. It can be applied a notch filter in this frequency. However, the FBG-based accelerometer did not suffer from this interference, illustrating the advantage of the optical sensor, since the filtering process implies increasing the computation cost in the data processing, mainly for online applications. Finally, since the FBG-based accelerometer recognized a vibration pattern similar to the PZT-based accelerometer measurements, it is assumed that fault condition 2 was well-identified by Accelerometer 2.

Figure 4.18 and 4.19 illustrate the frequency vibration spectra for the FBG-based Accelerometer 3 when the rotor operates at 17 and 35 rps, with additional variation for an unbalanced condition, comparing these results with the obtained by the PZT-based accelerometer attached to bearing 2. The Accelerometer 3 was attached to bearing 2, which contains a healthy ball bearing and is located further from the motor than Accelerometer 2. From Accelerometer 3 results, it can be seen 1X, 3X, 5X, and high-order frequencies. For all unbalanced conditions, the signal amplitude was enhanced at the nominal frequency. The measured spectra of FBG-based accelerometer

3 were characteristic of fault condition 2. The BFO and BFI were more clearly identified by the Accelerometer 2 because it is attached to the bearing that contains the faulted ball-bearing and it is subjected to higher acceleration amplitudes, enhancing the signal modulation for fault recognition. Finally, these results are compared and validated by the PZT-based attached at bearing 2, in which 1X, 3X, and high-order frequencies were identified, shown in Figures 4.18 and 4.19. In those results, the 120 Hz (the second harmonic of the 60 Hz electric network) has the highest signal amplitude, distorting the frequency domain signal analysis since the amplitude of this signal stands out from the mechanical vibration signal and can impact the automatic peak identification process by algorithms in online applications. Since the frequency vibration spectrum of the Accelerometer 3 was similar to the measured by the PZT-based accelerometer, despite the presence of the 120 Hz electric harmonic in the case of the PZT accelerometer, it is assumed that the Accelerometer 3 could correctly identify the vibration pattern of fault condition 2.

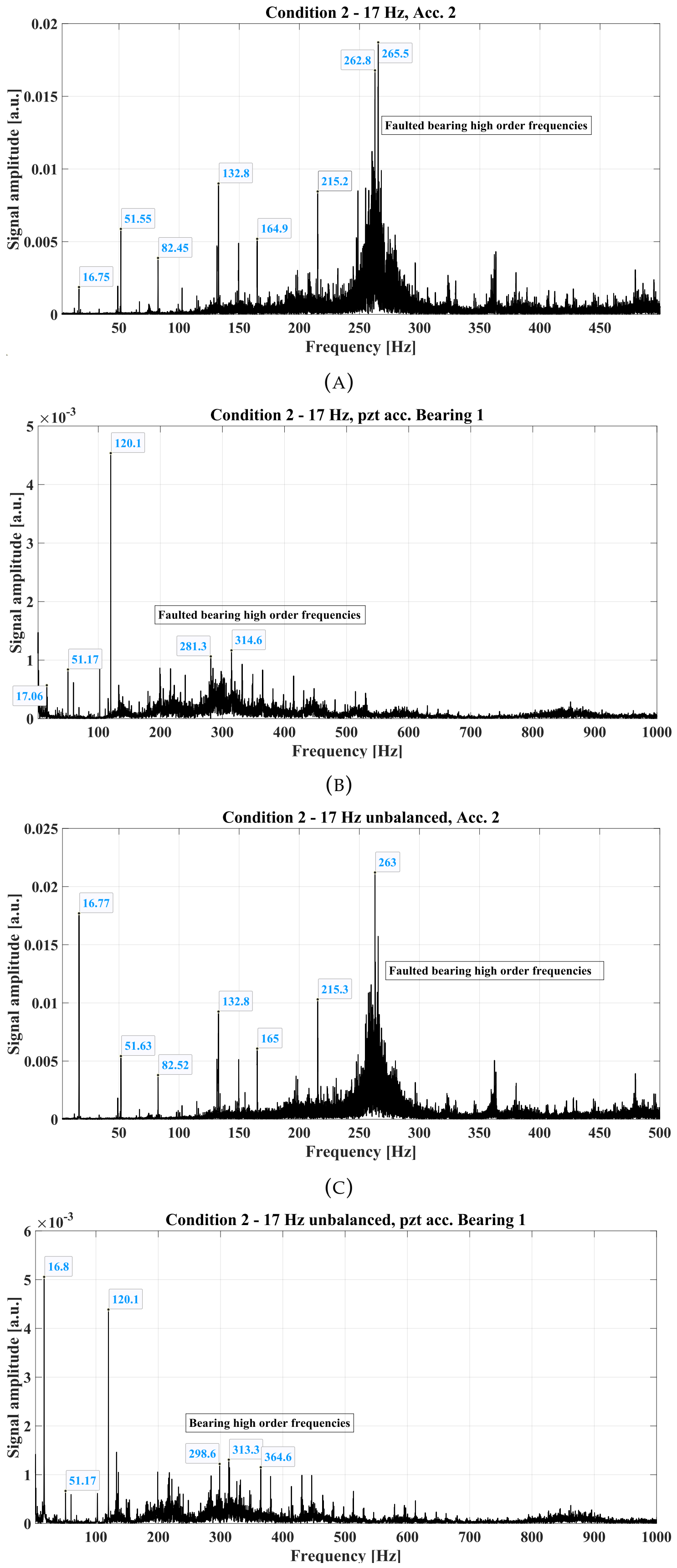

(A)

(B)

(C)

(D)

FIGURE 4.16: Fault condition 2 vibration frequency spectra for rotor speed at 17 rps for (A) FBG Acc. 2, (B) PZT Acc. at Bearing 1, (C) FBG Acc. 2 (unb), and (D) PZT Acc. at Bearing 1 (unb).

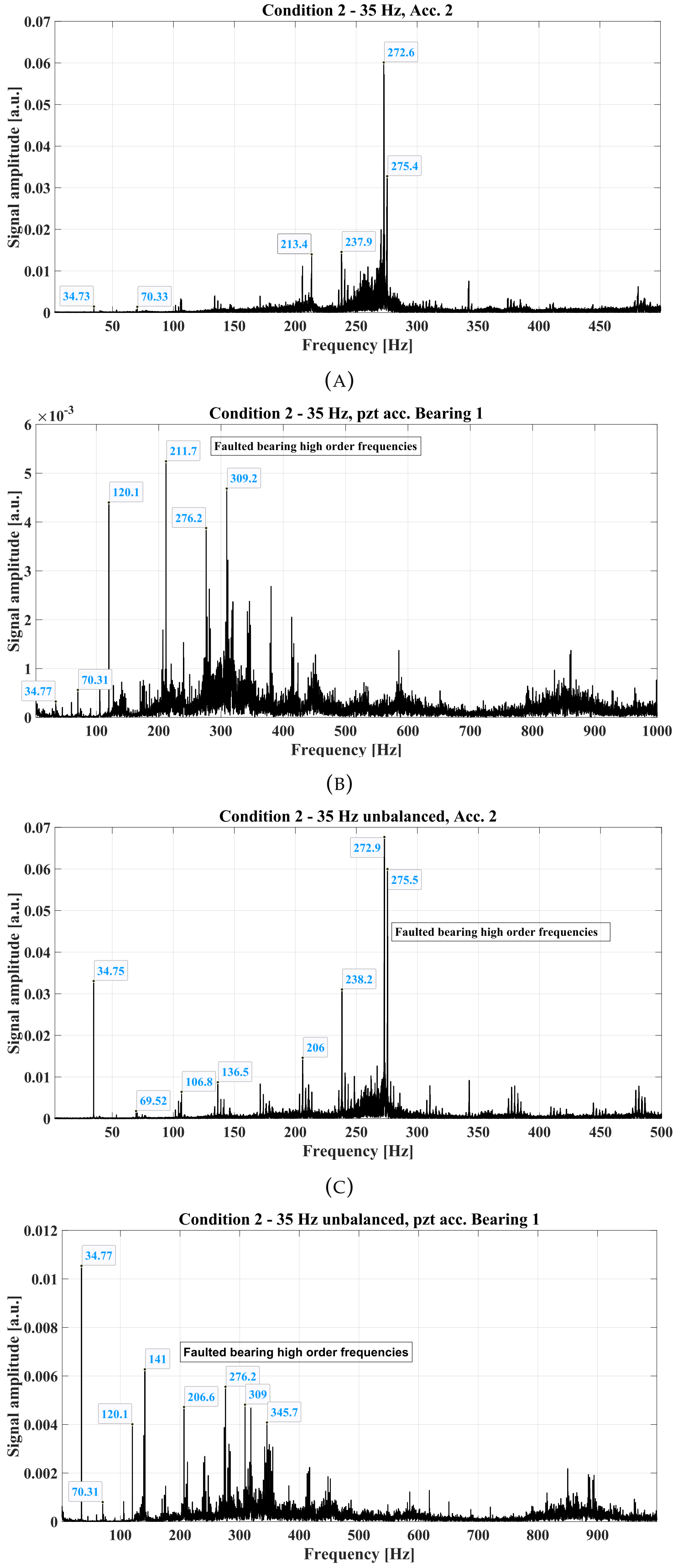

(A)

(B)

(C)

(D)

FIGURE 4.17: Fault condition 2 vibration frequency spectra for rotor speed at 35 rps for (A) FBG Acc. 2, (B) PZT Acc. at Bearing 1, (C) FBG Acc. 2 (unb), and (D) PZT Acc. at Bearing 1 (unb)

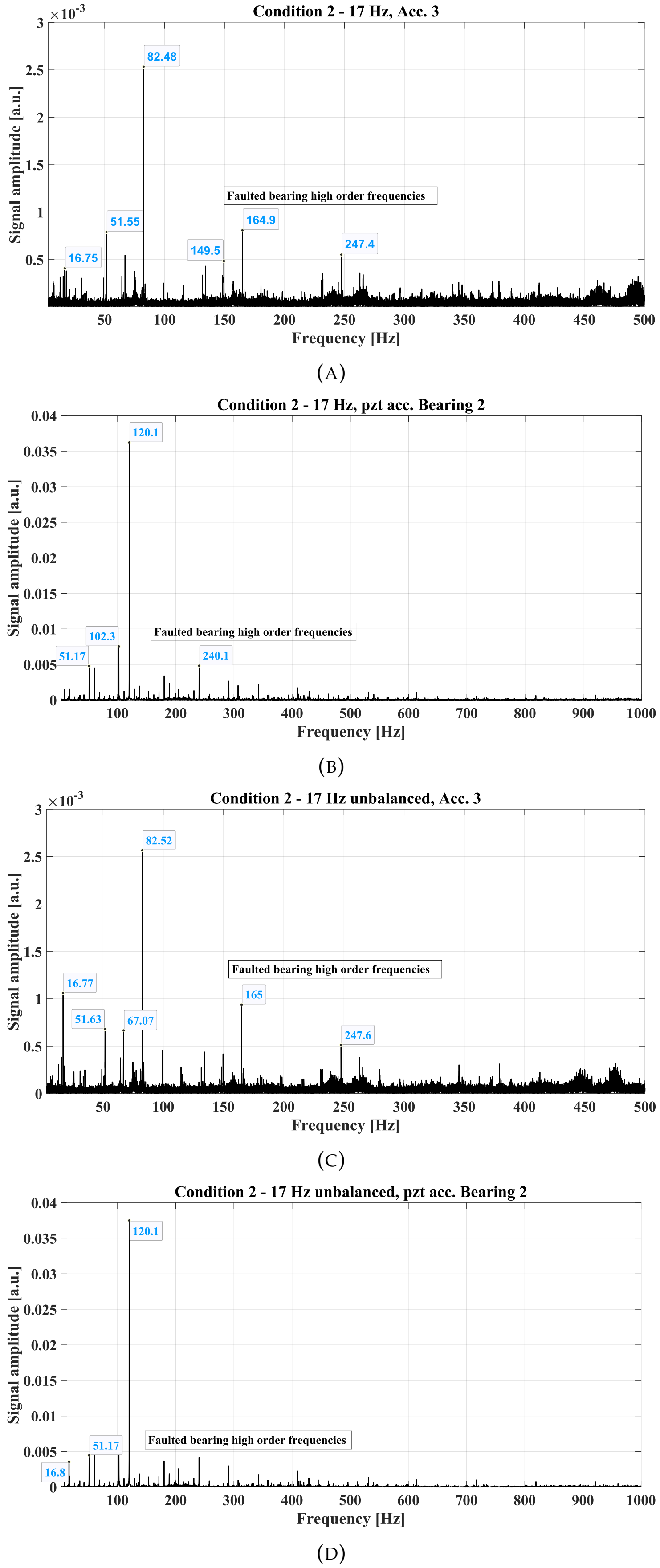

FIGURE 4.18: Fault condition 2 vibration frequency spectra for rotor speed at 17 rps for (A) FBG Acc. 3, (B) PZT Acc. at Bearing 2, (C) FBG Acc. 3 (unb), and (D) PZT Acc. at Bearing 2 (unb)

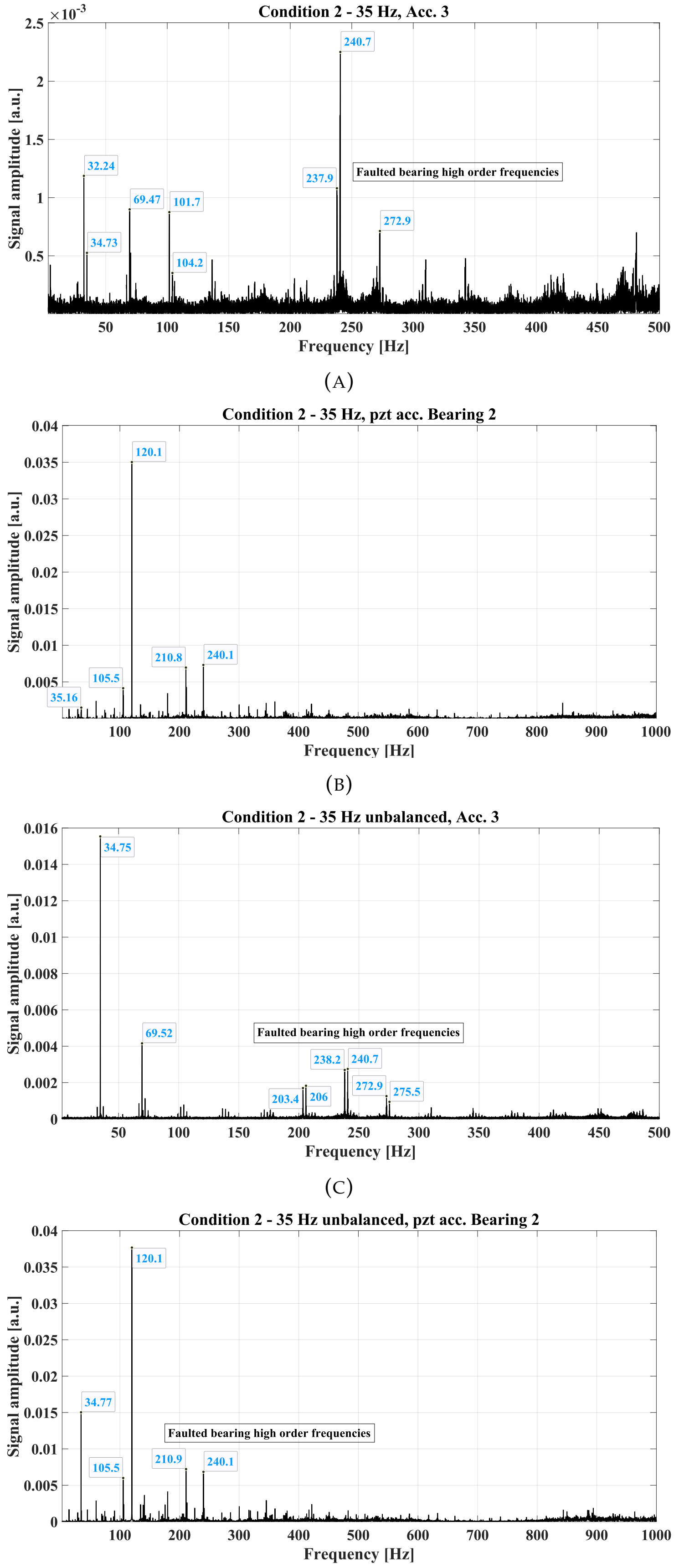

(A)

(B)

(C)

(D)

FIGURE 4.19: Fault condition 2 vibration frequency spectra for rotor speed at 35 rps for (A) FBG Acc. 3, (B) PZT Acc. at Bearing 2, (C) FBG Acc. 3 (unb), and (D) PZT Acc. at Bearing 2 (unb)

4.5.3 Fault condition 3

In fault condition 3, a ball bearing with an inner race fault is attached to bearing 1. It is common for the vibration spectrum of a ball bearing to exhibit distinct characteristics in the presence of an inner race fault. The primary characteristic of this bearing is the Ball Pass Frequency Inner Race (BPFI), which represents the rate at which the bearing elements traverse the damaged inner race. In the spectrum, BPFI appears to be the dominant frequency. There are also harmonics associated with BPFI, such as 2BPFI, 3BPFI, and so on, indicative of higher-order impacts from the fault. As a result of modulation effects, sidebands are generated around the BPFI frequency. Furthermore, frequencies associated with the rotation of the bearing cage may be present as well. Factors such as bearing design, speed, and fault severity can affect the exact frequencies and their amplitudes. For accurate fault detection and assessment in ball bearings, it is essential to analyze and interpret these characteristic frequencies. Additionally, harmonics of the nominal operating frequency of the rotor are also possible to appear in the vibration spectrum, in addition to the characteristic frequencies associated with the inner race fault. Various factors can contribute to harmonics emerging, such as manufacturing imperfections, unbalance, misalignment, or other mechanical problems within the machinery [58], [59], [64].

The results for Accelerometer 2, attached to bearing 1, are shown in Figures 4.20 and 4.21. These results are compared to the PZT-based attached to bearing 1 measurement, shown in the same figures. For the rotor operating at 17 rps, the harmonics 1X, 3X, 4X, and high-order frequencies were found. The prominence of the 3X harmonic is characteristic of misalignment between the rotor and the mechanical system [54]. High-order frequencies are characteristics of faulted bearings. For 17 rps, BFPI is located close to 260 Hz and its sideband frequencies were also detected in the frequency vibration spectra. The unbalanced load has increased the signal amplitude at the nominal frequency in the unbalanced condition. For the rotor at 35 rps, 1X, 2X, 3X, 4X, and high-order harmonics were identified. For the condition without an unbalanced load, the second harmonic (3X) was prominent compared to the other harmonics, indicating mechanical looseness in the experimental setup assembly [54]. BFPI was also identified at 35 rps, around 213 Hz, and its sideband high-order frequencies. Finally, these results are validated and compared to the measurements of the PZT-based accelerometer attached to bearing 1. For 17 rps, 1X, 3X, 8X, and high-order frequencies were identified. For 35 rps, the second harmonic (3X) was prominent as obtained for FBG-based accelerometer 2. At this rotation speed, 1X, 2X, 3X, 4X, and high-order frequencies were identified. Finally, since the vibration pattern by the FBG-based accelerometer 2 was similar to the measurements of the PZT-based used as a reference, with respect to harmonic identification, it is concluded that the Accelerometer 2 could detect fault condition 3.

The results for Accelerometer 3, attached to bearing 2, are shown in Figures 4.22 and 4.23. These results are compared to the PZT-based attached to bearing 2 measurement, shown in the same figures. At 17 rps, 1X, 3X, 4X, and high-order frequencies were found, with 4X prominence related to a coupling problem between the rotor shaft and the mechanical system shaft [54]. For the unbalanced condition, 1X, 2X, 3X, and high-order frequencies were identified, in which the prominence of the second harmonic (3X) is related to intrinsic misalignment in the assembly between the rotor and the mechanical system [54]. At 35 rps, 1X, 2X, 3X, and high-order frequencies were identified, in which the prominence of the first harmonic (2X) is due to misalignment and/or mechanical looseness in the assembly [54]. Moreover, for the unbalanced condition, the prominence of the nominal frequency is characteristic of this fault condition. All cases identified high-order frequencies (the main characteristic of faulted bearings). Finally, these results are validated by the measurements of the PZT-based accelerometer attached to bearing 2. In these frequency vibration spectra, some of the nominal frequency harmonics are identified as well as the high-order frequencies caused by the faulted bearing. Since these measurements are similar to the results obtained by the FBG-based accelerometer 3, it is assumed that this accelerometer could identify the fault condition 3.

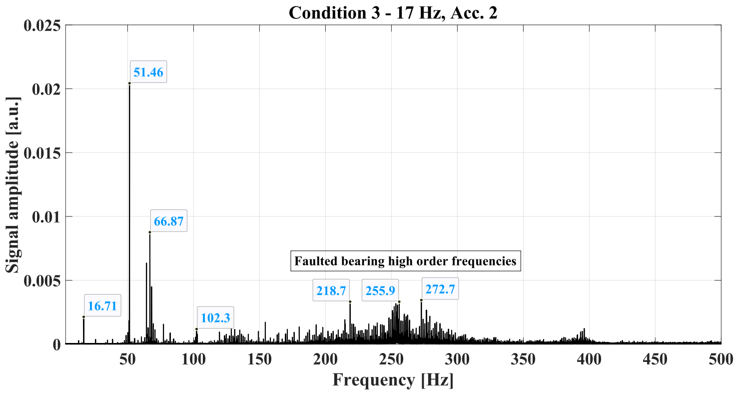

(A)

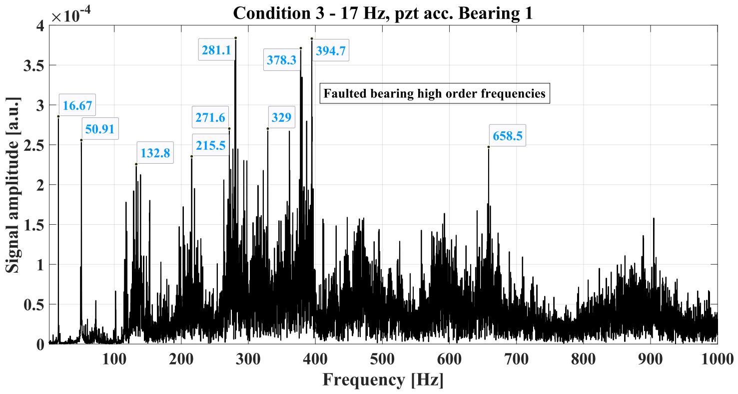

(B)

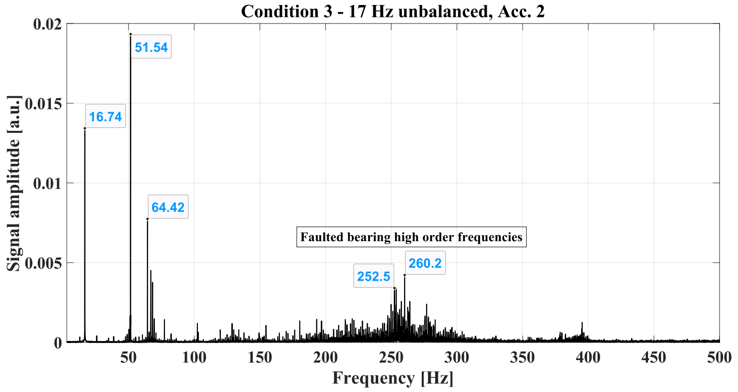

(C)

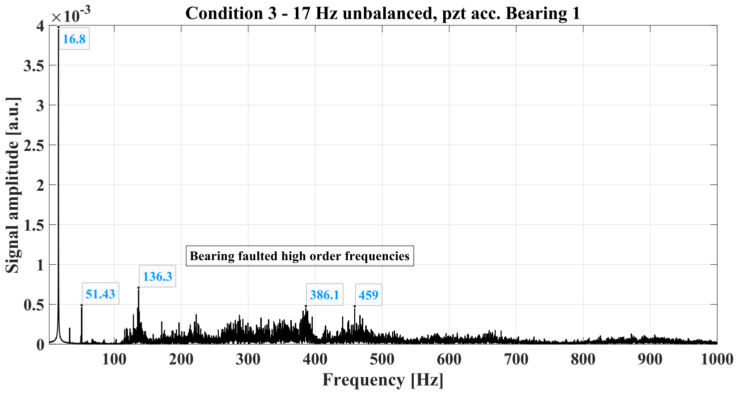

(D)

FIGURE 4.20: Fault condition 3 vibration frequency spectra for rotor speed at 17 rps for (A) FBG Acc. 2, (B) PZT Acc. at Bearing 1, (C) FBG Acc. 2 (unb), and (D) PZT Acc. at Bearing 1 (unb).

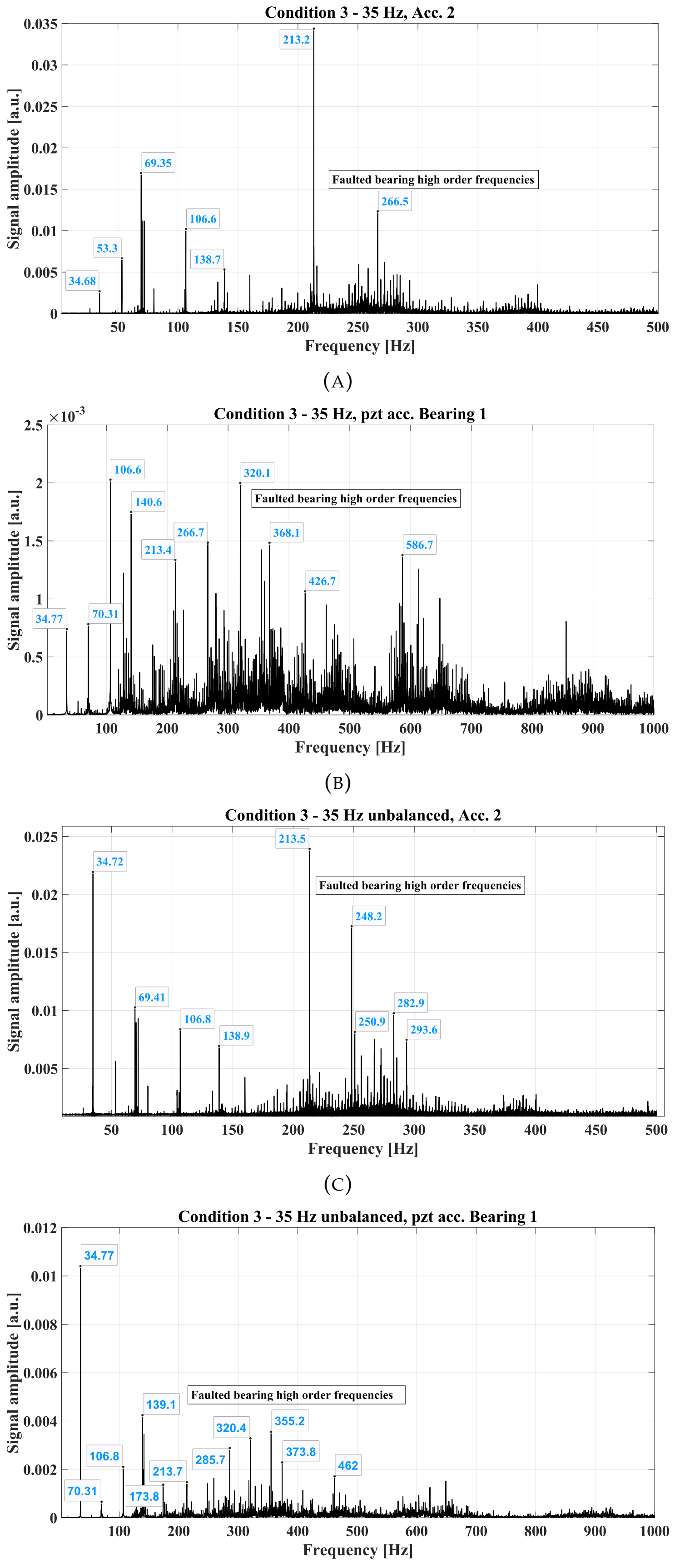

FIGURE 4.21: Fault condition 3 vibration frequency spectra for rotor speed at 35 rps for (A) FBG Acc. 2, (B) PZT Acc. at Bearing 1, (C) FBG Acc. 2 (unb), and (D) PZT Acc. at Bearing 1 (unb)

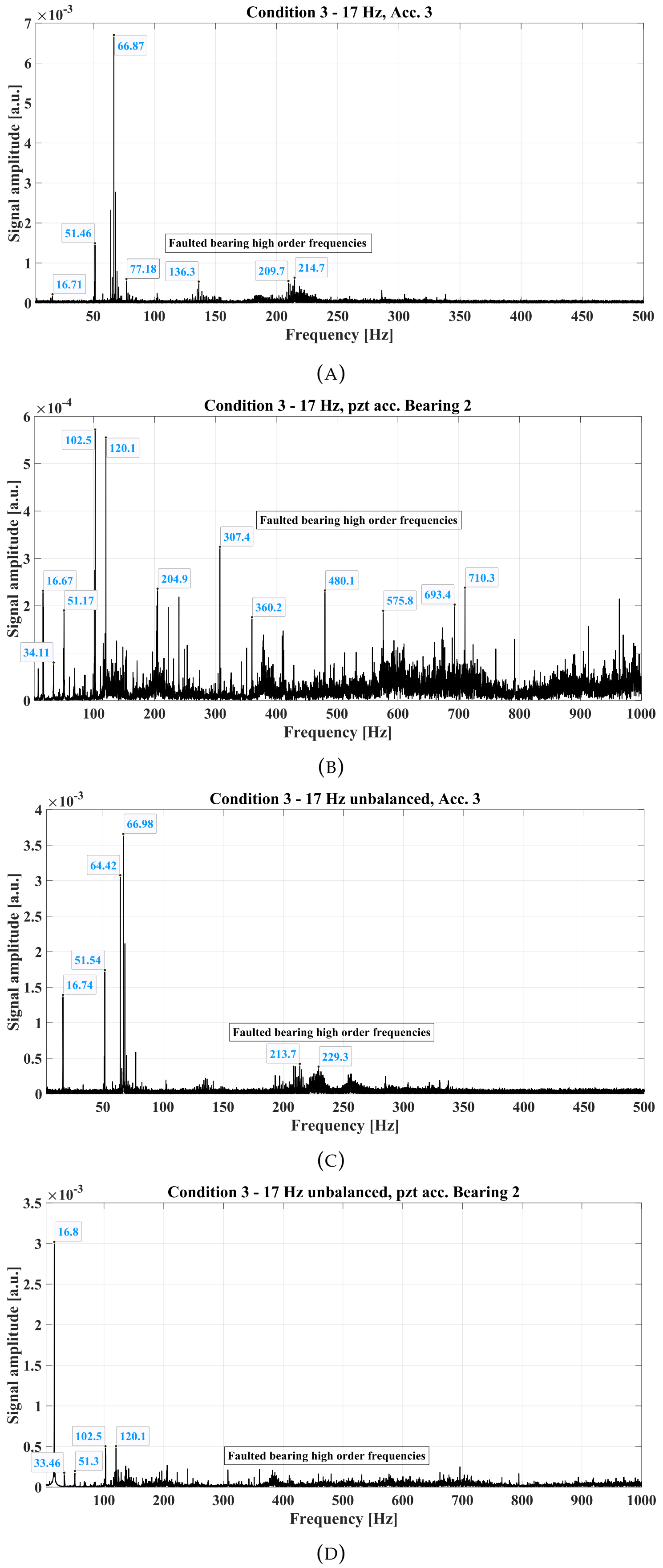

FIGURE 4.22: Fault condition 3 vibration frequency spectra for rotor speed at 17 rps for (A) FBG Acc. 3, (B) PZT Acc. at Bearing 2, (C) FBG Acc. 3 (unb), and (D) PZT Acc. at Bearing 2 (unb)

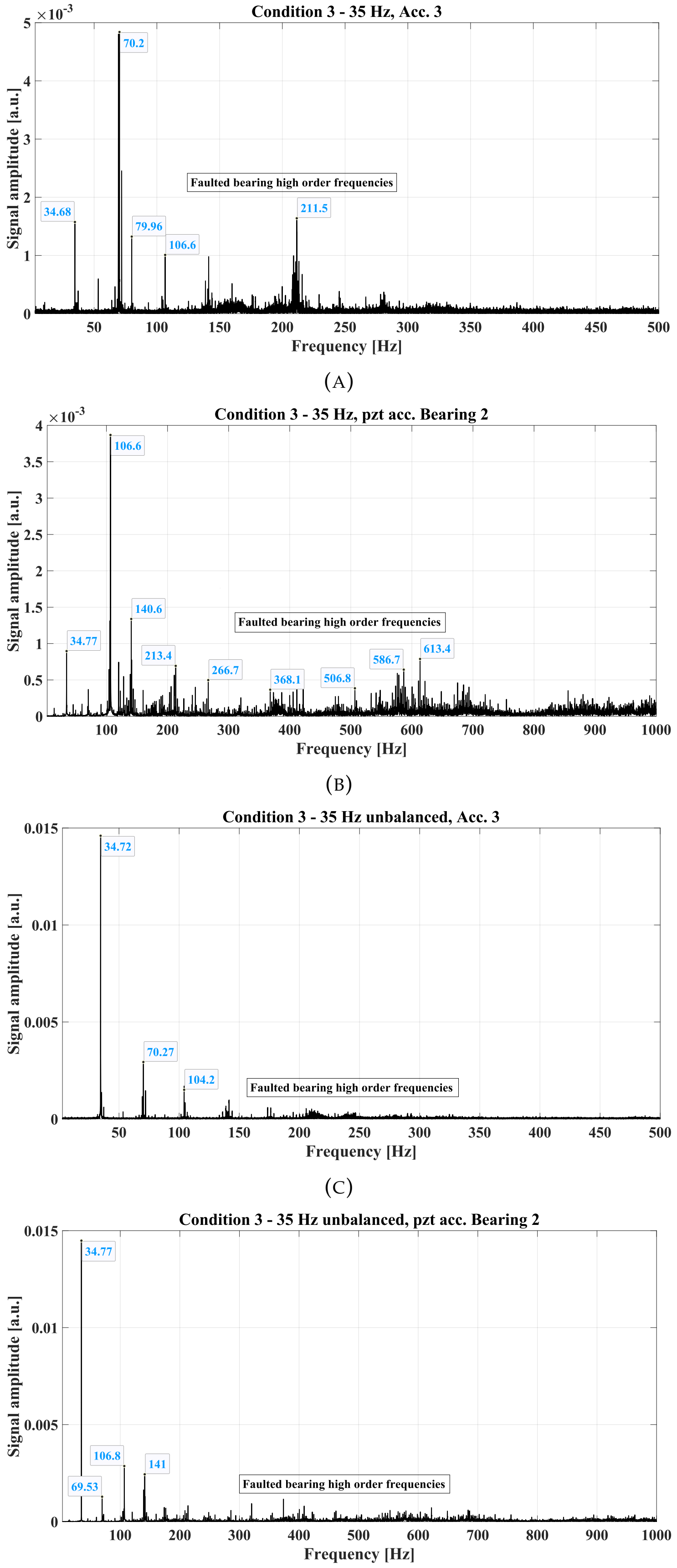

(A)

(B)

(C)

(D)

FIGURE 4.23: Fault condition 3 vibration frequency spectra for rotor speed at 35 rps for (A) FBG Acc. 3, (B) PZT Acc. at Bearing 2, (C) FBG Acc. 3 (unb), and (D) PZT Acc. at Bearing 2 (unb)

4.5.4 Fault condition 4

In fault condition 4, a ball bearing with an outer race fault is attached to bearing 1. As in the case of the inner race fault, in the outer race fault, the primary characteristic of this bearing is the Ball Pass Frequency Outer Race (BPFO), which represents the rate at which the roller elements traverse the damaged outer race. Due to the dynamic interaction between the damaged outer race and the rolling elements, an outer race fault can modulate the frequency vibration spectrum of a ball bearing. In this modulation effect, sidebands are introduced around the fundamental frequency, which is typically the BFPO. When the faulty outer race encounters each rolling element, intermittent impacts or variations in loading result. As a result of these impacts, the BPFO frequency is modulated in amplitude. Therefore, sidebands are observed at frequencies offset from the BPFO by the rate of modulation, which can be affected by factors such as bearing geometry and rotational speed. It is these sidebands that provide valuable diagnostic information, as they can indicate the severity of an outer race fault and differentiate it from other possible problems within the machinery [58], [59].

The results for Accelerometer 2, attached to bearing 1, are shown in Figures 4.24 and 4.25. These results are compared to the PZT-based attached to bearing 1 measurement, shown in the same figures. For 17 rps, the prominence of the second harmonic (3X) indicates the intrinsic misalignment between the rotor and the mechanical system, also perceived at 35 rps by the first harmonic (2X) [54]. In all cases, the high-order frequencies and sideband frequencies around the BFPO were identified. For 17 rps, the BFPO is close to 265 Hz, and for 35 Hz around 276 Hz. These frequencies were identified as the highest signal amplitude of the high-order frequencies present in the vibration frequency spectrum. Finally, these results are compared to the PZT-based accelerometer measurements attached to bearing 1, in which some harmonics of the nominal rotation are detected and, mainly, the high-order frequencies characteristic of faulted bearings are recognized. Since the vibration spectra measured by the FBG-based accelerometer 2 are similar to the results obtained by the PZT-based accelerometer, it is concluded that Accelerometer 2 identifies fault condition 4. The results for Accelerometer 3, attached to bearing 2, are shown in Figures 4.26 and 4.27. These results are compared to the PZT-based attached to bearing 2 measurements, shown in the same figures. At 17 rps, the second harmonic (3X), the third harmonic (4X), and the fourth harmonic (5X) were prominent and these harmonics are related mainly to coupling problems and misalignment between the rotor and the mechanical system [54]. Moreover, in all cases, high-order frequencies were identified in the frequency vibration spectra, besides the BFPO close to 210 Hz. These results are similar to the measurements performed by the PZT-based accelerometer attached to bearing 2, where it can be seen the prominence of the high-order frequencies caused by the faulted bearing. Finally, since the vibration pattern obtained by the FBG-based accelerometer was close to the one obtained by the sensor used as a reference, it is concluded that Accelerometer 3 was able to accurately diagnose fault condition 4.

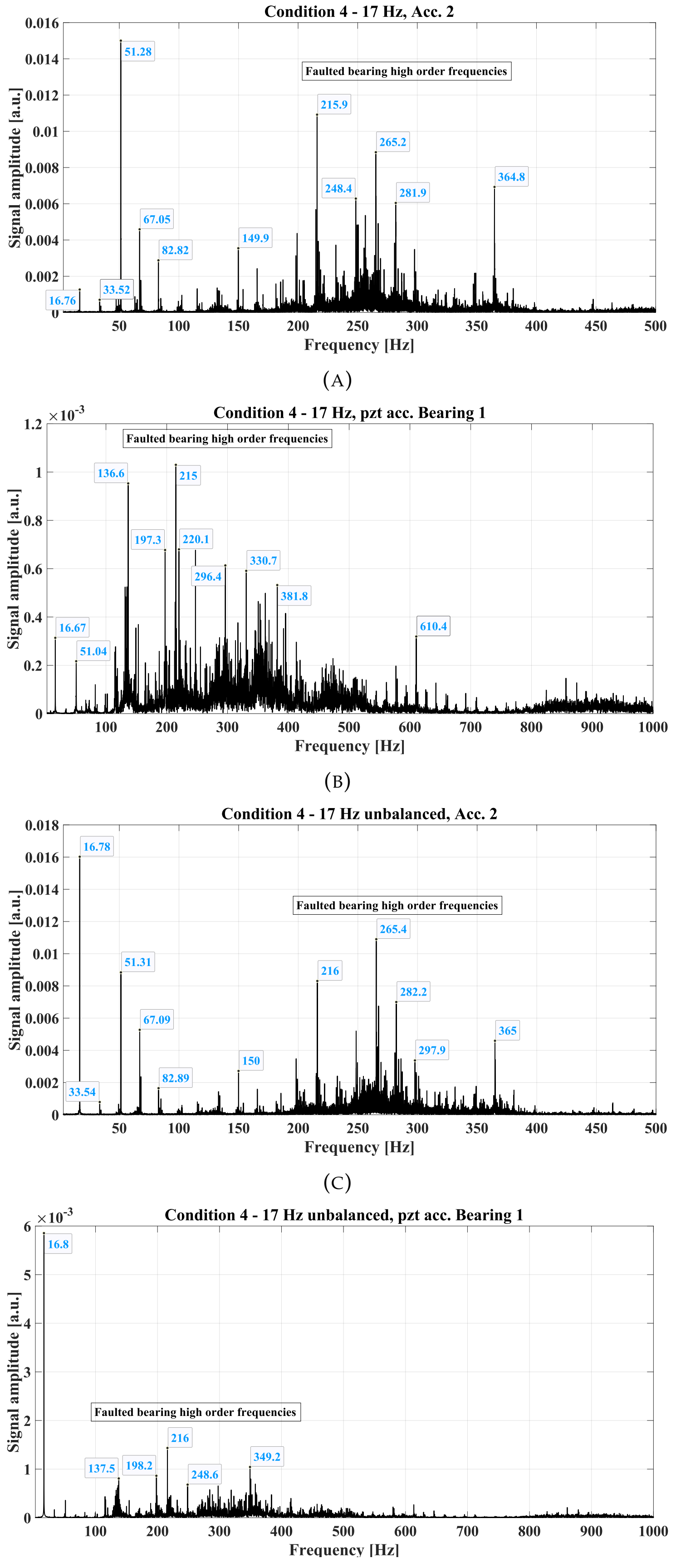

(A)

(B)

(C)

(D)

FIGURE 4.24: Fault condition 4 vibration frequency spectra for rotor speed at 17 rps for (A) FBG Acc. 2, (B) PZT Acc. at Bearing 1, (C) FBG Acc. 2 (unb), and (D) PZT Acc. at Bearing 1 (unb).

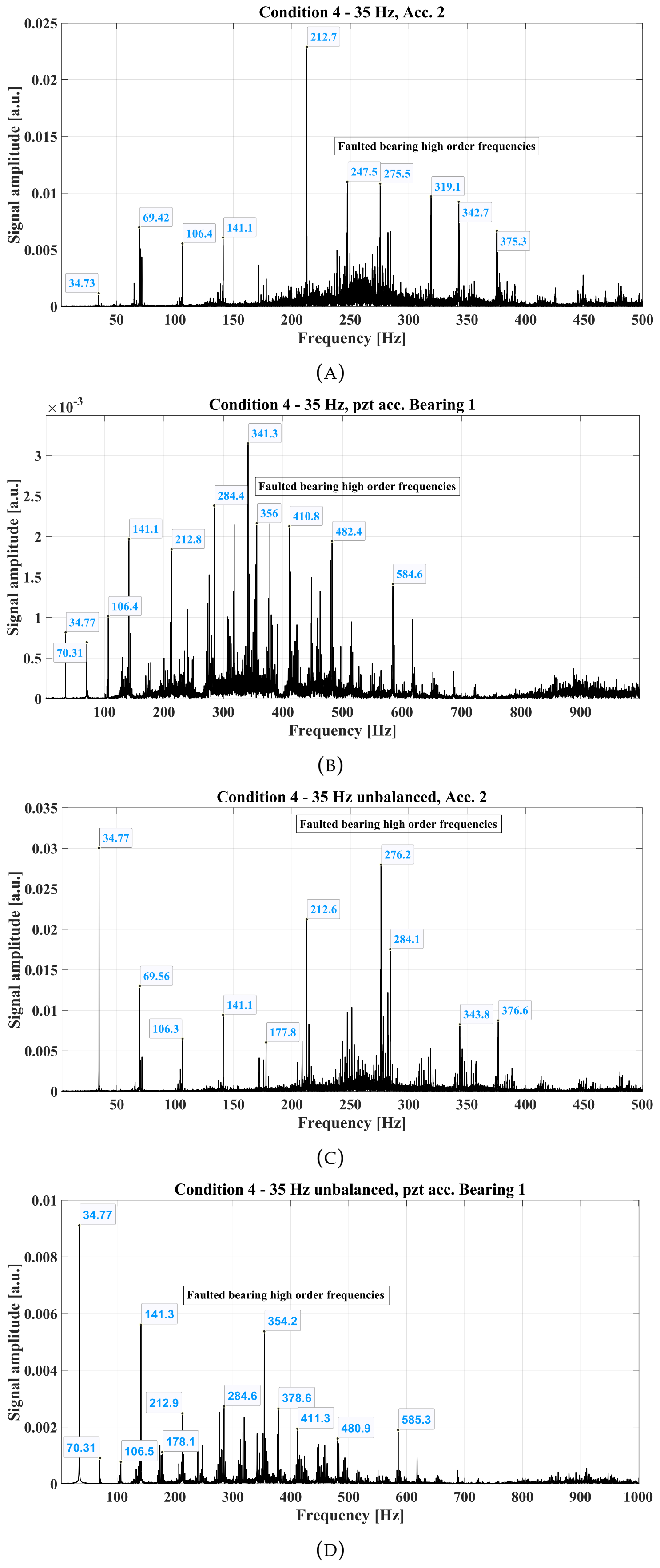

(A)

(B)

(C)

(D)

FIGURE 4.25: Fault condition 4 vibration frequency spectra for rotor speed at 35 rps for (A) FBG Acc. 2, (B) PZT Acc. at Bearing 1, (C) FBG Acc. 2 (unb), and (D) PZT Acc. at Bearing 1 (unb).

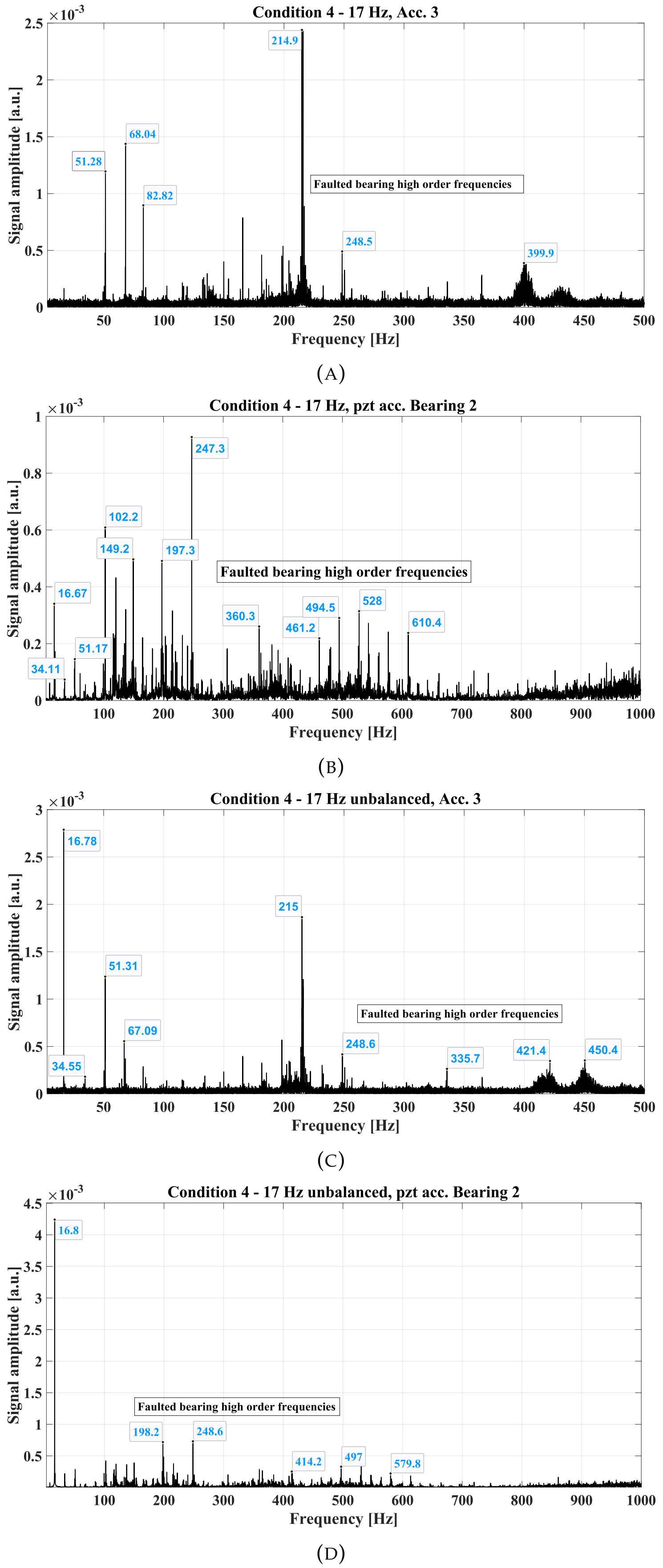

FIGURE 4.26: Fault condition 4 vibration frequency spectra for rotor speed at 17 rps for (A) FBG Acc. 3, (B) PZT Acc. at Bearing 2, (C) FBG Acc. 3 (unb), and (D) PZT Acc. at Bearing 2 (unb).

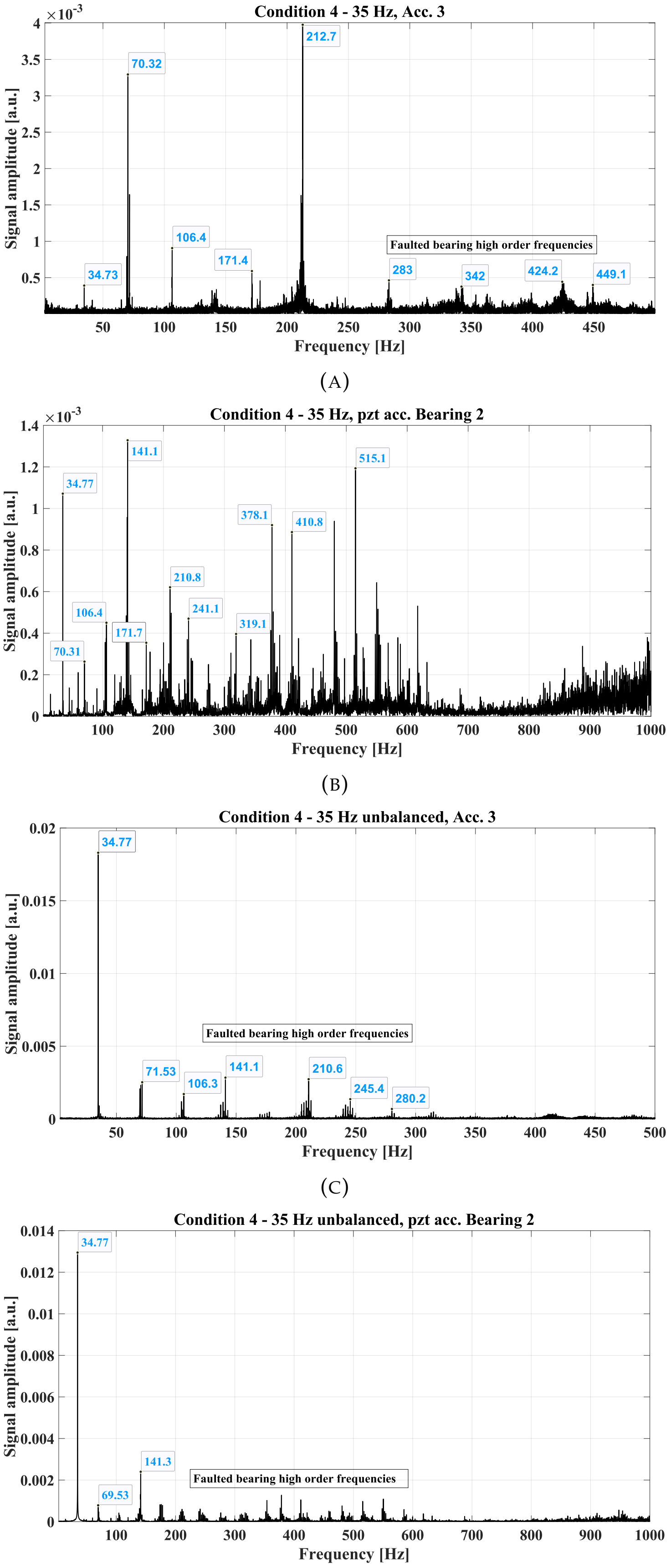

(A)

(B)

(C)

(D)

FIGURE 4.27: Fault condition 4 vibration frequency spectra for rotor speed at 35 rps for (A) FBG Acc. 3, (B) PZT Acc. at Bearing 2, (C) FBG Acc. 3 (unb), and (D) PZT Acc. at Bearing 2 (unb).

4.5.5 Fault condition 5

In fault condition 5, there is no pre-established fault condition in the motor or mechanical system. The frequency vibration spectrum for this healthy condition is the prominence of the nominal frequency at which the rotor operates. The results for Accelerometer 2, attached to bearing 1, are shown in Figures 4.28 and 4.29. These results are compared to the PZT-based accelerometer attached to the bearing 1, shown in the same figure. For 17 and 35 rps, it can be seen the prominence of the third harmonic (4X), indicating a coupling problem between the rotor and the mechanical system [54]. Moreover, high-order frequencies have been found in these frequency vibration spectra, indicating an unidentified bearing problem (since they are characteristic of faulted bearing conditions, as previously demonstrated). In all cases, the unbalanced load increased the signal amplitude at the nominal frequency. These results are validated by the measurements of the PZT-based accelerometer attached to bearing 1, where the third harmonic (4X) and high-order frequencies are prominent. Similar results were obtained for Accelerometer 3 (Figures 4.30 and 4.31) and the PZT-based accelerometer attached to bearing 2. These results show the prominence of the third harmonic (4X) and the appearance of some high-order frequencies. Finally, since the FBG-based accelerometer measurements were similar to the PZT-based accelerometer pattern, its results were validated by the reference sensor.

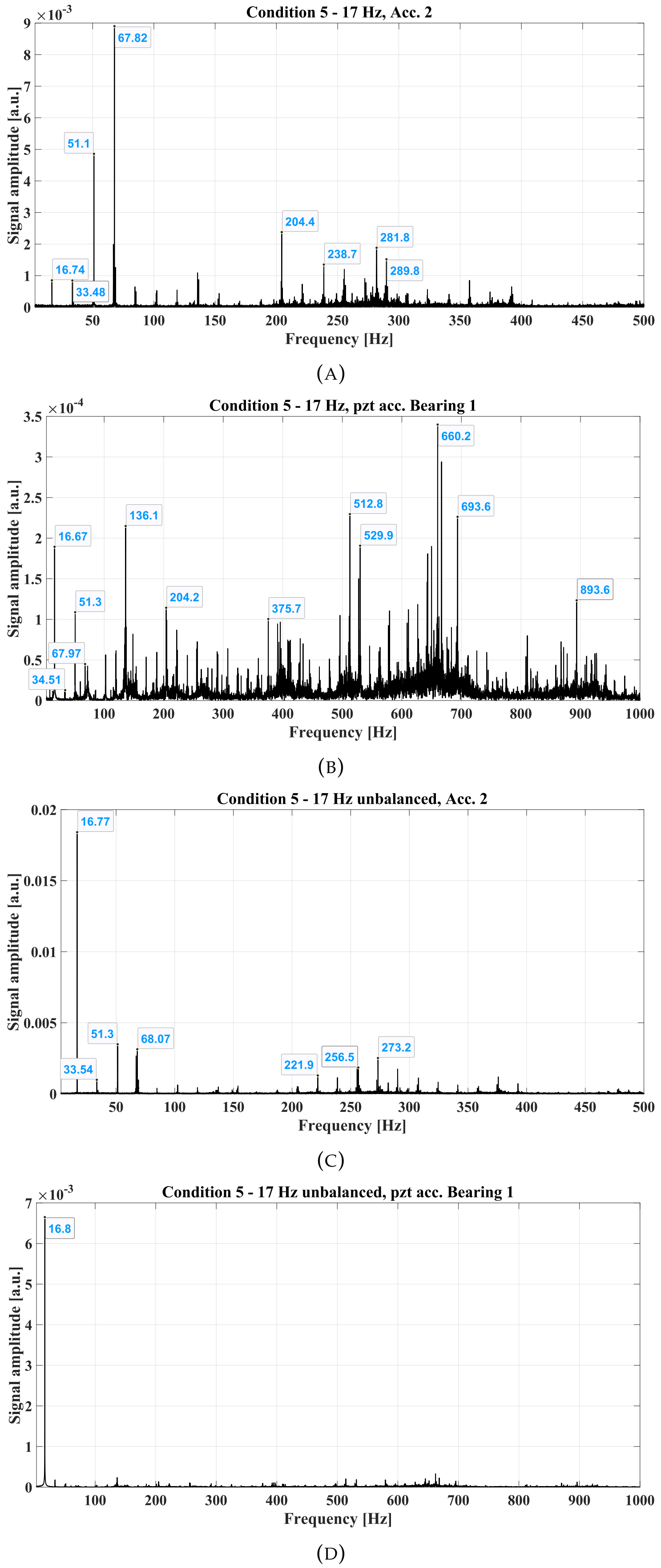

(A)

(B)

(C)

(D)

FIGURE 4.28: Fault condition 5 vibration frequency spectra for rotor speed at 17 rps for (A) FBG Acc. 2, (B) PZT Acc. at Bearing 1, (C) FBG Acc. 2 (unb), and (D) PZT Acc. at Bearing 1 (unb).

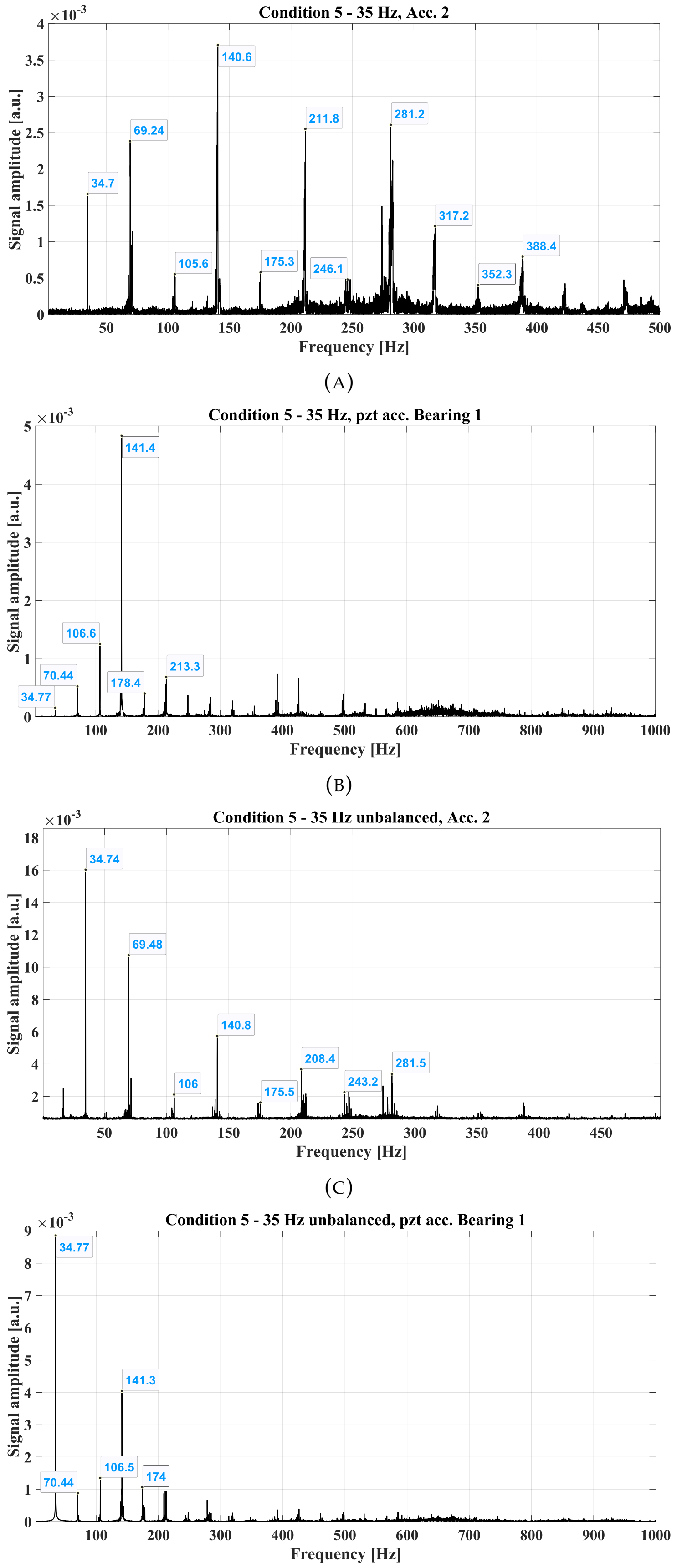

(A)

(B)

(C)

(D)

FIGURE 4.29: Fault condition 5 vibration frequency spectra for rotor speed at 35 rps for (A) FBG Acc. 2, (B) PZT Acc. at Bearing 1, (C) FBG Acc. 2 (unb), and (D) PZT Acc. at Bearing 1 (unb).

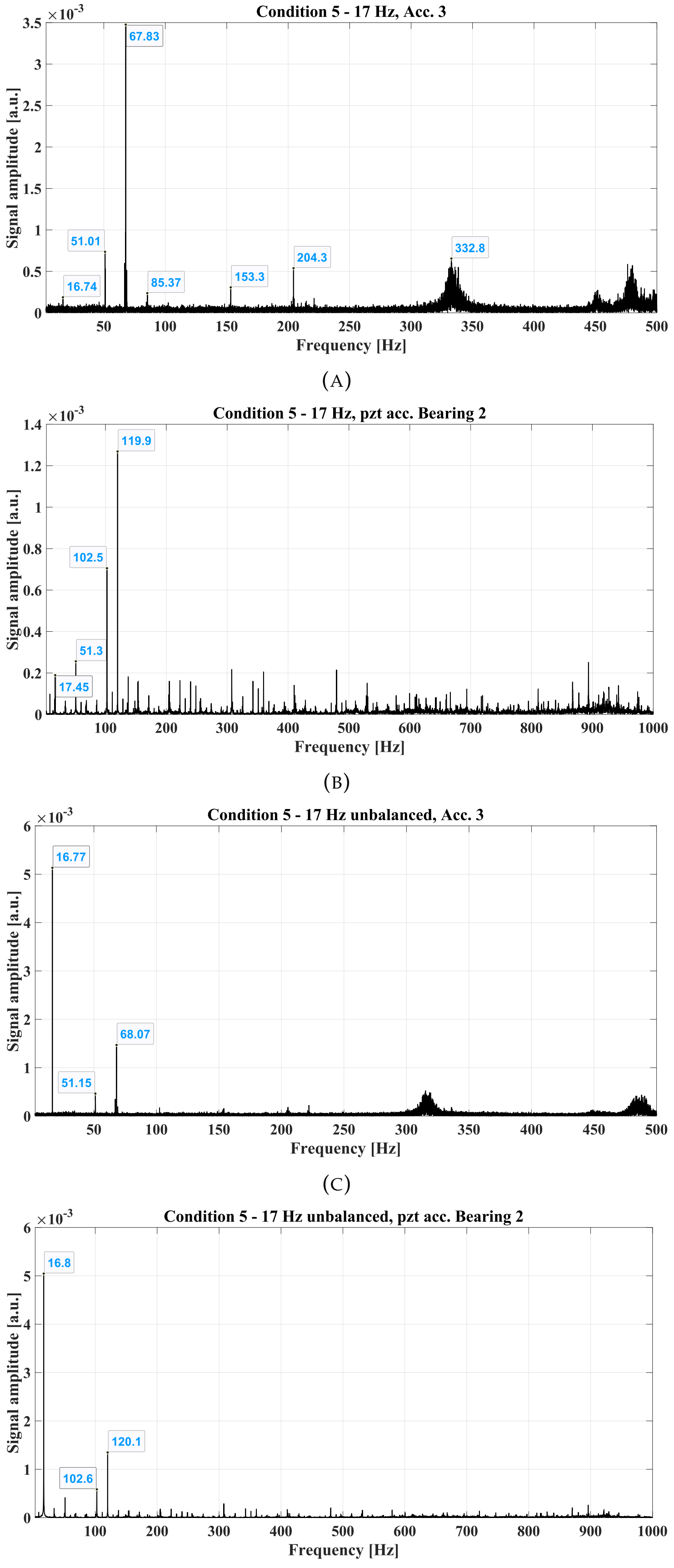

(A)

(B)

(C)

(D)

FIGURE 4.30: Fault condition 5 vibration frequency spectra for rotor speed at 17 rps for (A) FBG Acc. 3, (B) PZT Acc. at Bearing 2, (C) FBG Acc. 3 (unb), and (D) PZT Acc. at Bearing 2 (unb).

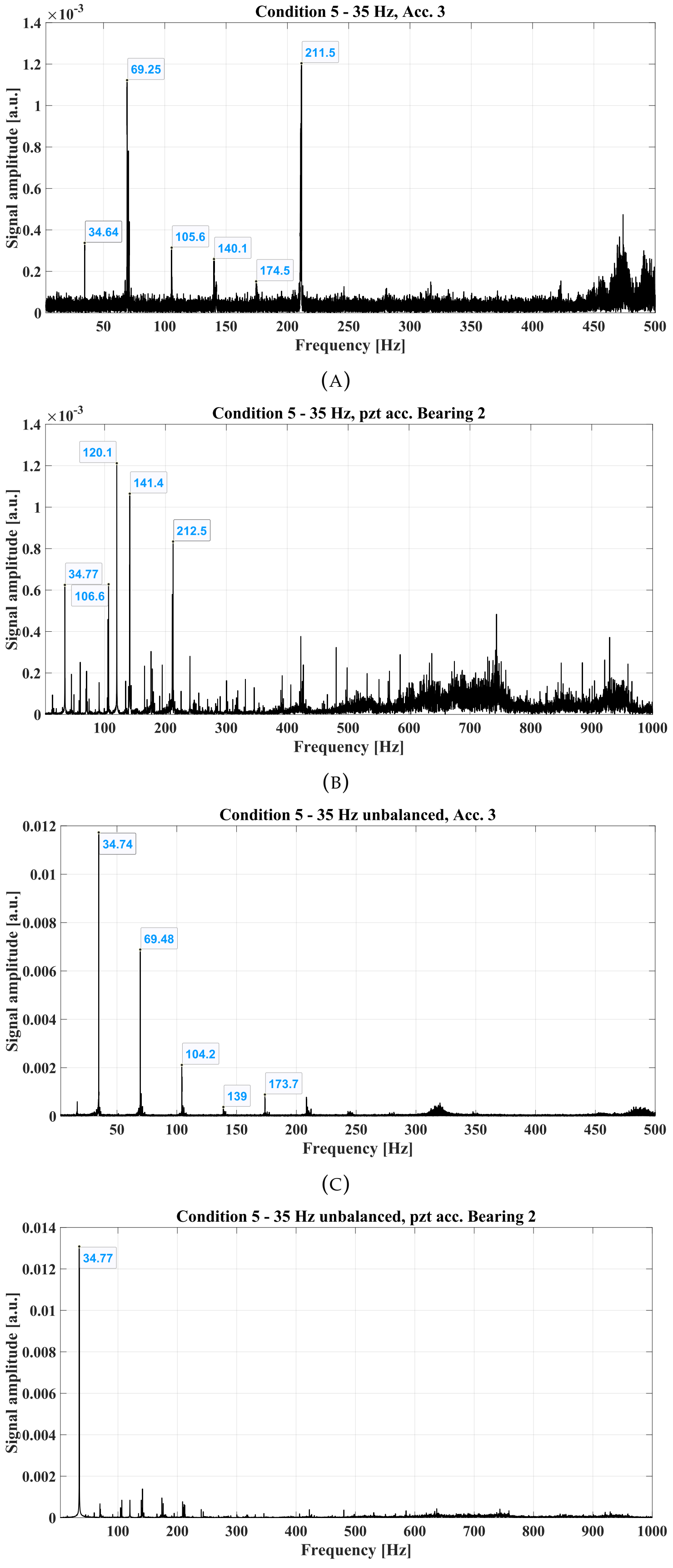

(A)

(B)

(C)

(D)

FIGURE 4.31: Fault condition 5 vibration frequency spectra for rotor speed at 35 rps for (A) FBG Acc. 3, (B) PZT Acc. at Bearing 2, (C) FBG Acc. 3 (unb), and (D) PZT Acc. at Bearing 2 (unb).

4.5.6 Fault condition 6

In fault condition 6, the used AC motor has broken rotor bars. The slip sidebands around the fundamental frequency and its harmonics are the primary frequencies used in this fault condition to detect broken rotor bars. When a motor is in proper working condition, the rotor bars and the rotor core laminations form a squirrel cage. This produces a uniform and consistent magnetic field. As a result of a rotor bar breaking, this symmetry is disrupted, resulting in an asymmetry in the rotor's magnetic field. As a result of this asymmetry, the motor current spectrum and the vibration spectrum display slip sidebands due to rotation at the slip frequency relative to the stator magnetic field. Additionally, the broken rotor bars may result in uneven resistance (resistance to the magnetic field) of the rotor. As the stator's magnetic field rotates, this variable resistance rotates at the slip frequency. As a result of the rotational asymmetry of the stator magnetic field, sideband frequencies are generated around the fundamental stator electrical frequency and its harmonics. A multiple of the slip frequency separates these sidebands [81], [82]. The results for Accelerometer 2, attached to bearing 1, are shown in Figures 4.32 and 4.33. For the rotor speed at 17 rps, the nominal frequency (1X), 2X, 3X, and 4X harmonics were identified. Moreover, it can be seen the slip frequency provoked by inside broken rotor bars, for example, in the case of 33.6 Hz for 34 Hz (2X), and 69.08 Hz for 68 Hz (3X). Moreover, the prominence of the second harmonic (3X) indicates intrinsic misalignment between the rotor and the mechanical system. At 35 rps, these results are also obtained, where slip frequencies around nominal frequency harmonics can be seen in the frequency vibration spectra. Finally, these results are validated by the PZT-based accelerometer attached to bearing 1 (shown in Figure Figures 4.32 and 4.33), where it can be seen slip frequencies around nominal frequency harmonics. The results for Accelerometer 3, attached to bearing 2, are shown in Figures Figures 4.34 and 4.35. Accelerometer 3 exhibited the same vibration pattern as Accelerometer 2, showing slip frequencies characteristic of rotor broken bars fault conditions. Additionally, high-order frequencies have appeared in these sensor results, probably related to an incipient fault in the ball bearing. These results are validated by the similar vibration spectra obtained by the sensor used as a reference, the PZT-based accelerometer attached to bearing 2, shown in Figures 4.34 and 4.35.

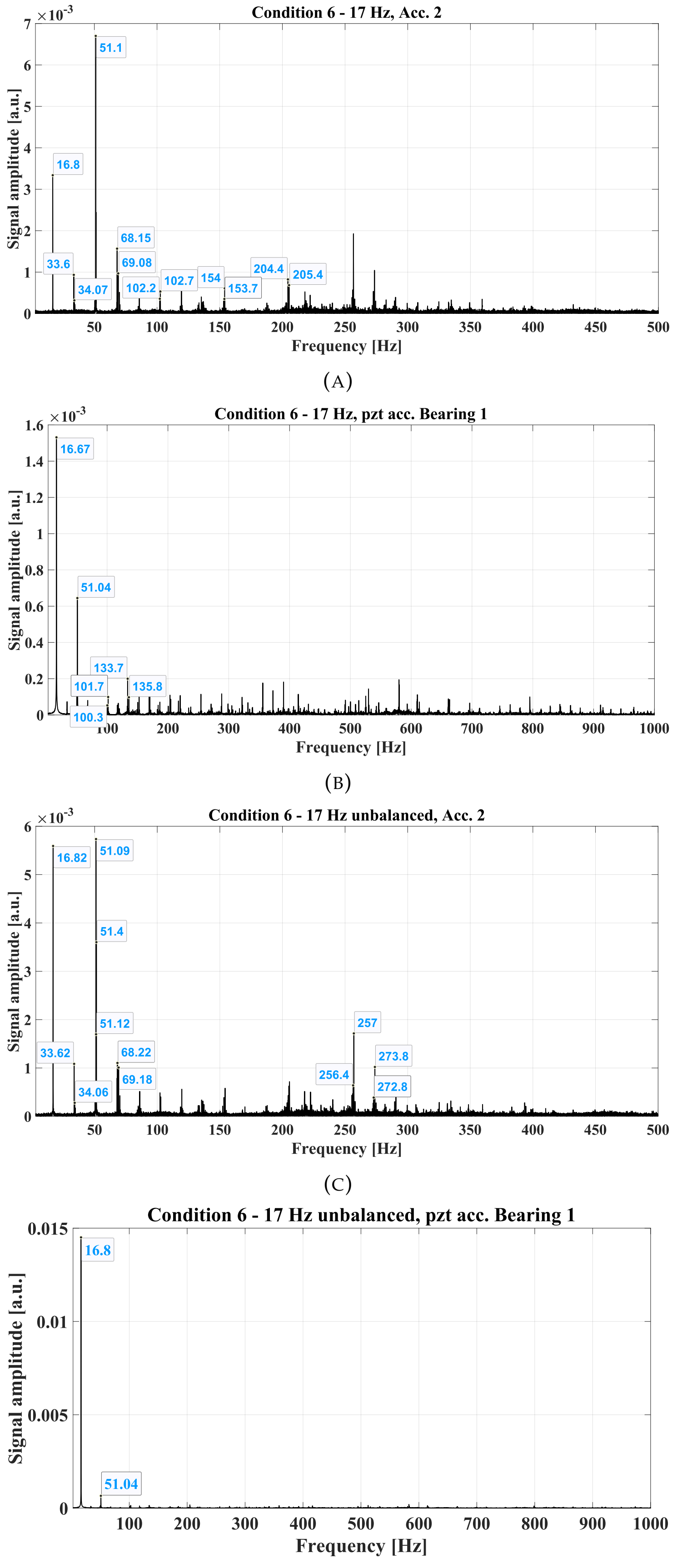

(A)

(B)

(C)

(D)

FIGURE 4.32: Fault condition 6 vibration frequency spectra for rotor speed at 17 rps for (A) FBG Acc. 2, (B) PZT Acc. at Bearing 1, (C) FBG Acc. 2 (unb), and (D) PZT Acc. at Bearing 1 (unb).

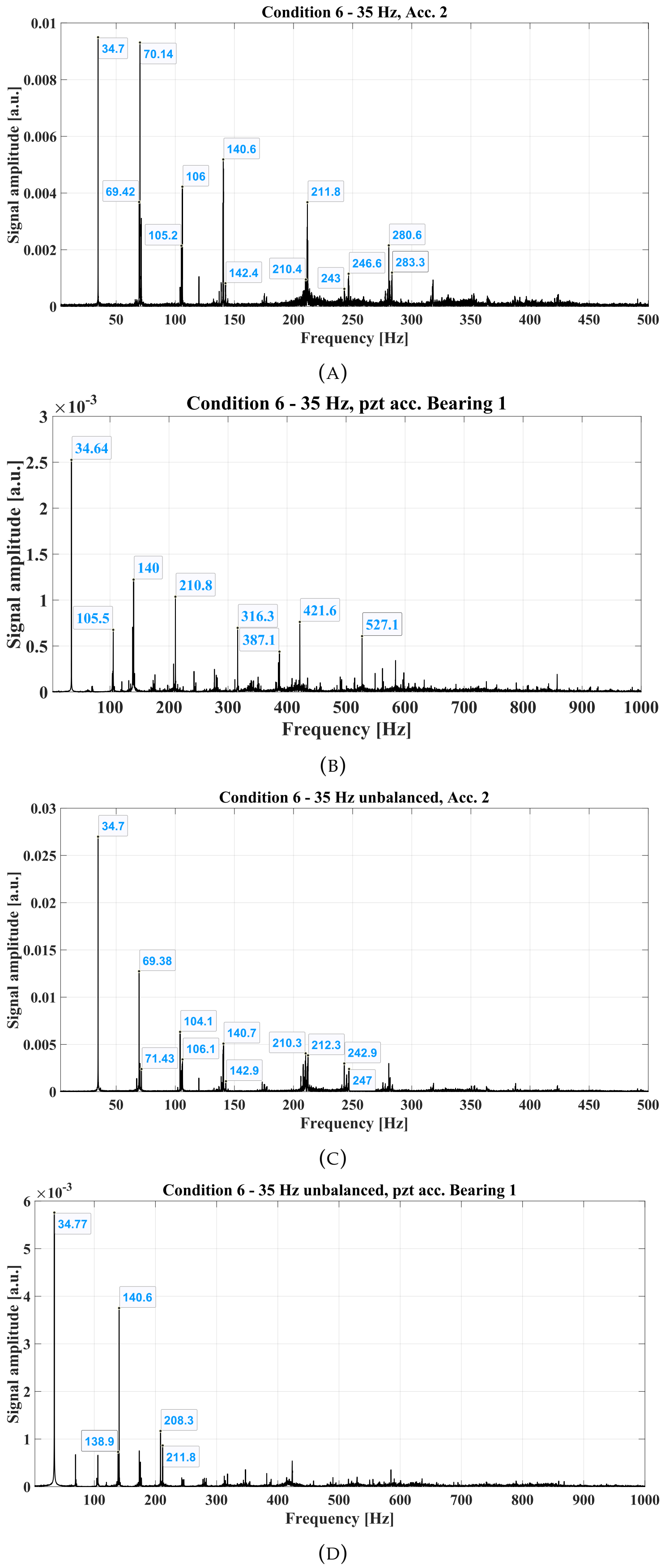

(A)

(B)

(C)

(D)

FIGURE 4.33: Fault condition 6 vibration frequency spectra for rotor speed at 35 rps for (A) FBG Acc. 2, (B) PZT Acc. at Bearing 1, (C) FBG Acc. 2 (unb), and (D) PZT Acc. at Bearing 1 (unb).

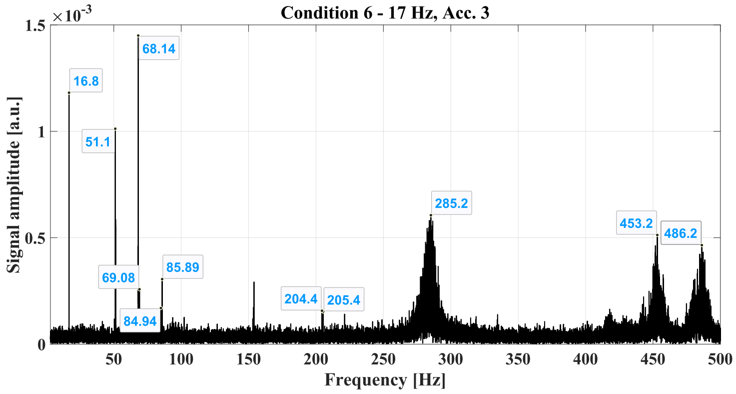

(A)

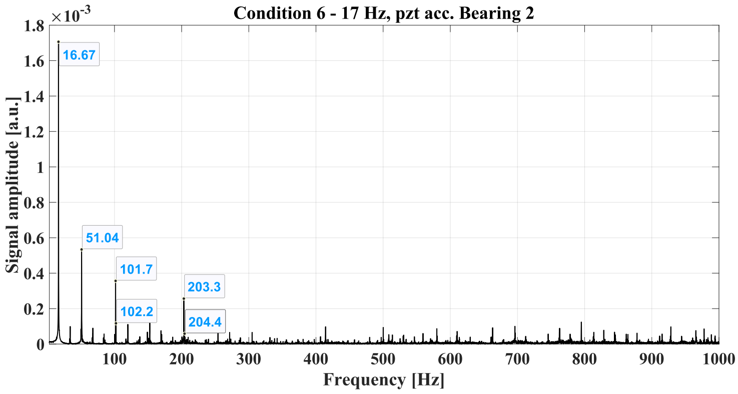

(B)

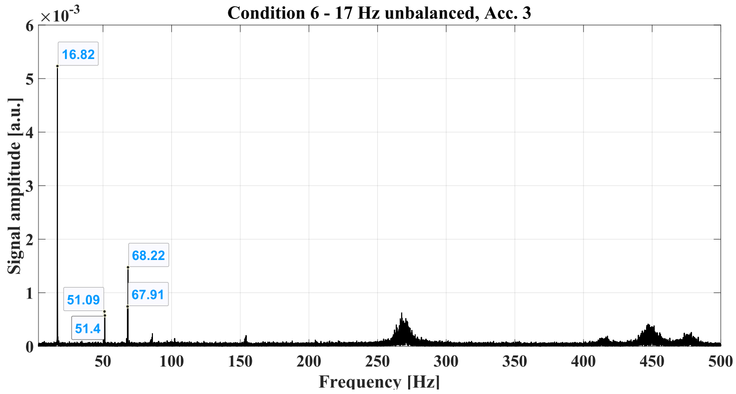

(C)

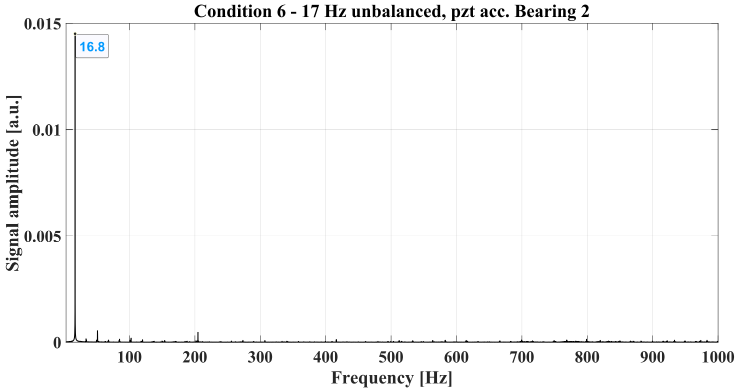

(D)

FIGURE 4.34: Fault condition 6 vibration frequency spectra for rotor speed at 17 rps for (A) FBG Acc. 3, (B) PZT Acc. at Bearing 2, (C) FBG Acc. 3 (unb), and (D) PZT Acc. at Bearing 2 (unb).

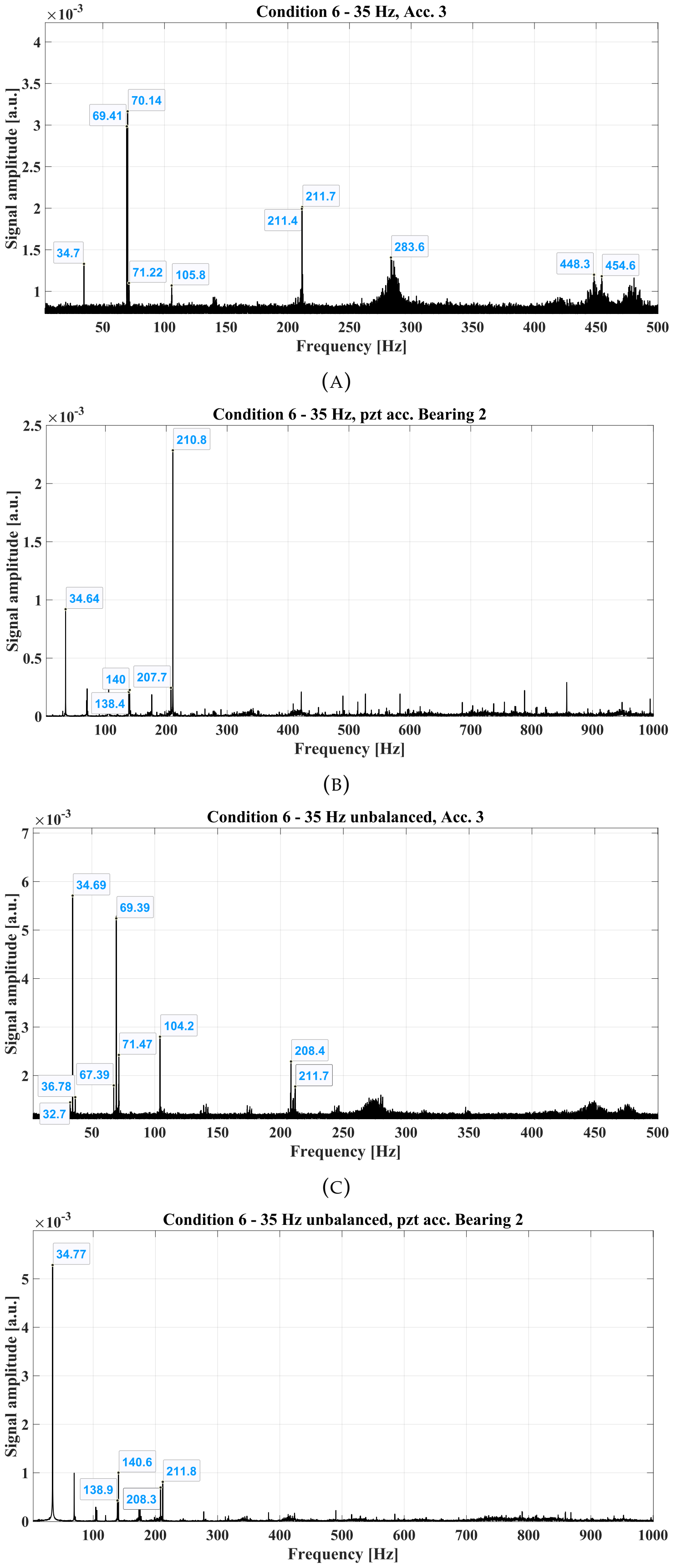

(A)

(B)

(C)

(D)

FIGURE 4.35: Fault condition 6 vibration frequency spectra for rotor speed at 35 rps for (A) FBG Acc. 3, (B) PZT Acc. at Bearing 2, (C) FBG Acc. 3 (unb), and (D) PZT Acc. at Bearing 2 (unb).

4.5.7 Fault condition 7

In fault condition 7, Accelerometer 2 was attached to bearing 2, and Accelerometer 3 was attached to bearing 1. For this condition, the electric motor is the same as for condition 6. Then, the expected frequency vibration spectra are similar to fault condition 6. Accelerometer 2 results are shown in Figure 4.36. At 17 rps, the nominal frequency and high-order frequencies were found. These results show that Accelerometer 2 does not have sufficient sensitivity to recognize the vibration pattern associated with broken rotor bars at this rotation velocity. At 35 rps, Accelerometer 2 identified the fault condition vibration pattern, where slip frequencies can be seen around the harmonics. Since the rotation has increased, compared to the 17 rps condition, the amplitude of acceleration also increased and this sensor had sensitivity to identify the vibration pattern. The results for Accelerometer 3 are shown in Figure 4.37, where it can be seen that the vibration pattern characteristic of rotor broken bars fault condition was characterized by the presence of slip frequency of the nominal frequency harmonics. These results are validated by PZT-based measurements in fault condition 6.

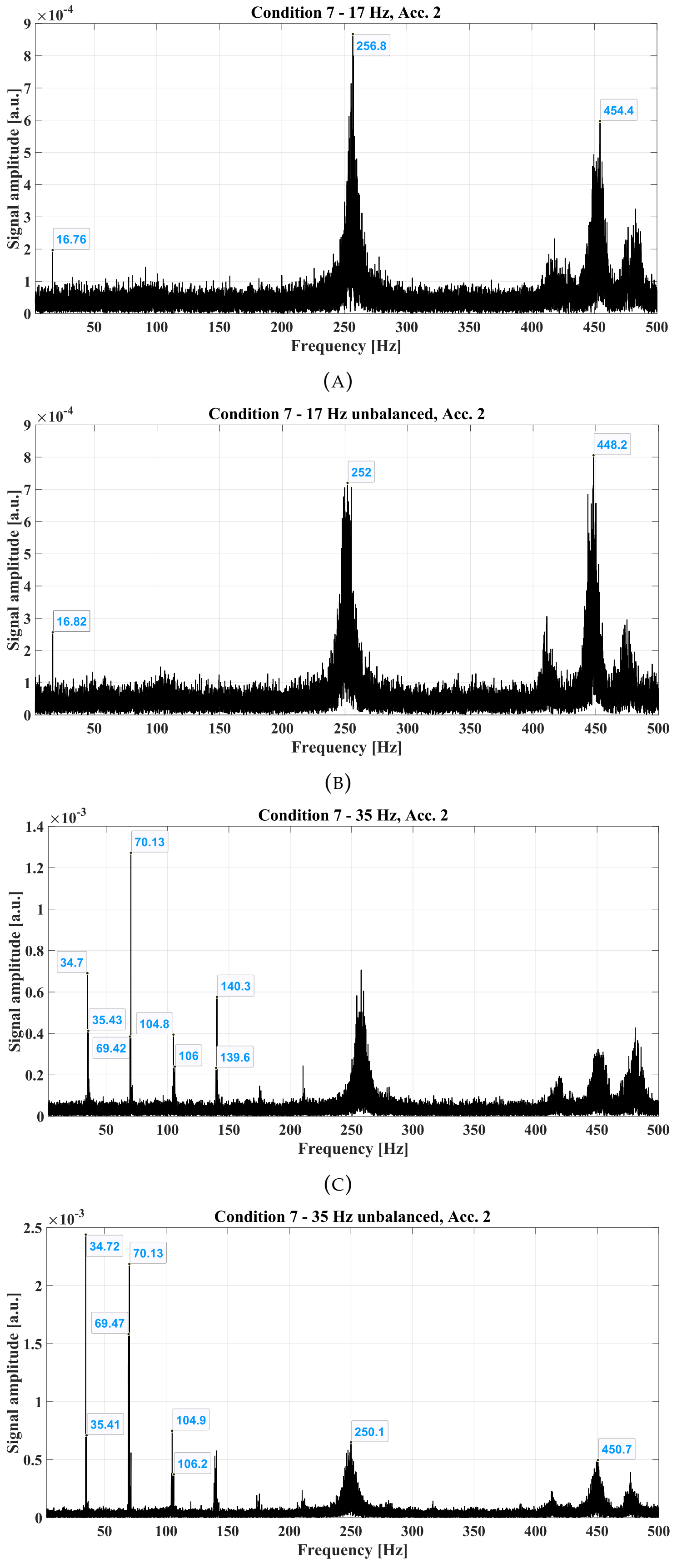

(A)

(B)

(C)

(D)

FIGURE 4.36: Fault condition 7 vibration frequency spectra for Accelerometer 2 for rotor speed at (A) 17 rps, (B) 17 rps (unbalanced), (C) 35 rps, and (D) 35 rps (unbalanced).

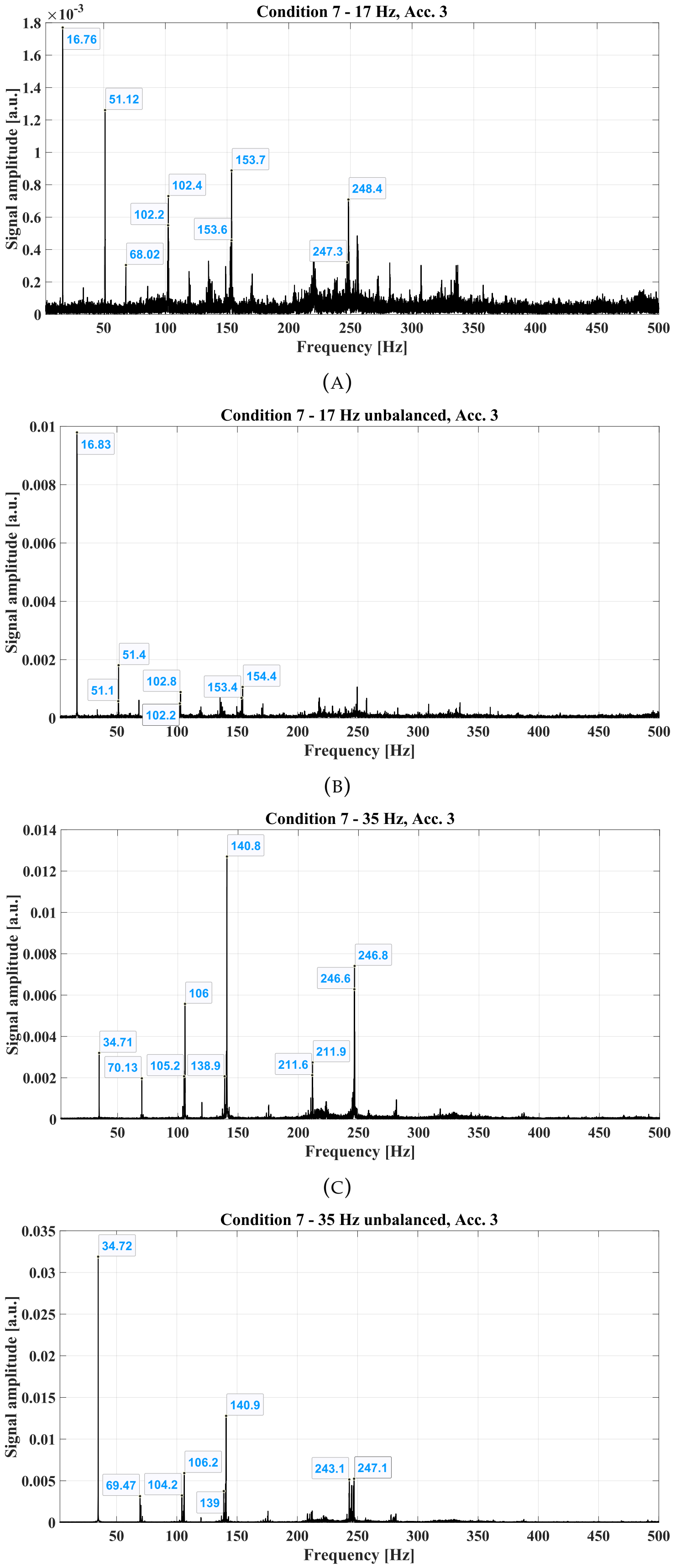

FIGURE 4.37: Fault condition 7 vibration frequency spectra for Accelerometer 3 for rotor speed at (A) 17 rps, (B) 17 rps (unbalanced), (C) 35 rps, and (D) 35 rps (unbalanced).

4.5.8 Fault condition 8

The used AC motor in condition 8 has an internal bearing fault and there is no preestablished fault in the mechanical system. The results for Accelerometer 2, attached to bearing 2, are shown in Figures 4.38 and 4.39. At 17 rps, Accelerometer 2 did not have the sensitivity to identify the vibration pattern of fault condition 8, where the signal amplitude order is 10^{-4}. Nonetheless, the frequency vibration spectra at this rotation speed, for both balanced and unbalanced conditions, contain high-order frequencies also identified by Accelerometer 2 in fault condition 7. These frequencies may be related to an incipient fault in the healthy ball-bearing attached to bearing 2. At 35 rps, Accelerometer 2 recognized the vibration pattern of the rotor bearing faulted condition, where it can be seen the presence of different harmonics and high-order frequencies caused by the failure in the rotor bearing, as can be seen in the appearance of 280 Hz and 350 Hz. Moreover, it is worth mentioning the first harmonic (2X) prominence related to the misalignment between the electric motor and the mechanical system. These results are validated by the measurements of the PZT-based accelerometer attached to bearing 2, shown in Figures 4.38 and 4.39, where it can be seen the high-order frequencies appear due to the failure at the electric motor bearing. The results for Accelerometer 3, attached to bearing 1, are shown in Figures 4.40 and 4.41. In these results, some nominal frequency harmonics have appeared in addition to the high-order frequencies characteristic of the rotor faulted bearing. These results are validated by the measurements of the PZT-based accelerometer attached to bearing 1, where similar frequency vibration spectra were achieved as shown in Figures 4.40 and 4.41.

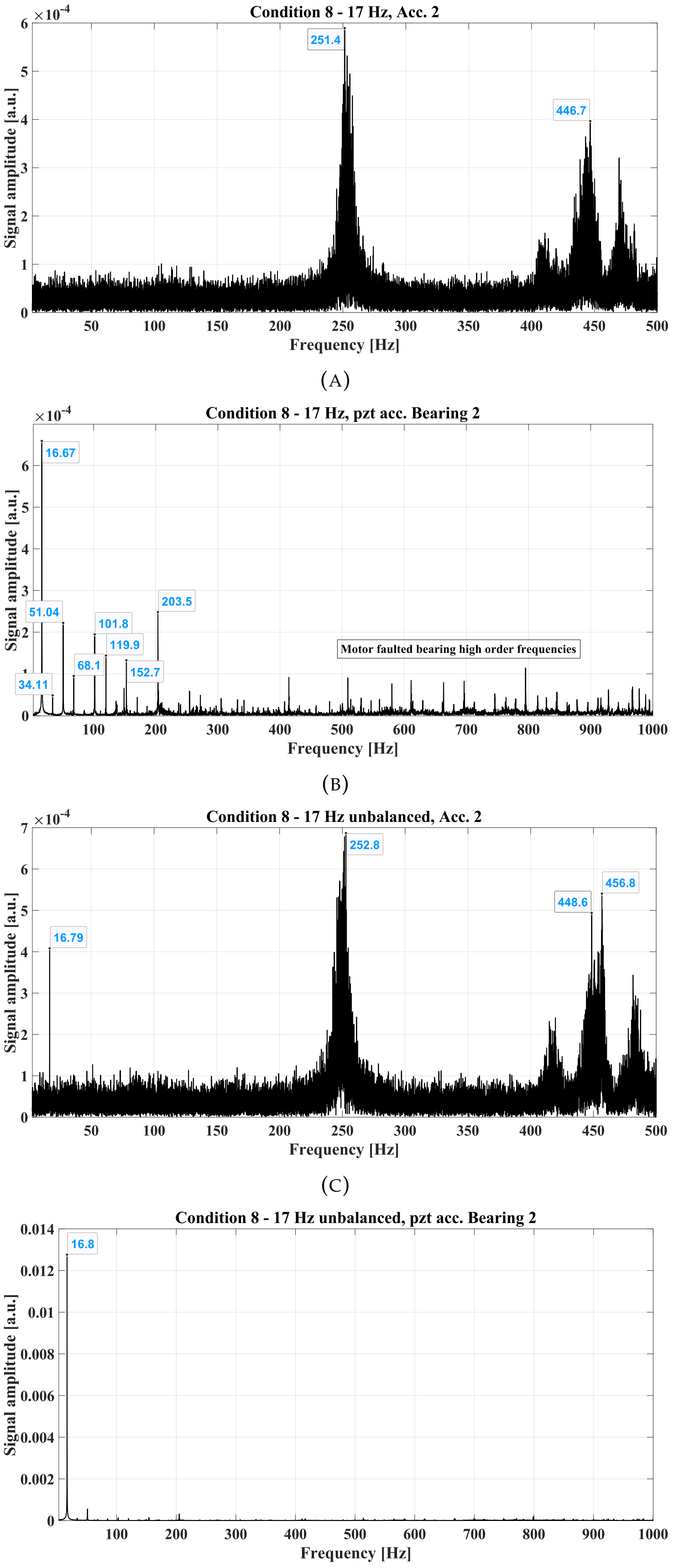

(A)

(B)

(C)

(D)

FIGURE 4.38: Fault condition 8 vibration frequency spectra for rotor speed at 17 rps for (A) FBG Acc. 2, (B) PZT Acc. at Bearing 2, (C) FBG Acc. 2 (unb), and (D) PZT Acc. at Bearing 2 (unb).

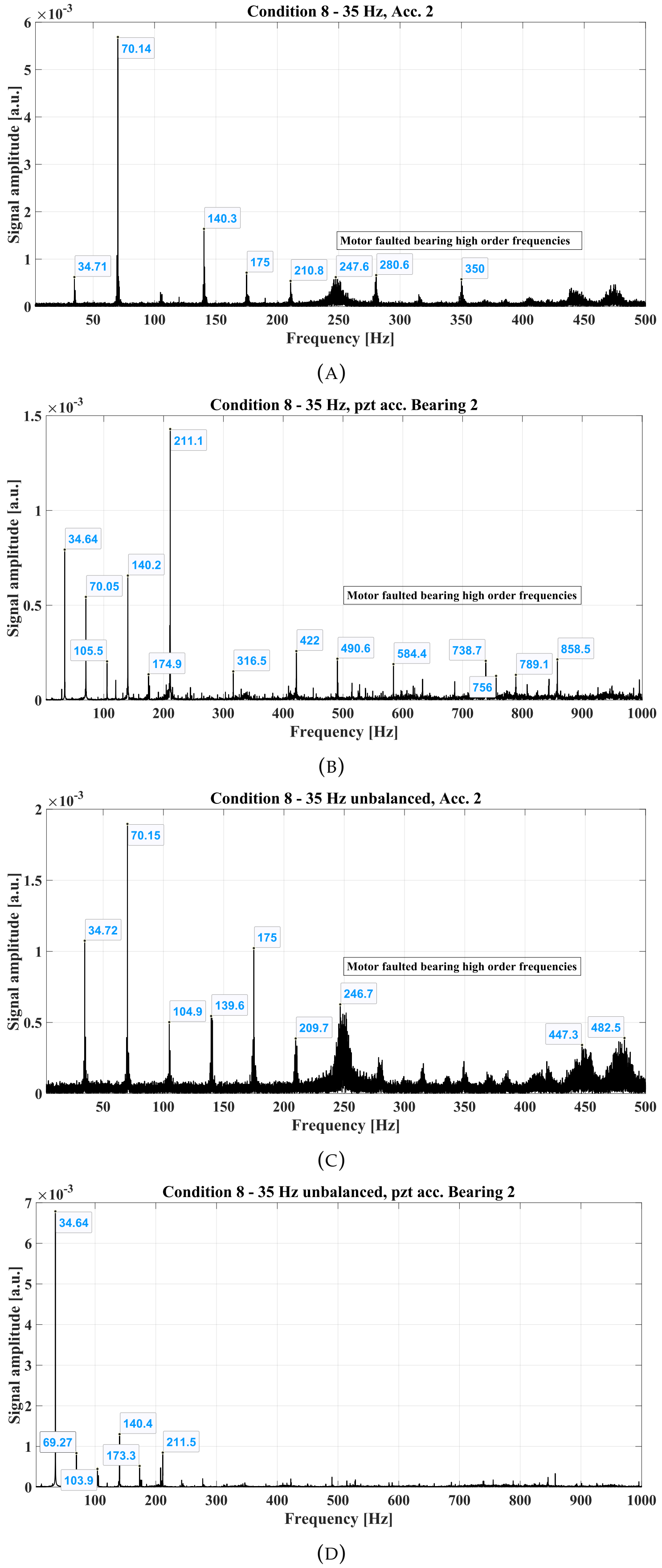

(A)

(B)

(C)

(D)

FIGURE 4.39: Fault condition 8 vibration frequency spectra for rotor speed at 35 rps for (A) FBG Acc. 2, (B) PZT Acc. at Bearing 2, (C) FBG Acc. 2 (unb), and (D) PZT Acc. at Bearing 2 (unb).

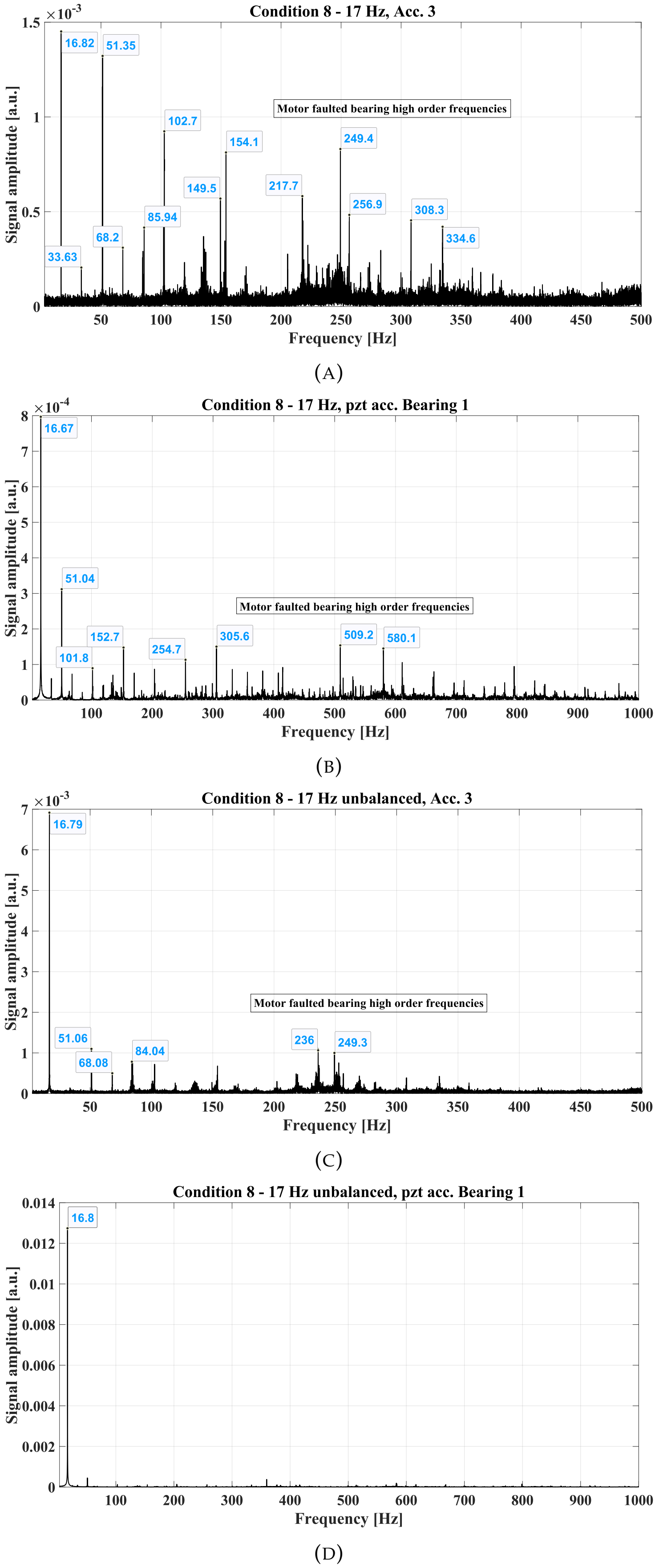

FIGURE 4.40: Fault condition 8 vibration frequency spectra for rotor speed at 17 rps for (A) FBG Acc. 3, (B) PZT Acc. at Bearing 1, (C) FBG Acc. 3 (unb), and (D) PZT Acc. at Bearing 1 (unb).

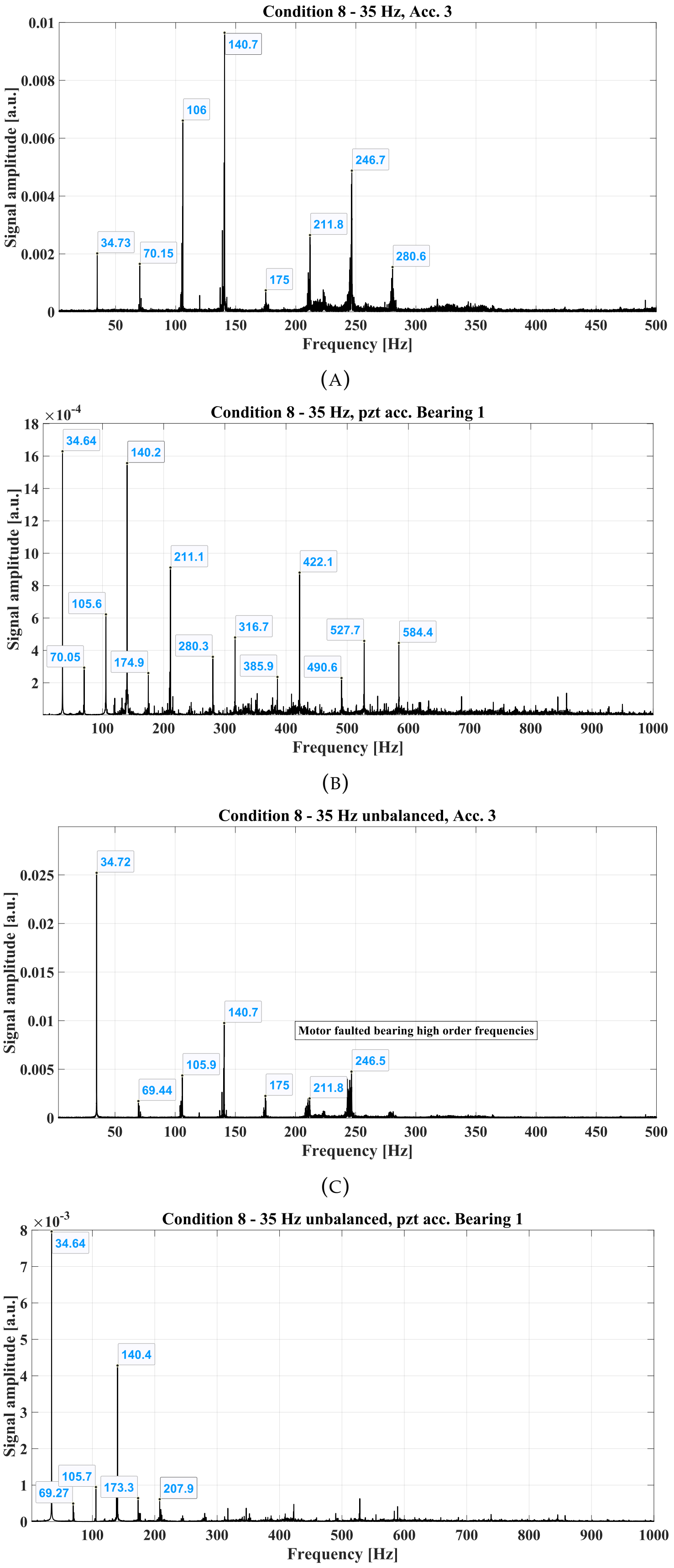

(A)

(B)

(C)

(D)

FIGURE 4.41: Fault condition 8 vibration frequency spectra for rotor speed at 35 rps for (A) FBG Acc. 3, (B) PZT Acc. at Bearing 1, (C) FBG Acc. 3 (unb), and (D) PZT Acc. at Bearing 1 (unb).

4.5.9 Fault condition 9

Fault condition 9 has the same fault configuration as fault condition 8, however, accelerometers 2 and 3 are interchanged. In the frequency vibration spectrum of an electric motor, multiple harmonics of the rotation speed are often associated with bearing failures. The harmonics, also known as shaft harmonics, are the result of irregularities resulting from damaged bearing components, such as inner and outer races and rolling elements. During their interaction within the bearing, these components generate vibrations at frequencies that are multiples of the motor's rotational speed, which manifest as harmonics (e.g., 2X, 3X, 4X, 5X, and further). Their presence, amplitudes, and phase relationships provide valuable diagnostic information about the bearing. As a result of complex bearing faults, modulation effects, and other factors within the bearing, multiple harmonics can be present simultaneously, assisting with the identification and timely maintenance of electric motor bearing issues in order to prevent further damage or motor failure [234]–[236]. The results for Accelerometer 2, attached to bearing 1, and for Accelerometer 3, attached to bearing 2, are shown in Figures 4.42 and 4.43, respectively. For both accelerometers, different harmonics of the nominal frequency have been identified, configuring the characteristic frequency vibration spectra of electric motors with faulted bearings. Moreover, these vibration patterns are similar to the results obtained by the PZT-based accelerometers in condition 8 (Figures **??** and **??**), validating the FBG-based accelerometers measurements for fault condition 9.

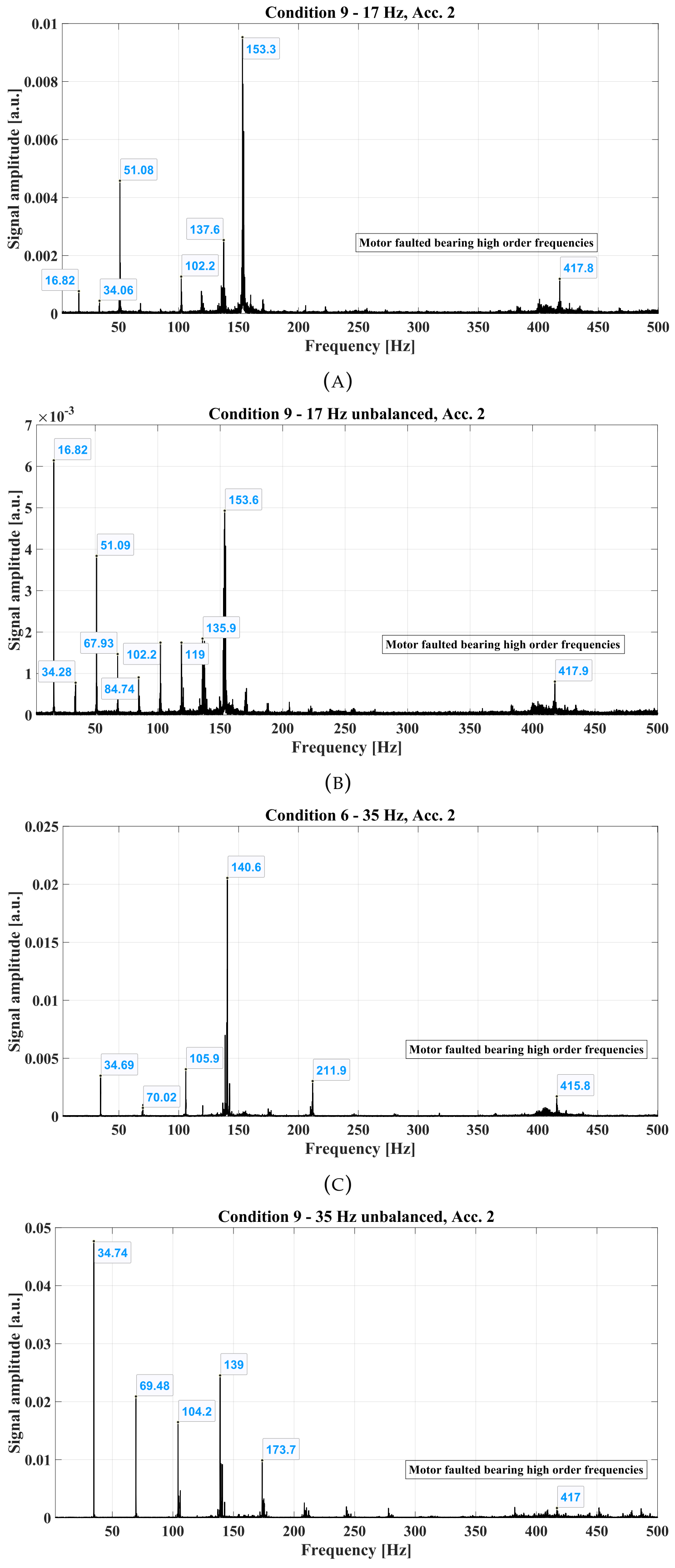

(A)

(B)

(C)

(D)

FIGURE 4.42: Fault condition 9 vibration frequency spectra for Accelerometer 2 for rotor speed at (A) 17 rps, (B) 17 rps (unbalanced), (C) 35 rps, and (D) 35 rps (unbalanced).

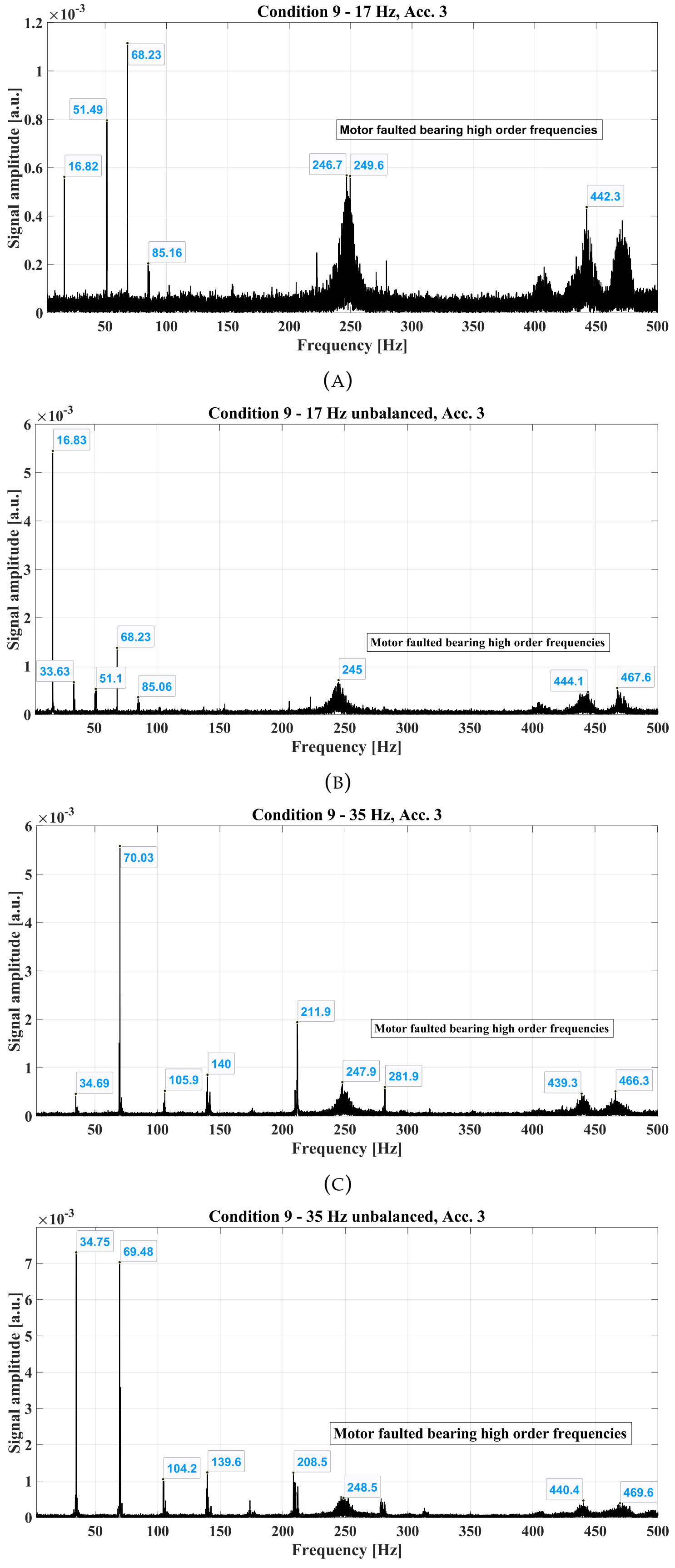

(A)

(B)

(C)

(D)

FIGURE 4.43: Fault condition 9 vibration frequency spectra for Accelerometer 3 for rotor speed at (A) 17 rps, (B) 17 rps (unbalanced), (C) 35 rps, and (D) 35 rps (unbalanced).

4.5.10 Results summary

Table 4.11 summarizes the harmonic identification in each fault condition. Besides the high-order frequency harmonics, some nominal frequency harmonics have been identified for conditions 1 to 4. In most cases, nominal harmonics are caused by mechanical looseness, misalignment between the mechanical system and the electrical motors, and coupling problems. A faulted ball bearing was used in the assembly of the experimental setup under those conditions. These high-order frequencies are characteristic of these fault conditions and were identified by both FBG-based accelerometers and PZT-based accelerometers. According to condition 5, there are no faults with the mechanical system or the electrical motors. Nevertheless, some nominal harmonics have been detected in the frequency vibration spectra for this case. There are many factors that contribute to the appearance of nominal frequency harmonics in real-life applications, including mechanical looseness in the assembly process, misalignment, and clearance. It should be noted, however, that the signal amplitude of these harmonics must be compared with the nominal frequency, and if the harmonic signal amplitude exceeds the nominal frequency, a fault condition will result. Consequently, real-time monitoring is critical to detecting faults in machinery at their earliest stages. Both accelerometers were able to detect the slip-frequency characteristics of rotor broken bars under conditions 6 and 7. Finally, for conditions 8 and 9, the FBG-based accelerometers identified some nominal frequency harmonics, which are characteristics of faulted bearings in electric motors. As a point of clarification, all of the results were validated and compared with the measurements of the PZT-based accelerometers used as a reference. All data analysis in this study was performed offline. The data set achieved in this work can be used to develop artificial intelligence algorithms for automatic fault recognition in online applications. This is done by comparing the real-time measurement with the well-known fault conditions frequency vibration spectra. Furthermore, a preliminary study should be conducted to determine the number of points required to carry out the Fast Fourier Transform, where an optimized number of points must be used to reduce the data processing time without compromising fault diagnosis. The comparison between the identified peaks by the FBG-based accelerometers with the results obtained by the PZT-based accelerometers can be used to estimate an average relative error. For the FBG-based accelerometer 2, the relative errors are 0.48%, 0.62%, 0.50%, 0.32%, 0.76%, 0.26%, 0.39%, 0.40%, and 0.48%, for fault conditions 1, 2, 3, 4, 5, 6, 7, 8, and 9, respectively. For the FBG-based accelerometer 3, the relative errors are 0.27%, 0.72%, 0.39%, 0.22%, 0.95%, 0.29%, 0.29%, 0.40%, and 0.85%, for fault conditions 1, 2, 3, 4, 5, 6, 7, 8, and 9, respectively. These errors were calculated by comparing the identified peaks by each accelerometer and taking the average of the relative errors of each identified peak. These errors are mainly related to the fluctuations in the current used to feed the frequency inverter, responsible for controlling the rotor velocity. Nonetheless, these errors indicate that the FBG-based accelerometers were able in correctly identify all the 9 fault conditions, validated by the commercial PZT-based accelerometers.

TABLE 4.11: Frequency vibration harmonics identification summary.

Fault condition	**Identified harmonics**			
	Accelerometer 1		**Accelerometer 2**	
	17 rps	**35 rps**	**17 rps**	**35 rps**
1	1X, 3X, 4X, high-order frequencies	1X, 3X, 4X, 5X high-order frequencies	1X, 3X, 4X, high-order frequencies	1X, 3X, 4X, 5X high-order frequencies
2	1X, 3X, 4X, high-order frequencies	1X, 3X, 4X, high-order frequencies	1X, 3X, 4X, high-order frequencies	1X, 2X, 3X, 6X high-order frequencies
3	1X, 3X, 4X, high-order frequencies	1X, 2X, 3X, 4X, high-order frequencies	1X, 3X, 4X, high-order frequencies	1X, 2X, 3X, 4X, high-order frequencies
4	1X, 2X, 3X, 4X, 5X, high-order frequencies	1X, 2X, 3X, 4X, high-order frequencies	1X, 3X, 4X, high-order frequencies	1X, 2X, 3X, 5X high-order frequencies
5	1X, 2X, 3X, 8X, high-order frequencies	1X, 2X, 3X, 4X, 5X, high-order frequencies	1X, 3X, 4X, high-order frequencies	1X, 2X, 3X, high-order frequencies
6	1X, 2X, 3X, 4X, slip frequencies	1X, 2X, 3X, 4X, slip frequencies	1X, 2X, 3X, 4X, slip frequencies	1X, 2X, 3X, 4X, slip frequencies
7	1X, high-order frequencies	1X, 2X, 3X, 4X, 5X, slip frequencies, high-order frequencies	1X, 3X, 4X, 6X slip frequencies	1X, 3X, 4X, 6X slip frequencies
8	1X, 2X, 3X, 4X, 5X, 6X high-order frequencies	1X, 2X, 3X, 4X, 5X, 6X, 7X, 8X high-order frequencies	1X, 2X, 3X, 4X, 5X, 6X high-order frequencies	1X, 2X, 3X, 4X, 5X, 6X, 7X
9	1X, 2X, 3X, 5X, 6X, 7X	1X, 2X, 3X, 4X, 6X, high-order frequencies	1X, 3X, 4X, 5X, high-order frequencies	1X, 2X, 3X, 4X, 6X, 7X, 8X, high-order frequencies

Chapter 5

Conclusions and future work

Different geometries were analyzed for the FBG-based accelerometer design in this study. Based on analytical models, the flexible hinge structure was found to provide the most efficient balance between natural frequency and sensitivity for this work requirement. With the analytical model of this structure, a multi-objective optimization was conducted and a combination of geometric parameters was determined. Through this procedure, we were able to find combinations of geometric parameters that are capable of meeting the project requirements by varying the geometric parameters. A total of four combinations were selected, adapted for fabrication, and analyzed using ANSYS 2019 R3. It was relevant to perform this analysis in order to evaluate more precisely the natural frequencies of the sensors because, in analytical models, some idealizations are adopted. These results were compared to the analytical model results, implying relative errors of 23%, 33%, 14%, and 6% for accelerometers 1, 2, 3, and 4, respectively. These errors are related to idealizations assumed and neglected effects in the analytical models. Experimentally, the fabricated sensors were characterized in terms of natural frequency and sensitivity. The experimental natural frequencies were 607.8 Hz, 366.7 Hz, 294.7 Hz, and 236.5 Hz for accelerometers 1, 2, 3, and 4, respectively. The experimental sensitivities are characterized by the exciting frequencies of 17 Hz, 35 Hz, and 50 Hz. For 17 Hz, the experimental sensitivities were 180 pm/g, 690 pm/g, 380 pm/g, and 400 pm/g, for accelerometers 1, 2, 3, and 4, correspondingly. For 35 Hz, the experimental sensitivities were 150 pm/g, 510 pm/g, 290 pm/g, and 230 pm/g, for accelerometers 1, 2, 3, and 4, respectively. For 50 Hz, the experimental sensitivities were 120 pm/g, 410 pm/g, 150 pm/g, and 160 pm/g, for accelerometers 1, 2, 3, and 4, respectively. The comparison between the identified peaks by the FBG-based accelerometers with the results obtained by the PZT-based accelerometers was used to estimate an average relative error. For the FBG-based accelerometer 2, the relative errors are 0.48%, 0.62%, 0.50%, 0.32%, 0.76%, 0.26%, 0.39%, 0.40%, and 0.48%, for fault conditions 1, 2, 3, 4, 5, 6, 7, 8, and 9, respectively. For the FBG-based accelerometer 3, the relative errors are 0.27%, 0.72%, 0.39%, 0.22%, 0.95%, 0.29%, 0.29%, 0.40%, and 0.85%, for fault conditions 1, 2, 3, 4, 5, 6, 7, 8, and 9, respectively. These errors are mainly related to fluctuations in the current used to feed the frequency inverter, responsible for controlling the rotor rotational velocity. In spite of the differences between experimental results and analytical/numerical results, the projected sensors were able to accurately identify the vibration pattern of the 9 fault conditions that were studied. Commercial piezoelectric accelerometers were used to compare and validate these results. Finally, it is concluded that the goal of this study was achieved, the FBG-based accelerometers were effectively projected, and they could be used for the detection of machinery faults.

As demonstrated during the development of this work, different structures can be adapted for FBG-based accelerometers. When dealing with accelerometer projects, there is a trade-off between sensitivity and natural frequencies, features that determine the application of the sensor. Different methods can be studied in this scenario in order to enhance the strain sensitivity of the used optical fiber sensor to increase acceleration sensitivity without affecting the natural frequency of the sensor. Studies such as these are strategic primarily in applications that require high levels of natural frequency and sensitivity at the same time. A further goal of this project is to test the project sensors in industrial applications to measure acceleration in various points of machinery simultaneously to assist in the diagnosis of faults. It will be necessary to develop artificial intelligence algorithms in order to enhance fault diagnosis, and preliminary studies can be conducted to determine the minimum data needed for fault diagnosis in order to optimize this application for online monitoring.

Appendix A

Analytical models mathematical full development

A.1 Analytical models

Different geometries must be considered and analyzed analytically and numerically when selecting an accelerometer design. The following geometries are considered in this work: a Double-L Cantilever, a Triangular Cantilever, a Clamped-Clamped Beam, a Single Cantilever, a Capillary Steel Tube, and a Flexible Hinge.

A.1.1 Double-L Cantilever Structure

The Double-L Cantilever analytical model considered in this work is based on [186]. The Double-L Cantilever based on FBGs geometry is schematically shown in Figure A.1.

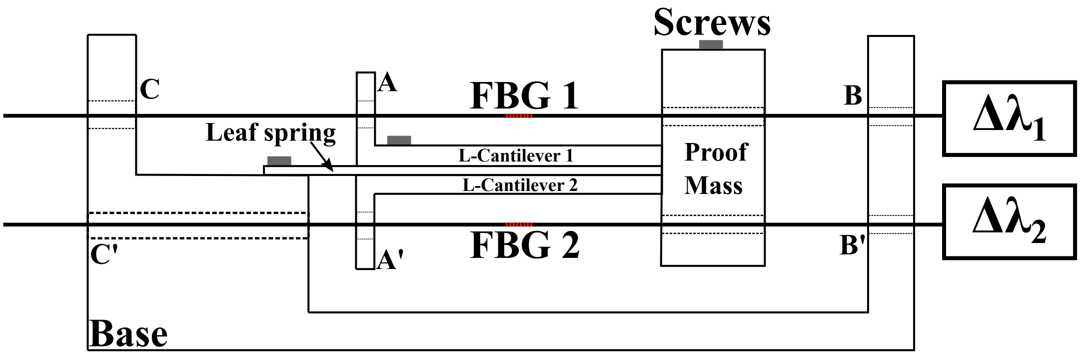

FIGURE A.1: Schematic representation of Double-L Cantilever based on FBGs.

According to Figure A.1, the mechanical sensor head consists of a thin rectangular leaf spring, two rigid L-shaped cantilevers, and an inertial mass. Each of these components is screwed together to form a single unit that is attached to the base at the leaf spring end. The proof mass, L-cantilevers, and walls of the base are drilled out to facilitate the insertion of two FBGs (FBG 1 and FBG 2). The FBGs are pretensioned and fixed at points A, B, A′, and B′.

When the Double-L Cantilever structure is subjected to an acceleration in its base, an inertial force (F) is induced on the proof mass (M), which undergoes a vertical deflection. The rigid-L cantilevers act as a translation mechanism converting the vertical deflection of the proof mass into axial deflections of the fiber. The axial strain caused in the fibers is proportional to acceleration. This axial strain implies a Bragg wavelength shift, also proportional to acceleration. Then, acceleration can be measured by Bragg wavelength shift monitoring. For vertically downward base acceleration, the proof mass moves upwards causing tensile strain in FBG 1, and an equal amount of compressive strain in FBG 2. The exact opposite happens for downward base acceleration. As aforementioned in the theoretical background section (Section 2.3), the Bragg wavelength is affected by thermal and strain effects. Using two FBGs, this configuration consists of a temperature self-compensated, enhancing the strain sensitivity. A mechanical model of the Double-L Cantilever structure is shown in Figure A.2.

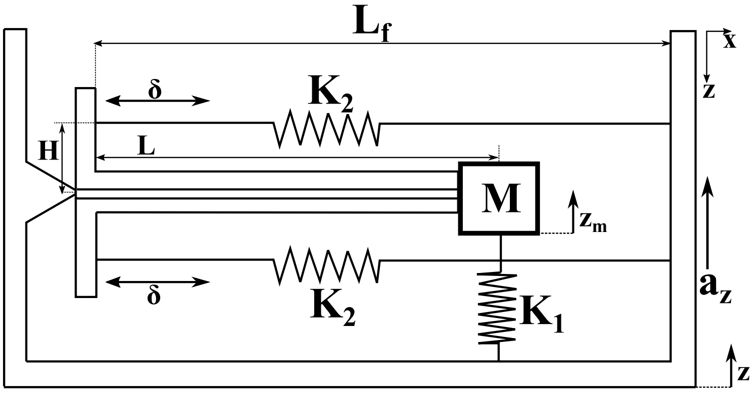

FIGURE A.2: Mechanical model of the Double-L Cantilever structure.

In the mechanical model shown in Figure A.2, the optical fibers are represented by the stiffness K_2, and K_1 represents the combination of Double-L Cantilever and the leaf spring stiffness. After fixing the Double-L Cantilever in the leaf spring using screws, its behavior becomes similar to a T-Cantilever [213]. In this model, L is the Double-L Cantilever length, L_f is the length of the sensing fiber between the fixation points A, and B, H is the L-shaped beam height, and M is the mass of the proof mass. The leaf spring is a rectangular sheet of metal of length L_s, width W_s, and thickness T_s. K_1 is mainly related to the geometric and material features and it is mathematically defined by Equation A.1.

$$K_1 = \frac{E_s W_s {T_s}^3}{4\left({L_s}^3 + 3{L_s}^2 L + 3L_s L^2\right)} \tag{A.1}$$

In Equation A.1, E_s is Young's modulus of spring steel. The stiffness K_2 is defined by Equation A.2.

$$K_2 = \frac{E_g A}{L_f} \tag{A.2}$$

In Equation A.2, E_g is Young's modulus of the optical fibers and A is its cross-sectional area, defined by $A = \frac{\pi d_f^2}{4}$, where d_f is the optical fibers diameter. Considering the accelerometer as a single-degree-of-freedom (SDOF) spring-mass system without damping, the equation of motion of the proof mass is represented by Equation A.3.

$$M\ddot{z} + K_{eq}z = -M\ddot{z_b} = -Ma \tag{A.3}$$

In Equation A.3, $z = z_m - z_b$ is the relative deflection of proof mass with respect to the base, z_b is the base displacement in z direction, and z_m is the mass displacement in z direction. K_{eq} is the equivalent stiffness of the system, defined by Equation

A.4.

$$K_{eq} = K_1 + 2K_2 \left(\frac{H}{L}\right)^2 \tag{A.4}$$

The equilibrium equation of motion of a spring-mass system is given by Equation A.5.

$$\ddot{z} + \omega_n^2 z = -\ddot{z_b} = a \tag{A.5}$$

In Equation A.5, ω_n is the undamped natural frequency of the SDOF system. Comparing Equations A.5 and A.3, the natural frequency of the system is defined by Equation A.6.

$$w_n = \sqrt{\frac{K_{eq}}{M}} = \sqrt{\frac{K_1 + 2K_2 \left(\frac{H}{L}\right)^2}{M}} \tag{A.6}$$

Considering a sinusoidal base acceleration, defined by $a = A \sin \omega t$, where A is the acceleration amplitude and ω the acceleration frequency, the corresponding steady-state response is given by $z = Z \sin \omega t$ where Z, the amplitude of the proof mass deflection, is given by Equation A.7.

$$Z = \frac{-A}{w_n^2} \left(\frac{1}{1 - \left(\frac{w}{w_n}\right)^2}\right) \tag{A.7}$$

Considering the excitation frequency is much smaller than the natural frequency of the system $\omega << \omega_n$, the peak deflection of the proof mass is defined by Equation A.8.

$$Z = \frac{-A}{\omega_n} \tag{A.8}$$

A geometrical representation of the Double-L Cantilever structure is represented in Figure A.3. For small angle deflection of the proof mass, the neutral axis of the leaf spring and Double-L Cantilever Structure can be assumed to be on a straight line. Assuming a small angle approximation, θ_1 and θ_2 are defined by Equation A.9.

$$\begin{aligned} \theta_1 &\approx \tan\theta_1 = \frac{z_m - z_b}{L_1} = \frac{z}{L_1} \\ \theta_2 &\approx \tan\theta_2 = \frac{\delta}{L_2} \end{aligned} \tag{A.9}$$

As $\theta_1 = \theta_2$, so $\frac{z}{L} = \frac{\delta}{H}$, yielding in Equation A.10.

$$\frac{\delta}{z} = \frac{H}{L} \tag{A.10}$$

Through Equation A.10, it can be observed that the factor $\frac{H}{L}$ defines the conversion of the vertical deflection of the cantilever structure into axial strain in the fibers.

The maximum value of the axial strain across the FBGs is given by Equation A.11.

$$\delta_{max} = z_{max} \left(\frac{H}{L}\right) = Z \left(\frac{H}{L}\right) \tag{A.11}$$

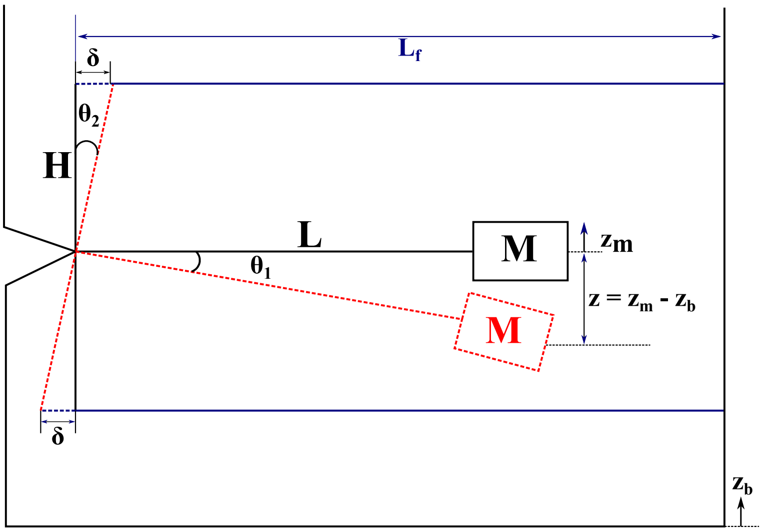

FIGURE A.3: Geometrical representation for Double-L Cantilever structure submitted to small angular displacement.

The maximum strain in the optical fiber can be obtained by dividing both sides of Equation A.11 by L_f, yielding in Equation A.12.

$$\varepsilon_{x,\max} = \frac{\delta_{\max}}{L_f} = \frac{Z}{L_f}\left(\frac{L_2}{L_1}\right) = \frac{-A}{L_f w_n^2}\left(\frac{H}{L}\right) \tag{A.12}$$

As aforementioned, in Equation A.12 can be observed that the acceleration is directly proportional to the strain in the FBGs. Finally, the strain sensitivity of the FBG is given by Equation A.13.

$$S_\varepsilon = \left|\frac{\varepsilon_{x,\max}}{A}\right| = \frac{1}{L_f w_n^2}\left(\frac{H}{L}\right) \tag{A.13}$$

A.1.2 Single Cantilever

The single cantilever analytical model considered in this work is based on [28], [214]. This structure and its mechanical model are schematically shown in Figure A.4, which is composed of a rectangular beam with width b, thickness h, length L, and mass m_b. This beam configuration is a clamped-free condition. At the free end, an inertial mass M is added to enhance the amplitude of the mechanical vibration. Yet in Figure A.4, a mechanical model of the structure is shown, configuring a spring-mass-damper system.

Considering the relative movement between the clamped base and the mass, $z(t) = x(t) - y(t)$, its time derivative is given by $\dot{z} = \dot{x} - \dot{y}$ and $\ddot{z} = \ddot{x} - \ddot{y}$. The harmonic base excitation and its time derivative are given by Equation A.14, where Y is the amplitude of excitation and ω_b is the excitation frequency.

$$\begin{aligned} y(t) &= Y \cdot \cos \omega_b t \\ \dot{y}(t) &= -Y \cdot \omega_b \cdot \sin \omega_b t \\ \ddot{y}(t) &= -Y \cdot \omega_b^2 \cdot \cos \omega_b t \end{aligned} \tag{A.14}$$

The movement equation of a base excited system is given by Equation A.15.

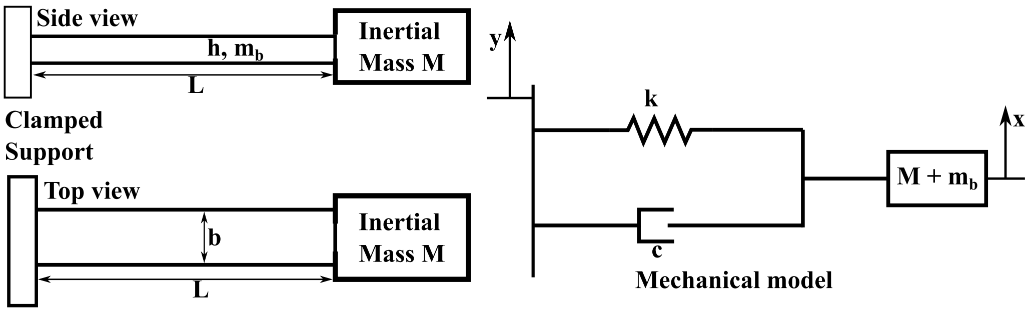

FIGURE A.4: Single cantilever structure and its mechanical model.

$$\begin{aligned} m\ddot{x}(t) + c\left[\dot{x}(t) - \dot{y}(t)\right] + k\left[x(t) - y(t)\right] = 0 \\ m\ddot{x}(t) + c\dot{z}(t) + kz(t) = 0 \end{aligned} \tag{A.15}$$

Subtracting $m\ddot{y}$ in both sides of Equation **??** and substituting Equation, yields in Equation **??**.

$$m\ddot{z}(t) + c\dot{z}(t) + kz(t) = -m\ddot{y} = Y\omega_b^2 \cos\omega_b t \tag{A.16}$$

The proposed solution for the differential Equation A.16 is given by Equation A.17.

$$z(t) = A \cdot e^{-\xi\cdot\omega_n\cdot t} \cdot \sin\left(\omega_d + \phi\right) + Z\cos\left(\omega_b \cdot t - \theta\right) \tag{A.17}$$

Analyzing the stationary regime, the homogeneous solution can be neglected in Equation A.17, yielding in Equation A.18.

$$z(t) = Z\cos\left(\omega_b \cdot t - \theta\right) \tag{A.18}$$

Where,

$$\begin{aligned} Z &= \frac{\omega_b^2 Y}{\sqrt{\left(\omega_n^2 - \omega_b^2\right)^2 + \left(2\xi\omega_n\omega_b\right)}} \\ \theta &= \arctan\frac{2\xi\omega_n\omega_b}{\left(\omega_n^2 - \omega_b^2\right)^2}. \end{aligned}$$

Let $r = \frac{\omega_b}{\omega_n}$, a relationship between the base displacement amplitude Y and the amplitude of the relative displacement between the mass and the base Z is defined in Equation A.19.

$$\frac{Z}{Y} = \frac{r^2}{\sqrt{(1-r^2)^2 + (2\xi r)^2}} \tag{A.19}$$

Factoring ω_n^2 out of the denominator, Equation A.18 can be rewritten in Equation A.20.

$$\omega_n^2 z(t) = \frac{1}{\sqrt{\left(1-r^2\right)^2 + (2\zeta r)^2}} \omega_b^2 Y \cos\left(\omega_b t - \theta\right) = \frac{-\ddot{y}(t)}{\sqrt{\left(1-r^2\right)^2 + (2\zeta r)^2}} \tag{A.20}$$

Aiming to determine the sensitivity of the structure to acceleration, consider $\omega_b \to 0$ and $r \to 0$, yielding in Equation A.21.

$$z(t) = \frac{-\ddot{y}(t)}{\omega_n^2} \tag{A.21}$$

Considering an Euler-Bernoulli beam, the maximum displacement caused by a load (inertial mass) applied to the free end of a clamped-free beam condition is defined by Equation A.22.

$$z(t) = \frac{PL^3}{3EI} = \frac{-\ddot{y}(t)}{\omega_n^2} \therefore P = \frac{-3EI\ddot{y}(t)}{\omega_n^2 L^3} \tag{A.22}$$

Applying Hooke's law, the bending stress at the beam's top surface caused due to the inertial mass movement is defined by Equation A.23.

$$\sigma = \frac{PLh}{2I} = E\epsilon \therefore P = \frac{2E\epsilon I}{Lh} \tag{A.23}$$

Substituting Equation A.23 into Equation A.22, the structure sensitivity to acceleration is given by Equation A.24.

$$S_0 = \frac{\epsilon}{\ddot{y}} = \frac{3h}{2L^2\omega_n^2} \tag{A.24}$$

Considering a perfect strain transmission from the beam's top surface to the FBG, since it is attached at the top surface, the S_0 sensitivity can be rewritten in terms of wavelength shift in nm/g in Equation A.25, considering an FBG centered near 1.55 μm.

$$S_\lambda \approx 1.2 \cdot 10^{-3} \cdot S_0 \cdot g \tag{A.25}$$

In Equation A.25, g is the acceleration due to gravity. For a rectangular beam, the stiffness is given by Equation A.26.

$$k = \frac{3EI}{L^3} \tag{A.26}$$

Finally, the natural frequency of the system is given by Equation 3.9, considering the beam's mass.

$$\omega_n = \sqrt{\frac{E \cdot b \cdot h^3}{4 \cdot L^3 \left(\frac{33}{140} \cdot m_b + M\right)}} \tag{A.27}$$

A.1.3 Triangular Cantilever

The triangular cantilever analytical model considered in this work is based on [214], [215]. Triangular cantilever structure is schematically shown in Figure A.5. In this structure, one of the ends of the triangular beam is fixed at a clamped support, and an inertial mass is attached at the free end. The triangular beam has, at the clamped end, width b and thickness h. The width varies along the beam length L, described by Equation A.28.

$$b_x = b\left(1 - \frac{x}{L}\right) = \frac{b}{L}(L - x) \tag{A.28}$$

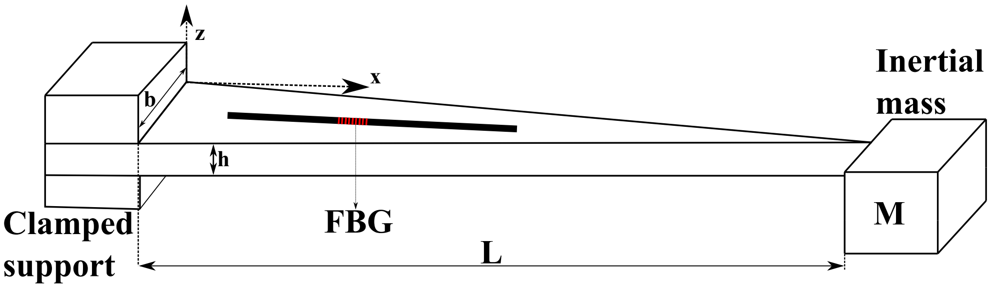

FIGURE A.5: Schematic of triangular cantilever structure.

Considering the applied load caused by the inertial mass ($F = M \cdot g$), where g is the gravity acceleration, the expression for the longitudinal strain at any cross-section at a distance z from the neutral axis and x from the fixed end caused by the bending moment is given by Equation A.29.

$$\epsilon_x = \frac{M_x z}{EI} = \frac{F(L-x)z}{EI} \tag{A.29}$$

In Equation A.29, E is the beam Young's modulus and I is its moment of inertial. The moment of inertia is defined by Equation A.30.

$$I = \frac{b_x h^3}{12} = \frac{b(L-x)h^3}{12L} \tag{A.30}$$

In this structure, the FBG is attached to the top surface of the triangular cantilever. Then, the FBG is subjected to a strain at $z = \frac{h}{2}$, where the strain is maximum in the z direction. Furthermore, considering that the FBG sensor is attached at the position $x = L/2$, the Equation A.30, yields in:

$$I_{L/2} = \frac{bh^3}{24} \tag{A.31}$$

Substituting Equation A.31 in Equation A.29 (assuming $z = h/2$), yields in Equation A.32.

$$\epsilon_x = \frac{F(L-x)h}{2EI_{L/2}} = \frac{6FL}{Ebh^2} \therefore F = \frac{\epsilon_x Ebh^2}{6L} \tag{A.32}$$

For a clamped-free beam condition, considering an Euler-Bernoulli Beam, the maximum displacement is given by Equation A.33.

$$z_{max_{x=L/2}} = \frac{FL^3}{3EI_{L/2}} = \frac{8FL^3}{Ebh^3} \tag{A.33}$$

Modeling the triangular beam structure as a spring-mass system, as developed for the single cantilever, the displacement caused by the inertial mass is given by Equation A.34.

$$z(t) = \frac{-\ddot{y}(t)}{\omega_n^2} = \frac{8FL^3}{Ebh^3} \therefore F = \frac{-Ebh^3\ddot{y}(t)}{8L^3\omega_n^2} \tag{A.34}$$

In Equation A.34, ω_n is the natural frequency of the system. Substituting Equation A.34 in Equation A.32, the system acceleration sensitivity, S_0, is defined in Equation A.35.

$$S_0 = \frac{\epsilon_x}{\ddot{y}} = \frac{3h}{4L\omega_n^2} \tag{A.35}$$

Considering a perfect strain transmission from the beam's top surface to the FBG, since it is attached at the top surface, the S_0 sensitivity can be rewritten in terms of wavelength shift in nm/g in Equation A.36, considering an FBG centered near 1.55 μm.

$$S_\lambda \approx 1.2 \cdot 10^{-3} \cdot S_0 \cdot g \tag{A.36}$$

In Equation A.36, g is the acceleration due to gravity. For a triangular beam, the stiffness, at $x = L/2$, is given by Equation A.37.

$$K = \frac{Ebh^3}{8L^3} \tag{A.37}$$

Finally, the natural frequency is given by Equation 3.13, where M is the mass attached to the free end of the beam.

$$\omega_n = \sqrt{\frac{K}{M}} \tag{A.38}$$

A.1.4 Clamped-Clamped Cantilever

The Clamped-Clamped beam model considered in this work is based on [216]. The clamped-clamped beam structure is schematically shown in Figure 3.7. This structure is composed of two parallel rectangular plates, each supported in such a way as to have clamped-free-clamped-free boundary conditions. A concentrated mass is placed between the plates. Because two of the plate edges are free, the modeling of the plates as beams is warranted for the lower-order vibration modes, and a Poisson correction factor can be added to account for two-dimensional effects.

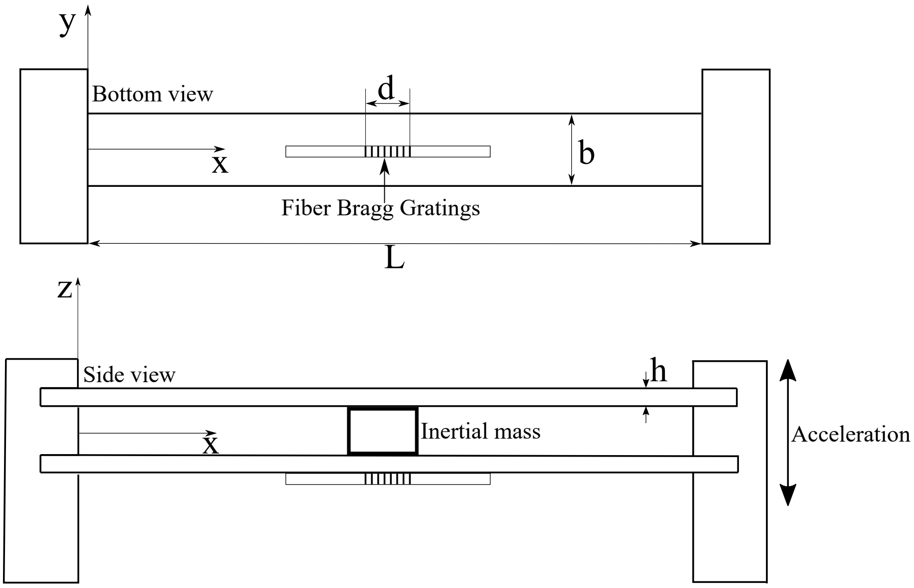

FIGURE A.6: Side and bottom view of a Clamped-Clamped beam structure.

The lowest natural frequency of the clamped-clamped beam structure is given by Equation A.39.

$$\omega_n = 0.915\sqrt{\frac{Ebh^3}{L^3\left(M + 0.793m_b\right)\left(1 - \nu^2\right)}} \tag{A.39}$$

In Equation A.39, E is the plate Young's modulus, b, h, L are its width, thickness, and length, respectively, M is the mass of the inertial mass and m_b is the total mass of the plates, and ν is the Poisson's ratio. This natural frequency corresponds to the first symmetric transverse vibration mode of the system, which has a maximum displacement at the center, where the concentrated mass is placed.

From a strain perspective, an average strain over the grating length will be sensed. For a surface strain field given by ϵ_{xx}, this average strain can be expressed by Equation A.40.

$$\bar{\epsilon}_{xx} = (1/d)\int_{L/2-d/2}^{L/2+d/2} \epsilon_{xx}dx \tag{A.40}$$

In this analytical model approach, an ideal strain transfer between the beam and the grating has been assumed. The division of the average strain by the magnitude of the acceleration, yields in Equation A.41.

$$S_f = \left(\frac{M + 1.046m_b}{M + 0.793m_b}\right)\left(\frac{gh}{4\pi^2L^2}\right)\left(\frac{10^6}{\omega^2 - \omega_n^2}\right)\Psi(\kappa) \tag{A.41}$$

In Equation A.41, $\Psi(\kappa) = (4.175\sin(2.365\kappa) - 0.555\sinh(2.365\kappa))/\kappa$, $\kappa = \frac{d}{L}$, g is the acceleration due to gravity, and ω is the excitation frequency. The limit of S_f as $\omega \to 0$ is the sensitivity S_0 of the device, given by Equation A.42.

$$S_0 = \left(\frac{0.030gL\left(M + 1.046m_b\right)\left(1 - \nu^2\right)10^6}{Ebh^2}\right)\Psi(\kappa) \tag{A.42}$$

Considering an FBG centered near 1.55 μm, the S_0 scale factor can be rewritten in terms of the wavelength shift (in nm/g), given by Equation A.43.

$$S_\lambda \approx 1.2 \cdot 10^{-3} \cdot S_0 \tag{A.43}$$

A.1.5 Steel Tube-Mass Block Elastic Structure

The steel tube-mass block elastic structure-based accelerometer analytical model is based on [217]. The structure of this accelerometer is shown schematically in Figure 3.8. This structure is composed of a capillary steel tube with length L, a cylinder-shaped mass block, a shell, and an optical fiber with two FBGs embedded in the steel tube. The capillary steel tube with FBGs is inserted in the shell and pre-stretched by rotating the nuts and then serves as a spring element. The two FBGs output opposite wavelength shifts caused by the inertial force of the mass along the axial vibration direction. Therefore, using the difference between the two opposite wavelength shifts of the two FBGs as the sensing signal, the influence of temperature cross-sensitivity could be avoided and the sensitivity can be improved.

The relationship between strain and acceleration in the structure is given by Equation A.44.

$$a = \frac{F}{m} = \frac{2ES}{m} \cdot \varepsilon \tag{A.44}$$

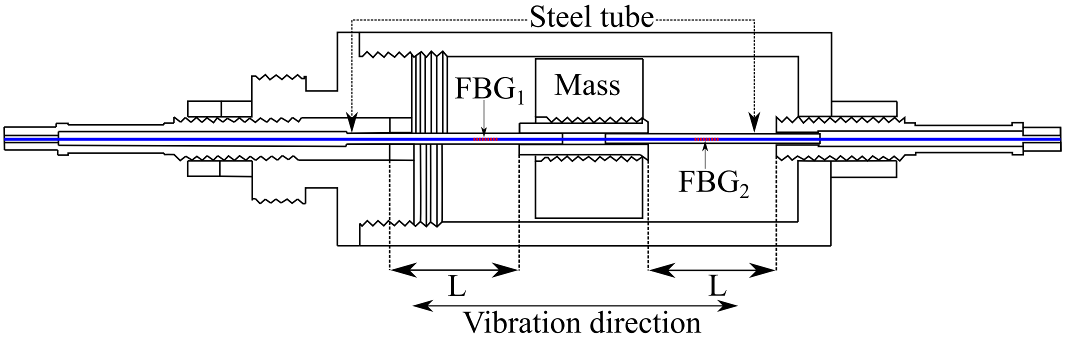

FIGURE A.7: Steel tube-mass block elastic structure-based accelerometer geometry.

In Equation A.44, F is the vibration inertia force of the mass block, S is the cross-sectional area of the capillary steel tube, m is the quality of mass black, and E is Young's modulus of the capillary steel tube. The stiffness of the capillary steel tube is defined by Equation A.45.

$$\begin{aligned} &F = 2ES \cdot \varepsilon = 2ES\frac{\Delta L}{L} = \left(\frac{2ES}{L}\right) \cdot \Delta L = k \cdot \Delta L, \\ &k = \frac{2ES}{L} \end{aligned} \tag{A.45}$$

The first natural frequency is given by Equation 3.21.

$$\omega_n = \sqrt{\frac{k}{m}} = \sqrt{\frac{2ES}{mL}} \tag{A.46}$$

Modeling the steel tube-mass block elastic structure as a spring-mass system, the sensitivity of the sensor is defined by Equation 3.22.

$$S_a = \frac{1}{\omega_n^2 L} = \frac{m}{2ES} \tag{A.47}$$

A.1.6 Flexible Hinges

The flexible hinges analytical model is based on [218]. The design of the structure is shown in Figure A.8. This sensor is composed of two inertial masses, three straight circular flexure hinges, two FBGs, and a base. This structure is symmetrical, the sizes of flexure hinge 2 and flexure hinge 3 are exactly the same. Two FBGs are pre-stretched and attached at the top and bottom surfaces of the structure.

In response to external acceleration excitations in the measurement direction, the two masses will rotate slightly around the center of flexible hinges-2 and 3, respectively, causing the FBGs to stretch or compress, which converts vibration acceleration into strains and wavelength shifts. The wavelength shifts of the two FBGs can be used to obtain vibration signals. Moreover, two FBGs will double the sensor's sensitivity while accomplishing temperature self-compensation.

As a result of inertial forces acting on the sensors, the two masses will rotate slightly around the center of the flexible hinges 2 and 3, respectively, when an external acceleration is applied to the sensor's sensitive direction. The mechanical model of the sensor is shown in Figure A.9. According to the principle of virtual displacement, the general dynamics equation for the system can be expressed by Equation A.48.

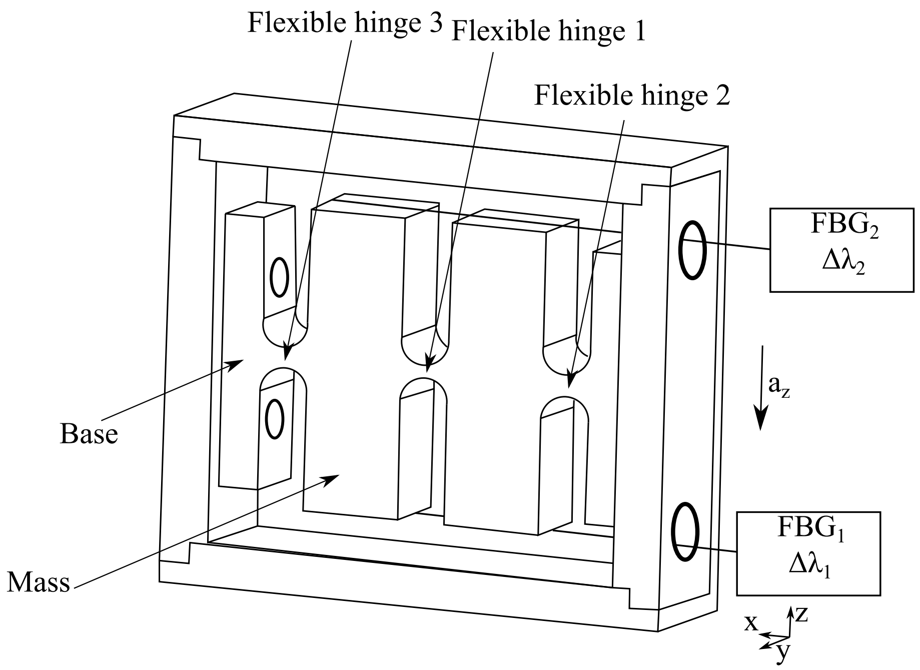

FIGURE A.8: Flexible hinges accelerometer structure.

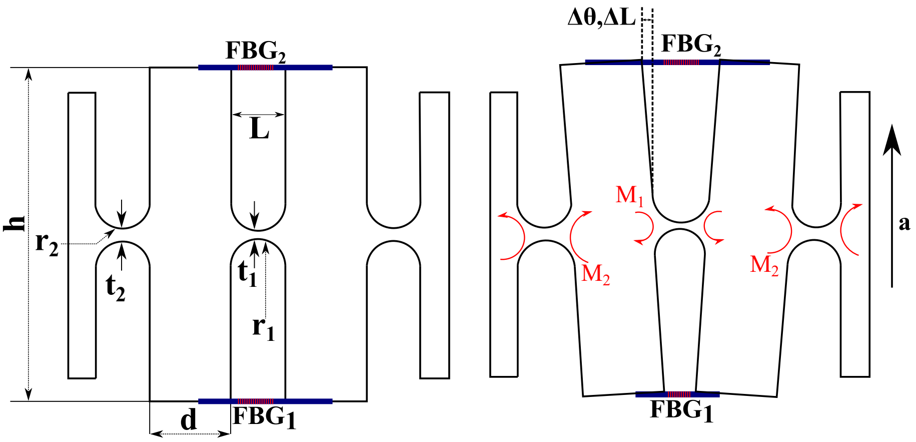

FIGURE A.9: Flexible hinges accelerometer mechanical model under an external acceleration.

$$(-2M_1 + 2M_2)\delta\theta + 2ma\delta z - 4F_f\delta\Delta l = 0 \tag{A.48}$$

In Equation A.48, θ is the rotation angle of the mass relative to flexible hinge 2, m is the mass of the mass block, a is the vibration acceleration in the z-axis of the sensor, z is the z-axis displacement of the mass center of the mass, F_f is the tensile force generated by the optical fiber, l is the optical fiber pasting span, and Δl is the displacement of the bonding point at one end of the optical fiber in the x-axis. The magnitude of the moment M_i is proportional to the stiffness K_i of the straight circular flexible hinge, expressed by Equation A.49.

$$\begin{aligned} &M_i = K_i\theta \quad (i = 1,2) \\ &K = \frac{EwR^2}{24} \Big/ \left[\frac{s^3\left(6s^2+4s+1\right)}{(2s+1)(4s+1)^2} + \frac{6s^4(2s+1)}{(4s+1)^{5/2}} \arctan\sqrt{4s+1} \right] \end{aligned} \tag{A.49}$$

In Equation A.49, E is Young's modulus of the flexible hinge, r is the radius of the straight circular flexible hinge, t is the thickness of the hinge waist, w is the width of the hinge, and $s = \frac{r}{t}$. The magnitude of the pulling force can be obtained by Equation A.50.

$$F_f = 2k_f \Delta l \tag{A.50}$$

In Equation A.50, k_f is the elastic coefficient of the optical fiber, defined by Equation A.51.

$$k_f = \frac{A_f E_f}{l}, \tag{A.51}$$

where l is the bonding span of the optical fiber, A_f is its cross-sectional area, and E_f its Young's modulus. Assuming θ as a small angle displacement, we can take $\sin\theta \approx \theta$. From the geometric relationship, the following relationships can be obtained in Equation A.52.

$$\begin{aligned} z &= \left(r_2 + \frac{d}{2}\right)\theta \\ \Delta l &= \frac{h}{2}\theta \end{aligned} \tag{A.52}$$

The strain applied to the optical fibers is defined by Equation A.53.

$$\epsilon = \frac{2\Delta l}{l} \tag{A.53}$$

The effects of strain and temperature on the Bragg wavelength shift can be expressed by Equation A.54.

$$\frac{\Delta\lambda}{\lambda} = (1 - P_e)\epsilon + (\alpha_f + \xi_f)\Delta T \tag{A.54}$$

In Equation A.54, λ is the Bragg central wavelength for the FBG, $\Delta\lambda$ is the Bragg wavelength shift of the FBG, α_f is the thermal expansion coefficient, ξ_f is the thermo-optical coefficient, and P_e is the photoelastic coefficient (theoretical value = 0.22). Since FBG 1 and FBG 2 are symmetrically arranged at both ends of the mass block, when FBG 1 is stretched, FBG 2 is compressed, implying in $\epsilon_1 = \epsilon$ and $\epsilon_2 = -\epsilon$. Considering the same sensitivity for both FBGs and that the central wavelengths are approximately equal, yields in $\lambda_1 = \lambda_2 = \lambda$. Then, applying Equation A.54 with this consideration, the temperature effects on the Bragg wavelength shift are self-compensated, as shown in Equation A.55.

$$\frac{\Delta\lambda}{\lambda} = \frac{\Delta\lambda_1}{\lambda} - \frac{\Delta\lambda_2}{\lambda} = 2(1 - P_e)\epsilon \tag{A.55}$$

Combining Equations A.48, A.52 and A.55, the sensitivity of the sensor is defined by Equation A.56 in pm/g.

$$S = \frac{\Delta\lambda}{a} = \frac{4\lambda\,(1 - P_\mathrm{e})\,\Delta l}{al} = \frac{\lambda\,(1 - P_\mathrm{e})}{l}\,\frac{2mh\left(r_2 + \frac{d}{2}\right)}{k_f h^2 + K_1 + K_2} \tag{A.56}$$

In Equation A.56, K_1 and K_2 are the stiffness for the flexible hinge 1 and the flexible hinge 2, respectively. Suppose J is the inertia moment of the mass around the center of hinge-2 and θ is the generalized coordinate for obtaining the Lagrangian function, as follows:

$$L = T_m - V_f - V_J \tag{A.57}$$

The strain potential energy of the optical fiber is expressed as follows:

$$V_f = 2 \cdot \frac{1}{2} k_f (h\theta)^2 \tag{A.58}$$

The elastic potential energy of the hinge can be obtained by the following:

$$V_J = 2 \cdot \frac{1}{2} (K_1 + K_2)\theta^2 \tag{A.59}$$

The kinetic energy of the mass block can be described as follows:

$$T_m = 2 \cdot \frac{1}{2} J\dot{\theta}^2 \tag{A.60}$$

The Lagrangian equation for the conservative force can be written as follows:

$$2J\ddot{\theta} + [2k_f h^2 + 2(K_1 + K_2)]\theta = 0 \tag{A.61}$$

The natural frequency of the system is defined by Equation A.62.

$$\omega_n = \sqrt{\frac{k_f h^2 + K_1 + K_2}{J}} \tag{A.62}$$

According to the moment of inertia formula and the parallel axis theorem, the moment of inertia can be obtained by the following:

$$J = m\frac{d^2 + h^2}{12} + m\left(r_2 + \frac{d}{2}\right)^2 \tag{A.63}$$

Bibliography

[1] A. Babbar, E. M. Ortiz, V. L. Syrmos, and M. M. Arita, "Advanced diagnostics and prognostics for engine health monitoring," 2009, ISBN: 9781424426225. DOI: 10.1109/AERO.2009.4839657.

[2] P. Cawley, "Structural health monitoring: Closing the gap between research and industrial deployment," *Structural Health Monitoring*, vol. 17, pp. 1225–1244, 5 Sep. 2018, ISSN: 17413168. DOI: 10.1177/1475921717750047.

[3] A. Santos, R. Santos, M. Silva, E. Figueiredo, C. Sales, and J. C. Costa, "A global expectation–maximization approach based on memetic algorithm for vibration-based structural damage detection," *IEEE Transactions on Instrumentation and Measurement*, vol. 66, no. 4, pp. 661–670, 2017. DOI: 0.1109/TIM.2017.2663478.

[4] Z. Ghemari, S. Saad, and K. Khettab, "Improvement of the vibratory diagnostic method by evolution of the piezoelectric sensor performances," *International Journal of Precision Engineering and Manufacturing*, vol. 20, pp. 1361–1369, 8 Aug. 2019, ISSN: 20054602. DOI: 10.1007/s12541-019-00154-5.

[5] K. M. Sousa, I. Brutkowski Vieira da Costa, E. S. Maciel, J. E. Rocha, C. Martelli, and J. C. Cardozo da Silva, "Broken bar fault detection in induction motor by using optical fiber strain sensors," *IEEE Sensors Journal*, vol. 17, no. 12, pp. 3669–3676, 2017. DOI: 10.1109/JSEN.2017.2695961.

[6] O. Wallscheid, "Thermal monitoring of electric motors: State-of-the-art review and future challenges," *IEEE Open Journal of Industry Applications*, vol. 2, pp. 204–223, Jun. 2021, ISSN: 26441241. DOI: 10.1109/ojia.2021.3091870.

[7] Z. Peng, N. J. Kessissoglou, and M. Cox, "A study of the effect of contaminant particles in lubricants using wear debris and vibration condition monitoring techniques," *Wear*, vol. 258, pp. 1651–1662, 11-12 Jun. 2005, ISSN: 00431648. DOI: 10.1016/j.wear.2004.11.020.

[8] F. Filippetti, G. Franceschini, C. Tassoni, and P. Vas, "Recent developments of induction motor drives fault diagnosis using ai techniques," *IEEE Transactions on Industrial Electronics*, vol. 47, no. 5, pp. 994–1004, 2000. DOI: 10.1109/41.873207.

[9] D. Pines and A. E. Aktan, "Status of structural health monitoring of long-span bridges in the united states," *Progress in Structural Engineering and materials*, vol. 4, no. 4, pp. 372–380, 2002. DOI: https://doi.org/10.1002/pse.129.

[10] C. C. K. Chan, C.-C. Chen, S. Delaney, and A. Ferworn, "A markerless high resolution structural health monitoring framework for smart cities," in *2021 IEEE Technology & Engineering Management Conference-Europe (TEMSCON-EUR)*, IEEE, 2021, pp. 1–5. DOI: 10.1109/TEMSCON-EUR52034.2021.9488617.

[11] M. Stankovic, R. Gupta, J. Figueroa, O. Authried, and T. Rueth, "Industry 4.0: Opportunities behind the challenge," in *Background Paper for UNIDO General Conference*, vol. 17, 2017, pp. 2017–11. [Online]. Available: `https://www.unido.org/gc17/industry40`.

[12] A. Pollak, A. Hilarowicz, M. Walczak, and D. Gąsiorek, "A framework of action for implementation of industry 4.0. an empirically based research," *Sustainability*, vol. 12, no. 14, p. 5789, 2020.

[13] I. Vuksanović Herceg, V. Kuč, V. M. Mijušković, and T. Herceg, "Challenges and driving forces for industry 4.0 implementation," *Sustainability*, vol. 12, no. 10, p. 4208, 2020. DOI: `https://doi.org/10.3390/su12104208`.

[14] J. Li and H. Hao, "A review of recent research advances on structural health monitoring in western australia," *Structural Monitoring and Maintenance*, vol. 3, pp. 33–49, 1 Mar. 2016, ISSN: 22886613. DOI: `10.12989/smm.2016.3.1.033`.

[15] D. O. Aikhuele and F. M. Turan, "A modified exponential score function for troubleshooting an improved locally made offshore patrol boat engine," *Journal of Marine Engineering & Technology*, vol. 17, no. 1, pp. 52–58, 2018. DOI: `https://doi.org/10.1080/20464177.2017.1286841`.

[16] F. B. Batista, P. C. M. Lamim Filho, R. Pederiva, and V. A. D. Silva, "An empirical demodulation for electrical fault detection in induction motors," *IEEE Transactions on Instrumentation and Measurement*, vol. 65, no. 3, pp. 559–569, 2016. DOI: `https://doi.org/10.1109/TIM.2015.2509398`.

[17] R. Upase and N. Ambhore, "Experimental investigation of tool wear using vibration signals: An ann approach," *Materials Today: Proceedings*, vol. 24, pp. 1365–1375, 2020. DOI: `https://doi.org/10.1016/j.matpr.2020.04.454`.

[18] M. Iorgulescu, R. Beloiu, and M. O. Popescu, "Vibration monitoring for diagnosis of electrical equipment's faults," in *2010 12th International Conference on Optimization of Electrical and Electronic Equipment*, IEEE, 2010, pp. 493–499. DOI: `https://doi.org/10.1109/OPTIM.2010.5510332`.

[19] I. Vamsi, G. Sabareesh, and P. Penumakala, "Comparison of condition monitoring techniques in assessing fault severity for a wind turbine gearbox under non-stationary loading," *Mechanical Systems and Signal Processing*, vol. 124, pp. 1–20, 2019. DOI: `https://doi.org/10.1016/J.YMSSP.2019.01.038`.

[20] R. M. Delgadillo and J. R. Casas, "Non-modal vibration-based methods for bridge damage identification," *Structure and Infrastructure Engineering*, vol. 16, no. 4, pp. 676–697, 2020. DOI: `https://doi.org/10.1080/15732479.2019.1650080`.

[21] M. Varanis, A. Silva, A. Mereles, and R. Pederiva, "Mems accelerometers for mechanical vibrations analysis: A comprehensive review with applications," *Journal of the Brazilian Society of Mechanical Sciences and Engineering*, vol. 40, 11 Nov. 2018, ISSN: 18063691. DOI: `10.1007/s40430-018-1445-5`.

[22] J. D. Smith, *Vibration measurement and analysis*. Butterworth-Heinemann, 2013, ISBN: 0-408-04101-3.

[23] J. S. Martin, D. J. Fenneman, F. T. Codron, *et al.*, "Ultrasonic displacement sensor for the seismic detection of buried land mines," in *Detection and Remediation Technologies for Mines and Minelike Targets VII*, SPIE, vol. 4742, 2002, pp. 606–616. DOI: `https://doi.org/10.1117/12.479132`.

[24] A. Maekawa, M. Noda, and M. Shintani, "Experimental study on a noncontact method using laser displacement sensors to measure vibration stress in piping systems," *Measurement*, vol. 79, pp. 101–111, 2016. DOI: `https://doi.org/10.1016/j.measurement.2015.10.012`.

[25] X. Rimpault, E. Bitar-Nehme, M. Balazinski, and J. Mayer, "Online monitoring and failure detection of capacitive displacement sensor in a capball device using fractal analysis," *Measurement*, vol. 118, pp. 23–28, 2018. DOI: `https://doi.org/10.1016/j.measurement.2018.01.006`.

[26] J. Burjánek, G. Gassner-Stamm, V. Poggi, J. R. Moore, and D. Fäh, "Ambient vibration analysis of an unstable mountain slope," *Geophysical Journal International*, vol. 180, no. 2, pp. 820–828, 2010. DOI: `https://doi.org/10.1111/j.1365-246X.2009.04451.x`.

[27] M. H. Mohd Ghazali and W. Rahiman, "Vibration analysis for machine monitoring and diagnosis: A systematic review," *Shock and Vibration*, vol. 2021, pp. 1–25, 2021. DOI: `https://doi.org/10.1155/2021/9469318`.

[28] D. J. Inman and R. C. Singh, *Engineering vibration*. Prentice Hall Englewood Cliffs, NJ, 1994, vol. 3, ISBN: 978-0132871693.

[29] A. Stefani, S. Andresen, W. Yuan, N. Herholdt-Rasmussen, and O. Bang, "High sensitivity polymer optical fiber-bragg-grating-based accelerometer," *IEEE Photonics Technology Letters*, vol. 24, no. 9, pp. 763–765, 2012. DOI: `10.1109/LPT.2012.2188024`.

[30] Y. Nemirovsky, A. Nemirovsky, P. Muralt, and N. Setter, "Design of novel thin-film piezoelectric accelerometer," *Sensors and Actuators A: Physical*, vol. 56, no. 3, pp. 239–249, 1996. DOI: `https://doi.org/10.1016/S0924-4247(96)01324-6`.

[31] J. Zhang, Y. Su, Q. Shi, and A. P. Qiu, "Microelectromechanical resonant accelerometer designed with a high sensitivity," *Sensors (Switzerland)*, vol. 15, pp. 30 293–30 310, 12 Dec. 2015, ISSN: 14248220. DOI: `10.3390/s151229803`.

[32] K.-l. Chau, S. Lewis, R. Howe, S. Bart, and R. Marcheselli, "An integrated force-balanced capacitive accelerometer for low-g applications," 1996, pp. 472–476.

[33] W. T. Ang, P. Khosla, and C. Riviere, "Design of all-accelerometer inertial measurement unit for tremor sensing in hand-held microsurgical instrument," IEEE, 2003, pp. 1781–1786, ISBN: 0-7803-7736-2. DOI: `10.1109/ROBOT.2003.1241852`. [Online]. Available: `http://ieeexplore.ieee.org/document/1241852/`.

[34] J.-M. Lopez-Hignera, M. Morante, and A. Cobo, "Simple low-frequency optical fiber accelerometer with large rotating machine monitoring applications," *Journal of Lightwave Technology*, vol. 15, no. 7, pp. 1120–1130, 1997. DOI: `10.1109/50.596957`.

[35] P. F. d. C. Antunes, H. F. T. Lima, N. J. Alberto, *et al.*, "Optical fiber accelerometer system for structural dynamic monitoring," *IEEE Sensors Journal*, vol. 9, no. 11, pp. 1347–1354, 2009. DOI: `10.1109/JSEN.2009.2026548`.

[36] E. Udd, "The emergence of fiber optic sensor technology," *Fiber Optic Sensors: An Introduction for Engineers and Scientists*, pp. 1–8, 2011. DOI: `https://doi.org/10.1002/9781118014103.ch1`.

[37] G.-D. Peng, *Handbook of Optical Fibers*. Springer, 2019, vol. 301, ISBN: 978-981-10-7087-7.

[38] H. Berthou and C. Jörgensen, "Optical-fiber temperature sensor based on upconversion-excited fluorescence," *Optics letters*, vol. 15, no. 19, pp. 1100–1102, 1990. DOI: `https://doi.org/10.1364/OL.15.001100`.

[39] C. A. Diaz, A. G. Leal-Junior, P. S. Andre, *et al.*, "Liquid level measurement based on fbg-embedded diaphragms with temperature compensation," *IEEE Sensors Journal*, vol. 18, no. 1, pp. 193–200, 2017. DOI: `https://doi.org/10.1109/JSEN.2017.2768510`.

[40] A. G. Leal-Junior, C. A. Dıaz, A. Frizera, C. Marques, M. R. Ribeiro, and M. J. Pontes, "Simultaneous measurement of pressure and temperature with a single fbg embedded in a polymer diaphragm," *Optics & Laser Technology*, vol. 112, pp. 77–84, 2019. DOI: `https://doi.org/10.1016/j.optlastec.2018.11.013`.

[41] A. Leal-Junior, A. Theodosiou, V. Biazi, *et al.*, "Temperature-insensitive curvature sensor with plane-by-plane inscription of off-center tilted bragg gratings in cytop fibers," *IEEE Sensors Journal*, vol. 22, no. 12, pp. 11 725–11 731, 2022. DOI: `https://doi.org/10.1109/JSEN.2022.3171039`.

[42] L. Macedo, R. W. M. P. Junior, A. Frizera, M. J. Pontes, and A. Leal-Junior, "An alternative to discarded plastic: A report of polymer optical fiber made from recycled materials for the development of biosensors," *Optical Fiber Technology*, vol. 72, p. 103 001, 2022. DOI: `https://doi.org/10.1016/j.yofte.2022.103001`.

[43] E. A. Souza, L. C. Macedo, A. Frizera, C. Marques, and A. Leal-Junior, "Fiber bragg grating array for shape reconstruction in structural elements," *Sensors*, vol. 22, no. 17, p. 6545, 2022. DOI: `https://doi.org/10.3390/s22176545`.

[44] L. Macedo, E. A. Souza, A. Frizera, M. J. Pontes, C. Marques, and A. Leal-Junior, "Static and dynamic multiparameter assessment of structural elements using chirped fiber bragg gratings," *Sensors*, vol. 23, no. 4, p. 1860, 2023. DOI: `https://doi.org/10.3390/s23041860`.

[45] Z. Wang, W. Zhang, J. Han, W. Huang, and F. Li, "Diaphragm-based fiber optic fabry–perot accelerometer with high consistency," *Journal of Lightwave Technology*, vol. 32, no. 24, pp. 4810–4815, 2014. DOI: `10.1109/JLT.2014.2367001`.

[46] M. R. Layton, B. A. Danver, J. D. Lastofka, and D. P. Bevan, "A practical fiber optic accelerometer," R. P. DePaula and E. Udd, Eds., Mar. 1988, p. 279. DOI: `10.1117/12.942519`. [Online]. Available: `http://proceedings.spiedigitallibrary.org/proceeding.aspx?doi=10.1117/12.942519`.

[47] T. Zhang, Y. Zhao, D. Wei, and J. Pan, "Fiber-optic michelson accelerometer based on frequency modulation," *IEEE Photonics Technology Letters*, vol. 26, no. 23, pp. 2361–2364, 2014. DOI: `10.1109/LPT.2014.2355256`.

[48] Y. Guozhen, L. Yongqian, and Y. Zhi, "A simple intensity modulation based fiber-optic accelerometer," *Optical Fiber Technology*, vol. 29, pp. 53–58, 2016, ISSN: 1068-5200. DOI: `https://doi.org/10.1016/j.yofte.2016.03.001`. [Online]. Available: `https://www.sciencedirect.com/science/article/pii/S1068520016300013`.

[49] R. Wang, Y. Li, and X. Qiao, "Recent advances in multidimensional fiber bragg grating accelerometers," *Journal of Lightwave Technology*, 2023. DOI: `https://doi.org/10.1109/JLT.2023.3241953`.

[50] W. Udos, Y.-S. Lee, K.-S. Lim, Z.-C. Ong, M. K. A. Zaini, and H. Ahmad, "Signal enhancement of fbg-based cantilever accelerometer by resonance suppression using magnetic damper," *Sensors and Actuators A: Physical*, vol. 304, p. 111 895, 2020. DOI: `https://doi.org/10.1016/j.sna.2020.111895`.

[51] J. Huang, D. T. Pham, C. Ji, Z. Wang, and Z. Zhou, "Multi-parameter dynamical measuring system using fibre bragg grating sensors for industrial hydraulic piping," *Measurement*, vol. 134, pp. 226–235, 2019. DOI: `https://doi.org/10.1016/j.measurement.2018.10.069`.

[52] S. Jeevanand, B. Singh, B. Panigrahi, and V. Negi, "State of art on condition monitoring of induction motors," in *2010 Joint International Conference on Power Electronics, Drives and Energy Systems & 2010 Power India*, IEEE, 2010, pp. 1–7. DOI: `https://doi.org/10.1109/PEDES.2010.5712465`.

[53] M. Devaney and L. Eren, "Detecting motor bearing faults," *IEEE Instrumentation Measurement Magazine*, vol. 7, no. 4, pp. 30–50, 2004. DOI: `10.1109/MIM.2004.1383462`.

[54] G. Betta, C. Liguori, A. Paolillo, and A. Pietrosanto, "A dsp-based fft-analyzer for the fault diagnosis of rotating machine based on vibration analysis," *IEEE Transactions on Instrumentation and Measurement*, vol. 51, no. 6, pp. 1316–1322, 2002. DOI: `10.1109/TIM.2002.807987`.

[55] J. Zarei, M. A. Tajeddini, and H. R. Karimi, "Vibration analysis for bearing fault detection and classification using an intelligent filter," *Mechatronics*, vol. 24, no. 2, pp. 151–157, 2014, ISSN: 0957-4158. DOI: `https://doi.org/10.1016/j.mechatronics.2014.01.003`.

[56] F. Immovilli, A. Bellini, R. Rubini, and C. Tassoni, "Diagnosis of bearing faults in induction machines by vibration or current signals: A critical comparison," *IEEE Transactions on Industry Applications*, vol. 46, no. 4, pp. 1350–1359, 2010. DOI: `10.1109/TIA.2010.2049623`.

[57] R. Schoen, T. Habetler, F. Kamran, and R. Bartfield, "Motor bearing damage detection using stator current monitoring," *IEEE Transactions on Industry Applications*, vol. 31, no. 6, pp. 1274–1279, 1995. DOI: `10.1109/28.475697`.

[58] H. Ocak and K. A. Loparo, "Estimation of the running speed and bearing defect frequencies of an induction motor from vibration data," *Mechanical systems and signal processing*, vol. 18, no. 3, pp. 515–533, 2004. DOI: `https://doi.org/10.1016/S0888-3270(03)00052-9`.

[59] F. Immovilli, C. Bianchini, M. Cocconcelli, A. Bellini, and R. Rubini, "Bearing fault model for induction motor with externally induced vibration," *IEEE Transactions on Industrial Electronics*, vol. 60, no. 8, pp. 3408–3418, 2013. DOI: `10.1109/TIE.2012.2213566`.

[60] T. H. Patel and A. K. Darpe, "Experimental investigations on vibration response of misaligned rotors," *Mechanical Systems and Signal Processing*, vol. 23, no. 7, pp. 2236–2252, 2009, ISSN: 0888-3270. DOI: `https://doi.org/10.1016/j.ymssp.2009.04.004`. [Online]. Available: `https://www.sciencedirect.com/science/article/pii/S0888327009001289`.

[61] M. Xu and R. Marangoni, “Vibration analysis of a motor-flexible coupling-rotor system subject to misalignment and unbalance, part i: Theoretical model and analysis,” *Journal of Sound and Vibration*, vol. 176, no. 5, pp. 663–679, 1994, ISSN: 0022-460X. DOI: `https://doi.org/10.1006/jsvi.1994.1405`. [Online]. Available: `https://www.sciencedirect.com/science/article/pii/S0022460X84714052`.

[62] A. a. Sekhar and B. Prabhu, “Effects of coupling misalignment on vibrations of rotating machinery,” *Journal of Sound and vibration*, vol. 185, no. 4, pp. 655–671, 1995. DOI: `https://doi.org/10.1006/jsvi.1995.0407`.

[63] P. Goldman and A. Muszynska, “Application of full spectrum to rotating machinery diagnostics,” *Orbit*, vol. 20, no. 1, pp. 17–21, 1999.

[64] D. H. C. de Sá Só Martins, D. P. Viana, A. A. de Lima, *et al.*, “Diagnostic and severity analysis of combined failures composed by imbalance and misalignment in rotating machines,” *The International Journal of Advanced Manufacturing Technology*, vol. 114, no. 9-10, pp. 3077–3092, 2021. DOI: `https://doi.org/10.1007/s00170-021-06873-2`.

[65] A. Djalilov, O. Matchonov, A. Abubakirov, J. Abdunabiev, and A. Saidov, “System for measuring and analysis of vibration in electric motors of irrigation facilities,” *IOP Conference Series: Earth and Environmental Science*, vol. 868, no. 1, p. 012 032, Oct. 2021. DOI: `10.1088/1755-1315/868/1/012032`. [Online]. Available: `https://dx.doi.org/10.1088/1755-1315/868/1/012032`.

[66] R. Kiliç, “Determination of imbalance problem in electric motor and centrifugal pump by vibration analysis,” *Acta Physica Polonica A*, vol. 130, no. 1, pp. 487–491, 2016.

[67] S. Gopinath, “Study on electric motor mass unbalance based on vibration monitoring analysis technique,” in *2010 International Conference on Mechanical and Electrical Technology*, 2010, pp. 539–542. DOI: `10.1109/ICMET.2010.5598417`.

[68] S. Dutta, B. Basu, and F. A. Talukdar, “Classification of induction motor fault and imbalance based on vibration signal using single antenna’s reactive near field,” *IEEE Transactions on Instrumentation and Measurement*, vol. 70, pp. 1–9, 2021. DOI: `10.1109/TIM.2021.3108230`.

[69] J. Jung, S. B. Lee, C. Lim, C.-H. Cho, and K. Kim, “Electrical monitoring of mechanical looseness for induction motors with sleeve bearings,” *IEEE Transactions on Energy Conversion*, vol. 31, no. 4, pp. 1377–1386, 2016. DOI: `10.1109/TEC.2016.2583473`.

[70] P. Balakrishna and U. Khan, “An autonomous electrical signature analysis-based method for faults monitoring in industrial motors,” *IEEE Transactions on Instrumentation and Measurement*, vol. 70, pp. 1–8, 2021. DOI: `10.1109/TIM.2021.3059466`.

[71] E. Fournier, A. Picot, J. Régnier, C. Andrieux, J. Saint-Michel, and P. Maussion, “Effects of transmission belt looseness on electrical and mechanical measurements of an induction motor,” in *2015 IEEE 10th International Symposium on Diagnostics for Electrical Machines, Power Electronics and Drives (SDEMPED)*, 2015, pp. 259–265. DOI: `10.1109/DEMPED.2015.7303699`.

[72] N. Bachschmid, P. PENNACCHI, and A. Vania, “Identification of multiple faults in rotor systems,” *Journal of sound and vibration*, vol. 254, no. 2, pp. 327–366, 2002. DOI: `https://doi.org/10.1006/jsvi.2001.4116`.

[73] C. Di, X. Bao, H. Wang, Q. Lv, and Y. He, "Modeling and analysis of unbalanced magnetic pull in cage induction motors with curved dynamic eccentricity," *IEEE Transactions on Magnetics*, vol. 51, no. 8, pp. 1–7, 2015. DOI: 10.1109/TMAG.2015.2412911.

[74] M. N. Uddin and M. M. Rahman, "Online current and vibration signal monitoring based fault detection of bowed rotor induction motor," in *2015 IEEE Energy Conversion Congress and Exposition (ECCE)*, 2015, pp. 2988–2994. DOI: 10.1109/ECCE.2015.7310078.

[75] A. Usman, N. T. Doiphode, and B. S. Rajpurohit, "Stator winding faults investigation in permanent magnet synchronous motor using motor signatures: Part i," in *2019 International Conference on Electrical Drives Power Electronics (EDPE)*, 2019, pp. 160–168. DOI: 10.1109/EDPE.2019.8883929.

[76] P. Pietrzak and M. Wolkiewicz, "On-line detection and classification of pmsm stator winding faults based on stator current symmetrical components analysis and the knn algorithm," *Electronics*, vol. 10, no. 15, p. 1786, 2021. DOI: https://doi.org/10.3390/electronics10151786.

[77] C. Jin, A. P. Ompusunggu, Z. Liu, H. D. Ardakani, F. Petré, and J. Lee, "Envelope analysis on vibration signals for stator winding fault early detection in 3-phase induction motors," *International Journal of Prognostics and Health Management*, vol. 6, no. 1, 2015. DOI: https://doi.org/10.36001/ijphm.2015.v6i1.2239.

[78] M. Sudha and P. Anbalagan, "A novel protecting method for induction motor against faults due to voltage unbalance and single phasing," in *IECON 2007 - 33rd Annual Conference of the IEEE Industrial Electronics Society*, 2007, pp. 1144–1148. DOI: 10.1109/IECON.2007.4460176.

[79] F. J. T. E. Ferreira, A. M. Silva, and A. T. de Almeida, "Single-phasing protection of line-operated motors of different efficiency classes," *IEEE Transactions on Industry Applications*, vol. 54, no. 3, pp. 2071–2084, 2018. DOI: 10.1109/TIA.2018.2797884.

[80] G. K. Singh and S. A. K. S. Ahmed, "Vibration signal analysis using wavelet transform for isolation and identification of electrical faults in induction machine," *Electric Power Systems Research*, vol. 68, no. 2, pp. 119–136, 2004. DOI: https://doi.org/10.1016/S0378-7796(03)00154-8.

[81] S. Halder, S. Bhat, D. Zychma, and P. Sowa, "Broken rotor bar fault diagnosis techniques based on motor current signature analysis for induction motor—a review," *Energies*, vol. 15, no. 22, p. 8569, 2022. DOI: https://doi.org/10.3390/en15228569.

[82] Y. Gritli, A. O. Di Tommaso, F. Filippetti, R. Miceli, C. Rossi, and A. Chatti, "Investigation of motor current signature and vibration analysis for diagnosing rotor broken bars in double cage induction motors," in *International Symposium on Power Electronics Power Electronics, Electrical Drives, Automation and Motion*, 2012, pp. 1360–1365. DOI: 10.1109/SPEEDAM.2012.6264465.

[83] A. Sharma, L. Mathew, S. Chatterji, and D. Goyal, "Artificial intelligence-based fault diagnosis for condition monitoring of electric motors," *International Journal of Pattern Recognition and Artificial Intelligence*, vol. 34, 13 Dec. 2020, ISSN: 02180014. DOI: 10.1142/S0218001420590430.

[84] W. Lang, Y. Hu, C. Gong, X. Zhang, H. Xu, and J. Deng, "Artificial intelligence-based technique for fault detection and diagnosis of ev motors: A review," *IEEE Transactions on Transportation Electrification*, vol. 8, no. 1, pp. 384–406, 2022. DOI: `10.1109/TTE.2021.3110318`.

[85] S. Personick, "Review of fundamentals of optical fiber systems," *IEEE Journal on Selected Areas in Communications*, vol. 1, no. 3, pp. 373–380, 1983. DOI: `10.1109/JSAC.1983.1145958`.

[86] Z. Fang, K. Chin, R. Qu, and H. Cai, *Fundamentals of optical fiber sensors*. John Wiley & Sons, 2012, vol. 226, ISBN: 978-0-470-57540-6.

[87] S. Shimada, "Systems engineering for long-haul optical-fiber transmission," *Proceedings of the IEEE*, vol. 68, no. 10, pp. 1304–1309, 1980. DOI: `10.1109/PROC.1980.11849`.

[88] S. Addanki, I. Amiri, and P. Yupapin, "Review of optical fibers-introduction and applications in fiber lasers," *Results in Physics*, vol. 10, pp. 743–750, 2018, ISSN: 2211-3797. DOI: `https://doi.org/10.1016/j.rinp.2018.07.028`. [Online]. Available: `https://www.sciencedirect.com/science/article/pii/S2211379718314268`.

[89] L. Jeunhomme, M. Fraise, and J. P. Pocholle, "Propagation model for long step-index optical fibers," *Appl. Opt.*, vol. 15, no. 12, pp. 3040–3046, Dec. 1976. DOI: `10.1364/AO.15.003040`.

[90] T. Ishigure, M. Satoh, O. Takanashi, *et al.*, "Formation of the refractive index profile in the graded index polymer optical fiber for gigabit data transmission," *Journal of Lightwave Technology*, vol. 15, no. 11, pp. 2095–2100, 1997. DOI: `10.1109/50.641528`.

[91] P. Sillard, S. Richard, L.-A. de Montmorillon, and M. Bigot-Astruc, "Micro-bend losses of trench-assisted single-mode fibers," in *36th European Conference and Exhibition on Optical Communication*, 2010, pp. 1–3. DOI: `10.1109/ECOC.2010.5621585`.

[92] X. Zheng, G. Ren, L. Huang, *et al.*, "Bending losses of trench-assisted few-mode optical fibers," *Appl. Opt.*, vol. 55, no. 10, pp. 2639–2648, Apr. 2016. DOI: `10.1364/AO.55.002639`. [Online]. Available: `https://opg.optica.org/ao/abstract.cfm?URI=ao-55-10-2639`.

[93] Y. Lian, G. Ren, Y. Jiang, *et al.*, "Ultralow bending-loss trench-assisted single-mode optical fibers," *IEEE Photonics Technology Letters*, vol. 29, no. 3, pp. 346–349, 2017. DOI: `10.1109/LPT.2017.2647741`.

[94] T. A. Birks, J. C. Knight, and P. S. J. Russell, "Endlessly single-mode photonic crystal fiber," *Opt. Lett.*, vol. 22, no. 13, pp. 961–963, Jul. 1997. DOI: `10.1364/OL.22.000961`.

[95] K. Tajima, K. Kurokawa, K. Nakajima, and I. Sankawa, "Photonic crystal fiber," *NTT Technical Review*, vol. 3, pp. 57–61, 8 Aug. 2005, ISSN: 13483447. DOI: `10.1126/science.1079280`.

[96] S. A. Cerqueira, "Recent progress and novel applications of photonic crystal fibers," *Reports on Progress in Physics*, vol. 73, no. 2, p. 024 401, Jan. 2010. DOI: `10.1088/0034-4885/73/2/024401`. [Online]. Available: `https://dx.doi.org/10.1088/0034-4885/73/2/024401`.

[97] S. T. Huntington, K. A. Nugent, A. Roberts, P. Mulvaney, and K. M. Lo, "Field characterization of a D-shaped optical fiber using scanning near-field optical microscopy," *Journal of Applied Physics*, vol. 82, no. 2, pp. 510–513, Jul. 1997, ISSN: 0021-8979. DOI: 10.1063/1.365608.

[98] C.-H. Chen, T.-C. Tsao, J.-L. Tang, and W.-T. Wu, "A multi-d-shaped optical fiber for refractive index sensing," *Sensors*, vol. 10, no. 5, pp. 4794–4804, 2010, ISSN: 1424-8220. DOI: 10.3390/s100504794. [Online]. Available: https://www.mdpi.com/1424-8220/10/5/4794.

[99] Y. Ying, G.-y. Si, F.-j. Luan, K. Xu, Y.-w. Qi, and H.-n. Li, "Recent research progress of optical fiber sensors based on d-shaped structure," *Optics Laser Technology*, vol. 90, pp. 149–157, 2017, ISSN: 0030-3992. DOI: https://doi.org/10.1016/j.optlastec.2016.11.021. [Online]. Available: https://www.sciencedirect.com/science/article/pii/S0030399216310301.

[100] G. An, S. Li, H. Wang, and X. Zhang, "Metal oxide-graphene-based quasi-d-shaped optical fiber plasmonic biosensor," *IEEE Photonics Journal*, vol. 9, no. 4, pp. 1–9, 2017. DOI: 10.1109/JPHOT.2017.2722543.

[101] M. Arumugam, "Optical fiber communication—an overview," *Pramana*, vol. 57, pp. 849–869, 5-6 Nov. 2001, ISSN: 0304-4289. DOI: 10.1007/s12043-001-0003-2. [Online]. Available: http://link.springer.com/10.1007/s12043-001-0003-2.

[102] D. Axelrod, T. P. Burghardt, and N. L. Thompson, "Total internal reflection fluorescence," *Annual review of biophysics and bioengineering*, vol. 13, no. 1, pp. 247–268, 1984.

[103] D. Singh, *Fundamentals of optics*. PHI Learning Pvt. Ltd., 2015, ISBN: 978-81-203-5146-2.

[104] W. Wadsworth, R. Percival, G. Bouwmans, *et al.*, "Very high numerical aperture fibers," *IEEE Photonics Technology Letters*, vol. 16, no. 3, pp. 843–845, 2004. DOI: 10.1109/LPT.2004.823689.

[105] J.-N. Maran, R. Slavik, S. LaRochelle, and M. Karasek, "Chromatic dispersion measurement using a multiwavelength frequency-shifted feedback fiber laser," *IEEE Transactions on Instrumentation and Measurement*, vol. 53, no. 1, pp. 67–71, 2004. DOI: 10.1109/TIM.2003.822008.

[106] E. A. J. Marcatili, "Modal dispersion in optical fibers with arbitrary numerical aperture and profile dispersion," *The Bell System Technical Journal*, vol. 56, no. 1, pp. 49–63, 1977. DOI: 10.1002/j.1538-7305.1977.tb00152.x.

[107] T. Izawa, N. Shibata, and A. Takeda, "Optical attenuation in pure and doped fused silica in the ir wavelength region," *Applied Physics Letters*, vol. 31, no. 1, pp. 33–35, Aug. 2008, ISSN: 0003-6951. DOI: 10.1063/1.89468. eprint: https://pubs.aip.org/aip/apl/article-pdf/31/1/33/7738593/33_1_online.pdf. [Online]. Available: https://doi.org/10.1063/1.89468.

[108] M. Barnoski, *Fundamentals of optical fiber communications*. Elsevier, 2012, ISBN: 978-3-527-41006-4.

[109] E. Guillermain, J. Kuhnhenn, D. Ricci, and U. Weinand, "Macro-bending influence on radiation induced attenuation measurement in optical fibres," *IEEE Transactions on Nuclear Science*, vol. 61, no. 4, pp. 1834–1837, 2014. DOI: 10.1109/TNS.2014.2306992.

[110] M.-J. Li, P. Tandon, D. C. Bookbinder, *et al.*, "Designs of bend-insensitive multimode fibers," in *2011 Optical Fiber Communication Conference and Exposition and the National Fiber Optic Engineers Conference*, 2011, pp. 1–3.

[111] W. B. Gardner, "Microbending loss in optical fibers," *The Bell System Technical Journal*, vol. 54, no. 2, pp. 457–465, 1975. DOI: 10.1002/j.1538-7305.1975.tb02848.x.

[112] S. Takahashi and S. Shibata, "Thermal variation of attenuation for optical fibers," *Journal of Non-Crystalline Solids*, vol. 30, no. 3, pp. 359–370, 1979, ISSN: 0022-3093. DOI: https://doi.org/10.1016/0022-3093(79)90173-X. [Online]. Available: https://www.sciencedirect.com/science/article/pii/002230937990173X.

[113] J. Chen, B. Liu, and H. Zhang, *Review of fiber bragg grating sensor technology*, Jun. 2011. DOI: 10.1007/s12200-011-0130-4.

[114] X. Dong, H. Zhang, B. Liu, and Y. Miao, *Tilted fiber bragg gratings: Principle and sensing applications*, Mar. 2011. DOI: 10.1007/s13320-010-0016-x.

[115] T. Osuch, T. Jurek, K. Markowski, and K. Jedrzejewski, "Simultaneous measurement of liquid level and temperature using tilted fiber bragg grating," *IEEE Sensors Journal*, vol. 16, no. 5, pp. 1205–1209, 2016. DOI: 10.1109/JSEN.2015.2501381.

[116] S. C. Kang, S. Y. Kim, S. B. Lee, S. W. Kwon, S. S. Choi, and B. Lee, "Temperature-independent strain sensor system using a tilted fiber bragg grating demodulator," *IEEE Photonics Technology Letters*, vol. 10, no. 10, pp. 1461–1463, 1998. DOI: 10.1109/68.720294.

[117] S. Korganbayev, M. Sypabekova, A. Amantayeva, *et al.*, "Optimization of cladding diameter for refractive index sensing in tilted fiber bragg gratings," *Sensors*, vol. 22, no. 6, 2022, ISSN: 1424-8220. DOI: 10.3390/s22062259. [Online]. Available: https://www.mdpi.com/1424-8220/22/6/2259.

[118] T. Guo, F. Liu, B.-O. Guan, and J. Albert, "[invited] tilted fiber grating mechanical and biochemical sensors," *Optics Laser Technology*, vol. 78, pp. 19–33, 2016, ISSN: 0030-3992. DOI: https://doi.org/10.1016/j.optlastec.2015.10.007. [Online]. Available: https://www.sciencedirect.com/science/article/pii/S0030399215303893.

[119] J. Albert, L. Y. Shao, and C. Caucheteur, *Tilted fiber bragg grating sensors*, Jan. 2013. DOI: 10.1002/lpor.201100039.

[120] G. Agrawal and S. Radic, "Phase-shifted fiber bragg gratings and their application for wavelength demultiplexing," *IEEE Photonics Technology Letters*, vol. 6, no. 8, pp. 995–997, 1994. DOI: 10.1109/68.313074.

[121] S. Deepa and B. Das, "Interrogation techniques for -phase-shifted fiber bragg grating sensor: A review," *Sensors and Actuators A: Physical*, vol. 315, p. 112 215, 2020, ISSN: 0924-4247. DOI: https://doi.org/10.1016/j.sna.2020.112215. [Online]. Available: https://www.sciencedirect.com/science/article/pii/S0924424720300571.

[122] X. Han and J. Yao, "Bandstop-to-bandpass microwave photonic filter using a phase-shifted fiber bragg grating," *Journal of Lightwave Technology*, vol. 33, no. 24, pp. 5133–5139, 2015. DOI: 10.1109/JLT.2015.2492818.

[123] A. Rosenthal, D. Razansky, and V. Ntziachristos, “High-sensitivity compact ultrasonic detector based on a pi-phase-shifted fiber bragg grating,” *Opt. Lett.*, vol. 36, no. 10, pp. 1833–1835, May 2011. DOI: `10.1364/OL.36.001833`. [Online]. Available: `https://opg.optica.org/ol/abstract.cfm?URI=ol-36-10-1833`.

[124] R. Min, C. Marques, O. Bang, and B. Ortega, “Moiré phase-shifted fiber bragg gratings in polymer optical fibers,” *Optical Fiber Technology*, vol. 41, pp. 78–81, 2018, ISSN: 1068-5200. DOI: `https://doi.org/10.1016/j.yofte.2018.01.003`. [Online]. Available: `https://www.sciencedirect.com/science/article/pii/S1068520017306132`.

[125] D. Uttamchandani and A. Othonos, “Phase shifted bragg gratings formed in optical fibres by post-fabrication thermal processing,” *Optics Communications*, vol. 127, no. 4, pp. 200–204, 1996, ISSN: 0030-4018. DOI: `https://doi.org/10.1016/0030-4018(96)00059-4`. [Online]. Available: `https://www.sciencedirect.com/science/article/pii/0030401896000594`.

[126] J. Burgmeier, C. Waltermann, G. Flachenecker, and W. Schade, “Point-by-point inscription of phase-shifted fiber bragg gratings with electro-optic amplitude modulated femtosecond laser pulses,” *Opt. Lett.*, vol. 39, no. 3, pp. 540–543, Feb. 2014. DOI: `10.1364/OL.39.000540`. [Online]. Available: `https://opg.optica.org/ol/abstract.cfm?URI=ol-39-3-540`.

[127] H. Wang, H. Guo, G. Xiao, N. Mrad, A. Kazemi, and D. Ban, “Phase-shifted fiber-Bragg-grating-based humidity sensor,” in *Photonic Applications for Aerospace, Commercial, and Harsh Environments IV*, A. A. Kazemi, B. C. Kress, and S. Thibault, Eds., International Society for Optics and Photonics, vol. 8720, SPIE, 2013, p. 872 019. DOI: `10.1117/12.2016600`. [Online]. Available: `https://doi.org/10.1117/12.2016600`.

[128] Q. Zhang, N. Liu, T. Fink, H. Li, W. Peng, and M. Han, “Fiber-optic pressure sensor based on π-phase-shifted fiber bragg grating on side-hole fiber,” *IEEE Photonics Technology Letters*, vol. 24, no. 17, pp. 1519–1522, 2012. DOI: `10.1109/LPT.2012.2207715`.

[129] I. S. Amiri, A. N. Z. Rashed, and P. Yupapin, “Analytical model analysis of reflection/transmission characteristics of long-period fiber bragg grating (lpfbg) by using coupled mode theory,” *Journal of Optical Communications*, 2020. DOI: `doi:10.1515/joc-2019-0187`. [Online]. Available: `https://doi.org/10.1515/joc-2019-0187`.

[130] W. Guo, P. Holmberg, F. Laurell, and M. Fokine, “Fabrication of long-period fiber gratings through periodic ablation using a focused co2-laser beam,” *Opt. Mater. Express*, vol. 5, no. 11, pp. 2702–2714, Nov. 2015. DOI: `10.1364/OME.5.002702`.

[131] L. Wang, W. Zhang, P. Geng, *et al.*, “Simultaneous directional bending and temperature measurement with overlapping long period grating and fiber bragg grating structure,” *Journal of Optics*, vol. 16, no. 5, p. 055 401, Mar. 2014. DOI: `10.1088/2040-8978/16/5/055401`. [Online]. Available: `https://dx.doi.org/10.1088/2040-8978/16/5/055401`.

[132] J.-N. Wang and J.-L. Tang, “Feasibility of fiber bragg grating and long-period fiber grating sensors under different environmental conditions,” *Sensors*, vol. 10, no. 11, pp. 10 105–10 127, 2010, ISSN: 1424-8220. [Online]. Available: `https://www.mdpi.com/1424-8220/10/11/10105`.

[133] G. M. Rego, H. M. Salgado, and J. L. Santos, "Interrogation of a fiber bragg grating using a mechanically induced long-period fiber grating," *IEEE Sensors Journal*, vol. 6, no. 6, pp. 1592–1595, 2006. DOI: `10.1109/JSEN.2006.883850`.

[134] H. Zou, D. Liang, and J. Zeng, "Dynamic strain measurement using two wavelength-matched fiber bragg grating sensors interrogated by a cascaded long-period fiber grating," *Optics and Lasers in Engineering*, vol. 50, no. 2, pp. 199–203, 2012, ISSN: 0143-8166. DOI: `https://doi.org/10.1016/j.optlaseng.2011.09.005`. [Online]. Available: `https://www.sciencedirect.com/science/article/pii/S0143816611002624`.

[135] C. Giles, "Lightwave applications of fiber bragg gratings," *Journal of Lightwave Technology*, vol. 15, no. 8, pp. 1391–1404, 1997. DOI: `10.1109/50.618357`.

[136] H. Patrick, G. Williams, A. Kersey, J. Pedrazzani, and A. Vengsarkar, "Hybrid fiber bragg grating/long period fiber grating sensor for strain/temperature discrimination," *IEEE Photonics Technology Letters*, vol. 8, no. 9, pp. 1223–1225, 1996. DOI: `10.1109/68.531843`.

[137] M. P. DeLisa, Z. Zhang, M. Shiloach, *et al.*, "Evanescent wave long-period fiber bragg grating as an immobilized antibody biosensor," *Analytical Chemistry*, vol. 72, pp. 2895–2900, 13 Jul. 2000, ISSN: 00032700. DOI: `10.1021/ac9912395`.

[138] K. Hill and G. Meltz, "Fiber bragg grating technology fundamentals and overview," *Journal of Lightwave Technology*, vol. 15, no. 8, pp. 1263–1276, 1997. DOI: `10.1109/50.618320`.

[139] D. Tosi, "Review of chirped fiber bragg grating (cfbg) fiber-optic sensors and their applications," *Sensors*, vol. 18, no. 7, 2018, ISSN: 1424-8220. DOI: `10.3390/s18072147`. [Online]. Available: `https://www.mdpi.com/1424-8220/18/7/2147`.

[140] A. Halstuch and A. Ishaaya, "Femtosecond inscription of chirped fiber bragg gratings and fiber bragg grating arrays using a single uniform phase-mask," *Optics and Lasers in Engineering*, vol. 160, p. 107 286, 2023, ISSN: 0143-8166. DOI: `https://doi.org/10.1016/j.optlaseng.2022.107286`. [Online]. Available: `https://www.sciencedirect.com/science/article/pii/S0143816622003396`.

[141] D. Kinet, P. Mégret, K. W. Goossen, L. Qiu, D. Heider, and C. Caucheteur, "Fiber bragg grating sensors toward structural health monitoring in composite materials: Challenges and solutions," *Sensors*, vol. 14, no. 4, pp. 7394–7419, 2014, ISSN: 1424-8220. DOI: `10.3390/s140407394`. [Online]. Available: `https://www.mdpi.com/1424-8220/14/4/7394`.

[142] Y. Barbarin, A. Lefrançois, S. Magne, *et al.*, "Dynamic high pressure measurements using a Fiber Bragg Grating probe and an arrayed waveguide grating spectrometer," in *Interferometry XVIII*, K. Creath, J. Burke, and A. A. G. Jr., Eds., International Society for Optics and Photonics, vol. 9960, SPIE, 2016, 99600U. DOI: `10.1117/12.2236651`. [Online]. Available: `https://doi.org/10.1117/12.2236651`.

[143] M. Wydra, P. Kisala, D. Harasim, and P. Kacejko, "Overhead transmission line sag estimation using a simple optomechanical system with chirped fiber bragg gratings. part 1: Preliminary measurements," *Sensors*, vol. 18, no. 1, 2018, ISSN: 1424-8220. DOI: `10.3390/s18010309`. [Online]. Available: `https://www.mdpi.com/1424-8220/18/1/309`.

[144] W. Coimbra, P. Oliveira, C. Marques, and A. Leal-Junior, "Chirped fiber bragg grating sensors for force intensity and location assessment in occlusal splints: A proof-of-concept," *IEEE Transactions on Biomedical Engineering*, vol. 70, no. 4, pp. 1189–1195, 2023. DOI: `10.1109/TBME.2022.3212478`.

[145] G. Alvarez-Botero, F. E. Baron, C. C. Cano, O. Sosa, and M. Varon, "Optical sensing using fiber bragg gratings: Fundamentals and applications," *IEEE Instrumentation Measurement Magazine*, vol. 20, no. 2, pp. 33–38, 2017. DOI: `10.1109/MIM.2017.7919131`.

[146] Y. Qiu, Y. Sheng, and C. Beaulieu, "Optimal phase mask for fiber bragg grating fabrication," *J. Lightwave Technol.*, vol. 17, no. 11, p. 2366, Nov. 1999. [Online]. Available: `https://opg.optica.org/jlt/abstract.cfm?URI=jlt-17-11-2366`.

[147] D. Grobnic, C. Hnatovsky, S. Dedyulin, R. B. Walker, H. Ding, and S. J. Mihailov, "Fiber bragg grating wavelength drift in long-term high temperature annealing," *Sensors*, vol. 21, no. 4, 2021, ISSN: 1424-8220. DOI: `10.3390/s21041454`. [Online]. Available: `https://www.mdpi.com/1424-8220/21/4/1454`.

[148] A. F. Sayed, F. M. Mustafa, A. A. Khalaf, and M. H. Aly, "An enhanced wdm optical communication system using a cascaded fiber bragg grating," *Optical and Quantum Electronics*, vol. 52, 3 Mar. 2020, ISSN: 1572817X. DOI: `10.1007/s11082-020-02305-9`.

[149] B. Zhang and M. Kahrizi, "High-temperature resistance fiber bragg grating temperature sensor fabrication," *IEEE Sensors Journal*, vol. 7, no. 4, pp. 586–591, 2007. DOI: `10.1109/JSEN.2007.891941`.

[150] B. Yun, N. Chen, and Y. Cui, "Highly sensitive liquid-level sensor based on etched fiber bragg grating," *IEEE Photonics Technology Letters*, vol. 19, no. 21, pp. 1747–1749, 2007. DOI: `10.1109/LPT.2007.905093`.

[151] I. Bennion, J. Williams, L. Zhang, K. Sugden, and N. Doran, "Uv-written in-fibre bragg gratings," *Optical and Quantum Electronics*, vol. 28, pp. 93–135, 2 Feb. 1996, ISSN: 0306-8919. DOI: `10.1007/BF00278281`. [Online]. Available: `http://link.springer.com/10.1007/BF00278281`.

[152] S. Kannan, J. Guo, and P. Lemaire, "Thermal stability analysis of uv-induced fiber bragg gratings," *Journal of Lightwave Technology*, vol. 15, no. 8, pp. 1478–1483, 1997. DOI: `10.1109/50.618380`.

[153] D. V. Przhiialkovskii and O. V. Butov, "High-precision point-by-point fiber bragg grating inscription," *Results in Physics*, vol. 30, p. 104 902, 2021, ISSN: 2211-3797. DOI: `https://doi.org/10.1016/j.rinp.2021.104902`. [Online]. Available: `https://www.sciencedirect.com/science/article/pii/S2211379721009372`.

[154] G. D. Marshall, R. J. Williams, N. Jovanovic, M. J. Steel, and M. J. Withford, "Point-by-point written fiber-bragg gratings and their application in complex grating designs," *Opt. Express*, vol. 18, no. 19, pp. 19 844–19 859, Sep. 2010. DOI: `10.1364/OE.18.019844`. [Online]. Available: `https://opg.optica.org/oe/abstract.cfm?URI=oe-18-19-19844`.

[155] J. He, B. Xu, X. Xu, C. Liao, and Y. Wang, *Review of femtosecond-laser-inscribed fiber bragg gratings: Fabrication technologies and sensing applications*, Jun. 2021. DOI: `10.1007/s13320-021-0629-2`.

[156] K. Zhou, M. Dubov, C. Mou, L. Zhang, V. K. Mezentsev, and I. Bennion, "Line-by-line fiber bragg grating made by femtosecond laser," *IEEE Photonics Technology Letters*, vol. 22, no. 16, pp. 1190–1192, 2010. DOI: `10.1109/LPT.2010.2050877`.

[157] K. Yang, J. He, C. Liao, *et al.*, "Femtosecond laser inscription of fiber bragg grating in twin-core few-mode fiber for directional bend sensing," *Journal of Lightwave Technology*, vol. 35, no. 21, pp. 4670–4676, 2017. DOI: `10.1109/JLT.2017.2750407`.

[158] V. Neeharika and P. K. Pattnaik, "Optical mems pressure sensors incorporating dual waveguide bragg gratings on diaphragms," *IEEE Sensors Journal*, vol. 16, no. 3, pp. 681–687, 2016. DOI: `10.1109/JSEN.2015.2482944`.

[159] C. M. Davis, "Fiber Optic Sensors: An Overview," *Optical Engineering*, vol. 24, no. 2, p. 242 347, 1985. DOI: `10.1117/12.7973482`. [Online]. Available: `https://doi.org/10.1117/12.7973482`.

[160] Y. Yao, D. Pan, J. Wang, *et al.*, "Design and modification of a high-resolution optical interferometer accelerometer," *Sensors*, vol. 21, no. 6, 2021, ISSN: 1424-8220. DOI: `10.3390/s21062070`. [Online]. Available: `https://www.mdpi.com/1424-8220/21/6/2070`.

[161] M. Suzuki, T. Takahashi, S. Aoyagi, Y. Amemiya, M. Fukuyama, and S. Yokoyama, "A study of mach-zehnder interferometer type optical modulator applicable to an accelerometer," *Japanese Journal of Applied Physics*, vol. 50, 4 PART 2 Apr. 2011, ISSN: 00214922. DOI: `10.1143/JJAP.50.04DG14`.

[162] D.-L. Tang, P. Wang, X.-D. Zhang, S. He, L. Zhang, and B. Dai, "Micro-mach–zehnder interferometer based on mmi used in seismic accelerometer," *Optik*, vol. 123, no. 19, pp. 1792–1796, 2012, ISSN: 0030-4026. DOI: `https://doi.org/10.1016/j.ijleo.2012.01.043`. [Online]. Available: `https://www.sciencedirect.com/science/article/pii/S0030402612001295`.

[163] B. Wu, "Hybrid-integrated michelson fiber optic accelerometer," *Optical Engineering*, vol. 43, p. 313, 2 Feb. 2004, ISSN: 0091-3286. DOI: `10.1117/1.1634593`.

[164] P. Zhang, S. Wang, J. Jiang, Z. Li, H. Yang, and T. Liu, "A fiber-optic accelerometer based on extrinsic fabry-perot interference for low frequency micro-vibration measurement," *IEEE Photonics Journal*, vol. 14, no. 4, pp. 1–6, 2022. DOI: `10.1109/JPHOT.2022.3183438`.

[165] P.-G. Jia, D.-H. Wang, G. Yuan, and X.-Y. Jiang, "An active temperature compensated fiber-optic fabry–perot accelerometer system for simultaneous measurement of vibration and temperature," *IEEE Sensors Journal*, vol. 13, no. 6, pp. 2334–2340, 2013. DOI: `10.1109/JSEN.2013.2251879`.

[166] B. Culshaw, "The optical fibre sagnac interferometer: An overview of its principles and applications," vol. 17, Institute of Physics Publishing, Jan. 2006. DOI: `10.1088/0957-0233/17/1/R01`.

[167] L. Htein, D. S. Gunawardena, W.-H. Chung, H.-Y. Au, and H.-Y. Tam, "Accelerometer employing a side-hole fiber in a sagnac interferometer," *Journal of Lightwave Technology*, vol. 39, no. 10, pp. 3303–3311, 2021. DOI: `10.1109/JLT.2021.3056474`.

[168] A. Vallan, M. L. Casalicchio, A. Penna, and G. Perrone, "An intensity based fiber accelerometer," in *2012 IEEE International Instrumentation and Measurement Technology Conference Proceedings*, 2012, pp. 1078–1082. DOI: `10.1109/I2MTC.2012.6229126`.

[169] Y. Li, Y. Wang, X. Li, F. Chen, R. Wang, and X. Qiao, "Enhancing the performance of fbg accelerometers by using in-fiber fabry perot interferometers," *IEEE Sensors Journal*, vol. 22, no. 24, pp. 23 931–23 936, 2022. DOI: `10.1109/JSEN.2022.3218677`.

[170] Y. Ge, K. S. Kuang, and S. T. Quek, "Development of a low-cost bi-axial intensity-based optical fibre accelerometer for wind turbine blades," *Sensors and Actuators A: Physical*, vol. 197, pp. 126–135, 2013, ISSN: 0924-4247. DOI: `https://doi.org/10.1016/j.sna.2013.03.016`. [Online]. Available: `https://www.sciencedirect.com/science/article/pii/S0924424713001337`.

[171] A. Sheikhaleh, K. Abedi, K. Jafari, and R. Gholamzadeh, "Micro-optoelectromechanical systems accelerometer based on intensity modulation using a one-dimensional photonic crystal," *Appl. Opt.*, vol. 55, no. 32, pp. 8993–8999, Nov. 2016. DOI: `10.1364/AO.55.008993`. [Online]. Available: `https://opg.optica.org/ao/abstract.cfm?URI=ao-55-32-8993`.

[172] B. Malayappan, U. P. Lakshmi, B. V. V. S. N. P. Rao, K. Ramaswamy, and P. K. Pattnaik, "Sensing techniques and interrogation methods in optical mems accelerometers: A review," *IEEE Sensors Journal*, vol. 22, no. 7, pp. 6232–6246, 2022. DOI: `10.1109/JSEN.2022.3149662`.

[173] E. Davies, D. S. George, M. C. Gower, and A. S. Holmes, "Mems fabry–pérot optical accelerometer employing mechanical amplification via a v-beam structure," *Sensors and Actuators A: Physical*, vol. 215, pp. 22–29, 2014, Special Issue of theMicromechanics Section of Sensors and Actuatorsbased upon contributions revised from the Technical Digest of the 26th IEEE International Conference on MICRO ELECTRO MECHANICAL SYSTEMS (MEMS-13; 20-24 January 2013, Taipei, Taiwan), ISSN: 0924-4247. DOI: `https://doi.org/10.1016/j.sna.2013.08.002`. [Online]. Available: `https://www.sciencedirect.com/science/article/pii/S0924424713003841`.

[174] S. Abozyd, A. Toraya, and N. Gaber, "Design and modeling of fiber-free optical mems accelerometer enabling 3d measurements," *Micromachines*, vol. 13, no. 3, 2022, ISSN: 2072-666X. DOI: `10.3390/mi13030343`. [Online]. Available: `https://www.mdpi.com/2072-666X/13/3/343`.

[175] T. Berkoff and A. Kersey, "Experimental demonstration of a fiber bragg grating accelerometer," *IEEE Photonics Technology Letters*, vol. 8, no. 12, pp. 1677–1679, 1996. DOI: `10.1109/68.544716`.

[176] T. Li, J. Guo, Y. Tan, and Z. Zhou, "Recent advances and tendency in fiber bragg grating-based vibration sensor: A review," *IEEE Sensors Journal*, vol. 20, no. 20, pp. 12 074–12 087, 2020. DOI: `10.1109/JSEN.2020.3000257`.

[177] Y. Yang, E. Wang, K. Chen, Z. Yu, and Q. Yu, "Fiber-optic fabry-perot sensor for simultaneous measurement of tilt angle and vibration acceleration," *IEEE Sensors Journal*, vol. 19, pp. 2162–2169, 6 Mar. 2019, ISSN: 1530437X. DOI: `10.1109/JSEN.2018.2885220`.

[178] H. E. Joe, H. Yun, S. H. Jo, M. B. Jun, and B. K. Min, *A review on optical fiber sensors for environmental monitoring*, Jan. 2018. DOI: `10.1007/s40684-018-0017-6`.

[179] Y. R. García, J. M. Corres, and J. Goicoechea, *Vibration detection using optical fiber sensors*, 2010. DOI: `10.1155/2010/936487`.

[180] L. Mescia and F. Prudenzano, *Advances on optical fiber sensors*, Mar. 2014. DOI: `10.3390/fib2010001`.

[181] A. Vallan, M. L. Casalicchio, and G. Perrone, "Displacement and acceleration measurements in vibration tests using a fiber optic sensor," *IEEE Transactions on Instrumentation and Measurement*, vol. 59, pp. 1389–1396, 5 2010, ISSN: 00189456. DOI: `10.1109/TIM.2010.2040934`.

[182] Y. Li, F. Chen, T. Guo, R. Wang, and X. Qiao, "Sensitivity enhancement of fiber bragg grating accelerometer based on short grating," *IEEE Transactions on Instrumentation and Measurement*, vol. 71, pp. 1–5, 2022. DOI: `10.1109/TIM.2021.3126848`.

[183] Q. Liu, W. Liu, C. Wang, *et al.*, "High figure of merit and low cross sensitivity fiber bragg grating accelerometer based on double grid-diaphragms," *IEEE Sensors Journal*, vol. 21, no. 24, pp. 27 503–27 509, 2021. DOI: `10.1109/JSEN.2021.3124030`.

[184] X. Luo, Y. Li, D. Feng, H. Gao, and J. Zhang, "Fiber bragg grating accelerometer based on symmetrical double flexure hinges," *Optical Fiber Technology*, vol. 68, p. 102 795, 2022, ISSN: 1068-5200. DOI: `https://doi.org/10.1016/j.yofte.2021.102795`. [Online]. Available: `https://www.sciencedirect.com/science/article/pii/S106852002100345X`.

[185] N. Basumallick, S. Bhattacharya, T. K. Dey, P. Biswas, and S. Bandyopadhyay, "Wideband fiber bragg grating accelerometer suitable for health monitoring of electrical machines," *IEEE Sensors Journal*, vol. 20, no. 24, pp. 14 865–14 872, 2020. DOI: `10.1109/JSEN.2020.3011414`.

[186] O. P. Parida, J. Thomas, J. Nayak, and S. Asokan, "Double-l cantilever-based fiber bragg grating accelerometer," *IEEE Sensors Journal*, vol. 19, no. 23, pp. 11 247–11 254, 2019. DOI: `10.1109/JSEN.2019.2936463`.

[187] S. S. Rao, *Mechanical vibrations*. 2019, ISBN: 978-0-134-36130-7.

[188] S. Rubin, "Design of Accelerometers for Transient Measurements," *Journal of Applied Mechanics*, vol. 25, no. 4, pp. 509–514, Jun. 2021, ISSN: 0021-8936. DOI: `10.1115/1.4011864`. eprint: `https://asmedigitalcollection.asme.org/appliedmechanics/article-pdf/25/4/509/6751237/509\_1.pdf`. [Online]. Available: `https://doi.org/10.1115/1.4011864`.

[189] L. Zhu, Y. Fu, R. Chow, B. F. Spencer, J. W. Park, and K. Mechitov, "Development of a high-sensitivity wireless accelerometer for structural health monitoring," *Sensors*, vol. 18, no. 1, 2018, ISSN: 1424-8220. DOI: `10.3390/s18010262`. [Online]. Available: `https://www.mdpi.com/1424-8220/18/1/262`.

[190] G. Yin, Y. Dai, J. Karanja, and J. Dai, "Optimization design for medium-high frequency fbg accelerometer with different eigenfrequency and sensitivity," *Sensors and Actuators A: Physical*, vol. 235, pp. 311–316, 2015, ISSN: 0924-4247. DOI: `https://doi.org/10.1016/j.sna.2015.10.018`. [Online]. Available: `https://www.sciencedirect.com/science/article/pii/S0924424715301795`.

[191] Y. Shi, Y. Zhao, H. Feng, *et al.*, "Design, fabrication and calibration of a high-g mems accelerometer," *Sensors and Actuators A: Physical*, vol. 279, pp. 733–742, 2018, ISSN: 0924-4247. DOI: `https://doi.org/10.1016/j.sna.2018.07.010`. [Online]. Available: `https://www.sciencedirect.com/science/article/pii/S0924424718301493`.

[192] M. Caramia and P. Dell'Olmo, *Multi-objective Management in Freight Logistics: Increasing Capacity, Service Level, Sustainability, and Safety with Optimization Algorithms*. Springer International Publishing, Jul. 2020, pp. 1–196, ISBN: 9783030508128. DOI: `10.1007/978-3-030-50812-8`.

[193] J. Blank and K. Deb, "Pymoo: Multi-objective optimization in python," *IEEE Access*, vol. 8, pp. 89 497–89 509, 2020, ISSN: 21693536. DOI: `10.1109/ACCESS.2020.2990567`.

[194] R. T. Marler and J. S. Arora, *Survey of multi-objective optimization methods for engineering*, Apr. 2004. DOI: `10.1007/s00158-003-0368-6`.

[195] A. Konak, D. W. Coit, and A. E. Smith, "Multi-objective optimization using genetic algorithms: A tutorial," *Reliability Engineering and System Safety*, vol. 91, pp. 992–1007, 9 Sep. 2006, ISSN: 09518320. DOI: `10.1016/j.ress.2005.11.018`.

[196] N. Gunantara, "A review of multi-objective optimization: Methods and its applications," *Cogent Engineering*, vol. 5, pp. 1–16, 1 Jan. 2018, ISSN: 23311916. DOI: `10.1080/23311916.2018.1502242`.

[197] J. L. J. Pereira, G. A. Oliver, M. B. Francisco, S. S. Cunha, and G. F. Gomes, *A review of multi-objective optimization: Methods and algorithms in mechanical engineering problems*, Jun. 2022. DOI: `10.1007/s11831-021-09663-x`.

[198] M. P. Lins, L. Angulo-Meza, and A. C. D. Silva, "A multi-objective approach to determine alternative targets in data envelopment analysis," vol. 55, Nature Publishing Group, 2004, pp. 1090–1101. DOI: `10.1057/palgrave.jors.2601788`.

[199] G. Chiandussi, M. Codegone, S. Ferrero, and F. Varesio, "Comparison of multi-objective optimization methodologies for engineering applications," *Computers Mathematics with Applications*, vol. 63, no. 5, pp. 912–942, 2012, ISSN: 0898-1221. DOI: `https://doi.org/10.1016/j.camwa.2011.11.057`. [Online]. Available: `https://www.sciencedirect.com/science/article/pii/S0898122111010406`.

[200] N. R. Costa and Z. L. Pereira, "Multiple response optimization: A global criterion-based method," *Journal of Chemometrics*, vol. 24, pp. 333–342, 6 2010, ISSN: 1099128X. DOI: `10.1002/cem.1312`.

[201] K. Deb, A. Pratap, S. Agarwal, and T. Meyarivan, "A fast and elitist multiobjective genetic algorithm: Nsga-ii," *IEEE Transactions on Evolutionary Computation*, vol. 6, no. 2, pp. 182–197, 2002. DOI: `10.1109/4235.996017`.

[202] P. Murugan, S. Kannan, and S. Baskar, "NSGA-II algorithm for multi-objective generation expansion planning problem," *Electric Power Systems Research*, vol. 79, no. 4, pp. 622–628, Apr. 2009. DOI: `10.1016/j.epsr.2008.09.011`. [Online]. Available: `https://doi.org/10.1016/j.epsr.2008.09.011`.

[203] S. Kannan, S. Baskar, J. D. McCalley, and P. Murugan, "Application of nsga-ii algorithm to generation expansion planning," *IEEE Transactions on Power Systems*, vol. 24, no. 1, pp. 454–461, 2009. DOI: `10.1109/TPWRS.2008.2004737`.

[204] Y. Yusoff, M. S. Ngadiman, and A. M. Zain, "Overview of NSGA-II for optimizing machining process parameters," *Procedia Engineering*, vol. 15, pp. 3978–3983, 2011. DOI: `10.1016/j.proeng.2011.08.745`. [Online]. Available: `https://doi.org/10.1016/j.proeng.2011.08.745`.

[205] T. M. Hamdani, J.-M. Won, A. M. Alimi, and F. Karray, "Multi-objective feature selection with NSGA II," in *Adaptive and Natural Computing Algorithms*, Springer Berlin Heidelberg, pp. 240–247. DOI: `10.1007/978-3-540-71618-1_27`. [Online]. Available: `https://doi.org/10.1007/978-3-540-71618-1_27`.

[206] S. Verma, M. Pant, and V. Snasel, "A comprehensive review on nsga-ii for multi-objective combinatorial optimization problems," *IEEE Access*, vol. 9, pp. 57 757–57 791, 2021. DOI: `10.1109/ACCESS.2021.3070634`.

[207] M. Jensen, "Reducing the run-time complexity of multiobjective eas: The nsga-ii and other algorithms," *IEEE Transactions on Evolutionary Computation*, vol. 7, no. 5, pp. 503–515, 2003. DOI: `10.1109/TEVC.2003.817234`.

[208] X. R. Liu, K. L. Shi, and J. L. Zou, "Multi-objective optimization design for piezoresistive accelerometer," WORLD SCIENTIFIC, Jan. 2018, pp. 321–326, ISBN: 978-981-323-279-2. DOI: `10.1142/9789813232808_0042`. [Online]. Available: `https://www.worldscientific.com/doi/abs/10.1142/9789813232808_0042`.

[209] S. Desrochers, D. Pasini, and J. Angeles, "Optimum design of a compliant uniaxial accelerometer," vol. 132, Apr. 2010, pp. 0 410 111–0 410 118. DOI: `10.1115/1.4001002`.

[210] M. Farnsworth, E. Benkhelifa, A. Tiwari, M. Zhu, and M. Moniri, "An efficient evolutionary multi-objective framework for MEMS design optimisation: Validation, comparison and analysis," *Memetic Computing*, vol. 3, no. 3, pp. 175–197, Aug. 2011. DOI: `10.1007/s12293-011-0067-6`. [Online]. Available: `https://doi.org/10.1007/s12293-011-0067-6`.

[211] N. Zeelanbasha, V. Senthil, and G. Mahesh, "A hybrid approach of NSGA-II and TOPSIS for minimising vibration and surface roughness in machining process," *International Journal of Operational Research*, vol. 38, no. 2, p. 221, 2020. DOI: `10.1504/ijor.2020.107071`. [Online]. Available: `https://doi.org/10.1504/ijor.2020.107071`.

[212] R. Min, B. Ortega, and C. Marques, "Latest achievements in polymer optical fiber gratings: Fabrication and applications," *Photonics*, vol. 6, no. 2, 2019, ISSN: 2304-6732. DOI: `10.3390/photonics6020036`. [Online]. Available: `https://www.mdpi.com/2304-6732/6/2/36`.

[213] O. P. Parida, J. Nayak, and S. Asokan, "Design and validation of a novel high sensitivity self-temperature compensated fiber bragg grating accelerometer," *IEEE Sensors Journal*, vol. 19, no. 15, pp. 6197–6204, 2019. DOI: `10.1109/JSEN.2019.2909186`.

[214] R. C. Hibbeler, *Resistência dos Materiais*, 10th ed. Pearson Universidades, 2019, ISBN: 8543024994.

[215] W. Zhou, X. Dong, Y. Jin, and C.-L. Zhao, "Cantilever-based fbg sensor for temperature-independent acceleration measurement," in *2009 Asia Communications and Photonics Conference and Exhibition (ACP)*, vol. 2009-Supplement, 2009, pp. 1–6.

[216] M. Todd, G. Johnson, B. Althouse, and S. Vohra, "Flexural beam-based fiber bragg grating accelerometers," *IEEE Photonics Technology Letters*, vol. 10, no. 11, pp. 1605–1607, 1998. DOI: 10.1109/68.726764.

[217] X. Wang, Y. Guo, L. Xiong, and H. Wu, "High-frequency optical fiber bragg grating accelerometer," *IEEE Sensors Journal*, vol. 18, no. 12, pp. 4954–4960, 2018. DOI: 10.1109/JSEN.2018.2833885.

[218] Z. Li, L. Liang, H. Wang, S. Dai, K. Jiang, and Z. Song, "A medium-frequency fiber bragg grating accelerometer based on flexible hinges," *Sensors*, vol. 21, no. 21, p. 6968, Oct. 2021, ISSN: 1424-8220. DOI: 10.3390/s21216968.

[219] R. R. Ribeiro and R. de Melo Lameiras, "Evaluation of low-cost mems accelerometers for shm: Frequency and damping identification of civil structures," *Latin American Journal of Solids and Structures*, vol. 16, 7 CILAMCE 2018 Jul. 2019, ISSN: 16797825. DOI: 10.1590/1679-78255308.

[220] M. K. Iwanaga, M. J. Brennan, B. Tang, O. Scussel, and F. C. L. Almeida, "Some features of the acceleration impulse response function," en, *Meccanica*, vol. 56, no. 1, pp. 169–177, Jan. 2021.

[221] M. A. Karami and D. J. Inman, "Equivalent damping and frequency change for linear and nonlinear hybrid vibrational energy harvesting systems," *Journal of Sound and Vibration*, vol. 330, pp. 5583–5597, 23 Nov. 2011, ISSN: 0022460X. DOI: 10.1016/j.jsv.2011.06.021.

[222] M. Amabili, "Nonlinear damping in large-amplitude vibrations: Modelling and experiments," *Nonlinear Dynamics*, vol. 93, pp. 5–18, 1 Jul. 2018, ISSN: 1573269X. DOI: 10.1007/s11071-017-3889-z.

[223] J. V. Amiri, A. Nikkhoo, M. R. Davoodi, and M. E. Hassanabadi, "Vibration analysis of a mindlin elastic plate under a moving mass excitation by eigenfunction expansion method," *Thin-Walled Structures*, vol. 62, pp. 53–64, 2013, ISSN: 02638231. DOI: 10.1016/j.tws.2012.07.014.

[224] A. Pospori, A. Ioannou, and K. Kalli, "Temperature and humidity sensitivity of polymer optical fibre sensors tuned by pre-strain," en, *Sensors (Basel)*, vol. 22, no. 19, p. 7233, Sep. 2022.

[225] H. Razak and F. Choi, "The effect of corrosion on the natural frequency and modal damping of reinforced concrete beams," *Engineering Structures*, vol. 23, no. 9, pp. 1126–1133, 2001, ISSN: 0141-0296. DOI: https://doi.org/10.1016/S0141-0296(01)00005-0. [Online]. Available: https://www.sciencedirect.com/science/article/pii/S0141029601000050.

[226] P. Pingulkar and B. Suresha, "Free vibration analysis of laminated composite plates using finite element method," *Polymers and Polymer Composites*, vol. 24, no. 7, pp. 529–538, 2016. DOI: 10.1177/096739111602400712.

[227] I. Ramu and S. Mohanty, "Modal analysis of functionally graded material plates using finite element method," *Procedia Materials Science*, vol. 6, pp. 460–467, 2014, 3rd International Conference on Materials Processing and Characterisation (ICMPC 2014), ISSN: 2211-8128. DOI: `https://doi.org/10.1016/j.mspro.2014.07.059`. [Online]. Available: `https://www.sciencedirect.com/science/article/pii/S2211812814004246`.

[228] M. Eltaher, A. E. Alshorbagy, and F. Mahmoud, "Vibration analysis of euler–bernoulli nanobeams by using finite element method," *Applied Mathematical Modelling*, vol. 37, no. 7, pp. 4787–4797, 2013, ISSN: 0307-904X. DOI: `https://doi.org/10.1016/j.apm.2012.10.016`. [Online]. Available: `https://www.sciencedirect.com/science/article/pii/S0307904X1200621X`.

[229] O. Vitek, M. Janda, V. Hajek, and P. Bauer, "Detection of eccentricity and bearings fault using stray flux monitoring," in *8th IEEE Symposium on Diagnostics for Electrical Machines, Power Electronics Drives*, 2011, pp. 456–461. DOI: `10.1109/DEMPED.2011.6063663`.

[230] P. Nivesrangsan and D. Jantarajirojkul, "Bearing fault monitoring by comparison with main bearing frequency components using vibration signal," in *2018 5th International Conference on Business and Industrial Research (ICBIR)*, 2018, pp. 292–296. DOI: `10.1109/ICBIR.2018.8391209`.

[231] C. Castejón, O. Lara, and J. García-Prada, "Automated diagnosis of rolling bearings using mra and neural networks," *Mechanical Systems and Signal Processing*, vol. 24, no. 1, pp. 289–299, 2010, ISSN: 0888-3270. DOI: `https://doi.org/10.1016/j.ymssp.2009.06.004`. [Online]. Available: `https://www.sciencedirect.com/science/article/pii/S0888327009001927`.

[232] C. Mishra, A. Samantaray, and G. Chakraborty, "Ball bearing defect models: A study of simulated and experimental fault signatures," *Journal of Sound and Vibration*, vol. 400, pp. 86–112, 2017, ISSN: 0022-460X. DOI: `https://doi.org/10.1016/j.jsv.2017.04.010`. [Online]. Available: `https://www.sciencedirect.com/science/article/pii/S0022460X17303176`.

[233] A. Khlaief, K. Nguyen, K. Medjaher, *et al.*, "Feature engineering for ball bearing combined-fault detection and diagnostic," in *2019 IEEE 12th International Symposium on Diagnostics for Electrical Machines, Power Electronics and Drives (SDEMPED)*, 2019, pp. 384–390. DOI: `10.1109/DEMPED.2019.8864899`.

[234] P. Borghesani, P. Pennacchi, R. Randall, N. Sawalhi, and R. Ricci, "Application of cepstrum pre-whitening for the diagnosis of bearing faults under variable speed conditions," *Mechanical Systems and Signal Processing*, vol. 36, no. 2, pp. 370–384, 2013, ISSN: 0888-3270. DOI: `https://doi.org/10.1016/j.ymssp.2012.11.001`. [Online]. Available: `https://www.sciencedirect.com/science/article/pii/S0888327012003950`.

[235] Y. Zhongming and W. Bin, "A review on induction motor online fault diagnosis," in *Proceedings IPEMC 2000. Third International Power Electronics and Motion Control Conference (IEEE Cat. No.00EX435)*, vol. 3, 2000, 1353–1358 vol.3. DOI: `10.1109/IPEMC.2000.883050`.

[236] M. Ojaghi, M. Sabouri, and J. Faiz, "Analytic model for induction motors under localized bearing faults," *IEEE Transactions on Energy Conversion*, vol. 33, no. 2, pp. 617–626, 2018. DOI: `10.1109/TEC.2017.2758382`.